Hybrid thin-film solar cells based on nano-structured silicon and semiconducting polymer

Pierre-Jean Alet

ÉCOLE POLYTECHNIQUE
Laboratoire de physique des interfaces et couches minces

Laboratoire de chimie des surfaces et interfaces

Pierre-Jean Alet

Hybrid thin-film solar cells based on nano-structured silicon and semiconducting polymer

Doctoral thesis in Materials Science

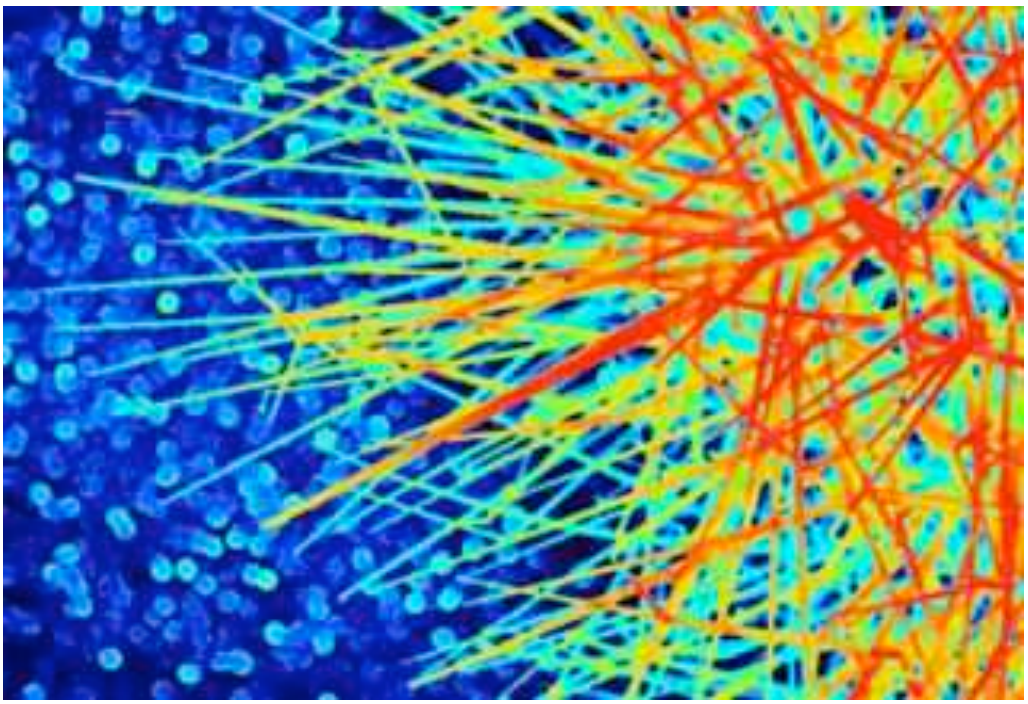

École Polytechnique

É c o l e P o l y t e c h n i q u e

Thèse

présentée en vue d'obtenir le grade de docteur, spécialité
Sciences des matériaux

par

Pierre-Jean Alet

Cellules photovoltaïques en couches minces à base de silicium nanostructuré et de polymère semiconducteur

Thèse soutenue le 14 novembre 2008 devant le jury composé de :

Dr.	Jean-Noël CHAZALVIEL	École polytechnique/CNRS	Président
Prof.	Anna FONTCUBERTA I MORRAL	EPFL, Lausanne	Rapporteur
Prof.	Jenny NELSON	Imperial College, London	Rapporteur
Dr.	Serge PALACIN	CEA Saclay	Encadrant
Dr.	Joaquim PUIGDOLLERS	Universitat Politècnica de Catalunya	Examinateur
Dr.	Pere ROCA I CABARROCAS	École polytechnique/CNRS	Directeur de thèse

To my sunshine

Acknowledgements

In the beginning was a dream team. They came from three laboratories, they imagined a challenging multidisciplinary project, and they accepted to entrust me with it. I am much thankful to them four: Pere Roca i Cabarrocas, Muriel Firon, Anna Fontcuberta i Morral, and Serge Palacin.

Changes in the strategy and organization at CEA forced Muriel to move to completely different activities. I was fortunate enough for she was still present during my first months. She largely contributed to give this thesis a good start. No matter how hectic her new position, she kept following my work throughout these three years. *Merci Muriel.*

Young scientists often have a nomadic life. Anna is no exception. Before I started my work, she had moved to Munich. I would have loved to work more with her, but at least her new positions gave her all the required titles and independence to be one of my rapporteurs. I could not have dreamt of someone more able for that role. I really appreciate she accepted it while moving again and starting a new team. *Thank you, merci, danke, graciès Anna.*

Serge Palacin welcomed me in his group in Saclay in spite of my large ignorance of chemistry. His administrative duties have constantly increased during these three years, my work remained far from his favorite research topics, yet he constantly supported me, trusted me, and appropriately advised me. He is for sure a great scientist. And he is an exceptionally fair group leader. *Merci Serge.*

I barely spent a week in Pere's group during my final year of master, but it was enough to make me change my mind about doing a PhD. Pere is impressive. He seems hardly human, as he knows all the tips and tricks of the reactors, as he works all the time, as he manages to cope with an overcrowded office and people queuing to see him, as he keeps track of everybody's activity and switches topics tens of times a day. And yet he is so human. He pays attention to everyone. He grows tomatoes. He is addicted to candied ginger. And he likes frogs. Even more important for me, he is an excellent PhD advisor. He knows the difficult art of stimulating without stressing, challenging without hitting, delegating without abandoning. I have been more than lucky to work with him. *Graciès Pere !*

I am much thankful to Jenny Nelson for accepting to be one of my rapporteurs. It was an intimidating honor to have my work reviewed by such an inspiring and dedicated scientist, and it was a pleasure to answer her stimulating questions. Jean-Noël

Chazalviel accepted to chair the jury, and he did so with great commitment. He read my manuscript with an impressive attention and contributed to expel errors of any kind from this final version. I am also thankful to Joaquim Puigdollers, who taught me a lot during my short stay in Barcelona, challenged my views on many occasions, and kindly accepted to be one of my examiners.

Most of this work would not have been possible without help and collaboration from many people. I am much indebted to the organic team of CEA INES in Chambéry, in particular Rémi de Bettignies, Stéphane Guillerez, and Séverine Bailly. They welcomed me on several occasions to perform intensive and fruitful — though sometimes disappointing — runs of experiments. In addition, Stéphane traveled several times all the way to Saclay just to discuss my work. *Merci beaucoup à vous trois !* Laurent Eude, Hee Jin Jeong, Leo Caristan, and Costel-Sorin Cojocaru, from PICM, were of great help with my first CVD experiments on the growth of silicon nanowires, and many SEM images could not have been obtained without them. Speaking of SEM, I am much thankful to Vincent Derycke, from LEM in Saclay, who trained me and allowed me to use theirs extensively.

In Saclay, Sylvain Foucard provided me on many occasions with the creative, reliable experimental setups and accessories he prepared in the mechanics workshop. Some of them have been of critical importance for this work. *Merci Sylvain.* I have often been rescued in front of reluctant reactors by the helpful technical staff of PICM, in particular Gary Rose, Jérôme Charliac, Cyril Jadaud, Olivier Godde.

I have been incredibly lucky with the qualities and friendliness of my colleagues. I shared my office, coffees, doubts, and discoveries with the outstandingly intelligent, generous, and fun *dottore dottore dottore* Alessandro Benedetto. *Grazie mille per tutto.* Guy Deniau helped me a lot in rebuilding Odile and discovering hidden treasures of Saclay. Pascale Jégou and Pascal Viel were strong and sensitive supporters; their attention has been priceless in times of distress or discouragement, not to mention their technical help. Bruno Jousselme is an enthusiastic experimenter and shares many scientific interests with me. We had lots of energizing discussions. Camille Mouton experimented my management skills. I am afraid I did not transmit her any passion for research, but she did a very serious work on P3HT and brought yet another touch of life and originality to LCSI. I shared with this group good science and lots of fun, lively lunches and numerous celebrations. *Merci à toutes et à tous, collectivement et individuellement :* Julienne, Brigitte, Lorraine, Vincent, Antoine, Tuan, Romain, Dimitri, Aidthia, Sébastien, Nabila, Federico, Alan, Fabrice, Achraf, Rachid, Thomas, Fabien, Corinne and Wall-E. *Je vous quitte avec émotion.*

In PICM, Linwei Yu deserves special acknowledgements. With his sustained enthusiasm, his hard work, and his sparkling curiosity, he gave a great boost to the research on silicon nanowires and to my final year. *Xièxie Linwei!* I wish you arrived sooner! Jérôme Damon-Lacoste, Alexei Abramov, and Erik Johnson introduced me to the intimidating ARCAM and helped me on many occasions. I shared friendly moments with them and fellow PhD students and post-docs: Roelene, Ning, Laurent, Makrina, Ingrid, Maher... Among them, I wish to thank Yassine Djeridane, Nans Pham and Martin Labrune, who were very helpful with experiments as well. Thanks also to

all the staff who make this lab, smoothly managed by Bernard Drévillon and Yvan Bonnassieux, a very pleasant place to work.

Some people have played a special role in my scientific education and hence to this thesis. Among them, Joaquim Nassar was a great deputy manager for research and education at ENSTA. He strongly supported me when I was considering starting a PhD, and he found the time to attend my defense. I am also grateful to committed and inspiring high school teachers who contributed to shape my intellectual life: M. Lainé, Mme Picard, M. Fischer. *Merci profondément à vous.*

Personal support outside work has been crucial during these years, not least to prevent me from getting (completely) crazy. I should first name my family, my mother Anne who proofread this entire document and produced a rather personal and literary summary, my father Bernard and my sisters Claire, Mathilde and Lucie. Though science is quite far from their personal interests, they have been present and helpful up to my defense. It was also a blessing to be surrounded by reliable friends throughout these years. *Merci* François, Marion, Xavier, Benoît, Kumiko, Romain, Lucie, Xin *et tous les autres.* I shall also thank my fellow members of MAIOT, with whom I shared so many Wednesday lunches, RER delays, and beers at the Piano Vache. *Merci à tous :* François, Satchin, Alessandro, Stéphane, Stéphane, Béatrice, Éric, Clémence, Bertrand, Charlotte *et al.*

On a sunny summer day of 2006, a light green dress entered my life. Since then the strongest personal support by far came from Gaëlle. She proofread this document, and she cooked macaroons. Day after day, she coped with my bad mood or my overexcitement. What she brought me is far beyond the few sentences I could write here. Just thank you for what you are and what we will be.

Contents

Introduction

> The ultimate answer to humanity's energy problems rises every morning and sets every evening.
>
> Editorial, *Nature, 14th August 2008*

There is a paradox in the world of photovoltaics. On one side, dozens, if not hundreds, of different materials and architectures have been investigated. They range from inorganic single-crystal single junctions to solution-processed organic tandem cells to hybrid organic/inorganic devices.[1] Many of them are still active topics, either in industry or in academic research, and we will introduce another new design in this work. On the other side, more than fifty years after the first report of cells based on crystalline silicon p-n junction,[2] this structure still represents more than 90% of the market![3]

It is indeed a mature technology, which developed in parallel to the microelectronics industry. It has reasonable power conversion efficiencies (module efficiency above 22% in laboratory),[4] its stability is good (performance are commonly guaranteed over 25 years). Most importantly, its energy payback time, *i.e.*, the required operation time for an installation to produce the amount of energy used during its production, is small (about two years) as compared to its lifetime.[5] So why bother developing something else? To make it short, crystalline silicon is too expensive. That is why, in spite of unique growth rates (between 30% and 40% per year for years), the contribution by photovoltaics to the global energy mix is still negligible.

The cost structure of photovoltaics is quite original. The primary source — sunlight — is *really* free, as it is not stored on earth, and it is almost unlimited: the sun provides the earth with 10000 times the human energy consumption. So at first glance,

[1] Goetzberger, Hebling, and Schock, "Photovoltaic materials, history, status and outlook", 2003 [GHS03]

[2] Chapin, Fuller, and Pearson, "A New Silicon p-n Junction Photocell for Converting Solar Radiation into Electrical Power", 1954 [CFP54]

[3] Platform, *The Status of PV Industry*, 2007 [Pla07]

[4] Green et al., "Short Communication Solar cell efficiency tables (Version 31)", 2008 [Gre+08]

[5] Fthenakis and Alsema, "Photovoltaics Energy Payback Times, Greenhouse Gas Emissions and External Costs: 2004–early 2005 Status", 2006 [FA06]

the power conversion efficiency (PCE) should not be an issue. But, unlike other energy sources like oil or uranium, sunlight is not concentrated. It is a flux spread all over the surface of earth. As a consequence, a given photovoltaic installation will receive a finite power, proportional to its surface (of the order of $1\,\mathrm{kW\,m^{-2}}$). So the cost per kilowatt of electricity it can produce will be determined, at a given location, by the ratio between the cost per square meter of panel and the PCE. The final cost of the produced energy, *i.e.*, the cost per kilowatthour of electricity, will in addition depend on the lifetime of the system.

The three components of the cost (power conversion efficiency, cost per square meter, lifetime) can hardly be optimized at the same time. The problem with crystalline silicon is its price per square meter. This is the very point thin-film photovoltaics, in particular organic, is intended to address. Three factors are used to decrease the costs:

- using less materials (the thickness of the active layer is between 100 nm and a few μm), and using cheap materials, as polymer semiconductors can be expected to be;
- using simple, fast, and non energy-intensive fabrication processes, like printing;
- using inexpensive, flexible substrates like metal foils or polyethylene terephtalate (PET).

In this work, we will not estimate production costs, as it is an exploratory study on a novel cell design. But we will keep in mind these three criteria, and developing simple, straightforward, low-temperature processes will be a constant guideline.

In spite of its low potential production costs, organic-based photovoltaics is not competitive yet because its power conversion efficiency is still too low, and its lifetime too short. The low efficiency comes from a major difference between organic and inorganic semiconductors. In organic semiconductors, light excitation does not create free charge carriers, but electron-hole pairs called *excitons*. As changes in electrical state and morphology are strongly correlated in organic semiconductors, these pairs cannot be easily separated: their binding energy is of the order of 0.1 eV. Thermal excitation (27 meV at room temperature) is thus too small. The difference in electron affinity at the interface between two materials is the only practical mean to dissociate excitons. In that case, the electron goes (or stays) to the material with the higher electron affinity (the *electron acceptor*), while the hole stays (or goes) in the material with the lower electron affinity (the *electron donor*). What is then critical is the short lifetime of excitons. After their creation, they can only diffuse over a few nanometers before recombining. They must be separated in between to contribute to the photocurrent. That gives the major criterion to make efficient organic solar cells: *any point of the active organic semiconductors must be within the exciton diffusion length from an interface with a material whose electron affinity is different enough.*

This requirement is hardly compatible with another one: *to avoid conduction losses, there must be an electrically continuous path from the active interfaces (where*

free charge carriers are generated) to the electrodes (where they are collected). Two different approaches to organic-based solar cells try to balance these two requirements.

The first approach is to make *blends*. In this structure, the electron acceptor and the donor are deposited at the same time, either from a single solution or by co-evaporation, and phase-separate to form nanometer-scaled domains. It has been first developed with polymer donors and fullerene derivatives as acceptors,[6] after fast and efficient electron transfer between these materials have been discovered.[7] The size of the domains is critical in this structure: if they are too small, the charge collection is difficult (the second requirement is not met), and if they are too large, excitons cannot be efficiently harvested at interfaces (the first requirement is not met). Therefore, major improvements in the PCE have been achieved by controlling this size. This has been done by changing the solvent used for the deposition[8] and by thermal annealing.[9] Intrinsic properties of the polymer donor, such as its bandgap and its mobility of charge carriers, also have a strong impact on the electrical performance. This was illustrated when poly(3-hexylthiophene) (P3HT) was introduced as donor.[10] This polymer is still the reference for organic-based solar cells. This structure, also called *bulk heterojunction*, resulted in the highest certified PCE for single-junction organic solar cells so far: 5.4% on 0.096 cm^2.[11] It is still limited by charge collection, as (i) the donor and acceptor domains, respectively, are not necessarily continuous, and (ii) conduction losses bound the thickness of the active layer to about 100 nm, and therefore incident light is only partially absorbed. Evolution of the morphology upon ageing can also be a drawback of this structure.

Solar cells based on blends have also been fabricated with inorganic nanocrystals as electron acceptors, instead of fullerene derivatives. In particular, II-VI compound semiconductors, such as CdSe,[12] have been investigated. These nanocrystals have several potential advantages: their shape can be tuned, from spheres to rods[13] to three-dimensional tetrapods;[14] they can absorb sunlight and their bandgap can be tuned to adapt the absorption spectrum of the active layer to the light. They are

[6] Yu et al., "Polymer Photovoltaic Cells: Enhanced Efficiencies via a Network of Internal Donor-Acceptor Heterojunctions", 1995 [Yu+95]

[7] Sariciftci et al., "Photoinduced Electron Transfer from a Conducting Polymer to Buckminsterfullerene", 1992 [Sar+92]

[8] Shaheen et al., "2.5% efficient organic plastic solar cells", 2001 [Sha+01]

[9] Padinger, Rittberger, and Sariciftci, "Effects of Postproduction Treatment on Plastic Solar Cells", 2003 [PRS03]

[10] Schilinsky, Waldauf, and Brabec, "Recombination and loss analysis in polythiophene based bulk heterojunction photodetectors", 2002 [SWB02]

[11] Laird et al., "Advances in Plexcore active layer technology systems for organic photovoltaics: rooftop and accelerated lifetime analysis of high performance organic photovoltaic cells", 2007 [Lai+07]

[12] Greenham, Peng, and Alivisatos, "Charge separation and transport in conjugated-polymer/semiconductor-nanocrystal composites studied by photoluminescence quenching and photoconductivity", 1996 [GPA96]

[13] Huynh, Dittmer, and Alivisatos, "Hybrid nanorod-polymer solar cells", 2002 [HDA02]

[14] Sun, Marx, and Greenham, "Photovoltaic devices using blends of branched CdSe nanoparticles and conjugated polymers", 2003 [SMG03]

still limited by the same morphological issues as all-organic bulk heterojunctions and by the less efficient charge transfer at their interface with polymers than at the polymer/fullerene interface. So far, the highest reported PCE under simulated solar light is 2.6%.[15] After efficient charge transfer between polymer semiconductors and TiO_2 has been evidenced,[16] metal oxide nanoparticles have also been used as acceptors in blends.[17]

The second approach is to use *nano-structured, porous layers* filled with an organic semiconductor. It has been inspired by Dye-Sensitized Solar Cells (DSSC), where a nano-structured metal oxide is covered by a monolayer of light-absorbing molecules (the dyes) and an electrolyte.[18] In this approach, light absorption and collection of one kind of charge carriers (generally, holes) is done by a polymer semiconductor, and collection of the other kind of charge carriers (generally, electrons) is done by the metal oxide. Excitons generated in the polymer are separated at its interface with the metal oxide. As the nano-structured inorganic layer is deposited on one electrode, then covered by the polymer, the second requirement (continuous paths) is automatically met. The other advantage of this structure is the stability of the domain size, as it is determined by the solid inorganic layer. On the other hand, as metal oxides are wide band-gap semiconductors, they do not contribute to the photo-current. In addition, achieving the right domain size (*i.e.*, pores with diameters about twice the diffusion length of excitons in the polymer), and a good coverage of the inorganic layer by the polymer is very challenging. That is why the PCE of devices based on this approach are still low: less than 0.3% when ZnO rods are used as the nano-structured layer.[19] A comprehensive review on this topic has been published by Bouclé *et al.*[20]

A novel concept has been proposed by groups from CEA Saclay and École polytechnique[21] to combine the advantages of nano-structured porous layers with those of II-VI nanocrystals used in blends. It is a design of *hybrid thin film solar cells based on nano-structured silicon and polymer semiconductor,* schematically shown on fig. 1. In this design, silicon nanowires are used to enhance charge collection and to broaden the absorption spectrum of the active layer. If the nanowires are grown directly on the bottom electrode, continuous paths from the active interface to the electrodes will

[15] Sun and Greenham, "Improved efficiency of photovoltaics based on CdSe nanorods and poly(3-hexylthiophene) nanofibers", 2006 [SG06]

[16] Arango, Carter, and Brock, "Charge transfer in photovoltaics consisting of interpenetrating networks of conjugated polymer and TiO2 nanoparticles", 1999 [ACB99]

[17] Kwong et al., "Poly(3-hexylthiophene):TiO_2 nanocomposites for solar cell applications", 2004 [Kwo+04]

[18] O'Regan and Grätzel, "A low-cost, high-efficiency solar cell based on dye-sensitized colloidal TiO_2 films", 1991 [OG91]

[19] Ravirajan et al., "Hybrid polymer/zinc oxide photovoltaic devices with vertically oriented ZnO nanorods and an amphiphilic molecular interface layer", 2006; Olson et al., "Effect of Polymer Processing on the Performance of Poly(3-hexylthiophene)/ZnO Nanorod Photovoltaic Devices", 2007 [Rav+06; Ols+07]

[20] Bouclé, Ravirajan, and Nelson, "Hybrid polymer-metal oxide thin films for photovoltaic applications." 2007 [BRN07]

[21] Firon et al., "Photoactive nanocomposite and method for the production thereof", 2006 [Fir+06]

be ensured. If the distance between two wires is about twice the exciton diffusion length in the polymer semiconductor (*i.e.*, 16 nm with P3HT), the morphological requirement for an efficient exciton harvesting will be met.

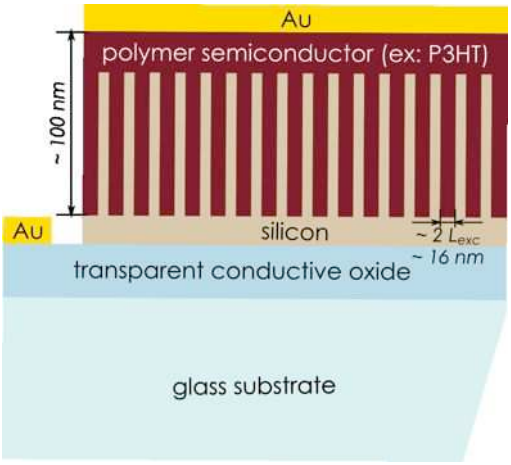

Figure 1 – *Diagram of a silicon/polymer nano-structured hybrid solar cell*

In this thesis, our aim will be to determine if such devices are experimentally feasible, and to analyze their behavior. Indeed, to determine the relevance of this design for photovoltaic applications, several questions are to be answered. Is it possible to grow silicon nanowires directly on transparent conductive oxides (TCO)? Can this growth be done with simple, low-temperature processes? Does the interface between silicon and polymer allow charge transfer and separation of excitons? Is it possible to fill the nano-structured silicon layer with the polymer? How does the nano-structure change the performance of the devices?

In the first chapter, we will investigate the hetero-junction between silicon and the polymer semiconductor we chose (P3HT). We will first present the different active materials to be used in this work. We will then discuss, on the basis of published studies, how the hetero-junction between silicon and P3HT can be described, and what its potential for photovoltaics is. Then we will experimentally investigate this hetero-junction by making and characterizing bilayer devices made of P3HT and various kinds of flat silicon thin films. One structure will be selected and optimized; it will be used as our reference afterward. Part of this work has been published.[22]

In the second chapter, we will focus on the fabrication process and on issues raised by *real* interfaces. We will try to find the origin and to tackle some problems evidenced in the first chapter in the electrical behavior of the cells. In addition, we will simplify the fabrication process, and make it more reliable. We will also change the design of our samples to get more information from each experiment and prevent losses of samples because of *e.g.*, short-circuits.

In the third chapter, we will aim at growing silicon nanowires on transparent conductive oxides. For that, we will present methods to grow silicon nanowires. We will

[22] Alet et al., "Hybrid Solar Cells Based on Thin-Film Silicon and P3HT", 2006 [Ale+06]

then select and adapt one, which is commonly used on crystalline substrates: Chemical Vapor Deposition (CVD) with metallic catalyst droplets. A major step will be to find a simple way to obtain nanometer-scaled metallic aggregates and to characterize them. We chose to make these aggregates by annealing thin evaporated metallic layers. Their size and density, and their evolution mechanism, will be determined through automated analysis of SEM images. A journal article has been published on the basis of this work.[23]

In the fourth chapter, we will try to reduce the growth temperature of silicon nanowires by using Plasma-Enhanced CVD (PECVD). We will first present the potential advantages and drawbacks of PECVD for this. Then we will explore the effects of plasma treatments and deposition, both on metallic aggregates and on the substrates. This will allow us to define deposition processes for various nano-structured silicon thin films. In addition, we will be able to explain some surprising experimental observations made in chapter 3. Three articles and one patent application have been based on this part.[24]

In the fifth and last chapter, we will combine all these results to make and characterize solar cells based on nano-structured silicon thin films. Then we will discuss our results on the basis of other published studies. We will also present some possible ways for future improvements and investigations.

[23] Alet et al., "Transition from thin gold layers to nano-islands on TCO for catalyzing the growth of one-dimensional nanostructures", 2008 [Ale+08b]

[24] Alet, Palacin, and Cabarrocas, "Low-temperature growth of nano-structured silicon thin films on ITO initiated by metal catalysts", 2009; Alet et al., "In-situ generation of indium catalyst to grow crystalline silicon nanowires at low temperature on ITO", 2008; Yu et al., "Synthesis, morphology and compositional evolution of silicon nanowires directly grown on SnO_2 substrates", 2008 [APC09; Ale+08a; Yu+08]

Silicon and P3HT: can they talk together?

1

Make things as simple as possible, but not simpler.

Albert Einstein

Contents

THIS first chapter will be devoted to the study of the hetero-junction between silicon and poly(3-hexylthiophene). In particular, the relevance of such an hetero-junction for photovoltaic conversion will be investigated. We will first present the main electrical and optical properties of the active materials to be used in this study. Then we will focus on the junction. On the basis of published studies, the possible nature and behavior of the organic/silicon junction will be discussed. Possible inorganic structures will be explored and criteria for optimal devices will be given. The behavior of optimal devices will be based on optical and electrical characterizations of the materials and the devices.

The description of fabrication and characterization methods for thin-film solar cells, as given in appendix B, might be helpful at some points of this chapter.

Part of this work has been published in the *European Physical Journal — Applied Physics*.[1]

[1] Alet et al., "Hybrid Solar Cells Based on Thin-Film Silicon and P3HT", 2006 [Ale+06]

1.1 Introduction to the materials used in this study

1.1.1 Semiconductors for solar cells

Why are solar cells based on semiconductors?

Solar cells are power converters: they transform energy carried by sun-light into electrical energy. This conversion is based on energy transfer from photons to electrons. To achieve power production, electrons must remain in an excited state long enough to reach the outer circuit. In other words, the desexcitation rate (either radiative or non-radiative) must be much lower than the excitation rate under illumination. In addition, an energetic asymmetry is required to drive these excited electrons in a particular direction, thus creating a macroscopic current.

Semiconductors are defined as materials where, at 0 K, the higher energy band occupied by electrons is completely full and is separated from the upper band by an *energy gap*, *i.e.*, a range of energy without any possible electronic state. The same definition stands for insulators; the difference lies in the width of the energy gap, E_g. A somewhat arbitrary limit is set around 5 eV:[2] when E_g is below that value, the material is considered a semiconductor; when it is higher, the material is considered an insulator. This energy gap in semiconductors ensures separation between excited and ground states, which is the first requirement for an active material in solar cells. It is, in turn, one of the major constraints on the performance of the devices. Indeed, photons with energy lower than E_g will not be able to excite an electron from the ground state. On the other hand, electrons excited at energies above E_g can desexcite very fast until they reach the top edge of the energy gap. So all the energy difference between the photon energy and E_g is lost for the outer circuit. Now, sun-light is not monochromatic, but white. Its spectrum is much like the black body spectrum at 5760 K. So the conversion efficiency is limited both by the amount of photons which have energies lower than E_g and by the amount of energy lost by electrons excited at energies higher than E_g. Hence a compromise is necessary between these two sources of losses, which is presented on fig. 1.1. The power density of sun-light at the surface of earth is plotted along with its fraction available for conversion by a crystalline silicon solar cell ($E_g = 1.12$ eV). When choosing a material for photovoltaic conversion, a major criterion is to maximize the ratio between the light and the dark gray areas. When thermodynamics is taken into account, the optimal value for E_g in a single-material solar cell is shown to be around 1.4 eV, which is close to the band-gap of GaAs (1.42 eV). In that case, the maximum theoretical efficiency is 33%.

The second requirement for solar cells (energetic asymmetry) is met by making rectifying *junctions*, *i.e.*, by joining two materials where the chemical potential of electrons at equilibrium is different. Such junctions can be either metal/semiconductor junctions (*Schottky junctions*) or semiconductor/semiconductor junctions.

Further details on the physics of photovoltaic converters can be found in text-

[2] This corresponds, *e.g.*, to diamond.

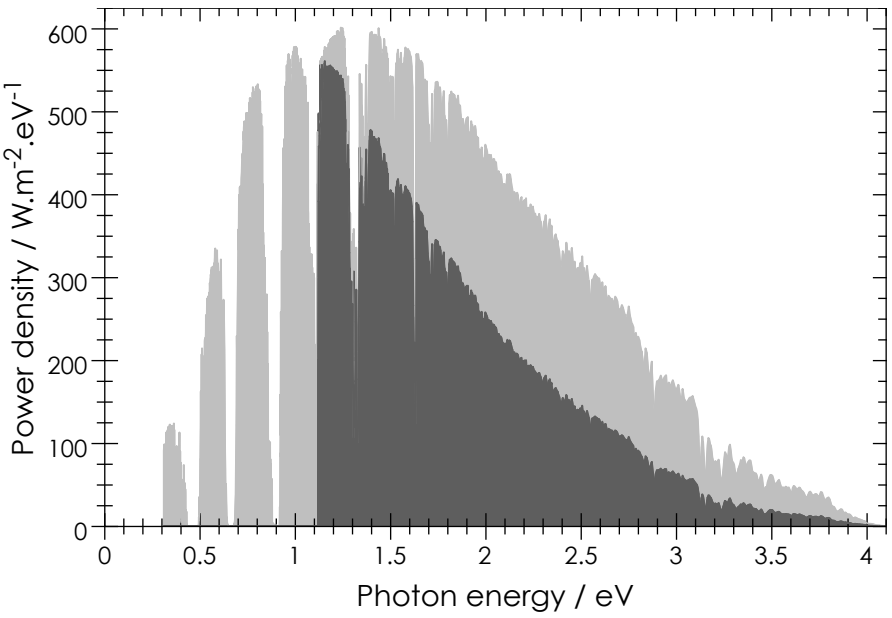

Figure 1.1 – *Power density spectrum of the sun-light at the surface of earth (light gray) and its fraction available for conversion by a crystalline silicon solar cell (dark gray)*

books,[3] and characterization methods used in this study are described in appendix B.

Characteristic quantities of semiconductors

As mentioned before, semiconductors are primarily defined by their energy band-gap. Here we will define some of their properties that will be used throughout this document. They are schematically shown on fig. 1.2.

The *valence band* is the band of highest energy populated by electrons at 0 K. At that temperature, no free state is available in this band. The energy of its upper edge is written E_v.

No allowed states at all for electrons can be found in a range of energy above the valence band edge. The range is called the *band-gap*. Its width is called the band gap energy, often shortened as *gap*, and is written E_g.

The *conduction band* is separated from the valence band by the band gap. Its lower edge is written E_c. At 0 K, the conduction band is completely empty. As there are no states in the band gap, an electron (from the valence band) must be provided an energy larger than E_g to reach the conduction band. In general, possible energy values for electrons in a material depend on its momentum, and so do E_c and E_v. When the maximum value for E_v occurs for the same momentum value as the minimum of E_c, direct transitions from the valence band to the conduction band are possible. In that case, the material is called a *direct band gap* semiconductor. Otherwise, a transition

[3] Fonash, *Solar Cell Device Physics*, 1981; Nelson, *The Physics of Solar Cells*, 2003 [Fon81; Nel03]

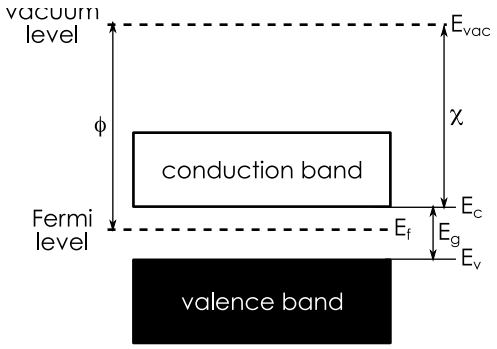

Figure 1.2 – *Simplified band diagram of a semiconductor evidencing its characteristic energy levels*

from the valence band to the conduction band requires a change in the electron momentum through interaction with a phonon[4]. The material is called an *indirect band gap* semiconductor. This is the case of crystalline silicon. Absorption of a photon of energy E_g to promote an electron in the conduction band is much less likely in an indirect band gap semiconductor, where it is a three-body interaction (photon-electron-phonon), than in a direct band gap semiconductor, where it is a two-body interaction. As a consequence, the absorption coefficient of an indirect band gap semiconductor is lower than for a direct one.

The *Fermi energy*, noted E_f, is rather a thermodynamic quantity. Indeed, it is defined by the Fermi function f, which is the probability for a electronic state at an energy E to be occupied when the temperature is T:

$$f = \frac{1}{1+\exp\frac{(E-E_f)}{k_B T}} \tag{1.1}$$

The profile of the Fermi function for various temperatures is plotted on fig. 1.3. The Fermi energy corresponds to the fixed point of the function family: the occupation probability is 0.5 at E_f, whatever the temperature. It can also be seen as a measure of the chemical potential of free electrons of lowest energy in a material.[5] In a semiconductor, the actual probability of finding an electron at a given energy is given by the product of the Fermi function with the density of states, which is derived from the potential created by atoms in the material. When the semiconductor is *intrinsic*, *i.e.*, there are no foreign atoms in the material, the Fermi energy lies roughly in the middle of the band gap.

The *electron affinity*, noted χ, is the difference between the *vacuum level* E_{vac} and the lower edge of the conduction band E_c. The *work function*, noted ϕ, is the minimum energy to provide for an electron to be extracted from the surface of the material. In pure metals, it is well defined as the difference between the Fermi level and

[4]Quantum of vibration energy of the lattice

[5]Rockett, *The Materials Science of Semiconductors*, 2008 [Roc08]

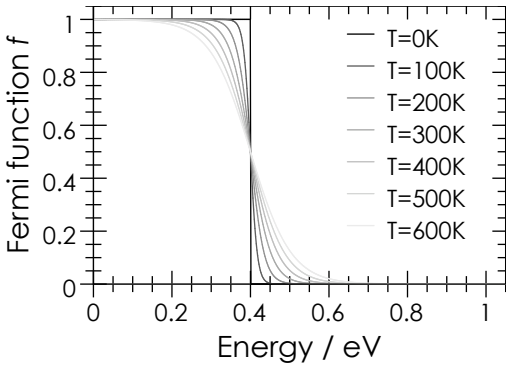

Figure 1.3 – *Plots of the Fermi function for temperatures ranging from 0*K *to 600*K *and a Fermi energy* $E_f = 0.4\,\text{eV}$

the vacuum level, and it can thus be measured by photo-emission spectroscopy. In semiconductors, though, it strongly depends on impurities and surface states.

Such impurities are called *dopant* when they are introduced on purpose in semiconductors. When they have one extra valence electron with respect to the lattice atoms, they are generally *donors*, *i.e.*, they create states in the band gap near the lower edge of the conduction band. This way, they raise the Fermi energy in the semiconductor. They are called *n-dopant*, as they increase the density n of free electrons in the material. Phosphorus is a typical n-dopant for silicon. Conversely, when they have one fewer valence electron than the lattice atoms, they are generally *acceptors*, *i.e.*, they create states near the upper edge of the valence band and they lower the Fermi energy. They are called *p-dopant*, as they increase the density p of free holes[6] in the material. Boron is a typical p-dopant in silicon. A purified semiconductor without any dopant is called *intrinsic*.

The electrical *conductivity* σ links the current flowing through a material to an external electric field. If $\mathbf{J}$ is the current density and $\mathbf{E}$ is the external electric field then, in the absence of diffusion, $\mathbf{J} = \sigma\mathbf{E}$. The current can be carried by electrons and by holes, so the conductivity can be divided in two parts, each of which is proportional to the densities n and p of electrons and holes, respectively. This relationship is written as follows, where q is the charge of the electron:

$$\sigma = q\left(\mu_n n + \mu_p p\right) \tag{1.2}$$

The proportionality constants μ_n and μ_p are called the electron and hole *mobilities*, respectively. They are defined (eq. 1.3) by the critical velocity $\mathbf{v}_c$ of these charge carriers when they are accelerated by an external electric field $\mathbf{E}$ and slowed down by scattering events, which are characteristic of the material. If τ is the average time between scattering events and m^* is the effective mass of the carrier, which depends on

[6]Holes are "missing electrons" but they behave as real particles of positive charge

its nature and on the potential created by the lattice atoms, then:

$$\mathbf{v}_c \triangleq \mu\mathbf{E} = \frac{q\tau}{m^*}\mathbf{E} \tag{1.3}$$

1.1.2 Silicon

Silicon is the basis for current electronics and photovoltaics, so it is the most widely studied and described semiconductor. Here are given a few properties which will be of major importance in this study.

Silicon atoms are four-fold coordinated. Its basic pattern in solids is made of tetrahedrons, each atom being bonded to four other ones. When a silicon atom is bonded to less than four others, some of its valence electrons are unpaired: they are called *dangling bonds*. Dangling bonds are reactive sites, and they create deep electronic states in the energy band gap. They are especially abundant at the surface of the solid, and at grain boundaries in poly-crystalline materials.

A fundamental property of silicon is its amorphous, passivating oxide, SiO_2. A *native oxide* layer grows spontaneously on the surface of silicon when exposed to air. It is then 2 nm to 3 nm thick. A denser, thicker and more uniform layer can be grown on purpose, for example by exposure to an oxygen plasma.

Crystalline silicon

Bulk crystalline silicon (c-Si) has a cubic, diamond-like crystalline structure. It is an indirect band gap semiconductor. As a consequence, its absorption coefficient in the visible range is relatively low (between $1\times10^3\,\mathrm{cm}^{-1}$ at 1.5 eV and $1\times10^5\,\mathrm{cm}^{-1}$ at 3.1 eV), which means that a thickness about 100 µm is required to completely absorb daylight. Its band gap at room temperature is 1.12 eV.

In bulk crystalline silicon, charge transport is dominated by delocalized electrons in the conduction band and holes in the valence band. The electron mobility is lower or equal to $\mu_n = 1400\,\mathrm{cm}^2\,\mathrm{V}^{-1}\,\mathrm{s}^{-1}$ and the hole mobility is lower or equal to $\mu_p = 450\,\mathrm{cm}^2\,\mathrm{V}^{-1}\,\mathrm{s}^{-1}$. The intrinsic density of carriers at $T = 300\,\mathrm{K}$ is $n_i = 9\times10^9\,\mathrm{cm}^{-3}$, so the conductivity of pure crystalline silicon is about $2.7\times10^{-6}\,\Omega^{-1}\,\mathrm{cm}^{-1}$. Crystalline silicon can be n-doped with *e.g.*, phosphorus, and p-doped with *e.g.*, boron. Typical doping levels in a p-n crystalline silicon solar cell are $1\times10^{19}\,\mathrm{cm}^{-3}$ for n-type and and $1\times10^{16}\,\mathrm{cm}^{-3}$ for p-type. The current record efficiency for such a solar cell is 24.7±0.5%.[7]

Micro-crystalline silicon (µc-Si) is made of crystallites (with typical dimensions of a few tens of nm to 100 nm) embedded in a matrix of hydrogenated amorphous silicon (*cf.* section 1.1.2). Its optical properties are similar to c-Si, but its transport properties are dominated by grain boundaries. Indeed, they suffer both from dangling bonds[8] and from impurities, which tend to accumulate at grain boundaries. As a consequence, the charge mobilities are much lower than in c-Si: the electron mobility

[7] Green et al., "Short Communication Solar cell efficiency tables (Version 31)", 2008 [Gre+08]

[8] Dangling bonds can be partially passivated by hydrogen

μ_e is between $10\,cm^2\,V^{-1}\,s^{-1}$ and $30\,cm^2V^{-1}s^{-1}$, and the hole mobility μ_p is between $0.5\,cm^2\,V^{-1}\,s^{-1}$ and $1\,cm^2V^{-1}s^{-1}$ in intrinsic μc-Si.[9] It is usually incorporated in devices as a thin film (a few µm in thickness). In this work, micro-crystalline silicon is deposited by Plasma-Enhanced Chemical Vapor Deposition (PECVD, see appendix A).

Amorphous silicon

Both the structure and the properties of amorphous silicon are very different from crystalline silicon. It is still based on tetrahedron-bonded silicon atoms, but there are large variations (up to ±10°) of bonding angles with respect to what they are in c-Si (109°28′). As a consequence, whereas in c-Si rings[10] have always six atoms, in amorphous silicon they can have down to four and up to eight atoms (six is still the most probable number). This also leads to an increase in the amount of dangling bonds, even in the bulk of the material. Bonding distortions induce a modification of the density of states at the edge of the valence and conduction bands: instead of a parabolic decrease to zero, there are smooth transitions, which are called *band tails*, between the bands of spatially delocalized states (conduction and valence bands) and the band gap. In addition, dangling bonds create a continuum of localized states between the conduction and the valence bands. Consequently, there is no real band gap, *i.e.*, an energy range where the density of states would be zero. The density of states is still several orders of magnitude lower between the conduction and valence bands than in these bands. This region is called the *mobility band gap* because the mobility of charge carriers in spatially localized states is much lower than in delocalized states. The typical shape of the density of states in amorphous silicon is shown on fig. 1.4.

Pure amorphous silicon is quite useless for electronic applications. In particular, the Fermi level is mainly defined by the dangling bonds. Since their number is very large, it can hardly be modified by doping. This problem has been solved by alloying amorphous silicon with hydrogen.[11] Hydrogen atoms are small enough to insert in the lattice, where they bond to silicon atoms bearing unpaired electrons. Thus they passivate dangling bonds and reduce the density of states in the mobility band gap by up to four orders of magnitude. The resulting material is called *hydrogenated amorphous silicon* (in short, a-Si:H). Thanks to the passivation of dangling bonds by hydrogen, a-Si:H can be doped with, *e.g.*, boron or phosphorus. Hydrogenated amorphous silicon can be deposited from silane (SiH_4) by PECVD (see appendix A). In a-Si:H, dangling bonds are passivated not only in the bulk but also at the surface. As a consequence, it is more stable in air than c-Si or μc-Si.

The optical properties of amorphous silicon derive from its particular distribution of density of states. In particular, its absorption spectrum has a quadratic part, which results from band-to-band absorption, and an exponential part, which results from

[9] Damon-Lacoste, "Vers une ingénierie de bandes des cellules solaires à hétérojonctions a-Si:H/c-Si. Rôle prépondérant de l'hydrogène." 2007 [DL07]

[10] Shortest circuit through individual bonds from an atom back to it

[11] Spear and Le Comber, "Substitutional doping of amorphous silicon", 1975; Street, "Doping and the Fermi Energy in Amorphous Silicon", 1982 [SLC75; Str82]

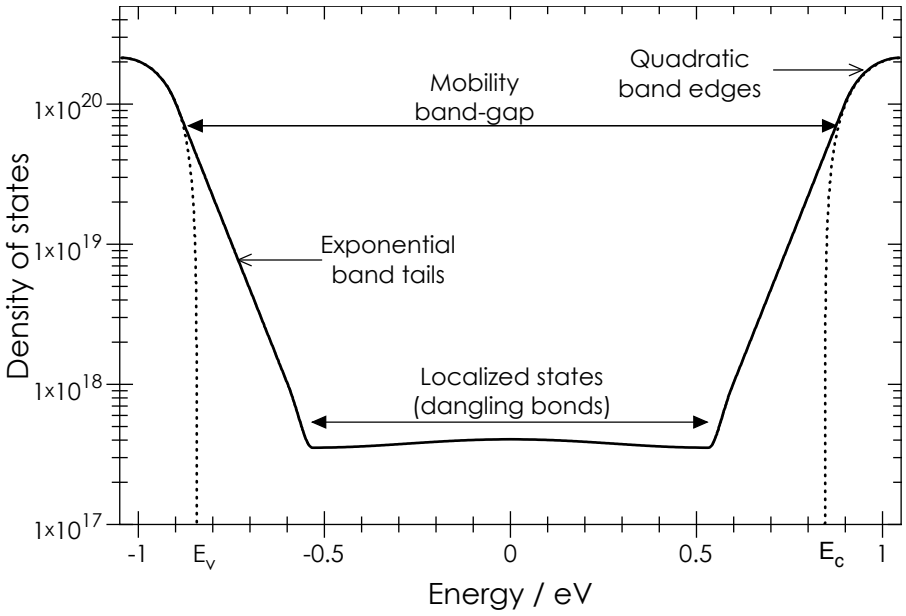

Figure 1.4 – *Typical shape of the density of states in amorphous silicon (continuous lines). The dashed lines represent the case of a crystalline semiconductor with similar band gap (quadratic band edges)*

tail-to-tail absorption. In the quadratic region, the absorption coefficient α is given by: $\alpha = \text{Cste} \times (E - E_{\text{Tauc}})^2$. The characteristic energy E_{Tauc} is called the Tauc gap and is generally considered the value of the optical band gap. Depending on the models, the difference between mobility and absorption band gaps is a constant, which is of the order of 0.1 eV. Amorphous materials have necessarily direct optical band gaps.[12] As a result, absorption is much stronger in amorphous silicon than in crystalline silicon (about one order of magnitude higher in the visible range). In the case of a-Si:H, the Tauc gap depends on the hydrogen content and ranges between 1.5 eV and 1.9 eV.[13] Hydrogenated silicon layers used in this study have typical band gaps of 1.7 eV to 1.8 eV.

Conduction can be split in three mechanisms:

1. Band conduction: as in crystalline semi-conductors, charge can be carried by electrons and holes in delocalized band states (in the conduction band and the valence band, respectively).

2. Hopping between tail states.

[12] The wavenumber **k** of the electrons cannot describe their motion in disordered materials because of their random scattering. As a result, no dispersion relation $E = f(\mathbf{k})$ exists, and indirect transitions are undefined.

[13] Heuvel, Geerts, and Metselaar, "The relation between the optical properties and the hydrogen concentration in a-Si:H", 1991 [HGM91]

3. Tunneling between deep localized states.

As could be expected from a disordered material, the mobilities of charge carriers are low as compared to crystalline silicon: it is about $1\,cm^2\,V^{-1}\,s^{-1}$ for electrons and $1\times10^{-2}\,cm^2V^{-1}s^{-1}$ for holes.

1.1.3 Organic semiconductors

Organic molecules are based on carbon backbones, hydrogen, and functional groups based on other atoms (mainly oxygen, nitrogen, and sulfur). They are called this way because life on earth is based on such molecules. They are also the basis for many common materials such as plastics, which are insulators.

Organic semiconductors are *conjugated* molecules, *i.e.*, their backbone is made of alternate single (σ) and double ($\sigma+\pi$) bonds between carbon atoms. Each atom contribute on average to one single and one double bond with its neighbors, so there are two equivalent configurations of the molecule. Resonance between those two states induce delocalization of the π bonds. Those two states for *trans*-polyacetylene[14] are shown on fig. 1.5. Defects are created when this alternating pattern of single and double bonds is broken and one carbon atom is single bonded to both its neighbors. This carbon atom bears an unpaired valence electron so it is highly reactive. This unpaired electron can be removed through an oxidation reaction, which leaves a positively charged carbon atom (a *carbocation*) in the backbone of the molecule. Alternatively, a reduction reaction can bring an additional electron to stabilize the unpaired electron. This reaction leaves a negatively charge carbon atom (a *carbanion*) in the molecule. Both kinds of charged defects can move along the backbone and carry current. That is how organic semiconductors can be made conductive. From an electrical point of view, carbocations behave as holes do in inorganic materials and carbanions behave as electrons, so they are commonly called this way for convenience.

As the length of single and double bonds is different,[15] there is a coupling between electronic states and atomic positions. Creation of free charge carriers, as described above, induces a modification of the bonding pattern. As a consequence, it creates a distortion of the molecule, which coherence distance in polymers is typically 2 nm. This coupling is a fundamental characteristic of organic semiconductors. In particular, *excitons*, *i.e.*, carbocation/carbanion pairs, are bonded together by electrostatic interaction, and by the force which tends to minimize the distortion of the molecule by keeping the defect localized. This way, their binding energy ranges typically between 0.1 eV and 1 eV, whereas the binding energy of electron-holes pairs in inorganic semiconductors is below the thermal energy at room temperature (25 meV). The most developed application of organic semiconductors to-date, OLED[16], takes advantage

[14] Metallic conductivity in this polymer, when doped with iodine, was discovered in 1974 by Alan Heeger, Alan MacDiarmid and Hideki Shirakawa, who were therefore granted the Nobel prize for chemistry in 2000

[15] It is 0.145 nm and 0.135 nm, respectively, in a linear carbon chain

[16] Organic Light-Emitting Diodes

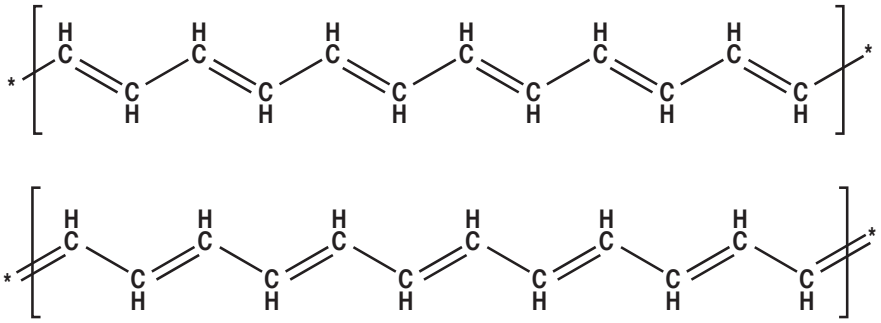

Figure 1.5 – *Diagram of a part of a fully conjugated polymer (polyacetylene) showing its two possible states*

of this spatial confinement of electron-holes pairs, as this maximizes their probability to recombine radiatively. Unfortunately, for solar cells, recombination of electrons with holes is a major source of losses and easy separation of excitons is sought.

Organic semiconductors have some sort of a band structure, which comes from the hybridization of atomic orbitals of their constituent atoms into molecular orbitals. In particular, an energy gap separates the filled, bonding (π) states from the empty, anti-bonding (π^*) states. The highest π state is called *HOMO* (Highest Occupied Molecular Orbital) and the lowest π^* state is called *LUMO* (Lower Unoccupied Molecular Orbital). An analogy is usually drawn between, first, the HOMO level and the valence band edge E_v and, second, the LUMO level and the conduction band edge E_c. This analogy is convenient but one must keep in mind that, as stated in their names, the HOMO and LUMO levels are defined for molecules (including polymers), not for materials. This has two major consequences. First, as the number of atoms in a molecule is limited, there is no continuum of states in the π and π^* bands. Second, optical properties, which derive from the band structure, are modified by inter-molecular interactions when one goes from isolated molecules (*e.g.*, in solution) to thin films.

The power of organic synthesis allows to create a huge range of different molecules. This is an advantage, as their properties (in particular, optical absorption) can be tailored for specific applications. This is also a drawback, as their number and their diversity make it difficult to draw a consistent picture of their behavior, and to check their relevance for application in real devices. Indeed, optimal device structure depends on the material, and it is difficult to predict potential performance of a material from the results on unoptimized devices.

Organic molecules are split in "small" molecules (*i.e.*, without repetition of a pattern) and polymers, made of a large (>100) number of similar units bonded together. Small molecules are generally deposited by evaporation under vacuum, whereas polymers are processed in solution at atmospheric pressure. A complete discussion of the structure and properties of organic semiconductors is far beyond the scope of this

document. For further details, numerous reviews and books are available.[17] P3HT was chosen as the organic semiconductor for this study. Its main properties and reasons for this choice are presented in the next section.

1.1.4 P3HT

P3HT stands for *poly(3-hexylthiophene)*. It is a conjugated polymer based on thiophene rings, *i.e.*, conjugated ring with four carbon atoms and one sulfur. Oligothiophenes[18] and polythiophenes have been widely studied for electronic (thin-film transistors) and opto-electronic (solar cells) applications. Some of the most efficient all-organic solar cells to date are based on P3HT blended with fullerene derivatives, with power conversion efficiencies about 4.4% and short-circuit current densities higher than $10\,\mathrm{mA\,cm^{-2}}$.[19] In addition, both accelerated and real, outdoor ageing measurements have shown that these devices are among the most stable organic ones.[20]

Organization and electrical properties of thin films

Alkyl side-chains, among which hexyl chains, have been added to polythiophene to make it soluble in organic solvents. One-dimensional transport and optical properties of isolated polymer chains essentially depend on the thiophene backbone. In particular, the optical band gap decreases when the number of thiophene units increases. But the materials properties, such as the charge carrier mobility in thin-film transistors, or the absorption spectrum of deposited layers, have been shown to be highly dependent on the organization of the polymer chains with respect to each other and to the substrate. Indeed, two-dimensional transport requires charge transfers between different polymer chains. As charges are mainly carried in π orbitals, overlap between such orbitals of neighbor chains is highly desirable. This can be achieved when conjugated (thiophene) rings of different chains are close and parallel to each other.[21] Such an organization is called "π-stacking". Side chains play a major role in this organization. In particular, they can be bonded to the thiophene ring at two different places (on each of the carbon atom not bonded to neighbor rings). The regularity of this position has a dramatic impact on the properties of polythiophenes: whereas regio-random[22]

[17] Coropceanu et al., "Charge Transport in Organic Semiconductors", 2007; Attias, "Polymères conjugués et polymères conducteurs électroniques", 2002 [Cor+07; Att02]

[18] Ackermann, "Study of the growth and the electronic properties of thin films based on oligothiophenes : Influence of the molecule structure", 2002 [Ack02]

[19] Kim et al., "A strong regioregularity effect in self-organizing conjugated polymer films and high-efficiency polythiophene:fullerene solar cells", 2006 [Kim+06]

[20] De Bettignies et al., "Accelerated lifetime measurements of P3HT:PCBM solar cells", 2006; Hauch et al., "Flexible organic P3HT:PCBM bulk-heterojunction modules with more than 1 year outdoor lifetime", 2008 [DB+06; Hau+08]

[21] Sirringhaus et al., "Two-dimensional charge transport in self-organized, high-mobility conjugated polymers", 1999 [Sir+99]

[22] where alkyl side-chains have random positions on the thiophene rings

P3HT makes amorphous films, regio-regular[23] P3HT shows some crystallinity.[24] Even the band gap is modified, from 2.1 eV in regio-random P3HT to 1.7 eV in regio-regular P3HT. That is why the latter is used in this study, as in most research to date. For simplicity, we will still refer to it simply as P3HT. Its formula is sketched on fig. 1.6. Synthesizing polymers with high regio-regularity is a difficult task, which makes them expensive (around 300€ per gram in research quantities). It is based on Zn mediators.[25] Commercial polymers have been used throughout this study. Most results have been obtained with only two batches, one from Sigma-Aldrich[26] and one from Rieke Metals.

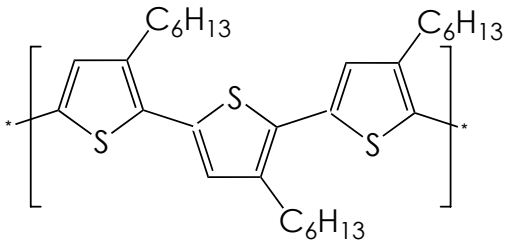

Figure 1.6 – *Formula of regio-regular, head-to-tail poly(3-hexylthiophene-2,5-diyl) (in short, P3HT), as used in this work*

Many other factors have significant impact on the properties of P3HT, especially on its charge carriers mobility: deposition technique,[27] substrate, boiling point of the solvent,[28] thermal treatments,[29] molecular weight (proportional to the number of thiophene units per polymer chain).[30] In general, long chains and well crystallized layers give the best results. That is why using high boiling point solvents (which evaporate slowly), and slowly cooling down[31] annealed layers enhance the performance, as polymer chains have more time to organize. Highest reported mobilities of undoped P3HT is about $0.1\,\mathrm{cm^2\,V^{-1}\,s^{-1}}$ for holes and $1\times10^{-4}\,\mathrm{cm^2\,V^{-1}\,s^{-1}}$ for electrons. They

[23] where the positions of alkyl side-chains follow a periodic pattern

[24] Chen, Wu, and Rieke, "Regiocontrolled Synthesis of Poly(3-Alkylthiophenes) Mediated by Rieke Zinc - Their Characterization and Solid-State Properties", 1995 [CWR95]

[25] Chen and Rieke, "The first regioregular head-to-tail poly(3-hexylthiophene-2,5-diyl) and a regiorandom isopolymer: nickel versus palladium catalysis of 2(5)-bromo-5(2)-(bromozincio)-3-hexylthiophene polymerization", 1992 [CR92]

[26] Batch number: 10118TB, molecular weight: $4115\,\mathrm{g\,mol^{-1}}$, received September 2004, open March, 10th, 2005

[27] Surin et al., "Relationship between the microscopic morphology and the charge transport properties in poly(3-hexylthiophene) field-effect transistors", 2006 [Sur+06]

[28] Chang et al., "Enhanced Mobility of poly(3-hexylthiophene) transistors by spin-coating from high-boiling-point solvents", 2004 [Cha+04]

[29] Cho et al., "Thermal annealing-induced enhancement of the field-effect mobility of regioregular poly(3-hexylthiophene) films", 2006 [Cho+06]

[30] Verilhac et al., "Effect of macromolecular parameters and processing conditions on supramolecular organisation, morphology and electrical transport properties in thin layers of regioregular poly(3-hexylthiophene)", 2006 [Ver+06]

[31] Typical time-scale: 10 min

have been obtained for large molecular weight ($> 30\,kg\,mol^{-1}$), highly regio-regular (>98%) polymers dissolved in trichlorobenzene (boiling point: 213 °C). Whereas the hole mobility is very similar to what it is in a-Si:H, the electron mobility is four orders of magnitude lower.

Deposition

Most polymer depositions in this work have been done by *spin-coating*. The principle of this method is schematized on fig. 1.7. Aspiration by a small pump maintain the substrate on its holder without mechanical constraint. After a small amount of polymer in solution is deposited on the substrate, high speed rotation (typically 1000 to 3000 revolutions per minute) first spreads evenly the liquid on the substrate, then helps uniform evaporation of the solvent. Such a method is very convenient for fast deposition of thin (from 10 nm to few hundreds of nanometers), uniform layers on small substrates (typically, few square centimeters). In the case of P3HT, π-stacking of the polymer chains occurs during evaporation of the solvent. It induces a change in color, from orange to bronze. In this work, chlorobenzene and ortho-dichlorobenzene were generally used as solvents. The standard procedure for spin-coating was: 40 s at 1500 rpm with 4 s ramp-up for spreading the solution, followed by 20 s at 2000 rpm with 4 s ramp-up for evaporating the solvent.

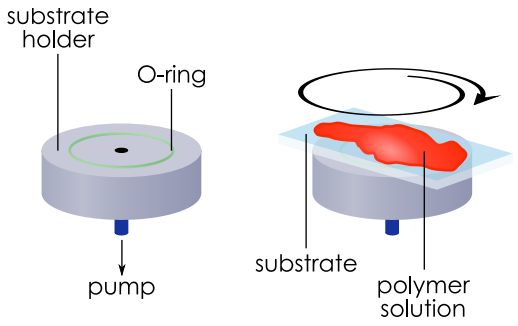

Figure 1.7 – *Principle of polymer deposition by spin-coating*

The thickness of spin-coated layers can be controlled by several parameters: solvent (viscosity and boiling point), concentration of the polymer solution and rotation speed. The influence of these parameters is shown on fig. 1.8. In our experiments, the thickness showed a polynomial dependence on the concentration, with large differences when the solvent is changed (fig. 1.8a). On the other hand, it decreases exponentially when the rotation speed during the first step increases (fig. 1.8b).

Optical properties and energy levels

Position of the HOMO and LUMO levels in P3HT is a debated question and seems to depend on many processing parameters. As shown on tab. 1.1, reported values for the

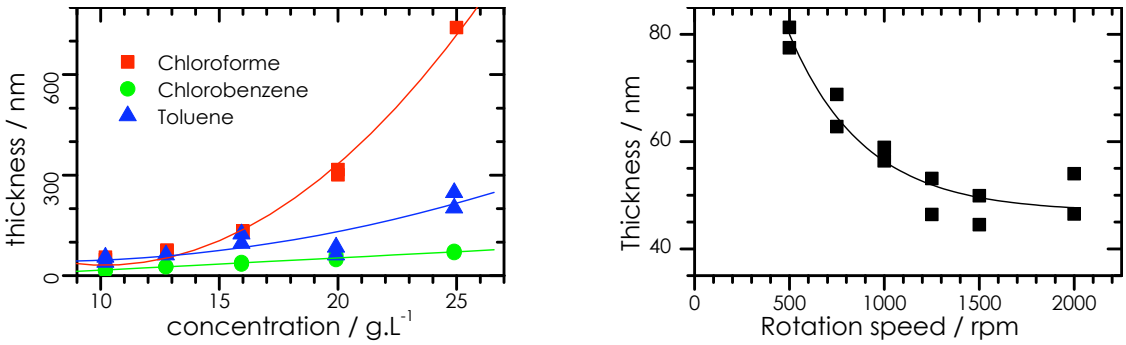

(a) *Influence of the solvent and the solution concentration*

(b) *Influence of the rotation speed during the first step*

Figure 1.8 – *Influence of process parameters on the thickness of spin-coated P3HT layers*

HOMO level vary over a range of 0.5 eV.[32]

Level/eV	Method	Reference
-4.7	photo-electron spectroscopy measurements in air	[Tak+05]
-4.7 to -5.1	electrical measurements under vacuum on Au/P3HT/Au sandwich devices	[Chi+03]
-4.77	electrosprayed P3HT on ITO, measurement by Ultraviolet Photo-electron Spectroscopy under Ultra-High Vacuum	[Yi+06]
-4.9	literature survey	[Rav+06]
-5.2	derived from electrical measurement under vacuum after 6 h storage at 1×10^{-6} mbar	[Tha+07]

Table 1.1 – *Reported positions of P3HT HOMO with respect to the vacuum level*

As we will see later, such a variation is a major concern for us. Indeed, P3HT will be contacted with gold, whose work function is 4.8 eV.[33] If the HOMO level of P3HT is lower than −4.8 eV, the contact with gold will be non-ohmic. Cyclic voltammetry

[32] Takahashi et al., "Porphyrin dye-sensitization of polythiophene in a conjugated polymer/TiOp-n hetero-junction solar cells", 2005; Chirvase et al., "Electrical and optical design and characterisation of regioregular poly(3-hexylthiophene-2,5diyl)/fullerene-based heterojunction polymer solar cells", 2003; Yi et al., "Characterization of indium tin oxide surfaces and interfaces using low intensity x-ray photoemission spectroscopy", 2006; Ravirajan et al., "Hybrid polymer/zinc oxide photovoltaic devices with vertically oriented ZnO nanorods and an amphiphilic molecular interface layer", 2006; Thakur et al., "Charge injection mechanism across the Au-poly(3-hexylthiophene-2,5-diyl) interface", 2007 [Tak+05; Chi+03; Yi+06; Rav+06; Tha+07]

[33] Anderson, "Work Function of Gold", 1959 [And59]

measurements on P3HT from the same source as what was used for this study provided values for the HOMO and LUMO levels of −5.2 eV and −3.53 eV, respectively, hence a band gap of 1.67 eV.[34] There are fewer variations in the reported optical band gap as in the HOMO level: E_g is reported to be between 1.7 eV and 1.9 eV. The differences seem to come mainly from the model used to derive E_g from optical absorption measurements.

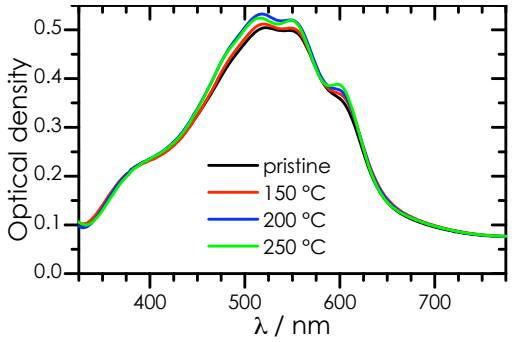

Figure 1.9 – *Absorption spectra of P3HT layers on ITO, as deposited and after 1*h *annealing at various temperatures under nitrogen*

All published absorption spectra are similar to what we measured on our own samples (fig. 1.9). Maximum absorption occurs at 512 nm, where the absorption coefficient α is $1 \times 10^5\,\mathrm{cm}^{-1}$. As can be seen on this graph, post-deposition annealing in inert atmosphere has negligible impact on the optical properties of the layer. On the other hand, P3HT is very sensitive to O_2, which can easily dope it, and hence induce major variations of its electrical properties. Such an effect is shown on fig. 1.10. After one hour annealing in air at 150 °C, fluorescence of the polymer layer is almost completely quenched, whereas no modification of the absorption spectrum nor chemical change can be measured. This means that radiative relaxation of excited states is replaced by non-radiative recombination or by larger charge transfers to the substrate.[35] At the opposite, fluorescence is unchanged or even enhanced upon annealing under inert atmosphere, so contaminants are not absorbed, and may even be released.

1.2 Potential of the silicon/P3HT heterojunction for photovoltaics

Silicon and P3HT have each been successfully used in photovoltaic devices, but what can be expected from their combination? In particular, are charge transfer and separation possible at their interface?

[34] Al-Ibrahim et al., "The influence of the optoelectronic properties of poly(3-alkylthiophenes) on the device parameters in flexible polymer solar cells", 2005 [AI+05]

[35] In that case, ITO.

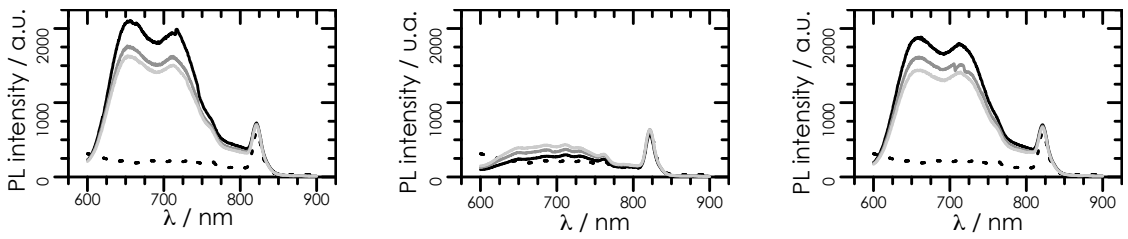

(a) *As-deposited layer* **(b)** *After annealing in air* **(c)** *After annealing under* N_2

Figure 1.10 – *Fluorescence spectra of ITO (dotted line) and P3HT thin films (plain lines) as deposited and after 1*h *annealing at 150*°C *under various atmospheres; on each plot, the three lines correspond to subsequent measurements on the same sample (black: first one, light gray: last one)*

1.2.1 Junctions involving semiconductors

Electronic devices involve several materials, which can form different kinds of junctions at their interface. Such junctions are well described for inorganic semiconductors.

Ohmic contact It occurs when majority charge carriers do not face any potential barrier at the interface between a metal and a semiconductor. This is the case when the Fermi level of an n-type semiconductor[36] lies below the Fermi level of the metal. This way, electrons flow from the metal into the semiconductor upon contact. Conversely, ohmic contact occurs when the Fermi level of a p-type semiconductor[37] lies above the Fermi level of the metal. This condition allows electrons to flow from the semiconductor to the metal upon contact. In both cases, the resulting band bending in the semiconductor is favorable to the transfer of majority charge carriers to the metal (fig. 1.11).

Schottky contact It is a rectifying metal/semiconductor junction. It occurs in opposite cases as ohmic junction, *i.e.*, when majority carriers are extracted from the semiconductor upon contact with the metal. In that case, the resulting band bending at the interface opposes transfer of majority carriers to the metal during operation (fig. 1.12).

p-n junction It is a rectifying semiconductor homojunction. It occurs at the interface between two pieces of one semiconductor, with different doping (fig. 1.13). Qualitatively, electrons diffuse upon contact from the n-type region to the p-type region until their chemical potential,*i.e.*, the Fermi level, is the same in both parts. Conversely, holes flow from the p-doped region to the n-doped region. Due to ionized

[36] where electrons are majority carriers
[37] where holes are majority carriers

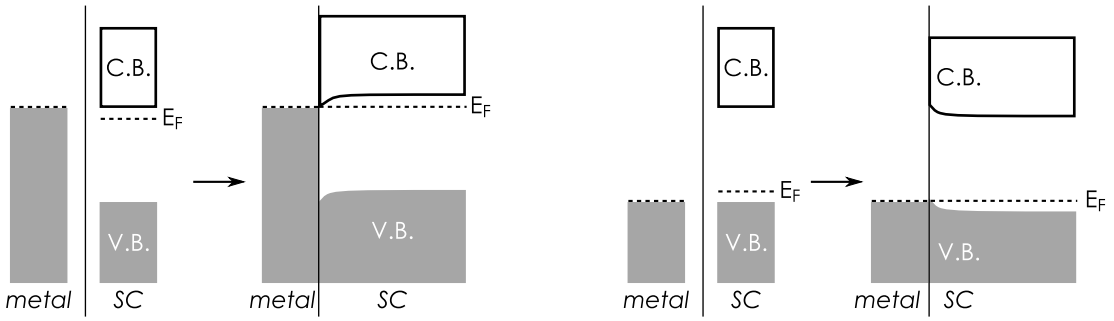

(a) *With n-type semiconductor* **(b)** *With p-type semiconductor*

Figure 1.11 – *Band diagrams of Ohmic junction before ((left) and after (right) contact between a metal and a doped semiconductor*

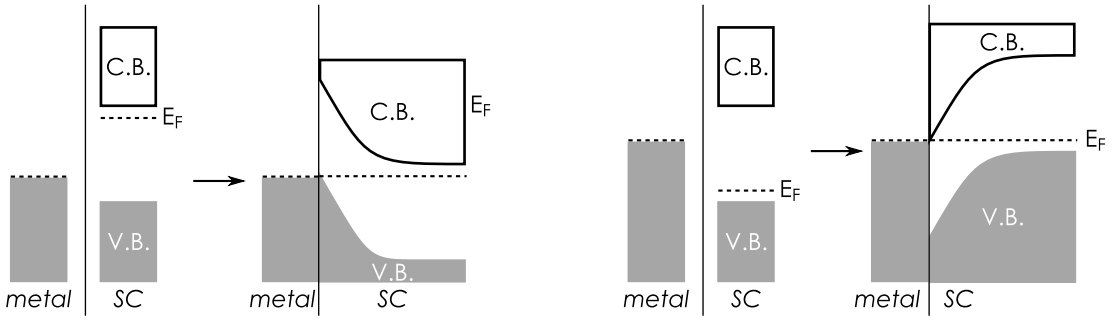

(a) *With n-type semiconductor* **(b)** *With p-type semiconductor*

Figure 1.12 – *Band diagrams of Schottky junction before ((left) and after (right) contact between a metal and a doped semiconductor*

dopants left behind, an electric field appears at the interface between the two materials, which prevents further diffusion of majority charge carriers. At equilibrium, a region around the interface contains a negligible amount of free carriers.[38] It is called the *depletion region*. The potential drop across the junction is called the *built-in potential* V_{bi}. Both the built-in potential and the width of the depletion region can be derived analytically for crystalline semiconductors. In particular, it can be shown that, when the doping level is not the same in the p-doped and the n-doped regions, the depletion region extends more in the region with the lower doping level. This kind of junctions is the basis for crystalline silicon solar cells.

p-i-n junction It can be seen as an extreme case of a p-n junction, where the depletion region extends over most of the material. It has been mainly developed for a-Si:H devices because it is difficult in amorphous silicon to minimize the defect density and

[38] Of the same order of magnitude as in the intrinsic semiconductor

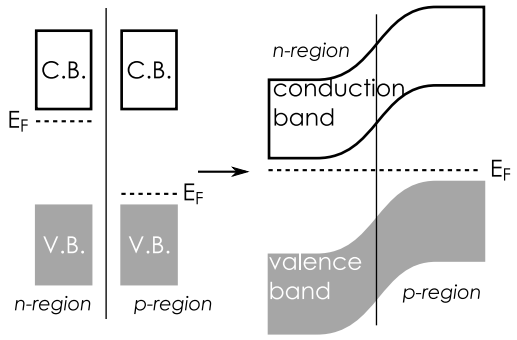

Figure 1.13 – *Band diagram of a p-n junction before (left) and after (right) contact*

to dope at the same time. As a consequence, p-n junctions cannot be effectively prepared. In this structure, a "thick" layer of intrinsic material (several hundreds of nm) is sandwiched between two thin (few tens of nm), heavily doped layers. These doped layers ensure good contact to the electrodes and create the built-in electric field. If the defect density in the intrinsic layer is low enough, this field extends over all of it.

MIS junction It is a metal/semiconductor junction whose rectifying behavior comes from a thin interfacial insulating layer, *i.e.*, a layer with a band gap significantly higher than the semiconductor. Charge carriers are transferred between the semiconductor and the metal by tunneling, so the current flowing through the device shows an exponential dependence on the applied voltage.

Semiconductor heterojunctions occur at the interface between two different semiconductors, with different band gaps, either similarly doped or not. When the doping types or levels in the two materials are different, a depletion region appears. But the conduction and valence band edges cannot be continuous across the junction because of the difference in band gaps. A discontinuity, called *band offset* appears at least on one of the band edges. Many questions arise about such junctions regarding the position and height of the band offsets, the position of the Fermi level at equilibrium, the width of the depletion region, *etc.* A first model has been proposed in 1962,[39] and an extensive review of experimental and theoretical works are available.[40] Still, the diversity of possible cases and the sensitivity of the heterojunction properties to interface states make both theoretical predictions and experimental reproduction of results difficult.

1.2.2 Silicon/organic heterojunction in the literature

Silicon/organic heterojunctions cannot directly fit in any of these categories, not even heterojunctions. Indeed, not only the doping and the band gaps, but also the

[39] Anderson, "Experiments on Ge-GaAs heterojunctions", 1962 [And62]
[40] Franciosi and Walle, "Heterojunction band offset engineering", 1996 [FW96]

structure and the conduction mechanisms are different between those two kinds of materials.

First reports on silicon/organic heterojunctions date back to 1982.[41] At that time, devices were based on small molecules (3,4,9,10-perylenetetracarboxylic dianhydride, or PTCDA) evaporated on crystalline silicon wafers. These experiments were focused on the improvement of silicon/metal Schottky diodes, and particularly of their rectifying ratio. They have been successfully described by a model where charge transport in the organic layer is determined by the injection from one ohmic source (metal electrode) and one blocking source (silicon), and limited by space-charge phenomena.[42] According to this model, the depletion layer is in the silicon substrate only. Barrier heights at the interface have been determined for the holes (on p-doped silicon) and for electrons (on n-doped silicon). As their sum is larger than the band gap of silicon, some band bending must occur at the interface upon contact. The dark current densities were at least ten times lower than for Schottky Si/Au diodes. Similar results have been obtained with another class of organic semiconductors (phtalocyanine), except that the latter strongly interact with silicon. This creates interface states, which pin the Fermi level at the interface.[43]

The use of such heterojunctions for photovoltaic applications has been first reported with pyrene[44] as the organic compound.[45] Radiative energy transfer was evidenced from pyrene to silicon, but no charge transfer. Thin PTCDA and copper phtalocyanine (CuPc) layers (80 nm to 100 nm) evaporated on silicon wafers were later found to improve the performance of solar cells with respect to devices based on Si/metal Schottky junction.[46] The improvement came from a higher open-circuit voltage (V_{oc}). On the other hand, the short-circuit current density was unchanged and the fill factor was low (0.3 to 0.4) because of a high series resistance. In these devices, the organic semiconductor played an active role, as there was a strong correlation between their spectral response and the absorption spectra of the organic compounds. In addition, the photocurrent was increased when layers of the two organic materials (PTCDA and CuPc), instead of a single one, were successively evaporated on a silicon wafer. Comparable results were obtained with tetraphenylporphyrin (TTP) evaporated on n-doped silicon.

More recent studies have investigated junctions between semiconductor polymers and silicon. Good quality diodes ($n = 2$) have been obtained with poly(3-methylthiophene) electro-polymerized on n-doped crystalline substrates.[47] Rectification behav-

[41] Forrest et al., "Organic-on-inorganic semiconductor contact barrier devices", 1982 [For+82]

[42] Forrest, Kaplan, and Schmidt, "Organic-on-inorganic semiconductor contact barrier diodes. I. Theory with applications to organic thin films and prototype devices", 1984 [FKS84]

[43] So and Forrest, "Dependence of the electrical characteristics of organic-on-inorganic semiconductor contact barrier diodes on organic thin-film composition", 1988 [SF88]

[44] $C_{16}H_{10}$, made of four fused benzene rings

[45] McCaffrey and Prasad, "Organic-thin-film-coated solar cells: Energy transfer between surface pyrene molecules and the silicon semiconductor substrate", 1984 [MP84]

[46] Al-Mohamad and Soukieh, "Solar cells and high efficiency photo-diodes having metal-organic thin film-semiconductor structures", 1995 [AMS95]

[47] Kokado, Hosokawa, and Hoshino, "Properties of Heterojunction of Si/Poly(3-methylthiophene) as

ior was attributed to chemical bonding between silicon and the polymer, as opposed to tunneling. Indeed, treatment of the devices by aqueous HF after deposition induced no change in the forward current, but it dramatically decreased the reverse current, so it lead to a 100-fold increase in the rectifying ratio.[48] Photodiodes have been fabricated by depositing a-Si:H by hot-wire chemical vapor deposition at 140 °C on poly(N-vinylcarbazole).[49] These devices had high photosensitivy (ratio between the reverse currents in light and in dark) and photogain (ratio between the forward current in light and in dark). On the other hand, they exhibited no photovoltaic action. This behavior was attributed to the polymer acting as a hole-blocking layer. Under illumination, the current in the device appeared to be limited by space-charge phenomena. Finally, charge redistribution upon contact between crystalline silicon and PEDOT:PSS, a hole transporting polymer, was evidenced by ellipsometry.[50] When silicon was p-doped, holes flew from silicon to the polymer. A depletion region thus appeared in c-Si and a conductive layer was formed in the polymer. Conversely, when silicon was n-doped, electrons flew from silicon to PEDOT:PSS, where they recombined with holes, thus decreasing the conductivity of the polymer.

In summary, organic compounds have mostly been used to enhance the blocking behavior of Si/metal Schottky diodes. Such diodes perform well, but no significant photovoltaic action had been demonstrated as of 2005. As regards the junction, some band alignment has been evidenced. In that case, the depletion layer is always in silicon. When conduction mechanisms have been investigated, space-charge phenomena played a major role.

1.2.3 Tentative band diagram

Tentative band diagrams of hybrid devices based on silicon and P3HT are shown on fig. 1.14. Uncertainties on the position of some levels are evidenced by blurred areas. Values used for silicon, P3HT and gold were presented in sections 1.1.2 and 1.1.4. The work function of ITO (In_2O_3:Sn, commonly called "indium-tin oxide") is highly sensitive to the way this material is deposited and cleaned.[51] These band diagrams are shown in flat-band conditions, *i.e.*, without any band bending due to transfer of charge carriers between materials upon contact. This is the most common representation when organic semiconductors are involved, as device characteristics primarily

a Function of Polymerization Condition", 1993 [KHH93]

[48] Hoshino, Ogata, and Kokado, "Improvement in Junction Properties of a n-Si/poly(3-methylthiophene) Heterojunction by Post-Treatment with aq.HF", 1995 [HOK95]

[49] Wang et al., "Hybrid organic-inorganic photoconductive diode", 2003 [Wan+03]

[50] Schubert et al., "Carrier redistribution in organic/inorganic (poly(3,4-ethylenedioxy thiophene/poly(styrenesulfonate)polymer)-Si) heterojunction determined from infrared ellipsometry", 2004 [Sch+04]

[51] Sugiyama et al., "Dependence of indium–tin–oxide work function on surface cleaning method as studied by ultraviolet and x-ray photoemission spectroscopies", 2000; Ke et al., "Au-ITO anode for efficient polymer light-emitting device operation", 2005; Centurioni and Iencinella, "Role of front contact work function on amorphous silicon/crystalline silicon heterojunction solar cell performance", 2003 [Sug+00; Ke+05; CI03]

depend on the respective positions of the valence and conduction band edges, and band bending, when it occurs, is still hardly predictable.

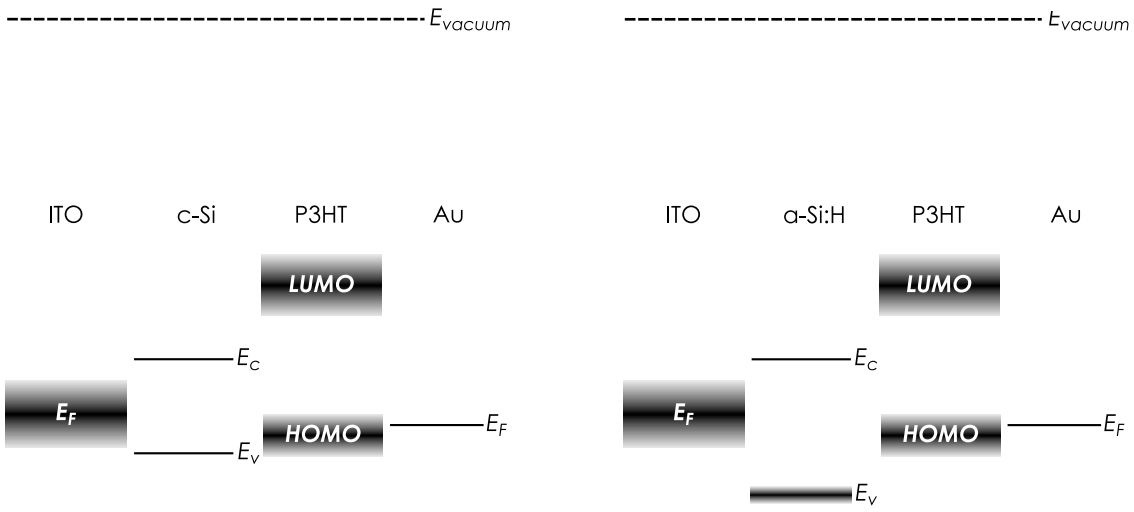

(a) *With crystalline silicon* **(b)** *With hydrogenated amorphous silicon*

Figure 1.14 – *Band diagrams of silicon/P3HT hybrid devices in flat-band conditions*

In this structure, P3HT, which has the smallest electron affinity, and which is a hole transporter, behaves as an electron donor. Conversely, silicon has a larger mobility for electrons than for holes, and has a higher electron affinity than P3HT. It behaves then as an electron acceptor. To accentuate this behavior, we will partially n-dope silicon layers. In this configuration, hydrogenated amorphous silicon might be more adapted to P3HT than (micro-)crystalline silicon. Indeed, light would first go through the silicon layer. As crystalline silicon has a smaller optical band gap than P3HT, the absorption spectrum of the polymer would be included in that of silicon. Conversely, a-Si:H has slightly higher an optical band gap than P3HT, so there is some complementarity between their absorption spectra. In addition, the valence band offset is larger at the a-Si:H/P3HT interface than at the c-Si/P3HT one. This offset may prevent holes from leaving P3HT and recombining with electrons.

1.3 Exploration of possible multi-layer configurations

1.3.1 Design and fabrication of devices

To investigate this interface experimentally, multi-layer devices have been prepared. Various silicon thin films, in terms of crystallinity and doping, have been deposited by PECVD in ARCAM (*cf.* appendix A). The method used to fabricate devices based on these thin films is described in appendix B. In that case, the concentration of the P3HT solution was $20\,\mathrm{g\,L^{-1}}$, and the resulting polymer layer was 65 nm thick. The

gold top electrode was 50 nm thick. Investigated structures for the inorganic part are summarized on tab. 1.2.

Number	TCO	n-doped layer		undoped layer		color
		type	d/nm	type	d/nm	
1	ITO	a-Si:H	26	a-Si:H	197	black
2	ITO	none	N/A	a-Si:H	193	red
3,4	ITO	a-Si:H	16	μc-Si	127	blue
5	ZnO	a-Si:H	18	μc-Si	122	dark cyan
6	ZnO	none	N/A	μc-Si	86	magenta
7	ZnO	none	N/A	μc-Si	122	navy

Table 1.2 – *Investigated structures for the inorganic part (colors refer to figures 1.16 to 1.20)*

1.3.2 Effect of the structure on photovoltaic parameters

These devices have been characterized electrically under simulated solar light. All of them exhibit a clear photovoltaic action. An example of J-V curve is shown on fig. 1.15. Low but significant photocurrents have been obtained, as well as photovoltages. A clear rectifying behavior is also visible, but it is limited by the current saturating under direct bias.

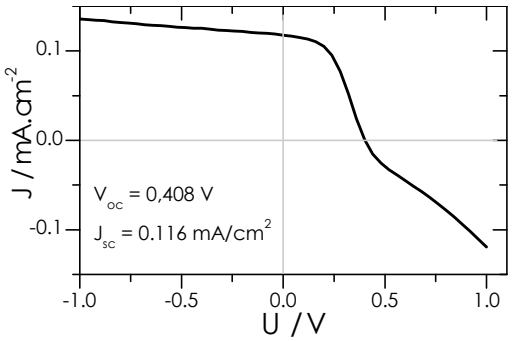

Figure 1.15 – *J-V characteristic of a cell of type 3: ITO | 16*nm *a-Si:H(n) | 127*nm *μc-Si(i) | 65*nm *P3HT | 50*nm *Au*

The fill factor (fig. 1.16) shows little dependence on the inorganic structure. Only cells based on ZnO/μc-Si(i) (structures 6 and 7) have values slightly lower than the average (about 40% instead of 45%). This value is lower for thicker μc-Si layer. Conversely, the fill factor of structures based on a-Si:H(n)/μc-Si(i) can reach 50%.

Open circuit voltage (fig. 1.17) is also almost constant at about 400 mV. Samples with an intrinsic layer only have slightly lower V_{oc} (350 mV on average), and a higher dispersion among samples. One structure, though, stands out: ITO/a-Si:H(n)/a-Si:H(i) (structure 1). These devices have a higher V_{oc} by about 200 mV than the others at

600 mV. This shows that, unlike in pure organic devices, the V_{oc} is not determined by the donor/acceptor interface only. Indeed, devices based on ITO/a-Si:H(i) (structure 2) have a significantly lower V_{oc} than those based on ITO/a-Si:H(n)/a-Si:H(i).

The short circuit current density (J_{sc}), on the other hand, varies over more than one order of magnitude. The lowest values have been obtained on cells with an intrinsic a-Si:H layer. On the other hand, highest values (>0.2 mA cm^{-2}) have been obtained on cells based on ZnO/μc-Si(i) (type 6 and 7). This is the opposite of V_{oc}. A trade-off between these two values is a general feature of solar cells. Here the difference in J_{sc} may be explained by the absorption in the silicon layer. Hydrogenated amorphous silicon has a higher band gap than μc-Si, so it is theoretically more adapted for use as an under-layer with P3HT. But it is also a direct band gap semiconductor, whereas μc-Si is an indirect one. So, for comparable thickness, much more light is absorbed in a-Si:H than in μc-Si. As a result, there is little overlap between the part of the solar spectrum transmitted by the a-Si:H layers used here and the absorption spectrum of P3HT;[52] this overlap is much larger with μc-Si (fig. 1.19). So less current can be generated in P3HT when it is deposited on these layers of a-Si:H than on μc-Si. This is a clue for P3HT playing a significant role in the generation of photocurrent. On the other hand, when comparing two structures based on ZnO/μc-Si(i) (type 6 and 7), it appears that the photocurrent is twice as large when the intrinsic layer is 122 nm-thick as when it is 86 nm-thick. This shows that the silicon layer actively contributes to the photocurrent.

Finally, the power conversion efficiency (fig. 1.20) follows the same trends than the short-circuit current density, because J_{sc} has the strongest dependence on the structure among the three components of the efficiency. Nonetheless, the dispersion is attenuated, because both V_{oc} and the fill factor follow an opposite trend. Unfortunately, for all structures, the efficiency is extremely low: below 0.04%.

1.4 Analysis of optimized devices

The most material-dependent characteristic of a solar cell is its open-circuit voltage. Conversely, the short-circuit current density can be optimized by changing the thickness of the layers. As devices based on ITO/a-Si:H(n)/a-Si:H(i) have the highest V_{oc}, they have been specifically investigated and optimized. The key was to reduce dramatically the thickness of the a-Si:H layer, so that P3HT can receive a significant amount of light in its absorption range. This optimization was very successful, as current densities larger than 1 mA cm^{-2} and efficiencies above 1% have been obtained. Optimized devices had an n-doped a-Si:H layer between 26 nm and 29 nm in thickness, an intrinsic a-Si:H layer between 52 nm and 66 nm in thickness, and a 65 nm-thick P3HT layer. The gold top electrodes were 28 nm or 50 nm thick. In this section, we will analyze the behavior of these devices.

[52] Overlap between the absorption spectrum of P3HT and the spectrum of the light transmitted by the silicon layer determines how much light can be effectively absorbed in P3HT. As a consequence, it determines charge carrier generation in P3HT.

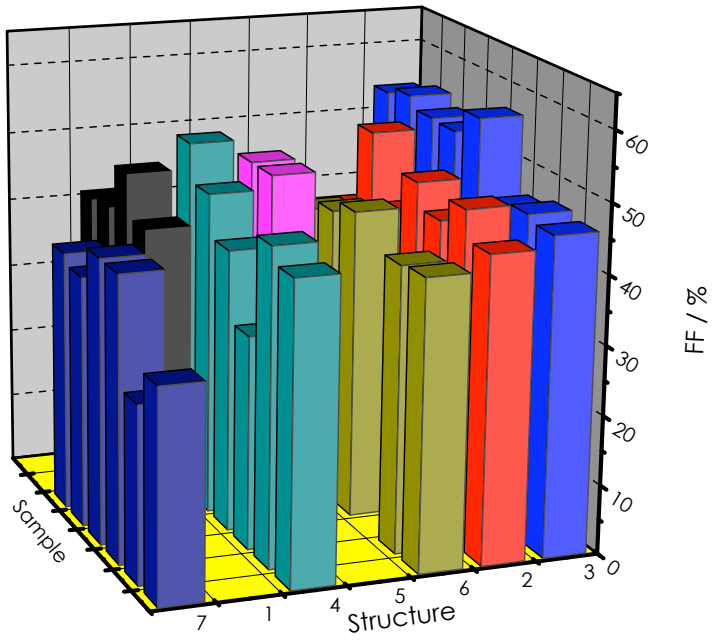

Figure 1.16 – *Fill-factor for various inorganic layers*

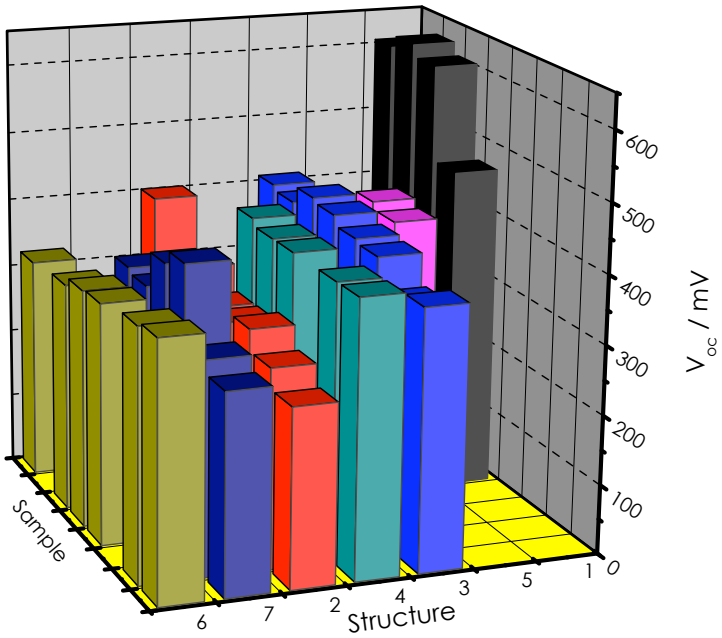

Figure 1.17 – *Open-circuit voltage for various inorganic layers*

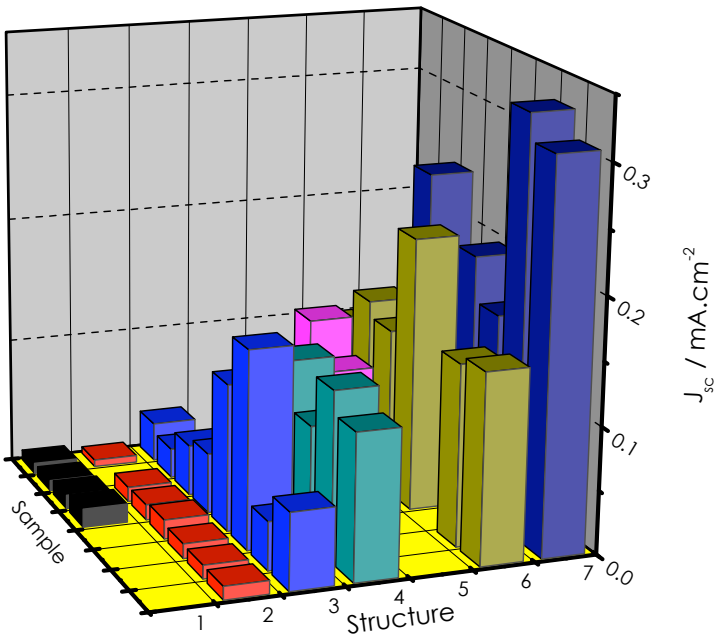

Figure 1.18 – *Short-circuit current density for various inorganic layers*

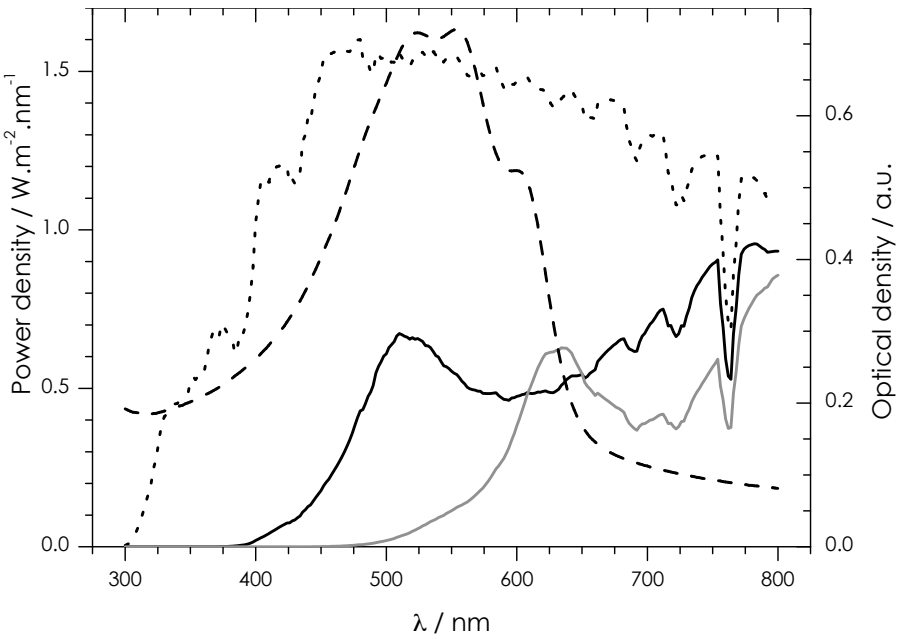

Figure 1.19 – *Power density of sun-light when reaching the earth (dotted curve), transmitted by the a-Si:H(i) layer of devices type 1 and 2 (gray solid line), and transmitted by µc-Si(i) layer of device type 6 (black solid line). The absorption spectrum of P3HT is indicated for comparison (dashed line)*

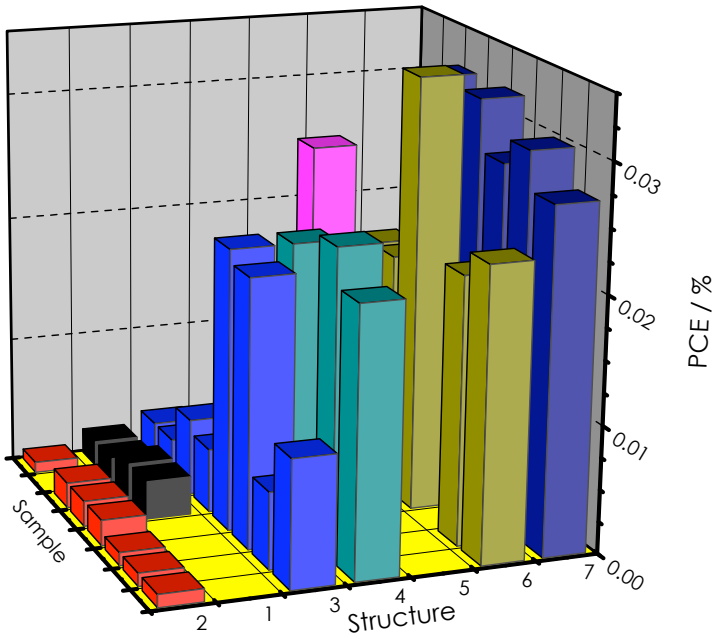

Figure 1.20 – *Power conversion efficiency for various inorganic layers*

1.4.1 Diode behavior

The rectification behavior has been investigated by measuring J-V characteristics in dark. At room temperature and under nitrogen, the devices have a clear rectifying behavior, even though their rectifying ratio at ±1 V ranges between 3 and 9000. The smallest reverse current density in dark is $1 \times 10^{-3}\,\mathrm{mA\,cm^{-2}}$, and the highest forward current density is $11.6\,\mathrm{mA\,cm^{-2}}$. Most of the dispersion of the rectifying ratio comes from the reverse current density, which ranges over four orders of magnitude. Temperature-dependent J-V characteristics were measured in dark and under vacuum to get further insight into the diode behavior (fig. 1.21). The curves have an exponential behavior under reverse voltage and low forward voltage (<0.4 V), but at higher forward voltage, a saturation of the current is visible. This is confirmed by fitting the curves to the diode equation: $J = J_s\left(\exp\frac{qV}{nk_BT} - 1\right)$. As shown on tab. 1.3, the ideality factor is higher than 3.7, and it increases with the temperature. An ideality factor larger than 2 corresponds to voltage-dependent resistances in the device, which are typical of deficient contacts. The saturation current density J_s itself depends exponentially on the temperature. It has been fitted to $J_s = J_0 \exp\left(-\frac{\Phi_B}{k_BT}\right)$ with a very good convergence. The barrier height is: $\Phi_B = (0.42 \pm 0.01)\,\mathrm{eV}$. This value is very close to the offset between the conduction band edge of a-Si:H and the LUMO level of P3HT, but it is significantly lower than the difference in the Fermi level position in n-doped and intrinsic a-Si:H (0.67 eV).[53] This suggest that the rectifying barrier is indeed at the

[53] Poissant, Chatterjee, and Cabarrocas, "No benefit from microcrystalline silicon n layers in single junction amorphous silicon p-i-n solar cells", 2003 [PCC03]

interface between silicon and P3HT.

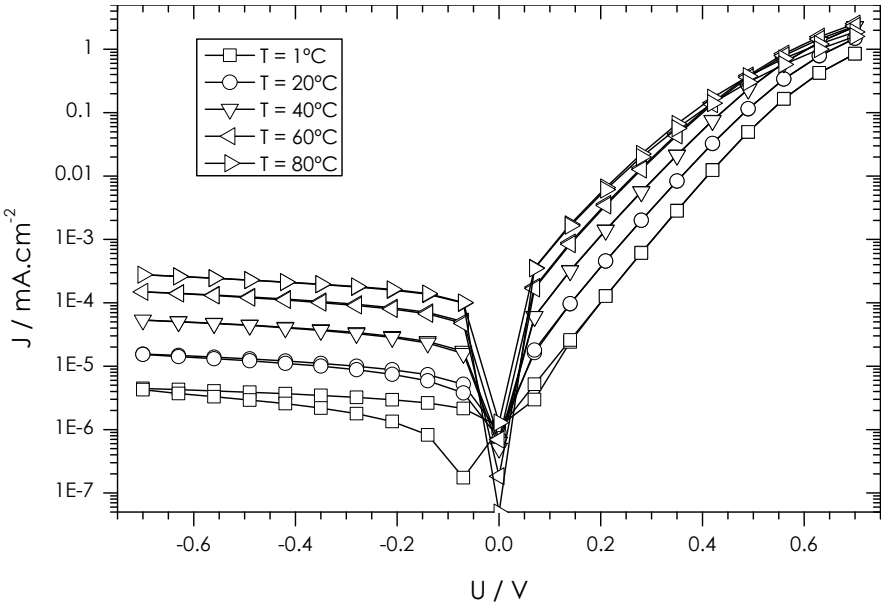

Figure 1.21 – *J-V characteristics in dark, at various temperatures, of an optimized device*

T/°C	J_s/mA cm^{-2}	n
1	2.9×10^{-4}	3.7
20	9.6×10^{-4}	3.8
35	2.4×10^{-3}	3.8
40	2.9×10^{-3}	3.9
60	7.5×10^{-3}	4.2
80	8.9×10^{-3}	4.3

Table 1.3 – *Results of the fit of J-V characteristics in dark to the diode equation*

1.4.2 Behavior under illumination

Under simulated solar illumination, optimized devices generate significant electrical power. A typical J-V characteristic is shown on fig. 1.22. There are little variations among the short-circuit current density of working devices: from 3.0 mA cm^{-2} to 4.2 mA cm^{-2}. The open circuit voltage ranges between 606 mV and 730 mV. There is no simple relationship between the thickness of the layers and the performance of the devices, though the highest short circuit current density has been obtained for

the thickest (66 nm) a-Si:H(i) layer, and the highest open-circuit voltage has been obtained for the thinnest (52 nm) a-Si:H(i) layer. The fill factor, in turn, varies from 25% to 59%. On average, a thinner a-Si:H(i) layer leads to higher fill factor. The rectifying ratio in dark is clearly linked to the fill factor: devices with rectifying ratios below 100 have a fill factor of about 25, and devices with rectifying ratios above 1000 have a fill factor larger than 50. The resulting power conversion efficiencies range from 0.6% to 1.6%. More than half the optimized devices had efficiencies larger than 1%.

The J-V curves in dark and under illumination cross each other at an applied voltage about 0.9 V. This crossing evidences a photo-conductivity effect in the devices.

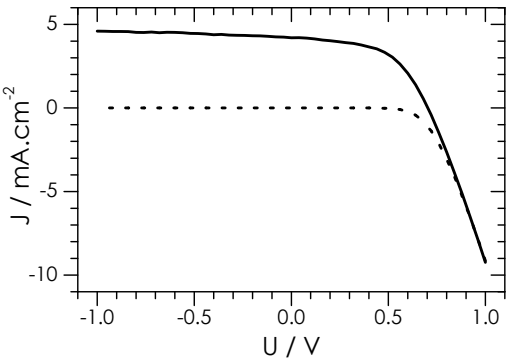

Figure 1.22 – *J-V characteristics of an optimized solar cell under illumination (solid line) and in dark (dotted line)*

Contribution of the materials to the generation and separation of charge carriers

The design of hybrid solar cells we are working on relies on generation of charge carriers in both organic and inorganic materials. The distribution of photo-generation can be investigated by spectral response measurements. The external quantum efficiency spectrum of an optimized device is shown on fig. 1.23. It shows a balance between generation in a-Si:H and P3HT. Indeed, it is clearly correlated to the product of the respective optical densities of a-Si:H and P3HT, except at wavelengths lower than 430 nm, where the a-Si:H layer absorbs light very efficiently. Thus little intensity is transmitted to the P3HT layer. This further confirms the observations made in section 1.3.2, *i.e.*, light absorption must be well balanced between the two layers.

On fig. 1.24, the spectral response of a device with similar structure (but a palladium top electrode) has been measured for two directions of the incident light: the usual way (light going through ITO and a-Si:H first), and the opposite direction (light going through the top electrode and P3HT first). The two curves have been normalized because absorption by the top electrode made the absolute values much lower in the second direction than in the usual one. When the light goes through ITO and a-Si:H first, the spectral response is similar to fig. 1.23. But when the light goes through P3HT first, the spectral response is split into two peaks, each of which corresponds to

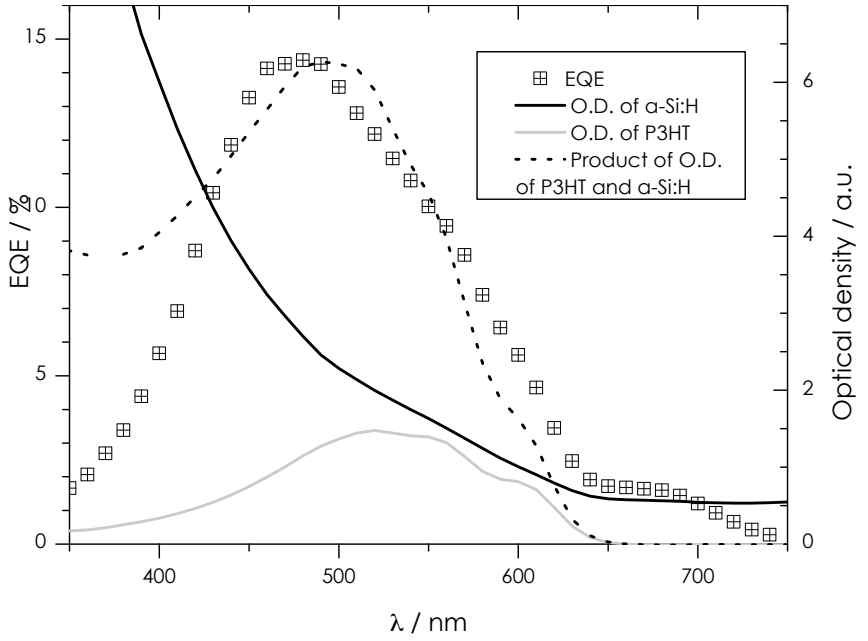

Figure 1.23 – *External quantum efficiency of an optimized device compared to the absorption spectra of the silicon layer and the polymer*

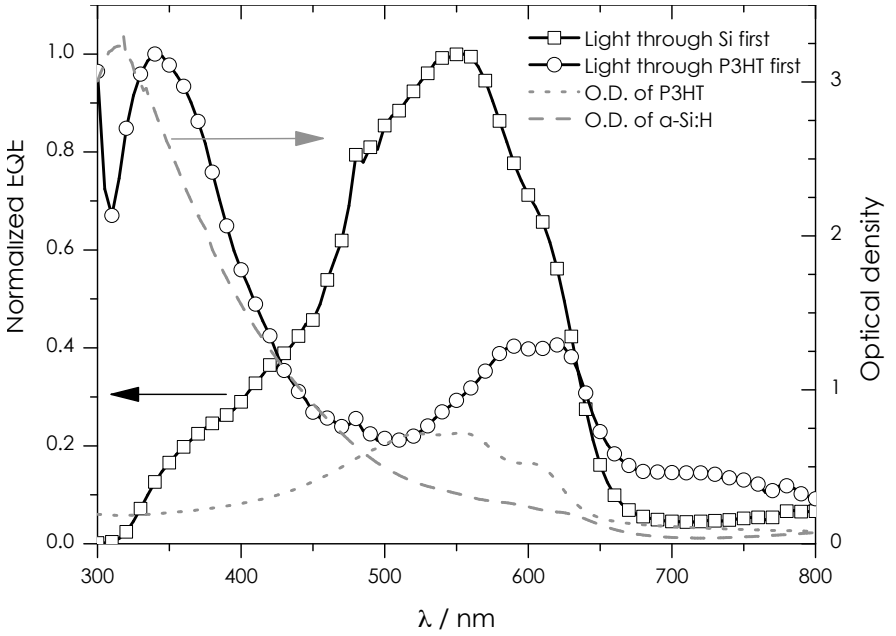

Figure 1.24 – *Normalized quantum efficiency of a device based on a-Si:H/P3HT hetero-junction: illumination from the silicon side (squares), and from the polymer side (circles). The absorption spectra of the silicon layer (gray dashed line) and P3HT (gray dotted line) are given for comparison.*

high absorption by P3HT and a-Si:H, respectively. As P3HT does not cut a significant range of the absorption spectrum of a-Si:H, balancing light absorption is not an issue when light goes through P3HT first. So this configuration should be more favorable to an efficient use of the solar spectrum.

In addition, in the second case (light going through P3HT first), the generation in the polymer is antibatic (*i.e.*, slope changes in the EQE and the absorption spectra are out of phase), whereas it was symbatic (*i.e.*, slope changes were in phase) in the first case. This difference shows that charge carriers generated in P3HT are indeed separated at the silicon/P3HT interface, not at the P3HT/metal interface.[54]

Summary

The interface between silicon and polymer semiconductors cannot be described with models classically used with inorganic semiconductors. It is indeed an extreme kind of hetero-junction, where not only the energetic levels, but also the generation and conduction mechanisms change across the interface. Most reported junctions between silicon and organic semiconductors aimed at enhancing the rectification behavior of Schottky metal/silicon diodes, and they performed well in that sense. Yet very little use of such diodes for photovoltaic conversion has been reported. In that case, both radiative energy transfers and charge carriers transfers were claimed.

Hybrid multi-layers devices have been prepared and characterized. An exploration of the influence of the inorganic part on the photovoltaic performance evidenced that (i) balancing light absorption (and charge carrier generation) between silicon and P3HT was necessary for good generation of photocurrent, and (ii) the open-circuit voltage was determined by the structure of the whole active layer, not only by the silicon/P3HT interface. This shows that this junction cannot be seen as a "classical" donor/acceptor junction (like in all-organic devices) either. The highest photo-voltages were obtained with devices based on a-Si:H(n)/a-Si:H(i) layers. Optimization of this structure led to devices showing a good diode behavior (rectification ratios up to 9000), photovoltages up to 730 mV, short-circuit current densities up to 4.3 mA cm^{-2}, fill factors up to 59% and power conversion efficiencies up to 1.6%. External quantum efficiency spectra showed that both silicon and P3HT contributed to the photocurrent and that balancing light absorption was indeed required. This condition can be more easily met when light goes through P3HT first than when it goes through a-Si:H first. A more optimal device structure could then be based on P3HT contacting the transparent electrode and a-Si:H contacting the metal electrode, *i.e.*, a reverse structure with respect to what was investigated so far.

Unfortunately, two phenomena hinder these results: there is a large dispersion among the performance of the devices, even inside one batch, and current in some cells seems to saturate under direct bias. This saturation leads to S-shaped J-V characteristics under illumination.

[54] Voz et al., "Photodiodes based on fullerene semiconductor", 2007 [Voz+07]

Controlling real interfaces: toward reproducibility

2

> LÉON *(hurle)*. C'est fini maintenant, assez rigolé chaque pièce sera contrôlée, et recontrôlée et recontrôlée, et si les points sont trop grands ou si c'est salopé, on recommencera jusqu'à ce que ce soit bien !
>
> Jean-Claude Grumberg, *L'Atelier (scène 6)*

Contents

THIS chapter will be focused on improving the reliability of the devices. In particular, we will investigate the origin of the variability of performances, and of S-shaped characteristics, *i.e.*, saturation of the forward current. In parallel, we will try to tackle these problems. The bulk of active materials, both silicon and P3HT, is reasonably controlled: most deposition parameters of silicon thin films can be monitored, and only two different batches of P3HT have been used for most devices. As a result, interfaces are supposed to be the origin of most of the variability. Potential issues may come in particular from the silicon/P3HT interface—as the samples are transferred between the deposition of the two materials—and from the P3HT/top electrode contact, which is very sensitive to the processing conditions. Both interfaces will be analyzed in details and ways to improve them will be investigated. In addition, the design of the device, and the global process may also have an impact on the reliability, which will be discussed.

2.1 Position of the problem

S-shaped characteristics have been mentioned in chapter 1. Another major concern as regards the reliability of the cells is the large dispersion in performance among similar devices. This problem is illustrated on fig. 2.1. Four performance parameters[1] of 110 samples measured in similar conditions under AM 1.5 simulated illumination are plotted in chronological order. All these samples were based on the optimal ITO/a-Si:H(n)/a-Si:H(i)/P3HT structure. Most of them were meant to reproduce the best devices and their nominal deposition parameters were identical. Only slight variations of processing conditions were therefore allowed for experimental reasons. However, significant variations of the performance occurred. This was especially the case for the short-circuit current density (fig. 2.1c), which varies over an order of magnitude. Nonetheless, for each of the three components of the efficiency (J_{sc}, V_{oc}, and FF), the values obtained for most samples can be split in two narrow groups. This is a clue for a dependence of the performance on hidden processing variables, which we will try to discover and control.

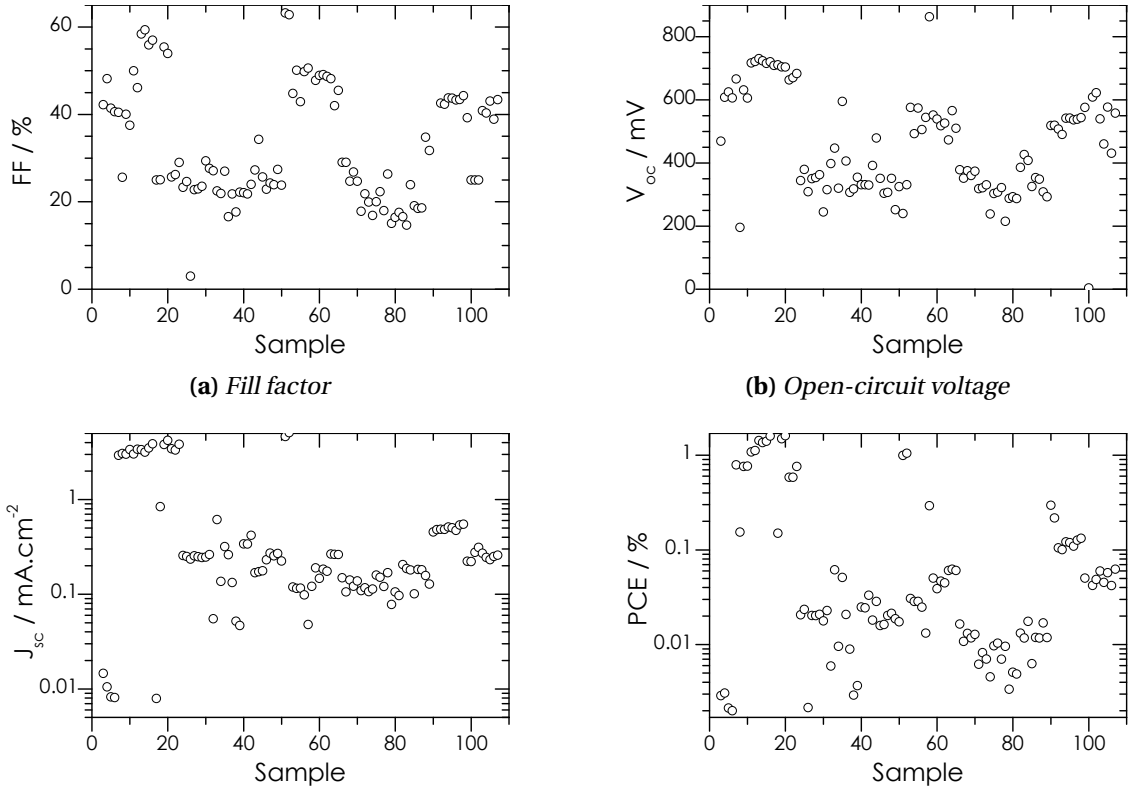

(a) *Fill factor*

(b) *Open-circuit voltage*

(c) *Short-circuit current density*

(d) *Power conversion efficiency*

Figure 2.1 – *Performance parameters of ITO/a-Si:H(n)/a-Si:H(i)/P3HT hybrid devices measured under similar conditions*

[1]Fill factor, open-circuit voltage, short-circuit current density, power conversion efficiency

2.2 Design and fabrication process

2.2.1 Improvements on the design and the fabrication process

The initial fabrication process, as described in appendix B, presents many drawbacks:

1. It offers only two cells, of similar size, per sample. This limits the possibilities of uniformity analysis, prevents from studying possible size effects, and makes it likely that some samples are completely lost in case of local shunts.

2. It requires many fabrication steps. In particular, two metal evaporations are necessary, and the ITO layer must be partially etched off.

3. The size and geometry of the cells are not well defined: the illuminated area is an 0.28 cm^2 circle, but the intersection between the top and bottom electrodes also includes the metallic strips between this circle and the electrical contact.

4. The metallic strip between the active area and the contact has to step over the total height of ITO and the active layer (about 200 nm), which is larger than its own thickness. This can result in breaks in this strip and conduction problems.

We therefore developed a new design and fabrication process. The prototype of the new devices is shown on fig. 2.2. We kept the same size of substrates, as the substrate holder in evaporators has been specifically designed for it. Each sample contains up to nine cells, of three sizes (small, medium and large),[2] defined by the evaporated top electrodes. In the final version of the design, for which the evaporation masks have been fabricated with punches,[3] the top electrodes are circles, and their areas are 0.196 cm^2, 0.071 cm^2 and 0.031 cm^2, respectively. Electrical contacts are directly taken on the top electrodes. The latter must as a consequence be thicker (about 150 nm) than in the previous design, so that they are not perforated by the pins.

The number of fabrication steps is significantly reduced:

1. only one evaporation, at the end, is required to deposit both the top and the bottom contacts

2. etching of the ITO layer is not necessary anymore

3. removal of P3HT outside the active region is of lower importance because it is not covered by the metallic strips anymore.

This approach proved to be efficient to enhance the homogeneity of the results. This is visible on fig. 2.1, where the last 20 samples have been made, in two batches, with this new design. The two batches are still different, which may be explained by a small change in the thickness of the intrinsic a-Si:H layer, but the results among each one are quite homogeneous.

[2] On some samples, the small top electrodes cannot be used because they are partially out of the active layer

[3] By the mechanical workshop at CEA Saclay

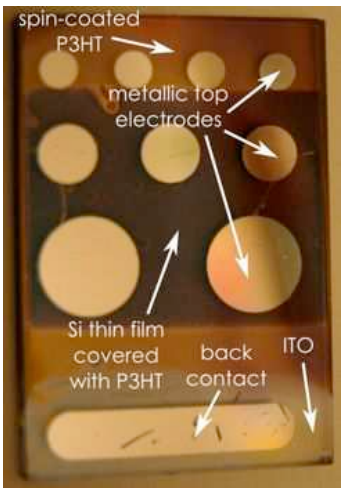

Figure 2.2 – *Picture of the prototype of devices with the new design*

2.2.2 Development of a new glovebox

As the performance of P3HT-based devices is very sensitive to contamination by O_2 and H_2O, all the fabrication process after deposition of silicon must be run under controlled atmosphere. In particular, samples after spin-coating of P3HT must be transferred to an evaporator, where top electrodes are deposited, without being exposed to air. This is possible with the equipment available at CEA-INES,[4] and devices have indeed been fabricated and characterized there. But it is at a distance of more than 500 km from École polytechnique and CEA Saclay, so this equipment could not be used on a day-to-day basis. That is why a new experimental setup, called ODILE,[5] has been developed at CEA Saclay. It is based on a stainless steel glovebox which is connected to an electron beam evaporator. Samples can be transferred between the glovebox and the evaporator by a transfer rod. The whole setup can be pumped out under high vacuum and stoved with infra-red lamps. This feature allows to change working conditions, *e.g.*, to switch from depositions in aqueous media to depositions in organic solvents under anhydrous atmosphere.

At the beginning of this work, the two chambers were installed but completely out of order: only pieces for the pumping circuits were available, no pressure regulation was planned, the gas purification system was dismantled. We then designed and built new pumping and gas circuits, which are schematically shown on fig. 2.3. Pictures of the setup in working conditions are displayed on fig. 2.4 and fig. 2.5.

Pumping out the glovebox is achieved by an Alcatel turbo-molecular pump, in series with a dry vacuum backing pump. Two plugs are used to isolate the gloves when the glovebox is under vacuum. The turbo-molecular pump is separated from the glovebox by an electro-pneumatic flap valve. The dry vacuum pump is also used to reach rough vacuum in the evaporator. Further pumping to high vacuum is obtained

[4] Le Bourget du Lac, Savoie, France

[5] Up to now, research failed to explain this name. Further investigations would be necessary.

with two adsorption pumps and an ion pump.

Gas purification is done by a refrigerated molecular sieve. A mixture of two zeolites is used: one specifically traps water molecules (zeolite X4) and one traps a broad family of organic vapors (zeolite X16). Cooling the molecular sieve down to $-50\,°C$ enhances absorption and favors condensation of the vapors. The sieve can be regenerated by pumping it out to rough vacuum at room temperature.

Pressure regulation is necessary when work is done in the glovebox (manipulations through the gloves changes the effective volume of gas in the setup). This is done through a Photohelic, *i.e.*, a differential pressure gauge working in the range 980 mbar to 1020 mbar which can be given upper and lower setup values. It controls two electrical circuits. Three states can be defined, as whether the measured pressure is above the upper setup values, below the lower setup value or in between. In our case, the Photohelic controls two electro-pneumatic valves: one allows fresh argon in the circuit (when the pressure is too low) and one releases gas from the setup to a diaphragm pump (when the pressure is too high).

When the glovebox contains no equipment, its pressure can go down to 2.6×10^{-7} mbar after 72 h of pumping. The lowest content in O_2 and H_2O is obtained by refilling the glovebox after a pump down, and by letting the gas purification system working in close circuit for a few hours. The amount of O_2 is then 180 vol. ppm and the amount of H_2O is 25 vol. ppm. As the refrigerated molecular sieve is very efficient to trap water, the concentration in H_2O tends to further decrease upon circulation of gas. On the other hand, the purification system does not filter oxygen, which can also diffuse into the glovebox (in particular, through the gloves). So the concentration of O_2 tends to increase upon time. Yet working in the glovebox balances this increase because the pressure regulation system replaces gas circulating in the setup with fresh argon. As a result, the typical volume concentrations in O_2 and H_2O during experiments are 0.1% and 20 ppm, respectively.

Equipments required to process polymers have been installed in the glovebox: a G3P spin-coater provided by SCS, a heating magnetic stirrer and a heating plate. Their control panels have been installed outside the glovebox for convenience (the available inner space is very limited). All the control signals and power supplies are centralized to an electrical panel, and transmitted to the equipments through a single 17-pin leak-free bushing. The spin-coater also requires to be connected by a flexible pipe to a small vacuum pump, which is naturally installed outside the glovebox. The pipe has been cut in two parts: one goes from the pump to the wall of the glovebox, where it is plugged in a leak-free feedthrough, which can be closed by a valve. The second part goes from the wall of the glovebox to the spin-coater. These leak-free connections allow to leave the large equipments in the glovebox when it is pumped out.[6] With equipments inside, the glovebox has not been pumped out for more than two hours. The lowest pressure reached under these conditions is 2×10^{-5} mbar.

The detailed operating procedure for ODILE is reported in appendix B.

[6] Small equipments, like pliers, and liquids are stored under argon at atmospheric pressure in the load-lock.

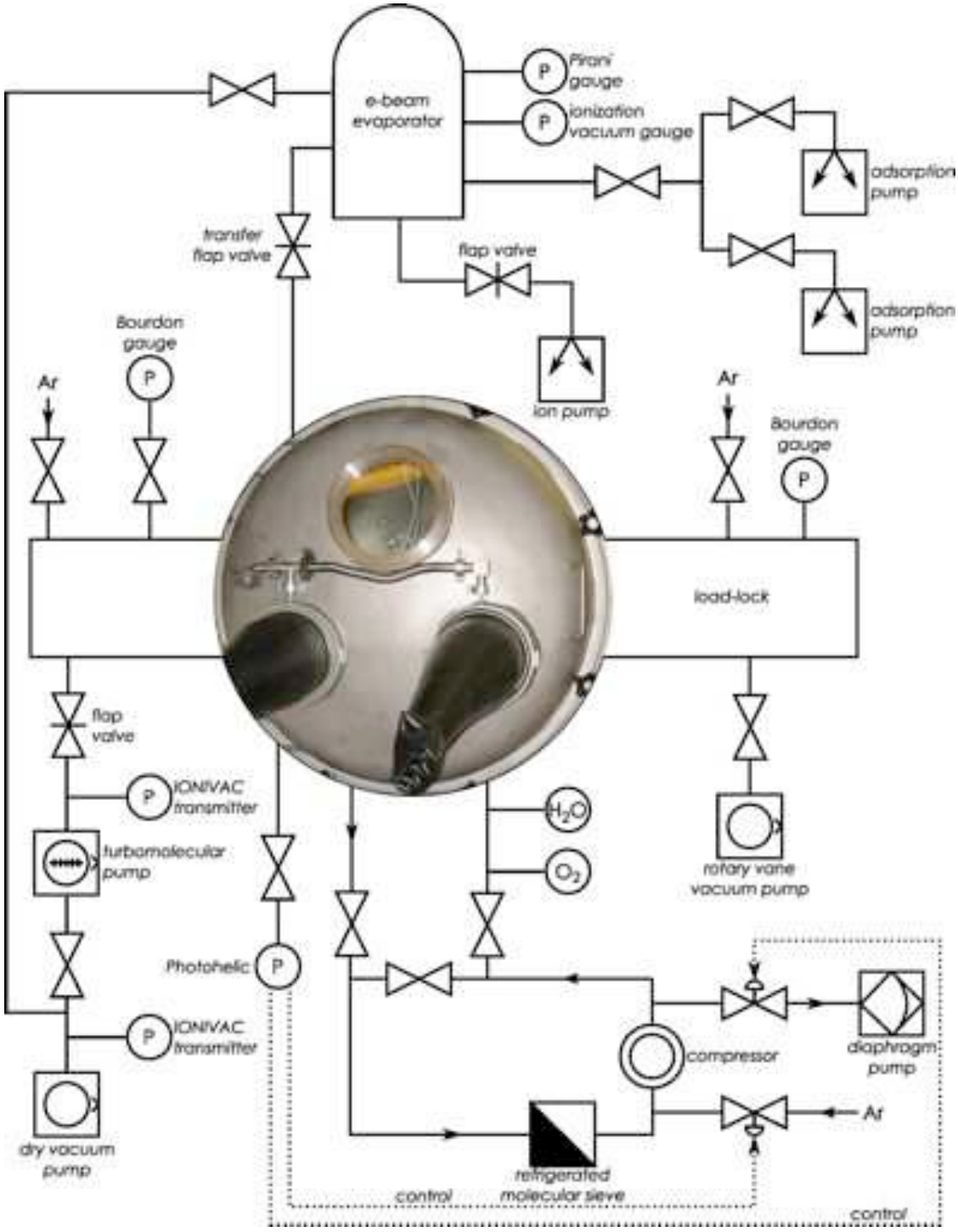

Figure 2.3 – *Diagram of the gas and pumping circuits for ODILE*

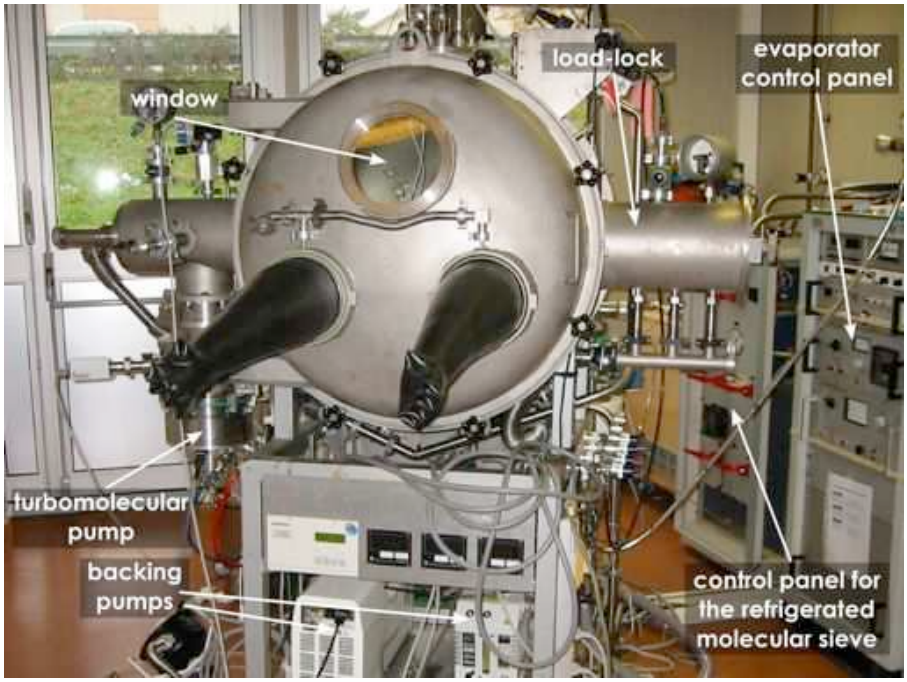

Figure 2.4 – *Front view of ODILE glovebox.*

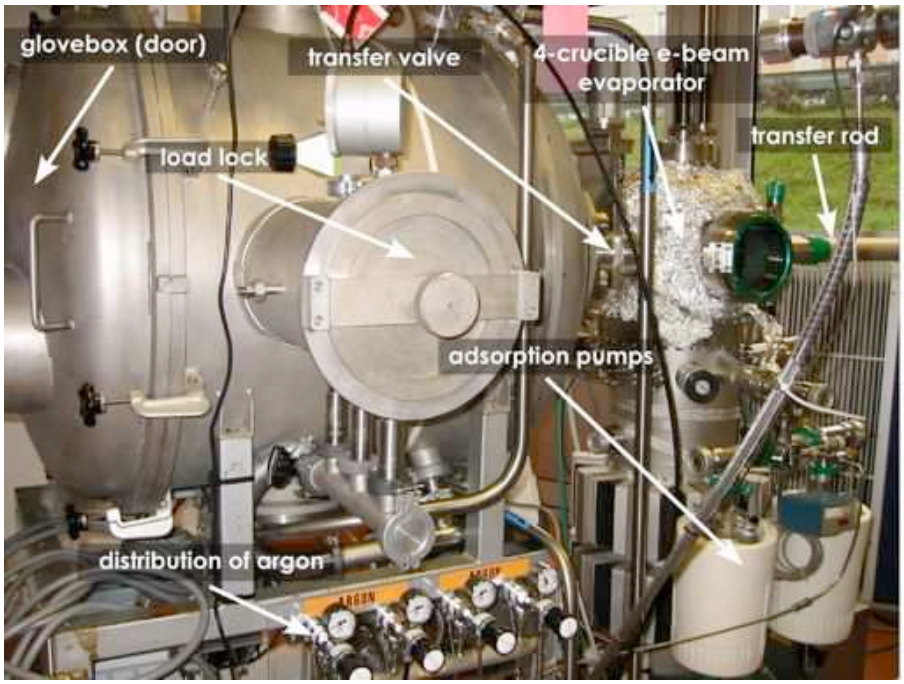

Figure 2.5 – *Sideview of ODILE glovebox*

2.3 Interface between silicon and P3HT

2.3.1 Technical approach: prevention and characterization of the contamination

Possible sources of contamination

PECVD reactors used during this work do not have load-locks, so the samples are necessarily exposed to air, even briefly, between the deposition of the silicon thin films and P3HT. Pollution or oxidation of the silicon surface is thus possible. This would lead to an insulating layer (either silicon dioxide or carbon contamination) at the interface between silicon and P3HT, which could explain the current saturation in devices. In addition, it could also account for the variability of the results, as contamination depends on the environment of the experiment (humidity, temperature, other running experiments, *etc.*). To prevent it, an airtight container provided by Fischer Bioblock was initially used. This container can be manually pumped out, and it contains a dessicator, so that samples are kept in a dry, low-pressure atmosphere. Yet it was used during the experiments reported in the previous chapter, so it is obviously not sufficient, if contamination is indeed critical.

That is why another transfer case has been developed, based on vacuum (KF) fittings, flanges, and plugs. It is adapted to a diaphragm pump located just next to the deposition reactors, so that less than a minute is necessary between opening the reactor and starting to pump out the case filled with samples. This container proved to remain at a pressure below 1 mbar for several hours when kept under static vacuum. It is equipped with two vacuum breaker valves. This way, the container includes two chambers, which can be opened independently. This allows to load the transport case with samples deposited in two subsequent runs without exposing the first batch to air. The container was designed to fit in the load-locks of glove boxes used during this work, so it could be opened in a controlled atmosphere.

Characterization

The characterization method has been chosen after three criteria:

1. The degradation of the samples during transfer, if any, was expected to be *surface contamination*.

2. A qualitative information, *i.e.*, the chemical nature of the pollution, was sought.

3. A quantitative information, *i.e.*, the amount of contamination, was required to evaluate the transfer process.

X-Ray Photoelectron Spectroscopy (XPS) was then chosen, at it is a powerful technique to get qualitative and quantitative information on the chemical composition

near the surface of materials.[7] It is based on the photoelectric effect: electrons are emitted by the material upon excitation by an energetic enough light beam. In the case of XPS, excitation is provided by a monochromatic X-Ray source.[8] The spectrometer measures the kinetic energy E_{kin} of the emitted electrons, which is related to their binding energy E_{binding} in the material by: $E_{\text{kin}} = h\nu - E_{\text{binding}} - \Phi_{\text{spectro}}$, where $h\nu$ is the energy of the X-Ray beam, and Φ_{spectro} is the spectrometer photo-electric work function.[9] Each energetic level of each element defines a binding energy. As a consequence, the photo-electron emission spectra are made of discrete peaks, whose position is characteristic of elements found in the material (fig. 2.6). In addition to the elemental composition, analysis of the XP spectrum gives access to the chemical bonds in the material. Indeed, they modify the density of valence electrons around atoms, which in turns changes the binding energy of core electrons. This induces displacements by up to a few eV of the peaks. The amplitude of the shift depends on the neighboring atoms. A general rule is that bonds with more electronegative atoms lead to a shift toward higher binding energies. As oxygen is the second most electronegative atom, oxidation is characterized by a sharp increase in binding energy (about 4 eV for silicon). Quantification of the composition is given by the areas of the peaks. That is why both qualitative and quantitative analysis of XP spectra are based on multi-peaks deconvolution.[10]

In addition, depth analysis can be done, though it is more complicated and requires some knowledge about the structure of the material. The materials are scanned very deeply by the X-Ray beam (its attenuation length is typically 500 nm), but the emitted electrons lose energy through inelastic collisions. As a consequence, only electrons emitted in the first 10 to 20 nm (depending on the material) from the surface are collected. Depth profiles can be obtained by changing the angle between the incident beam and the surface of the sample. Quantitative analysis of these profiles is difficult, as the density of the material, hence the electron mean free path, may vary with the depth. Scattered electrons also contribute to a continuous background in the signal called inelastic background.

2.3.2 Analysis of the oxidation

The efficiency of the transfer process to prevent oxidation has been analyzed on a-Si:H and μc-Si thin films. Amorphous silicon thin films were deposited on ITO substrates in PLASFIL[11] at 200 °C.[12] They were loaded in the transport case, which was immediately pumped out. After transfer (1 h), the transport case was opened in the

[7] Cardinaud, Goullet, and Minea, "Plasmas froids — Réactivité en volume et en surface", 2005 [CGM05]

[8] In our case, Al Kα (1486.6 eV).

[9] This relation stands for conductive samples in good electrical contact with the spectrometer.

[10] This peak analysis was done here with Avantage software, by Thermo VG.

[11] *cf.* appendix A

[12] $p = 60$ mTorr, 10 sccm of SiH_4, $P_{RF} = 2$ W, $V_{DC} = -18$ V; 35 min of deposition; 28 min of cooling under nitrogen flow.

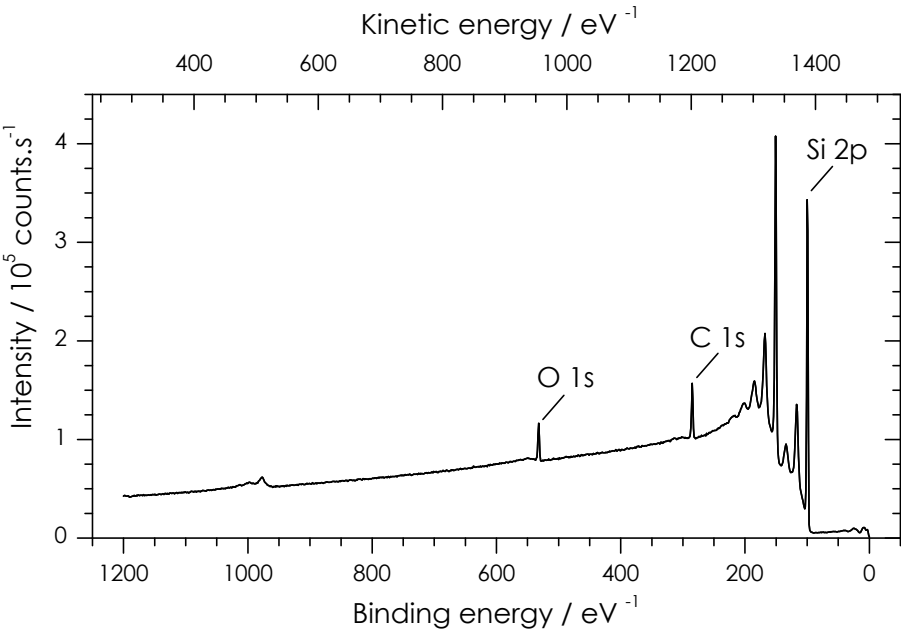

Figure 2.6 – *Full-range X-Ray photoelectron spectrum (measured on a µc-Si layer deposited on ITO in ARCAM)*

glovebox[13], where the samples were stored for one night. They were shortly exposed to air afterwards to be loaded in the X-Ray Photoelectron Spectroscope (XPS). The part of the measured spectrum corresponding to the Si2p orbitals is shown on fig. 2.7a.

As mentioned above, oxidation is characterized in XPS by a shift toward higher binding energies. The binding energy of 2p electrons in bulk crystalline silicon is reported to be around 99.5 eV, whereas Si 2p electrons in pure silica have binding energies about 104 eV.[14] After transfer and one night in the glovebox, no contribution of the oxidized state to the Si 2p peak is detectable. On the other hand, such a contribution is clearly visible on a sample stored for 60 h in air (fig. 2.7a). The coverage by SiO_2 was estimated in that case after the approach by Masuda*et al.*[15] The equivalent oxide thickness d_{ox} is given by:

$$d_{ox} = \lambda_{ox} \sin\theta \ln\left(\frac{I_{ox} M_{ox} \delta_{Si} \lambda_{Si}}{I_{Si} M_{Si} \delta_{ox} \lambda_{ox}} + 1\right) \tag{2.1}$$

where I, M, δ and λ are the integral signal intensity, molecular weight, density and escape length, respectively, and θ is the photo-electron take-off angle. The spectrum shown on fig. 2.7a was obtained with electrons leaving the surface of the sample at an angle of 90°. Two additional measurements were taken at angles of 60° and 30°. The

[13] 0.20 vol.% of O_2, 19.9 ppm of H_2O

[14] Bell and Ley, "Photoemission study of SiO_x ($0 \leq x \leq 2$) alloys", 1988; Feldman, Sun, and Farabaugh, "Bonding structure of silicon oxide films", 1988 [BL88; FSF88]

[15] Masuda et al., "Spectroscopic Study on N_2O-Plasma Oxidation of Hydrogenated Amorphous Silicon and Behavior of Nitrogen", 1993 [Mas+93]

three measurements consistently lead to an equivalent oxide thickness $d_{ox} = 0.2\,\text{nm}$. As the thickness of a monolayer of SiO_2 is 0.35 nm,[16] at most 60% of the surface is covered by SiO_2 after 60 h in air.

A similar experiment was done on μc-Si layers deposited in ARCAM.[17] The measured spectrum in the Si 2p region is shown on fig. 2.7b. As for a-Si:H, no contribution from silicon dioxide is detectable. A remarkable difference is the shape of the Si 2p peak at 99.5 eV. On μc-Si, two sub-peaks can be clearly identified. They correspond to the contribution by Si 2p 3/2 and Si 2p 1/2, respectively. On the contrary, these two sub-peaks cannot be separated on a-Si:H samples, whether oxidized or not. Consistently, the full width at half maximum of these two sub-peaks was significantly larger on a-Si:H than on μc-Si: 0.56 eV and 0.78 eV *vs.* 0.46 eV and 0.64 eV, respectively. The configuration of the XPS was the same for both measurements, so this broadening is an intrinsic property of a-Si:H. It is likely to come from the dispersion in bonding angles and lengths in this material (section 1.1.2).

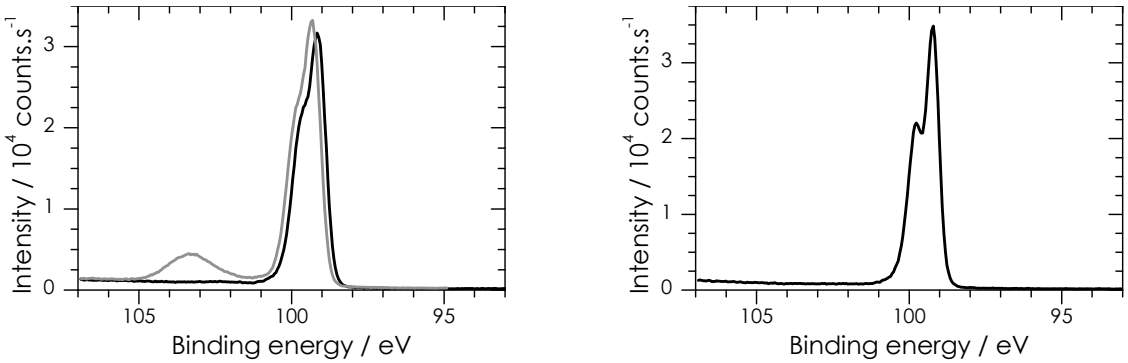

(a) *Amorphous silicon after transfer and one night in glovebox (black line), and after 60*h *in air (gray line)*

(b) *Micro-crystalline silicon after transfer (1.5*h*)*

Figure 2.7 – *XPS spectra of the Si2p orbital of various silicon thin films*

To further confirm the absence of oxide on the surface of transferred thin films, the XP spectrum in the region of the O 1s peak was investigated. The result is shown on fig. 2.8. The amount of oxygen after transfer is exactly the same on a-Si:H and μc-Si, so is the position of the peak. The latter can be decomposed in two peaks. The first one, centered at 531.7 eV, is attributed to hydroxides. The second one, centered at 532.6 eV, can be associated to several compounds, including SiO_2 gels. After normalization by the integrated intensity of the Si 2p peak, the amount of oxygen on the oxidized sample is about three times as much as on the vacuum transferred samples. In addition, the O 1s region then includes a single Gaussian peak centered at 533 eV. This position

[16] Haber and Lewis, "Infrared and X-ray Photoelectron Spectroscopic Studies of the Reactions of Hydrogen-Terminated Crystalline Si(111) and Si(100) Surfaces with Br_2, I_2, and Ferrocenium in Alcohol Solvents", 2002 [HL02]

[17] $T = 175\,°\text{C}$, $d = 17$, $p = 2.5\,\text{Torr}$, 200 sccm of H_2, 3 sccm of SiH_4, $P_{RF} = 10\,\text{W}$, $V_{DC} = -13\,\text{V}$. 15 min of deposition.

is characteristic of SiO_2. In the most pessimistic estimate, the amount of oxide on the vacuum-transferred samples is consequently one third of the amount on the sample exposed to air. Hence at most 20 % of the surface of the samples transferred under vacuum is covered by SiO_2.

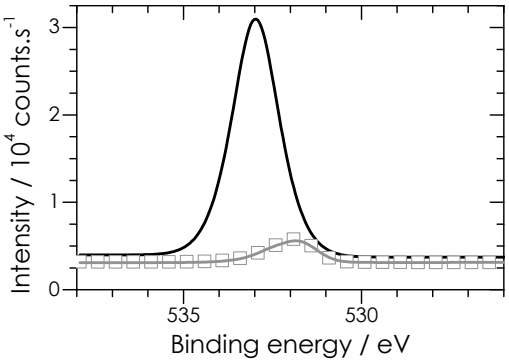

Figure 2.8 – *X-Ray photoelectron spectrum in the O 1s region measured on silicon layers deposited on ITO: a-Si:H exposed to air (black line), a-Si:H transferred under vacuum and stored in glovebox (gray line), and µc-Si transferrred under vacuum and stored in glovebox (gray boxes).*

2.3.3 Analysis of the carbon contamination

A significant amount of carbon was also detected on the previous samples transferred under vacuum. The ratio between the respective integrated intensities of C 1s and Si 2p peaks is 9.5×10^{-2} on a-Si:H and 13.5×10^{-2} on μc-Si. Surprisingly, this ratio is lower for samples exposed to air for 60 h: 4.2×10^{-2}. This indicates that, unlike oxygen, carbon contamination does not come from exposure to air. It is still surface contamination, though: in variable angle measurements, the (C 1s)/(Si 2p) ratio increases when the angle of incidence decreases, *i.e.*, when the scanned thickness decreases. Possible sources of contamination are:

- Retro-diffusion of pump oils, especially after deposition
- Fatty acids in air, which would adsorb on hot samples when taken out of the deposition reactors
- Tools used to manipulate the samples, such as pliers

Carbon contamination could be removed by solvent cleaning, or by annealing under controlled atmosphere. The choice of the solvent is yet constrained, as it should not induce oxidation of the silicon layer. In particular, this bans alcohols.[18] Contamination could also be prevented, if adsorption of fatty acids was its major source, by

[18]Haber and Lewis, "Infrared and X-ray Photoelectron Spectroscopic Studies of the Reactions of Hydrogen-Terminated Crystalline Si(111) and Si(100) Surfaces with Br_2, I_2, and Ferrocenium in Alcohol Solvents", 2002 [HL02]

Treatment	Surface coverage/%	J_{sc}/mA cm^{-2}
None (samples taken out at 130 °C)	7	0.10
1 h dipping in chloroform in glovebox	8	0.015
5 min annealing at 200 °C in glovebox	15	0.013
Cooling before reactor opening (samples taken out at 40 °C	33	0.026

Table 2.1 – *Effect of different treatments on the surface carbon contamination and the performance of the devices*

lowering the temperature at which the samples are taken out of the reactor. These solutions have been investigated. Their impact on carbon contamination has been measured by XPS,[19] and it has been correlated with the performance of solar cells fabricated in parallel. A rough estimate of the surface coverage has been made by considering the following model.

The respective contributions of aliphatic carbons and carbons in functional groups to the C 1s peak can be distinguished. Let us denote their integrated intensity $I_{C,\alpha}$ and $I_{C,f}$, respectively. Let us also denote I_{Si} the integrated intensity of the Si 2p peak. If one assumes that there is one functional group per adsorbed molecule on silicon, then the average length of the carbon chains is $n = I_{C,\alpha}/I_{C,f}$ and the surface coverage η is proportional to $I_{C,f}/I_{\mathrm{Si}} = I_{C,\alpha}/(n \cdot I_{\mathrm{Si}})$. The proportionality constant is estimated with a reference sample. We chose a self-assembled monolayer of dodecene, which is known to cover 100% of the surface of silicon.[20] In that case, $n = 12$ and $I_{C,alpha}/I_{\mathrm{Si}} = 0.796$.

The resulting estimations are given in tab. 2.1, along with the short-circuit current densities in the corresponding devices.

These results are quite disappointing: not only do the treatments fail to prevent or remove carbon contamination, but they even seem to increase it! Two important conclusions can be drawn, though. First, manipulations of the samples must be limited as much as possible. Second, significant contamination occurs when the reactor is cooled down under N_2 or H_2 flux before opening. This is a clue for pump oils to be a major source of surface contamination. There is no clear correlation between the contamination level and the electrical performance of the devices. This indicates that performance variations are dominated by another factor, which is independent of carbon contamination.

2.4 Interface between P3HT and the top electrode

As mentioned in section 1.4, even the best-performing devices have an ideality factor about 4, which is a clue for bad electrical contacts.

[19] on a-Si:H samples deposited in PLASFIL in similar conditions as for the study of oxidation.

[20] Lee et al., "Molecular Modeling of Alkyl Monolayers on the Si(100)-2 x 1 Surface", 2004 [Lee+04]

2.4.1 Defective interface between P3HT and metal electrode

Reasons to suspect this contact

Achieving reproducible and long-lasting ohmic contact with P3HT is known as a difficult task. In P3HT:PCBM devices, holes are collected at the ITO electrode. Even though the work function of ITO should allow an ohmic contact, charge collection proved to be uneven and to degrade fast upon aging. Therefore an intermediate layer of poly(ethyldioxythiophene) doped with poly(styrene sulfonate) (PEDOT:PSS) is deposited between ITO and the active layer. It ensures matching of work-functions between P3HT and the electrode. It is still not perfect, as PEDOT:PSS is acid, which can induce chemical degradation of P3HT at the interface.

In our architecture, holes must be collected at the top electrode. Therefore it was necessary to find a metal which can be easily evaporated, and whose work-function is large enough to form an ohmic contact with P3HT. Gold, whose work-function is reported to be between 4.86 eV and 5.1 eV, was the best candidate.

Chirvase *et al.* characterized sandwich devices made of ITO/P3HT/Au. The gold top electrode was evaporated under vacuum (base pressure: 1×10^{-6} mbar). The electrical characterization was performed in dark and under vacuum (1×10^{-5} mbar). In these conditions, they found the contact between gold and P3HT to be ohmic.[21]

On the other hand, contact resistances of the order of 1 MΩ have been measured between gold and P3HT on field effect transistors.[22] Moreover, Kaneto *et al.* obtained asymmetric J-V characteristics when measuring sandwich Au/P3HT/Au devices under vacuum (1×10^{-6} mbar). They observed a voltage-dependent contact resistance ranging up to 7.7 MΩ.[23] They found the barrier against charge transfer to be higher at the top electrode (0.13 eV) than at the bottom one (0.085 eV), even though both were prepared the same way.[24] Possible explanations to this asymmetry include the incorporation of impurities during evaporation of gold, and the formation of interface dipoles through chemical reactions leading to Si−Au bonds.[25] Rep *et al.*, who worked on similar Au/P3HT/Au devices, evidenced an effect of doping on the contact resistance.[26] They also got asymmetric J-V characteristics, and they found that lower doping leads to higher contact resistance. Their observations could not be described by thermo-ionic emission, as for Schottky diodes. They rather suggested that diffusion-limited current could account for them, *i.e.*, the current through the contact should be

[21] Chirvase et al., "Electrical and optical design and characterisation of regioregular poly(3-hexylthiophene-2,5diyl)/fullerene-based heterojunction polymer solar cells", 2003 [Chi+03]

[22] Hamadani, "Electronic Charge Injection And Transport In Organic Field-Effect Transistors", 2007 [Ham07]

[23] Mukherjee et al., "Minimization of contact resistance between metal and polymer by surface doping", 2007 [Muk+07]

[24] Thakur et al., "Charge injection mechanism across the Au-poly(3-hexylthiophene-2,5-diyl) interface", 2007 [Tha+07]

[25] Zehner et al., "Tuning the Work Function of Gold with Self-Assembled Monolayers Derived from X−[C_6H_4−CC−]nC_6H_4−SH (n = 0, 1, 2; X = H, F, CH_3, CF_3, and OCH_3)", 1999 [Zeh+99]

[26] Rep, Morpurgo, and Klapwijk, "Doping-dependent charge injection into regioregular poly(3-hexylthiophene)", 2003 [RMK03]

proportional to $\mu \exp\left(-\frac{q\phi_B}{k_B T}\right)$, where ϕ_B is the barrier height at the interface. Similar doping-dependent barriers at the interface have been observed by Hamadami *et al.* at the P3HT/Au interface.[27]

In addition, gold deposited on P3HT can diffuse. In the study mentioned above, Kaneto *et al.* estimated sputtered gold could diffuse up to 10 nm deep in the polymer layer. This distance is bound to be larger for evaporated gold, as the temperature of atoms reaching the polymer is higher with evaporation. We observed this phenomenon at the beginning of this work; it lead to severe shunts in the devices, even for P3HT layers significantly thicker than 10 nm.

Evidence for the influence of the metal on the S-shape

These reported observations were clues that the metal/polymer contact could be the origin of the S-shaped J-V characteristics. To obtain evidence that it was indeed the case, a batch of hybrid solar cells with two different metal electrodes has been prepared. One metal was gold, as previously. The other one was silver, which was chosen because it has one of the highest work-functions (4.7 eV) after gold among evaporable metals. In addition, it has been reported to make good contact with P3HT in hybrid solar cells based on metal oxides.[28]

These devices were based on our reference ITO/a-Si:H(n)/a-Si:H(i)/P3HT/metal structure. In that case, the total thickness of a-Si:H was set to 60 nm. The silicon thin films were deposited in ARCAM.[29] A 50 nm-thick P3HT[30] layer was spin-coated in ortho-dichlorobenzene under nitrogen at CEA-INES. Metal electrodes were evaporated under vacuum.[31] Their thickness was 120 nm with Au and 150 nm with Ag.

Resulting J-V characteristics are shown on fig. 2.9a. All of them were S-shaped. The behavior under reverse bias is very similar with both metals: the slope is the same on both characteristics, so the shunt resistance is independent of the top electrode, and the photo-current is also the same. If the characteristics were not S-shaped, the short-circuit current densities would be similar with both electrodes. The major difference is the position of the point of inflexion: it is about −0.22 V for Ag, and about 0.42 V for Au.

This behavior has been analyzed by simulation. An equivalent circuit, shown on fig. 2.10, has been modeled with SPICE 3f5.[32] As mentioned in appendix B, charge collection at the electrodes is generally modeled with a series resistance R_s. Such a model could not reproduce our experimental characteristics. As the latter show a rectifying

[27] Hamadani et al., "Doping-dependent charge injection and band alignment in organic field-effect transistors", 2005 [Ham+05]

[28] Coakley et al., "Ordered organic-inorganic bulk heterojunction photovoltaic cells", 2005 [Coa+05]

[29] a-Si:H(n) layer: chamber A, $d = 28$ mm, $T = 175$ °C; 100 sccm of H_2, 50 sccm of SiH_4, 2 sccm of PH_3; $p = 110$ mTorr; $P_{RF} = 0.5$ W, $V_{DC} = -22$ V; 4 min of deposition. a-Si:H(i) layer: chamber C, $d = 22$ mm, $T = 175$ °C; 100 sccm of H_2, 50 sccm of SiH_4; $p = 180$ mTorr; $P_{RF} = 2$ W, $V_{DC} = -30$ V; 7.5 min of deposition.

[30] Provided by Plextronics

[31] Base pressure: 4.8×10^{-6} mbar for Ag, 1.8×10^{-6} mbar for Au.

[32] We used most of all its implementation as MacSpice 3f5 (http://www.macspice.com/)

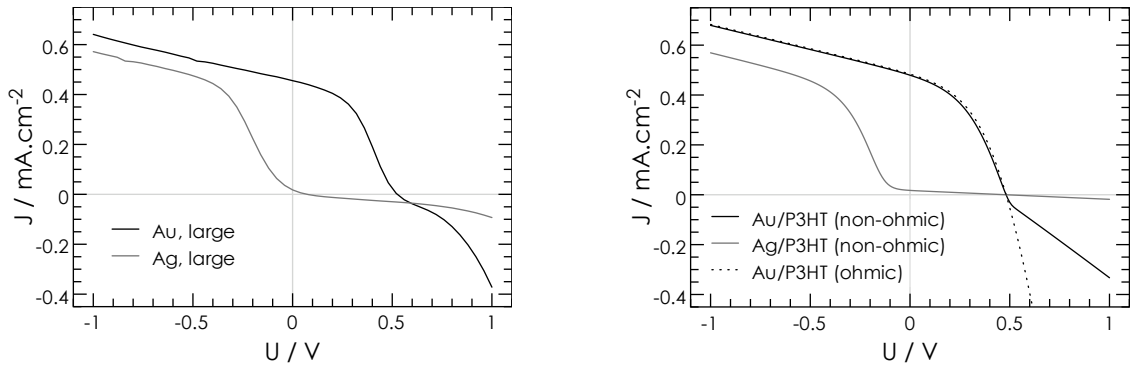

(a) *Measured J-V characteristics* **(b)** *Simulated J-V characteristics*

Figure 2.9 – *J-V characteristics under AM 1.5 simulated illumination of ITO/a-Si:H/P3HT/metal devices with Au and Ag top electrodes*

behavior which opposes current flowing under direct bias, we chose to model the contact by a diode D_e in parallel with a resistor R_{sh_e} and in series with another resistor R_s. The resistor in parallel allows to account for the amount of current which flows at high positive voltage. From a physical point of view, it may be seen as a quantification of the inhomogeneity of the interface between P3HT and metal, or, more precisely, as a measure of the fraction area over which ohmic contact is achieved. As can be seen on fig. 2.9b, this model reproduces very well the shape of the measured characteristics. The photo-generated current density and the main shunt resistance were determined after the experimental curves: $J_{ph} = 0.5\,\mathrm{mA\,cm^{-2}}$ and $R_{sh} = 1.79 \times 10^4\,\Omega$. The characteristics of the diode modeling the active part of the device, D_{cell}, were determined after the measurements on optimized devices reported in the previous chapter: $J_s = 2.65 \times 10^{-3}\,\mathrm{mA\,cm^{-2}}$ and $n = 3.7$. The parameters used to describe the contact are shown on tab. 2.2. The ideality factor n describes how sharp the transition to saturated current is, and the saturation current density J_s determines the position of the point of inflexion. If the saturation current in the contact diode is indeed proportional to $\exp\left(-\frac{q\phi_B}{nk_BT}\right)$, then the barrier heights at the metal/P3HT interface with two different metals are related as follows:

$$\phi_{B_2} = \frac{n_2 k_B T}{q} \ln \frac{J_{s_1}}{J_{s_2}} + \frac{n_2}{n_1} \phi_{B_1} \tag{2.2}$$

With the barrier heights reported by Kaneto *et al.* for the P3HT/Au contact (0.085 eV and 0.13 eV), then the barrier height for the Ag/P3HT contact would be between 0.92 eV and 1.1 eV. These values are within a reasonable order of magnitude, but they are significantly larger than what could be expected from the work-function of silver. This may be due to a different reactivity of silver and gold toward P3HT. Yet this model has been primarily meant for qualitative analysis. Extracting reliable quantitative data would require further developments.

Device	R_s/Ω	R_{she}/Ω	$J_s/\mathrm{mA\,cm^{-2}}$	n
Au/P3HT (ohmic)	500	N/A	N/A	N/A
Au/P3HT (non-ohmic)	500	$5.\times10^{3}$	3.6×10^{-5}	0.25
Ag/P3HT (non-ohmic)	$5.\times10^{-5}$	$1.\times10^{5}$	3.6×10^{-15}	1

Table 2.2 – *Parameters used to simulate contact between various top electrodes and the active layer in hybrid devices*

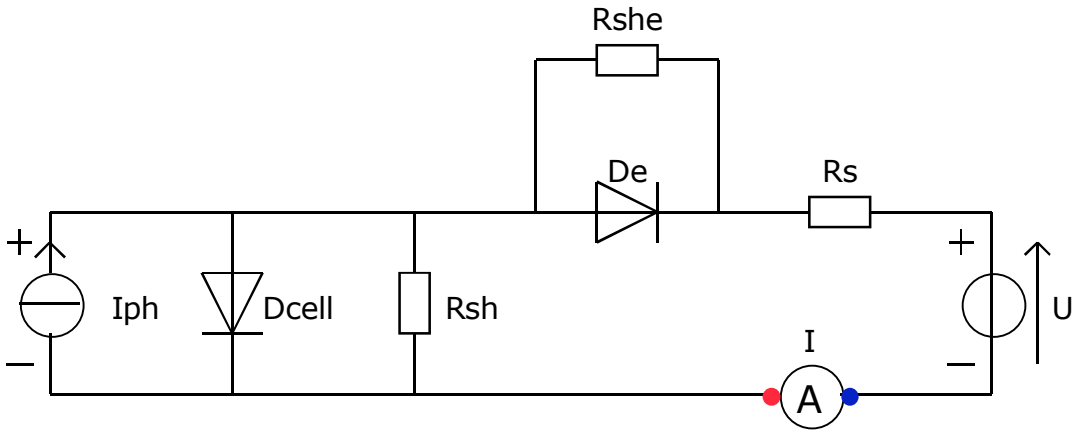

Figure 2.10 – *Diagram of the equivalent circuit to model solar cells with S-shaped characteristics*

2.4.2 Improvement of the contact

Once the contact between P3HT and the top metal electrodes identified as the origin of S-shaped characteristics, ways to improve this interface were still to be found. Replacing gold would require to find another metal with a larger work-function, which could still be evaporated. Palladium was the only relevant candidate. We actually prepared some cells with palladium as the top electrode. The results were comparable to what is obtained with gold. In particular, S-shaped characteristics were obtained on some batches, while good contacts were achieved on others. In addition, the melting point is higher for palladium (1554 °C) than for gold (1064.4 °C). This makes evaporation of palladium difficult,[33] and hot palladium atoms reaching the surface of P3HT seemed to "burn" it in some cases. As a consequence, two other ways to improve the contact at the top electrodes have been investigated: adding an intermediate layer and doping the surface of P3HT.

[33] It was possible by e-beam evaporation in ODILE but it could hardly be achieved by thermal evaporation at CEA-INES.

Surface doping

As mentioned above, the contact barrier at the interface between gold and P3HT has been reported by several groups to depend on the doping level of P3HT. More precisely, annealing the polymer layer under vacuum, which releases some light dopant like oxygen, increases the barrier height. We deposit the polymer layer under nitrogen or argon, anneal it as 110 °C for 5 min,[34] and evaporate the top electrodes under vacuum. One could think that this process is "too clean", and that oxygen doping at the interface would benefit to the performance of the devices.

To test this hypothesis, some cells have been prepared the same way as for the previous section, except that they have been exposed to air 20 min between annealing and evaporation. In addition, top electrodes were evaporated as soon as the pressure was low enough (3×10^{-6} mbar), so that oxygen would not desorb. The resulting J-V characteristics are shown on fig. 2.11. Doping by oxygen has a positive effect under direct bias for gold: the S-shape is attenuated, which means that the effective contact resistance is decreased. On the other hand, the contact resistance is not affected by this doping when silver is the top electrode. In both cases, though, bulk doping of P3HT is visible. Indeed, it increases dark reverse current, so it decreases the potential short-circuit current density.[35] The current density at -1 V under illumination is decreased by the same amount (0.2 mA cm^{-2}) for both top electrodes. This indicates that oxygen is not confined at the surface but diffuses in bulk P3HT. As a consequence, this method is not relevant to improve the overall performance of the devices, even if it actually reduces the contact resistance between gold and P3HT.

Intermediate layer

Superficial doping failed because the dopant diffused in the bulk of the polymer layer. To prevent this issue, one could imagine to deposit a solid layer at the interface between P3HT and the metal electrode. This method has been successfully used in previous works to improve hole collection at the interface between P3HT and ITO in all-organic solar cells. In that case, the intermediate layer is PEDOT:PSS, which is spin-coated on top of ITO before the active layer is deposited. We tried to adapt this method to our architecture. The difficulty was due to PEDOT:PSS coming in suspension in water, whereas P3HT is hydrophobic. This is shown on fig. 2.12. The contact angle of deionized water on P3HT is 86°. It is even higher with a dispersion of PEDOT:PSS in water: 104°. As spin-coating requires good wetting of the substrate by the solution, it is impossible to deposit PEDOT:PSS as it is by this method.

Use of intermediate solvents (ethanol, isopropanol, ethylene glycol) has been investigated in two ways. First, P3HT-coated samples have been dipped in such solvents for some time (typically, 30 min) so that a wetting layer forms on P3HT, which

[34] To remove traces of solvent.

[35] With silver, inflexion in the J-V curve occurs at negative voltage, so the short circuit current density is virtually zero in any case. By potential short-circuit current density, we mean the value of J_{sc} which would be obtained if the slope at $V < -0.5$ V was extended to 0 V.

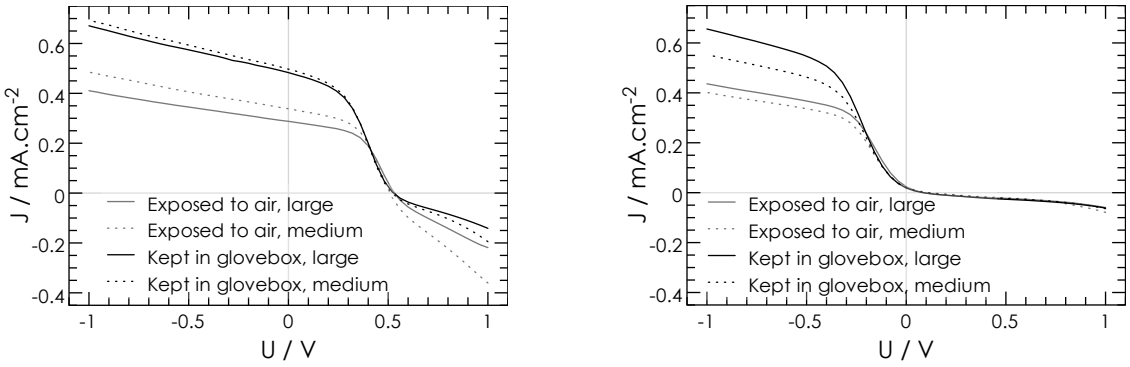

(a) *Top electrodes: gold* **(b)** *Top electrodes: silver*

Figure 2.11 – *J-V characteristics of hybrid cells exposed to air (20*min *between annealing of the polymer layer and evaporation of the top electrode), or kept in glovebox at the same time, for various top electrodes. Large cells: 0.196*cm^2*; medium cells: 0.071*cm^2*.*

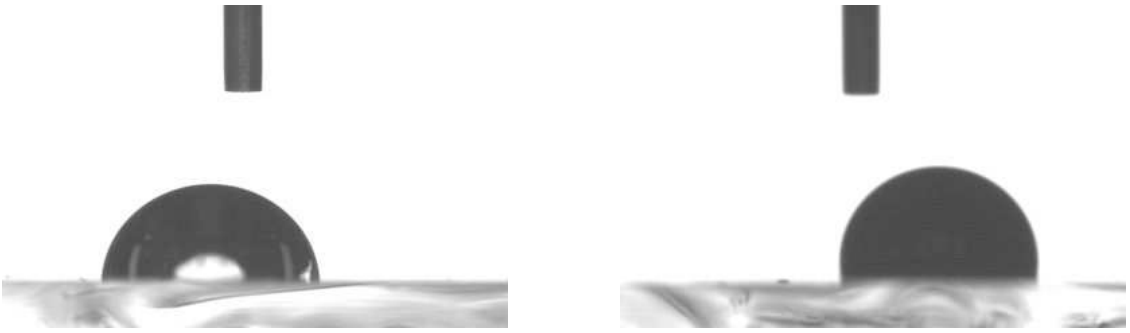

(a) *Pure water: contact angle is 86°* **(b)** *PEDOT:PSS dispersion in water: contact angle is 104°*

Figure 2.12 – *Contact angle measurements (in air) for deionized water and PEDOT:PSS dispersion on P3HT*

would allow the PEDOT:PSS dispersion to spread on the surface. Second, these solvents have been added in various amounts to the PEDOT:PSS dispersion (up to 20:1 in vol.) to decrease its interfacial tension with P3HT layers. Both methods failed. Even with several subsequent depositions, at increasing PEDOT:PSS/solvent volume ratios, no PEDOT:PSS layer could be deposited. In addition, when the PEDOT:PSS dispersion is diluted in isopropanol, precipitates are formed. Recently, PEDOT:PSS directly in dispersion in water-compatible organic solvents, such as ethylene glycol and isopropanol, have been made commercially available by Plextronics. We tried to use such a dispersion[36] on top of hybrid devices. As for previous attempts, no PEDOT:PSS film could be deposited, even after annealing the P3HT layer at 175 °C to remove possible traces of dichlorobenzene, or after seven subsequent spin-coating runs. At the opposite, uniform PEDOT:PSS films were obtained without any treatment on top of P3HT:PCBM bulk-heterojunction layers. It is likely that this difference comes from the methyl ester side-group of PCBM, which can participate in hydrogen bonds.

An alternate idea was then to use surfactants to reduce the surface tension at the interface between P3HT layers and the PEDOT:PSS water dispersion. Several criteria were to be fulfilled by the surfactant:

- It must be non-ionic, in order not to dissociate the macromolecular salt formed by PEDOT:PSS
- To act as a wetting agent, it must have an intermediate hydrophilic-lipophilic balance (HLB): between 7 and 9 after Griffin's definition
- Its critical micellar concentration (CMC) must be low, so that limited amounts are needed.

After these criteria, we chose $C_{12}H_{25}(OCH_2CH_2)_4OH$ (polyethylene glycol dodecyl ether, commercially known as Brij30). Its HLB is 9.7, and its CMC is about 1×10^{-3} vol.%. As can be seen on fig. 2.13, it is very effective to reduce the contact angle between deionized water or PEDOT:PSS water dispersion, and P3HT layers. For comparison, the contact angle of PEDOT:PSS water dispersion on ITO is 83°.

Spin-coating PEDOT:PSS on P3HT thin films could then be reasonably tried. We found the best process to be made of three steps: a first step at 300 rpm (45 s) for spreading the solution, a second one at 800 rpm (1 min) for spreading and smoothing the liquid film and a third step at 2000 rpm (1 min) for drying the film. When used with an equi-volume solution of PEDOT:PSS water dispersion and deionized water with 0.1 vol.% of Brij30, this method leads to the deposition of a PEDOT:PSS film on the surface of P3HT. The latter is not completely covered, though (fig. 2.14). Unfortunately, no electrical characterization of this intermediate layer has been done, but this method would be worth further investigations. Interestingly, another group recently reported the successful use of a surfactant in PEDOT:PSS dispersion to enhance the contact between P3HT and gold.[37] But in their case, they started with spin-coating

[36] Plextronics Plexcore PC AK-350, batch nr. 08-10483

[37] Mukherjee et al., "Minimization of contact resistance between metal and polymer by surface doping", 2007 [Muk+07]

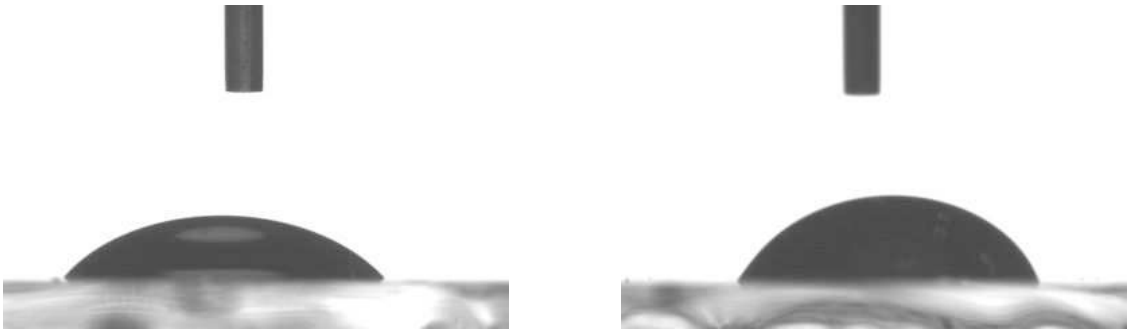

(a) *Pure water with 0.01 vol.% Brij30: contact angle is 38°*

(b) *Equi-volume solution of PEDOT:PSS water dispersion and deionized water with 0.01 vol.%: contact angle is 67°*

Figure 2.13 – *Contact angle measurements on P3HT films (in air) of deionized water and PEDOT:PSS water dispersion with Brij30*

the surfactant alone in water (dodecyl benzene sulfonic acid — DBSA) to use it as a dopant for P3HT. They eventually added PEDOT:PSS to immobilize DBSA at the surface of P3HT and prevent it from diffusing in the bulk of the polymer layer. Nevertheless, they obtained by this method an ohmic contact between gold and P3HT.

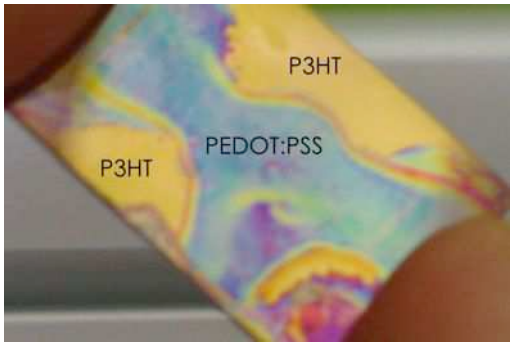

Figure 2.14 – *Picture of a PEDOT:PSS layer spin-coated on top of P3HT after addition of deionized water with 0.1 vol.% Brij30 to the dispersion*

Summary

A new sample design and a simplified fabrication process have been developed. They allow to get more information from each sample. In addition, the performance over each batch is more uniform than with the initial process. Nevertheless, strong variations remain among different batches. In particular, the generated photo-current seems to be highly sensitive to the thickness of the layers. As to now, performance

of the best devices is still difficult to reproduce. What can be guaranteed are a fill-factor of more than 40%, a short-circuit current density larger than 0.2 mA cm^{-2} and an open-circuit voltage of more than 580 mV.

When samples are transferred under vacuum in our home-made case, oxidation of the silicon surface is efficiently prevented. For both a-Si:H and μc-Si layers, the amount of oxide just before deposition of the polymer layer is guaranteed to be lower than 20% of a monolayer. Moreover, this amount is uniform over various samples. On the other hand, carbon contamination is stronger and more variable, both in its amount and its nature. No efficient way to remove it could be found, but pump oils have been identified as a major source of contamination. In addition, evidence shows that any manipulation of the samples contributes to this contamination, too. They should be therefore be limited as far as possible.

The major source for S-shaped J-V characteristics has been identified to be the contact between P3HT and the top metal electrodes. It is caused by a processing-dependent energy barrier, which can be described as a diode opposing charge transfer. The most promising way to enhance the contact is to use an intermediate layer of PEDOT:PSS, with a surfactant additive, deposited on top P3HT.

A new substrate for silicon nanowires: transparent conductive oxides

3

> Entropy's decreasing by the second, Will. Are you using Dream Topping in any of your nanomachines?
>
> Jasper Fforde, *Lost in a Good Book*

Contents

THE CORE of the device architecture we aim for is a nano-structured silicon layer, ideally a brush of silicon nanowires. In this chapter, we will investigate methods to grow such a layer on a new class of substrates: transparent conductive oxides — such as ITO — deposited on glass. They are rough and polycrystalline, and their surface properties are different from those of the usual crystalline silicon.

We will first review the main existing methods to grow silicon nanowires on substrates, with the simplicity and temperature of the process in focus.

As metallic nano-aggregates play a central role in the selected methods, we will investigate how they can be obtained from an evaporated thin film on ITO.

Finally, we will perform some depositions to check whether the selected method can be adapted to transparent conductive oxides.

3.1 How can silicon nanowires be grown on a substrate?

An extensive literature deals with the growth of semiconductor nanowires, whether in solution or on substrates. General reviews on this topic are available.[1]

Two main ways may be distinguished to obtain silicon nanostructures on substrates. The first one is a "top-down" approach. It consists in selectively etching a silicon surface. The second one consists in growing anisotropic structures, mainly from gas-phase precursors. This is a "bottom-up" approach.

3.1.1 The "top-down" approach: etching

Pr. Zhu's group (Tsinghua University, Beijing) has obtained silicon nanowires by etching crystalline silicon substrates with an HF:$AgNO_3$ solution[2]. They rationalized this result through localized micro-electrochemical reactions, where deposited metal seeds act as local cathodes. Such nanowires have diameters between 30 nm and 150 nm, and lengths between 20 µm and 50 µm. The same group later obtained well aligned nanowires perpendicular to the substrate using 20 nm-thick evaporated silver layers on crystalline silicon and subsequent etching in aqueous HF:H_2O_2 solution[3]. They also evidenced that the silver is eventually found at the bottom of the inter-wire gaps, which they explained by the fact that silver actually catalyses the etching process. The alignment of the wires may come from the organization of the silver layer. Indeed, at 20 nm, it forms a mesh whereas isolated islands are formed at lower thickness and thicker layers are continuous. Geometrical constraints due to this mesh may be sufficient to ensure vertical etching.

Lithography can also be used in a top-down approach to silicon nanowires. Optical lithography followed by plasma etching in HBr:O_2 allowed for the formation of 30 nm-wide and 500 nm-long wires.[4] Another lithographic method has been proposed by M.D McGehee's group in Stanford.[5] They used block copolymer as an evaporation mask for metal, which selectively protected silicon during reactive ion etching. By annealing a layer of poly(styrene-*b*-methylmethacrylate) (PS-*b*-PMMA) at 175 °C for 24 h, they obtained cylindrical micro domains perpendicular to the silicon surface. Exposure to UV irradiation then led to the degradation of PMMA and cross-linking of PS. After rinsing and exposure to O_2 plasma, a PS matrix with cylindrical holes remained on the substrate. 5 nm of Cr was then evaporated before lift-off. Good anisotropy was obtained after reactive ion etching with NF_3 because the etching rate by this gas is

[1] Lu and Lieber, "Semiconductor nanowires", 2006; Xia et al., "One-Dimensional Nanostructures: Synthesis, Characterization, and Applications", 2003 [LL06; Xia+03]

[2] Peng et al., "Synthesis of Large-Area Silicon Nanowire Arrays via Self-Assembling Nanoelectrochemistry", 2002 [Pen+02]

[3] Fang et al., "Silver catalysis in the fabrication of silicon nanowire arrays", 2006 [Fan+06]

[4] Agarwal et al., "Breakdown Enhancement in Silicon Nanowire p-n Junctions", 2007 [Aga+07]

[5] Gowrishankar et al., "Fabrication of densely packed, well-ordered, high-aspect-ratio silicon nanopillars over large areas using block copolymer lithography", 2006 [Gow+06a]

sixty times lower for chromium than for silicon, and because N is thought to passivate the walls of the nano-pillars, thus preventing lateral etching. This way, silicon nano-pillars have been obtained with aspect ratios larger than 10, heights about 100 nm and a periodicity of about 35 nm. Interestingly, this method has been recently used on thin amorphous silicon layers.[6]

All these methods are limited by the fact that they require substrates of the same nature as the nanowires to grow (in our case, silicon). Moreover, wet etching is not really compatible with thin films on transparent conductive oxides, as the latter are likely to be etched, too. To overcome these difficulties, investigating growth from vapor phase may be a good option.

3.1.2 The "bottom-up" approach: anisotropic growth

The general framework for the anisotropic growth of silicon nanostructures on substrates is the "Vapor-Solid-Liquid" (VLS) process and its variation, the "Vapor-Solid-Solid" (VSS) process. This growth mode has been first described by Wagner and Ellis in 1964.[7] It is a specific kind of Chemical Vapor Deposition (CVD) where metallic catalysts are used to localize the growth. It can be decomposed in the following steps, illustrated in the case of the growth of silicon nanowires from silane (SiH_4) on crystalline silicon substrates (fig. 3.1).

Dissociation of silane

The dissociation of SiH_4 upon chemisorption at a surface is a thermally activated process. The activation energy is much lower on copper[8] (0.87 eV) and gold[9] (0.53 eV) than on crystalline silicon (2 eV). This difference is essential for achieving highly anisotropic growth. Indeed, if the growth rate is limited by this step, it will be proportional to $\exp\left(\frac{-E_a}{kT}\right)$. For the values of the activation energy reported here, this leads to 11 orders of magnitude of difference between the growth rates on gold and on silicon at 400 °C, and still 8 orders of magnitude at 600 °C (cf. tab. 3.1). So an additional advantage of going to lower growth temperature, with a given catalyst, is to enhance the anisotropy of the growth. Yet the growth rate is noticeably reduced when the temperature decreases.

Diffusion of silicon in the catalyst

This step has a significant impact on the nucleation time of the nanowires. Indeed, A. Fontcuberta i Morral and her co-workers have shown that the nucleation time τ is

[6] Gowrishankar et al., "Exciton harvesting, charge transfer, and charge-carrier transport in amorphous-silicon nanopillar/polymer hybrid solar cells", 2008 [Gow+08]

[7] Wagner and Ellis, "Vapor-Liquid-Solid Mechanism of Single Crystal Growth", 1964 [WE64]

[8] Wiegand, Lohokare, and Nuzzo, "Silicon-hydrogen (Si-H) bond activation on copper: reaction of silane on Cu(111)", 1993 [WLN93]

[9] Kodambaka et al., "Diameter-Independent Kinetics in the Vapor-Liquid-Solid Growth of Si Nanowires", 2006 [Kod+06]

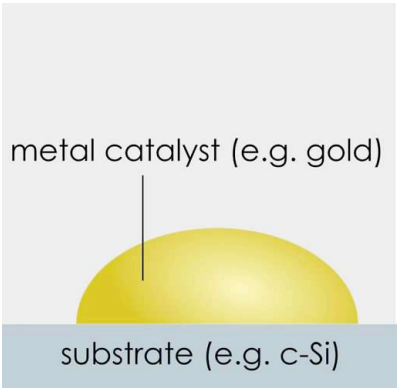

(a) *Nanometer-scaled metallic aggregates are formed on the substrate (e.g. crystalline silicon)*

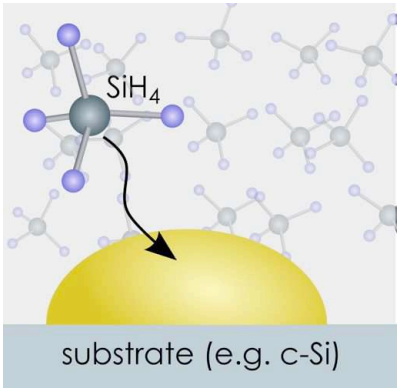

(b) *A flow of precursor gas (e.g. silane) is introduced in the heated reactor.*

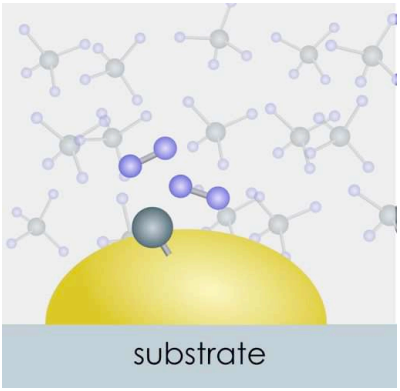

(c) *The precursor gas is decomposed at the surface of the metal catalyst through dissociative chemisorption.*

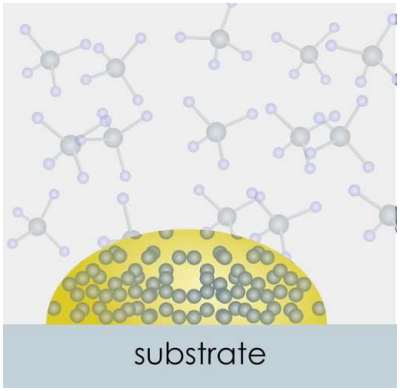

(d) *Continuous integration and diffusion of Si leads to a concentration gradient in the aggregate. An eutectic alloy may be formed.*

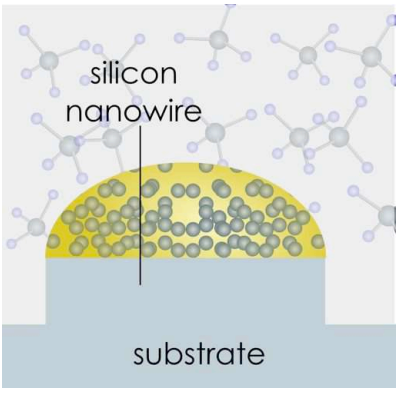

(e) *When the concentration reaches a saturation level, Si precipitates at an interface, which leads to the deposition of solid Si.*

Figure 3.1 – *Main steps of the VLS process*

Surface	E_a (eV)	Temperature (°C)			
		300	400	500	600
Si	2	1.00	4.11×10^2	3.56×10^4	1.11×10^6
Cu	0.87	8.73×10^9	1.20×10^{11}	8.33×10^{11}	3.72×10^{12}
Au	0.53	8.55×10^{12}	4.21×10^{13}	1.37×10^{14}	3.42×10^{14}

Table 3.1 – *Normalized dissociation rates of SiH_4 on different surfaces and at different temperatures*

given by:[10]

$$\tau \simeq \frac{h^2}{\langle D_{s0} \rangle \exp\left[\frac{-E_a}{kT}\right]}$$

where $\langle D_s \rangle = \langle D_{s0} \rangle \exp\left[\frac{-E_a}{kT}\right]$ is the average diffusion coefficient of silicon in the solid metal at the temperature T, and h is the height of the droplet.

This step may also be a limiting step during the growth of the nanowires. This motivates the use of catalysts with low melting points or low eutectic points with silicon. Indeed, the diffusion coefficient of silicon (like any other element) is generally much higher in a liquid than in a solid phase.

Saturation and precipitation of silicon

When the silicon concentration reaches a saturation level, precipitation happens. This occurs preferentially at an interface, not in the bulk, in order to minimize the increase in the surface energy. When the substrate is silicon (or when the permanent regime of growth is reached), there is even no increase in the surface energy upon precipitation at the metal/substrate interface.

3.1.3 Control of the orientation and the growth direction

The crystalline orientation of silicon nanowires has been shown to depend on their diameter. Wu *et al.*, from Lieber's group in Harvard, have classified nanowires grown on amorphous SiO_2 as a function of their size.[11] They observed that, for 95% of the wires whose diameter was between 3 nm and 10 nm, the growth direction was the ⟨110⟩ axis; for 61% of those whose diameter was between 10 nm and 20 nm, it was the ⟨112⟩ axis; for 64% of those whose diameter was between 20 nm and 30 nm, it was the ⟨111⟩ axis. Similar results have been obtained on silicon nanowires epitaxially grown on (100) crystalline silicon wafers by Schmidt, Senz and Gösele.[12] In addition, it is

[10] Kalache, Cabarrocas, and Morral, "Observation of incubation times in the nucleation of silicon nanowires obtained by the vapor-liquid-solid method", 2006 [KCM06]

[11] Wu et al., "Controlled Growth and Structures of Molecular-Scale Silicon Nanowires", 2004 [Wu+04]

[12] Schmidt, Senz, and Gosele, "Diameter-Dependent Growth Direction of Epitaxial Silicon Nanowires", 2005 [SSG05]

known since the first observation by Wagner and Ellis that the preferential direction for larger silicon nanowires and whiskers grown through the VLS process is the ⟨111⟩ axis.[13]

This dependence of the growth direction on the diameter of the wires can be analyzed in terms of minimization of their free energy. Indeed, two of the six terms in the latter depend on the crystalline orientation:[14] the interfacial tension σ_{ls} between the nanowire and the catalyst droplet, and the surface tension σ_s from the edge of the interface region.[15] These two terms have been calculated to be $\sigma_{ls} = 0.62\,\mathrm{J\,m^{-2}}$ and $\sigma_s = 1.53\,\mathrm{J\,m^{-2}}$ for silicon nanowires grown along the ⟨111⟩ direction; $\sigma'_{ls} = 0.76\,\mathrm{J\,m^{-2}}$ and $\sigma'_s = 1.28\,\mathrm{J\,m^{-2}}$ for silicon nanowires grown along the ⟨110⟩ direction. The respective contribution of each term depends on the geometry of the interface between the wire and the droplet, which itself depends on the crystalline orientation, and on the perimeter of the wire. Thus the free energy as a function of the radius of the wires has different slopes for the two different orientations. The crossover radius, above which the free energy starts to be lower for wires grown in the ⟨111⟩ direction, has been calculated to be approximately 10 nm, which is consistent with the experimental data.

A consequence of the growth direction essentially depending on the size of the nanowires is the orientation of the latter relative to the substrate (fig. 3.2). When they are grown on an amorphous SiO_2 layer, their orientation is random. But when nanowires larger than 20 nm (thus mainly along the ⟨111⟩ direction) are grown on ⟨100⟩ crystalline silicon substrates, their projections on the substrate follow two perpendicular axes and the nanowires themselves make a 45° angle with the substrate. On the other hand, when similar nanowires are grown on a ⟨111⟩ crystalline silicon substrate, they are perpendicular to the surface.

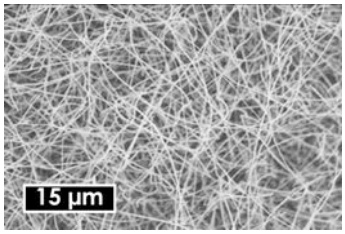

(a) *Substrate: SiO_2, catalyst: 1*nm *evaporated gold layer [Alb+06]*

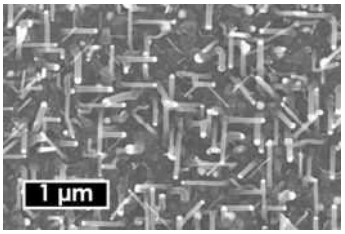

(b) *Substrate:* ⟨100⟩ *c-Si wafer, catalyst: 2*nm *evaporated gold layer [Ael+07]*

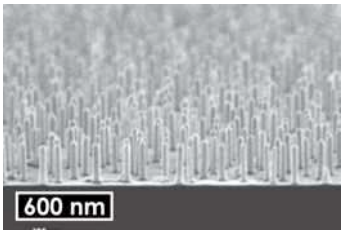

(c) *Substrate:* ⟨111⟩ *c-Si wafer, catalyst: 0.6*nm *evaporated aluminum layer [Wan+06]*

Figure 3.2 – *SEM images of silicon nanowires grown on various substrates*

[13] Wagner and Ellis, "Vapor-Liquid-Solid Mechanism of Single Crystal Growth", 1964 [WE64]

[14] Schmidt, Senz, and Gosele, "Diameter-Dependent Growth Direction of Epitaxial Silicon Nanowires", 2005 [SSG05]

[15] The other terms are the bulk free energies of the nanowire and the catalyst droplet, the line tension at the triple-phase gas/Si/Au-Si line and the surface tension of the catalyst droplet.

3.1.4 Choice and deposition of the metal catalysts

Controlled deposition of metal catalyst aggregates

Numerous methods have been investigated for depositing metallic aggregates to be used as catalysts. Many of them are detailed in a review on the growth of semiconductor nanowires.[16] The following ones are heavily investigated in this particular field:

- Lithography allows for a good geometrical control on the position of the nanowires. Photo-lithography has limited resolution, though, which makes it difficult to ensure that only one nanowire grows on each metallic dot. Electron-beam lithography allows to overcome this limit,[17] but it is a heavy and slow method, hence not suitable for large substrates.

- Colloidal solutions of several metals, especially gold, are available with a very narrow size distribution. This way, they allow for a very good control on the diameter of the nanowires.[18] Moreover, there is a linear relationship between the concentration of the colloidal solution and the final number density of nanowires. This method is simple, it can be used in air, but it is limited by the possible aggregation of the particles after deposition and by its strong requirements on the properties of the substrate (roughness, surface properties). In addition, there is little control on the spatial arrangement of the nanowires.

- Porous membranes can be prepared by anodization of aluminum. This way, hexagonal arrays of pores with narrow size distribution can be obtained over large substrates.[19] These alumina membranes can be used either as evaporation masks[20] or as patterns for electrochemical deposition of metal dots.[21] One of the major challenges in this technique is avoiding deposition on the walls of the membrane.

- Annealing a thin evaporated film so that it cracks (when continuous) or forms aggregates by coalescence (when discontinuous) is the most widely used technique. As it relies on diffusion on the surface of the substrate, it offers little control on the shape of the metallic particles and the size dispersion is high. It also requires weak adhesion of the metallic layer to the substrate. Though simple in principle, this method still requires to use an evaporator in addition to the CVD reactor, and generally to transfer the samples.

[16] Fan, Werner, and Zacharias, "Semiconductor Nanowires: From Self-Organization to Patterned Growth", 2006 [FWZ06]

[17] Chang et al., "Controlled formation of individually seeded, electrically addressable silicon nanowire arrays for device integration", 2006 [Cha+06]

[18] Hochbaum et al., "Controlled Growth of Si Nanowire Arrays for Device Integration", 2005 [Hoc+05]

[19] Li et al., "Hexagonal pore arrays with a 50–420 nm interpore distance formed by self-organization in anodic alumina", 1998 [Li+98]

[20] Lombardi et al., "Synthesis of high density, size-controlled Si nanowire arrays via porous anodic alumina mask", 2006 [Lom+06]

[21] Dayen et al., "Electronic transport of silicon nanowires grown in porous Al_2O_3 membrane", 2007 [Day+07]

Potential catalysts

Different criteria are taken into account in the selection of a catalyst:

- The melting point of the material and a possible eutectic point with silicon, which determines the minimum temperature for the VLS process to be possible.
- The surface diffusion of the material on the substrate, which determines its aggregation behavior upon annealing.
- The bulk diffusivity in the substrate, which can lead to the disappearance of a thin evaporated layer from the surface.
- The impact of the material on the electronic properties of silicon.
- The availability of a method to obtain small isolated aggregates of the material on the substrate.

Since the first report of the VLS growth, gold is the "standard" catalyst. The main reason is that it has a eutectic point with silicon at 363 °C,[22] which allows for VLS process at temperatures slightly higher than that. In addition, gold is easy to evaporate and colloidal solutions are widely available for research. Yet the diffusivity of gold in bulk silicon is high[23] ($1\times10^{-8}\,cm^2/s$ to $1\times10^{-7}\,cm^2/s$ at 900 °C). As a consequence, when a very thin film ($\leq 2\,nm$) is evaporated on bare silicon, it is likely to disappear in the bulk of the substrate. A barrier SiO_2 layer is often used to prevent this problem, but it also prevents epitaxial growth of nanowires. Even worse, gold also diffuses in nanowires and creates deep centers in the band gap, 0.54 eV below the conduction band and 0.29 eV above the valence band.[24] It is therefore not relevant for optoelectronic applications like solar cells.

Aluminum is in many ways a better candidate. It has a lower diffusivity in crystalline silicon than gold[25] ($1\times10^{-14}\,cm^2/s$ to $1\times10^{-13}\,cm^2/s$ at 900 °C) and it is an acceptor dopant, which creates centers 67 meV above the valence band. It also makes a eutectic with silicon, though at higher temperature than gold (577 °C). The main issue for using aluminum is its fast oxidizing. So far, ultra-high vacuum processes have been necessary to use this catalyst,[26] and oxides substrates are excluded.

Copper, in turn, diffuses very fast in silicon: its diffusivity at 900 °C has been reported to be $5\times10^{-5}\,cm^2/s$.[27] This fast diffusion influences the way copper changes

[22] When no specific source is given, all data about binary phase diagrams in this section come from—Massalski, *Binary Alloy Phase Diagrams*, 1998 [Mas98]

[23] Collins, Schroder, and Sah, "Gold Diffusivities in SiO_2 and Si Using the MOS Structure", 1966 [CSS66]

[24] When no specific source is given, all data about deep centers in silicon come from—Böer, "Survey of Semiconductor Physics", 1990 [B̈90]

[25] Krause, Ryssel, and Pichler, "Determination of aluminum diffusion parameters in silicon", 2002 [KRP02]

[26] Wang et al., "Epitaxial growth of silicon nanowires using an aluminium catalyst", 2006 [Wan+06]

[27] Istratov et al., "Intrinsic Diffusion Coefficient of Interstitial Copper in Silicon", 1998 [Ist+98]

the electrical properties of silicon: it does not remain electrically active at interstitial sites, but makes aggregates and precipitates. This way, in mono-crystalline silicon, copper has no effect on the carrier lifetime at concentrations up to $1 \times 10^{17}\,\mathrm{cm}^{-3}$. But, in poly-crystalline silicon, the precipitates behave as recombination centers and copper leads to a significant decrease in the charge carrier lifetime at concentrations just above $1 \times 10^{12}\,\mathrm{cm}^{-3}$.[28] Four deep levels in silicon have been attributed to copper, at 0.15 eV to 0.2 eV below the conduction band and at 0.41 eV to 0.46 eV, 0.20 eV to 0.23 eV, and 0.09 eV to 0.1 eV above the valence band, respectively. The phase diagram of the binary Si-Cu alloy is quite complicated, with numerous solid alloy phases and a eutectic temperature of 802 °C. Nevertheless, copper has been successfully used to grow silicon nanowires in the VSS mode.[29]

Gallium is a good candidate in many ways. Its melting point is low (30 °C), its diffusivity in bulk crystalline silicon is also low ($1 \times 10^{-14}\,\mathrm{cm}^2/\mathrm{s}$ at 900 °C).[30] It is an acceptor dopant which creates states at 27 meV above the valence band. Yet difficulties in its processing limit its use. In particular, its high surface diffusion coefficient leads to fast aggregation upon heating so it is difficult to obtain small particles of this metal.

Finally, indium has also a low melting point (156.63 °C). Its diffusivity in silicon ($1 \times 10^{-15}\,\mathrm{cm}^2/\mathrm{s}$ at 900 °C) is the lowest among the metals mentioned here.[31] But its use as a catalyst is limited by the deep acceptor level it creates in silicon (0.16 eV above the valence band) and above all by its oxidation.

3.2 Formation of metallic aggregates on transparent conductive oxides

Periodicity of the structure and homogeneity among the diameters of the wires are not crucial for the application we aim at. However, it is very important to have a process as simple and as straightforward as possible. That is why we chose to use the method based on metal evaporation followed by annealing. Here we will investigate the evolution of a thin evaporated gold layer on ITO. Gold has been chosen first because it is the "standard" catalyst for the growth of silicon nanowires, and second because it shows a sharp SEM contrast with the substrate, which allows extraction of quantitative data. Copper will also be investigated, though not as extensively.

[28] Istratov and Weber, "Electrical properties and recombination activity of copper, nickel and cobalt in silicon", 1998 [IW98]

[29] Arbiol et al., "Influence of Cu as a catalyst on the properties of silicon nanowires synthesized by the vapour-solid-solid mechanism", 2007; Yao and Fan, "Si nanowires synthesized with Cu catalyst", 2007 [Arb+07; YF07]

[30] Haridoss et al., "Diffusion of gallium in silicon", 1980 [Har+80]

[31] Suzuki, Tashiro, and Aoyama, "Diffusion coefficient of indium in Si substrates and analytical redistribution profile model", 1999 [STA99]

3.2.1 Deposition and annealing

The substrates used in this part were our usual ITO-coated glass samples provided by PGO. They were cleaned in the following sequence:

- Ultrasonic bath in ethanol (twice 10 min, power: 100%)
- Ultrasonic bath in acetone (twice 10 min, power: 100%)
- Exposure to O_3 in a UV-ozone reactor (10 min)

They were then immediately loaded into ODILE glovebox, where they were stored until the evaporation.

Thin layers of gold were deposited on the substrates using an electron beam evaporator (*cf.* appendix B). The base pressure was below 5×10^{-8} mbar. The actual deposition started between 3×10^{-7} mbar and 5×10^{-7} mbar for a wire intensity of 18 A. The pressure at the end of the deposition was around 7×10^{-7} mbar. The deposition rate was around 1 nm min^{-1}. The equivalent thickness of the layer, as measured by a quartz crystal microbalance, was varied between 1 nm and 4 nm. After evaporation, the setup was filled again up to the atmospheric pressure with argon and the samples were stored in the glovebox.

The samples were then transported in an airtight, low-pressure container filled with argon. They were loaded in the quartz tube reactor used for the CVD growth of silicon nanowires (fig. 3.15), which was immediately pumped down to 1×10^{-5} mbar. The samples were stored in the introduction chamber during the temperature ramp-up and cool-down. This introduction chamber is not separated from the main part of the tube by any valve or wall, so the pressure and gas content is the same. But it is way outside the infrared heaters, so it remains almost at room temperature. Samples were annealed at 70 °C, 210 °C, 300 °C, 360 °C, 435 °C, 530 °C and 650 °C for 15 min. Additionally, some samples were annealed at 70 °C and 140 °C for 5 min and 10 min.

3.2.2 Development and test of a characterization method

The samples were characterized by Scanning Electron Microscopy (SEM). For all of them, the working distance was 7 mm and the acceleration voltage was 25 kV. We developed an automated image analysis process based on ImageJ[32] in order to get quantitative information from the images. Our goal was to analyze several images for each sample (usually ten) to have good statistics, while keeping the method consistent over this large set of files.

The method is illustrated here on a sample with a 3 nm gold layer annealed at 530 °C for 15 min. Starting from the raw SEM image, the main steps are shown on fig. 3.3:

1. Crop the image to keep only the useful part by removing the borders and the text (fig. 3.3b).

[32] Abramoff, Magelhaes, and Ram, "Image Processing with ImageJ", 2004 [AMR04]

2. Level the saturated pixels by limiting the color histogram to $[\bar{x}-2\sigma;\bar{x}+2\sigma]$ (fig. 3.3c).

3. Enhance the contrast through histogram equalization.

4. Remove the noise by applying a median filter: each pixel is replaced by the median value of the pixels contained in a certain area around it (fig. 3.3d).

5. Binarize the image by setting a threshold gray level g_t (fig. 3.3e). Pixels with gray values above g_t will be considered white, pixels with gray values below it will be considered black. The value of g_t can be set either manually or automatically. The algorithm for automatic threshold determination which gave the best results on our images is the IsoData algorithm.[33] The result of this iterative algorithm is a threshold gray level g_t which is the average of (i) the average gray value of the dark part of the picture and (ii) the average gray value of the bright part: $g_t = \left(\langle g_{dark}\rangle + \langle g_{bright}\rangle\right)/2$. A manually fixed value of 100 for g_t, on the other hand, corresponds well to the visual impression on an image after contrast enhancement. The two methods give complementary results: the IsoData algorithm better separates the particles, whereas the fixed value gives better estimation of the surface covered by the metal.

6. Apply a watershed filter to cut non-convex aggregates at their constriction. This step is optional. It is used to separate small aggregates close to each other, which may not be well resolved by the thresholding. In practice, this step has been used only for the thinnest layers of metal (2 nm or less), which lead to small and quite round aggregates.

7. Remove the aggregates which are in contact with the border of the picture (the size measurements would not be correct on such aggregates) and those smaller than a critical size (considered as noise) (fig. 3.3f).

8. Count and measure (area, perimeter, effective diameter, shape parameters) all aggregates (fig. 3.3g).

3.2.3 Reliability of the image analysis

Reliability of the method has been heavily investigated, due to the unexpected results presented below. A first test was to check visually the quality of the aggregate detection. An ideal method would separate the aggregates while preventing any part of them from being considered as background. Such an ideal picture is not practically achievable, whether by hand or by automatic image analysis, because there is not a sharp transition from the aggregates to the substrate. This blurred transition comes from the spatial resolution of the SEM and the rounded shape of the aggregates.

[33] Ridler and Calvard, "Picture Thresholding Using an Iterative Selection Method", 1978 [RC78]

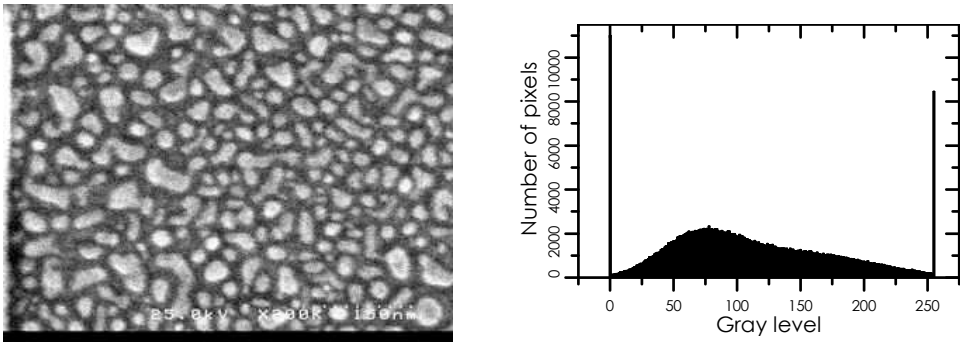

(a) *Raw SEM image of a 3*nm *gold layer annealed at 530*°C *for 15*min

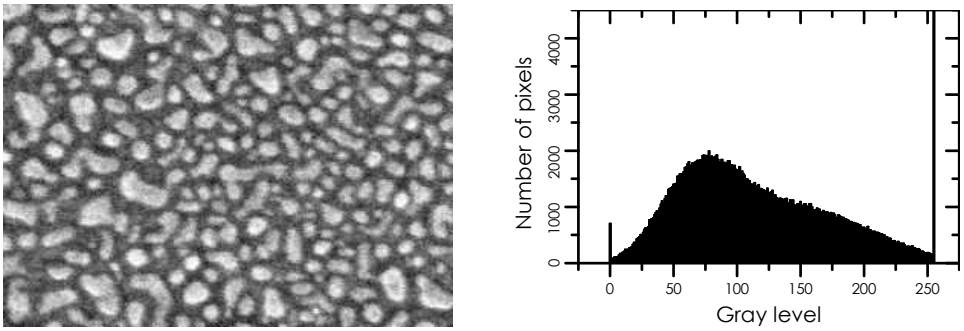

(b) *Cropped image (left) and its color histogram (right)*

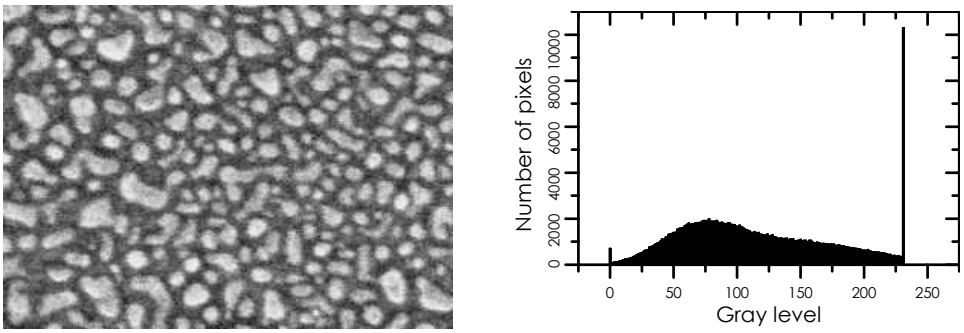

(c) *Image after leveling of the saturated pixels (left) and its color histogram (right)*

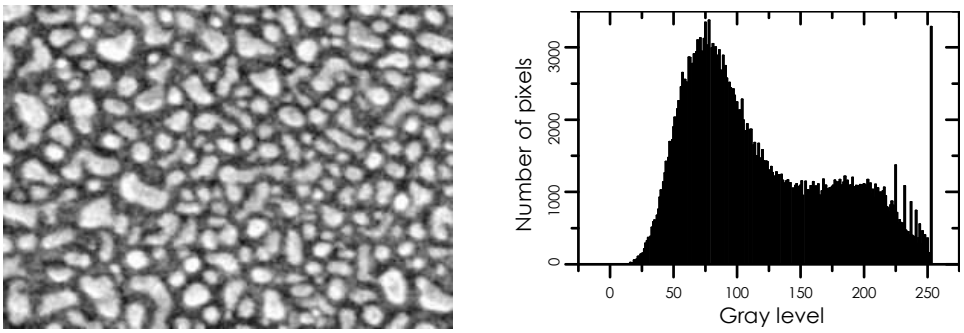

(d) *Image with enhanced contrast after noise removal*

Figure 3.3 – *Steps of the automated image analysis*

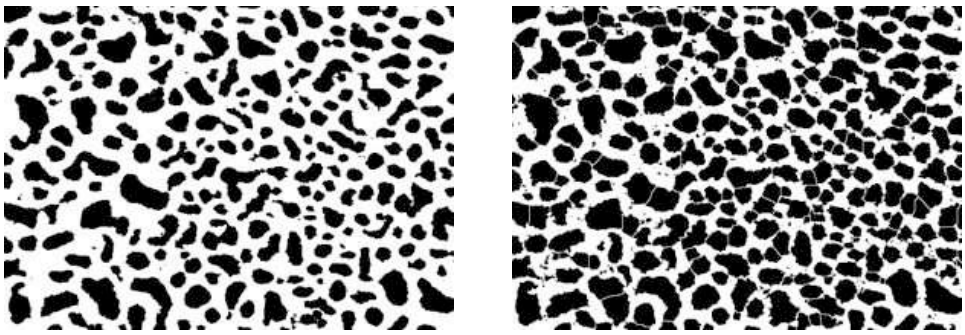

(e) *Image after automated thresholding (left) and manual thresholding ($g_t = 100$) with watershed (right)*

(f) *Aggregates larger than the critical size and not touching the edges of the picture*

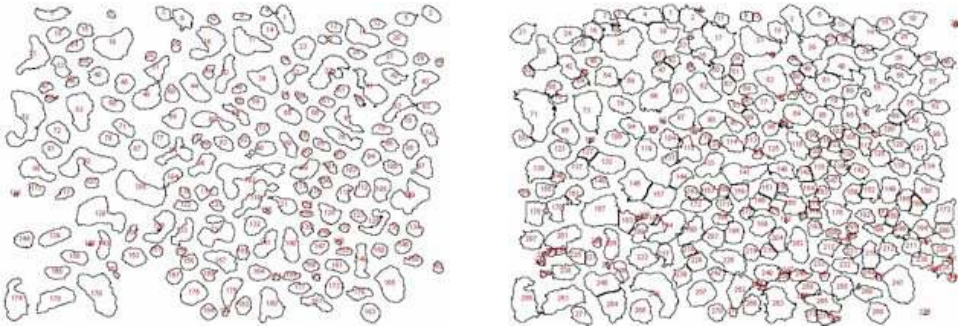

(g) *Individually labeled aggregates after measurements*

Figure 3.3 – *(continued) Steps of the automated image analysis*

Thresholding with the value determined by the IsoData algorithm leads to more selective a selection of aggregates than the fixed value of $g_t = 100$ (fig. 3.4). Hence automatic thresholding seems to be more accurate than manual one. On the other hand, part of what would be spontaneously considered aggregates is treated by automatic thresholding as background (fig. 3.5). So the measured areas, perimeters and effective diameters are probably slightly underestimated by this method.

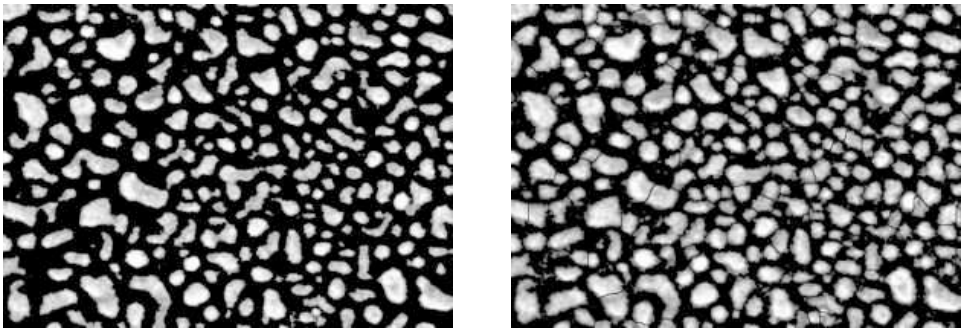

Figure 3.4 – *Part of the picture considered as aggregates when an automatic IsoData threshold (left) or a manual threshold (right) is applied.*

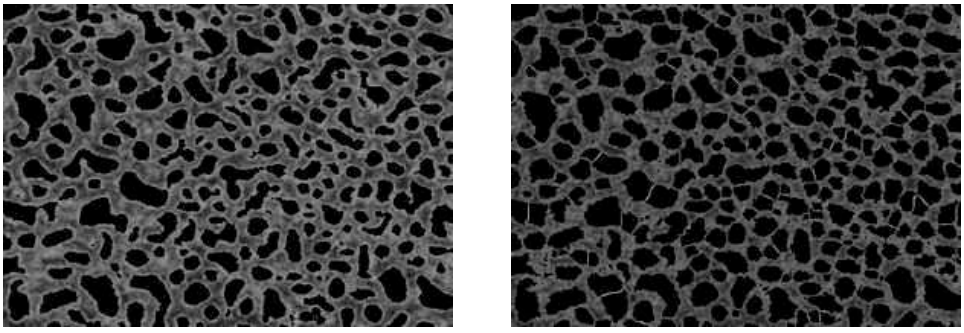

Figure 3.5 – *Part of the picture considered as background when an automatic IsoData threshold (left) or a manual threshold (right) is applied.*

The second, and more quantitative analysis performed was to compare the relative variation of the numerical parameters used in the automated analysis with that of the measurements output. The input numerical parameters are the radius of the median filter (in pixels), the threshold gray level and the minimum surface (in nm) for an aggregate to be analyzed. We chose a set of thirty-five SEM images (fig. 3.6), which are very different from each other in terms of contrast, quality and pattern.

Results of the effect of the variation of the threshold gray level are summarized on table 3.2. The most stable output parameter is the number of aggregates. Indeed, both the average and the median values of its relative variation are noticeably lower than the relative variation of g_t. The effective diameter is also a stable output parameter. The average surface, on the other hand, shows large variations when g_t changes by more than 5%.

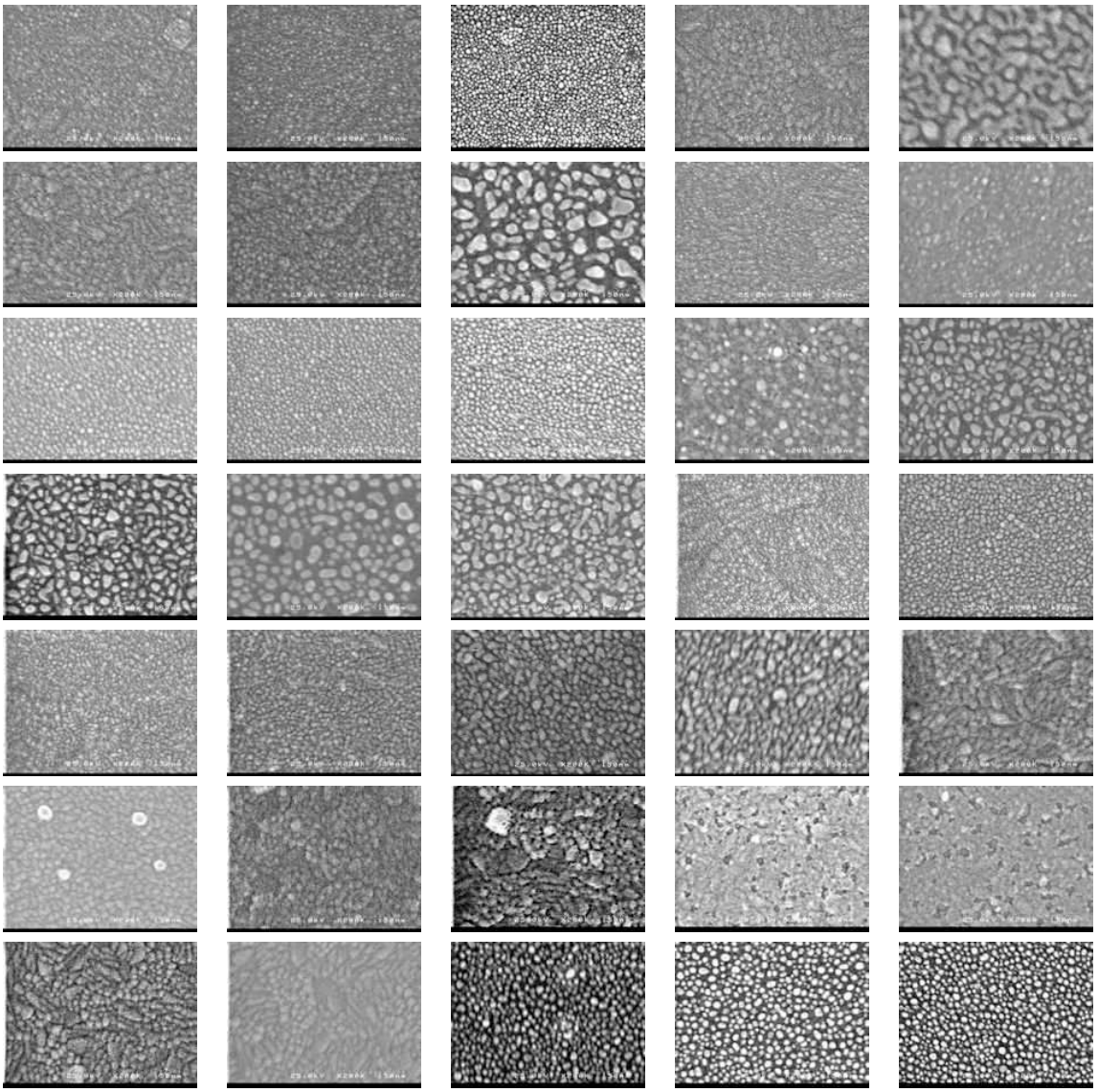

Figure 3.6 – *SEM images used to investigate the reliability of the automated image analysis*

g_t	Number of particles		Average surface/nm^2		Effective diameter/nm	
	Max	Median	Max	Median	Max	Median
90	17.76	7.14	35.86	17.91	17.15	8.59
95	11.92	3.46	21.09	8.04	10.37	4.17
99	3.46	0.00	7.15	0.37	3.15	0.11
101	4.55	0.00	8.11	0.00	6.01	0.00
105	14.47	2.61	16.36	8.07	14.10	4.66
110	19.30	5.16	23.55	14.35	15.98	8.36

Table 3.2 – *Maximum and median percentage of unsigned relative variation for three output parameters (number of particles, average surface and average effective diameter of the aggregates) when the threshold gray level g_t is changed with respect to the reference ($g_t = 100$)*

Modification	Number of particles		Average surface/nm^2		Effective diameter/nm	
	Max	Median	Max	Median	Max	Median
R=1	120.00	34.03	58.36	26.09	38.32	14.58
R=4	44.90	23.13	74.61	29.59	44.77	14.11
S=3	27.50	8.64	20.44	7.47	15.44	5.95
S=6	16.65	5.06	13.36	4.55	9.76	3.46
S=9	7.84	2.17	6.74	2.03	4.83	1.60
S=15	7.36	2.49	7.71	2.15	5.43	1.52

Table 3.3 – *Maximum and median percentage of the unsigned relative variation for three output parameters (number of particles, average surface and average effective diameter of the aggregates) when either the radius R (in pixels) of the median filter or the minimum surface S (in nm) for an aggregate to be included are changed with respect to the reference ($R = 2$ and $S = 12\,\text{nm}^2$)*

Similar results have been obtained upon variation of the other input parameters and are shown on table 3.3. All of the output parameters show little sensitivity to the minimum surface S required for an aggregate to be included. Indeed, their relative variation is smaller than 7% when S is changed by ±25%. The radius of the median filter has a stronger impact on the output measurements, especially on the number of aggregates. In most cases though, the relative variation of the output measurements is smaller than the variation of R. In addition, the median filter has a strong visual impact so it was easy to verify that $R = 2$ is the most relevant value for our images. The effects of variations in its value are therefore of smaller importance than for the other input parameters.

In conclusion, the analysis method is generally stable upon small variations of its input parameters so its results can be considered reliable. In particular, the most stable output value is the effective diameter, followed by the number of aggregates. One should keep in mind, though, that these output values are not directly measured, but

are computed. A systematic bias remains therefore possible and the output values should rather be compared among themselves than considered absolute.

3.2.4 Qualitative and quantitative evolution of the layer

Effect on the substrate

It could be feared that the ITO layer would be degraded upon annealing at high temperatures. Indeed, different thermal expansion of the ITO layer and its glass substrate could have led to cracks in the former. This risk has been investigated by annealing ITO-coated glass alone at the highest temperature used (600 °C) for 15 min at 5×10^{-6} mbar. The ITO exhibits a rough structure with 100 nm to 200 nm wide grains, whose surface itself is uneven. As can be seen on fig. 3.7, the morphology of this substrate is not modified upon annealing.

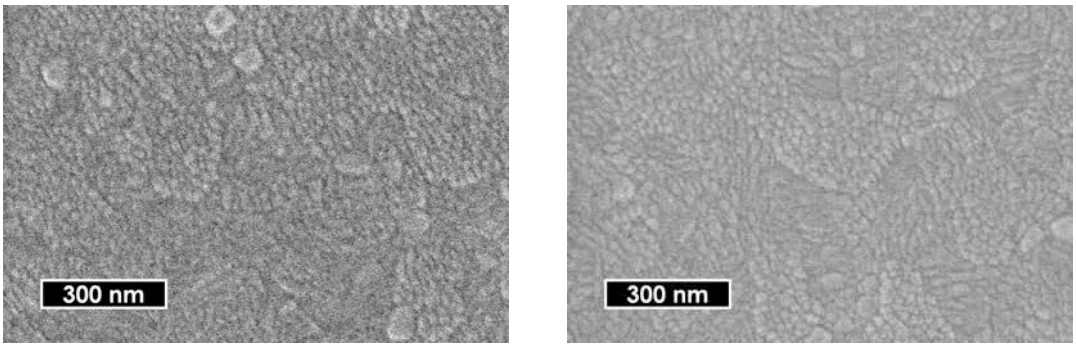

Figure 3.7 – *SEM picture of an ITO-coated glass substrate before (left) and after (right) 15* min *annealing at 600*°C

Qualitative evolution of the gold layer

The typical steps in the evolution of a gold layer on ITO are shown on fig. 3.8.

After evaporation of gold (fig. 3.8a), the ITO large grains are still visible but the fluctuations on their surface have almost disappeared. The coverage of the substrate by the gold layer can thus be assumed to be almost total and to follow the topography of the substrate. Yet the deposition is not perfectly homogeneous and brighter points are visible due to local hillocks. Indeed, gold does not form oxides, so it poorly adheres on ITO, as it does on glass.[34] Thus the gold layer grows on ITO following the Volmer-Weber mode.[35] Such islands are still visible when the equivalent thickness is lower or equal to 4 nm, and the hillocks are likely to be their traces.

When annealed at low temperature (e.g. 140 °C, fig. 3.8b), the gold layer begins cracking and dewetting the substrate. This leads to two domains: a thicker gold layer, which thus appears brighter and more uniform than before annealing, and the bare

[34] Benjamin and Weaver, "Adhesion of evaporated metal films on glass", 1961 [BW61]

[35] growth from islands, without an initial monolayer of metal on the substrate

surface of the substrate. Some hillocks remain visible, most of which are located at the edges of uncovered areas. Dewetting begins indeed where the gold layer is thinner, that is between the hillocks. This state is only visible for an initial thickness larger than 3 nm. At 1 nm and 2 nm, separated aggregates are visible even before annealing.

At temperature higher than 175 °C (fig. 3.8c), clearly separated droplets are formed. They are generally circular or egg-shaped but there is a wide dispersion among their sizes. The quantitative data discussed in the following sections are extracted from samples in this later stage.

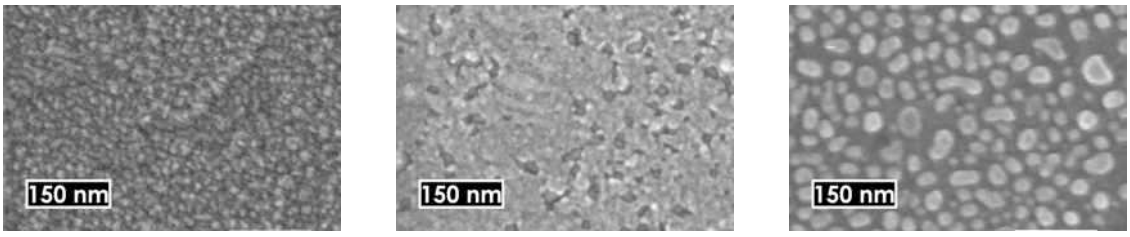

(a) *Pristine layer on ITO* **(b)** *Layer after 15*min *at 140*°C **(c)** *Layer after 15*min *at 435*°C

Figure 3.8 – *Evolution of a 3*nm *gold layer (scalebar is 150*nm*).*

Quantitative analysis: size dispersion and effects of the annealing parameters

The most reliable data from the automated image analysis are the effective diameter and the number of particles. This first part of the discussion will therefore be based on them.

As can be seen on fig. 3.9, the distribution of effective diameters is wide and shows little dependence on the annealing temperature (the histograms have been based on the 3186 first aggregates identified at each annealing temperature). A more detailed analysis is shown on tables 3.4 and 3.5, along with the number N of aggregates measured for each condition. The ratio of the standard deviation on the average value of the effective diameter is between 0.3 and 0.6; it is significantly lower when the initial equivalent thickness is 2 nm than when it is 3 nm.

Plots of the number of aggregates and the average effective diameter as a function of the annealing temperature for various initial thicknesses are shown on fig. 3.10 and 3.11. The error bars are omitted due to the large dispersion. Each point on the plots represents one sample.

Both the average effective diameter and the number of aggregates show little variations when the temperature varies between 175 °C and 600 °C. No trend is visible. On the other hand, the initial amount of metal has a strong impact: the effective diameter is roughly twice as large when the initial thickness is 3 nm than when it is 2 nm. Here the limited amount of data for thicknesses of 1 nm and 4 nm comes from the difficult analysis of such samples (due to the small size or the ill-defined shape of the aggregates).

T (°C)	σ (nm)	$\bar{x}$ (nm)	$\sigma/\bar{x}$	N
175	9.89	20.49	0.48	1028
300	13.06	21.54	0.61	953
435	11.97	29.50	0.41	106
530	10.11	22.43	0.45	1503
600	16.74	29.78	0.56	86

Table 3.4 – *Statistics on the effective diameters of aggregates obtained after annealing a 3nm gold layer on ITO*

T (°C)	σ (nm)	$\bar{x}$ (nm)	$\sigma/\bar{x}$	N
175	3.96	11.52	0.34	3186
360	4.28	11.7	0.37	5921
435	3.29	10.27	0.32	5620
530	3.71	11.11	0.33	3719
600	4.88	9.8	0.50	2723

Table 3.5 – *Statistics on the effective diameters of aggregates obtained after annealing a 2nm gold layer on ITO*

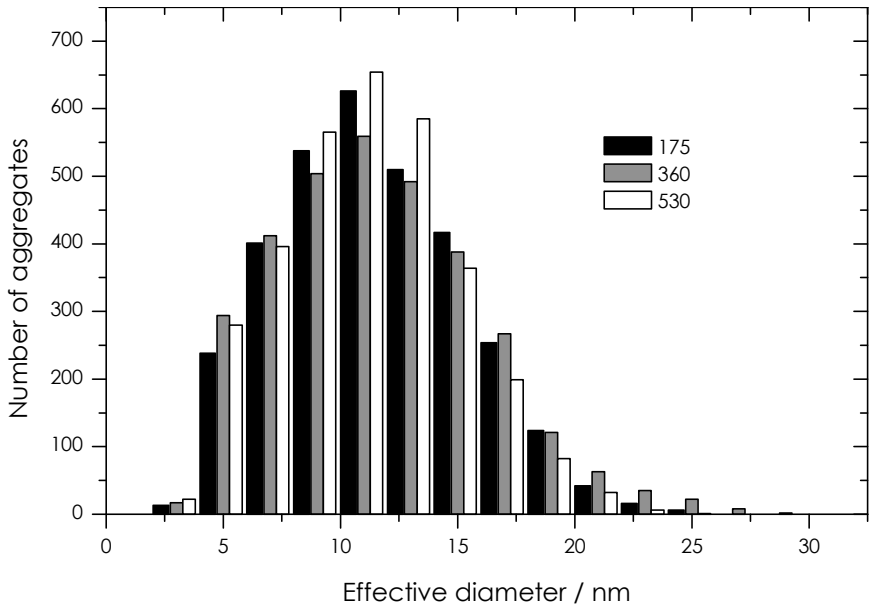

Figure 3.9 – *Distribution of the effective diameter of aggregates obtained by annealing of a 2*nm *gold layer on ITO for 15*min *at different temperatures.*

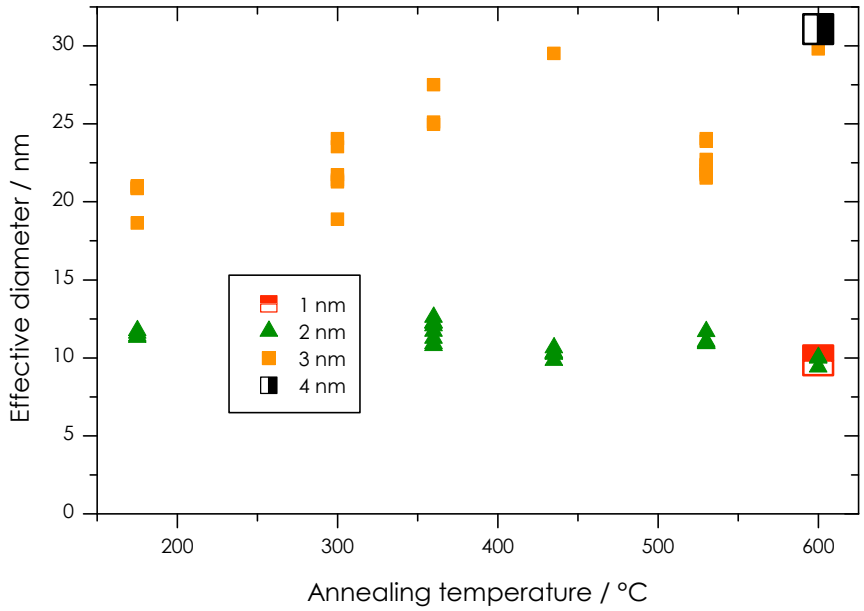

Figure 3.10 – *Average effective diameter of aggregates obtained by annealing of gold layers of different thicknesses on ITO with respect to the annealing temperature*

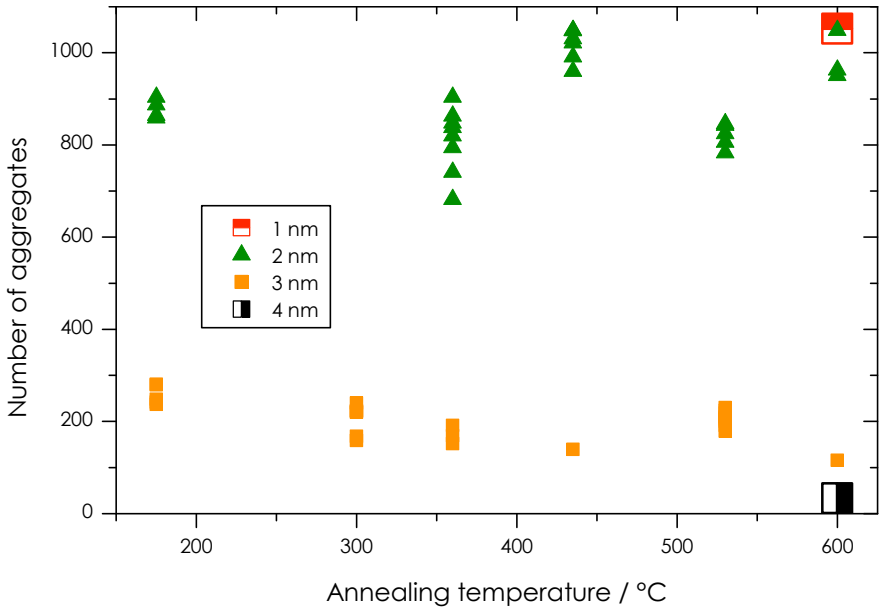

Figure 3.11 – *Number of aggregates obtained by annealing of gold layers of different thicknesses on ITO with respect to the annealing temperature*

Identification of the driving mechanism

Several phenomena have been put forward to explain the evolution of thin metallic layers on an oxide surface. Carey *et al.* studied nickel films (between 3 nm and 8 nm thick) deposited on crystalline silicon coated with oxidized titanium and explained their evolution toward islands by a phenomenon similar to Ostwald ripening.[36] Täschner *et al.*, who used 2 nm and 5 nm-thick Co layers on oxidized silicon to grow carbon nanotubes, explained the formation of droplets by the mismatch in the linear thermal expansion coefficient of the metal and the substrate.[37] According to Merkulov *et al.*, who studied 15 nm-thick nickel films on silicon, islands appear and reach an equilibrium size due to the competition between two phenomena:[38] the stress induced by the mismatch between the thermal expansion coefficient of silicon[39] ($\alpha_{Si} = 3 \times 10^{-6}\,K^{-1}$ at 400 K) and nickel ($\alpha_{Ni} = 13 \times 10^{-6}\,K^{-1}$), which tends to break the film apart, and the minimization of the surface energy of the film. They observed no aggregates when titanium was used instead of nickel. According to them, this result comes from a smaller difference in the thermal expansion coefficients ($\alpha_{Ti} = 8.5 \times 10^{-6}\,K^{-1}$) and by the higher melting point of titanium (1660 °C vs. 1453 °C for nickel). Rorak *et al.* studied the evolution of 5 nm-thick silver layers on mica at temperatures between 35 °C and 100 °C.[40] They showed that it was driven by kinetic aggregation until a temperature-dependent freezing time. Though not very common, diffusion and aggregation of gold have been reported on mica and graphite[41] and on WO_3.[42]

The difference between the thermal expansion coefficient of In_2O_3 and Au at 400 K is $\Delta\alpha_{Au/In_2O_3} = 6.8 \times 10^{-6}\,K^{-1}$. It lies between the difference between Ti and Si ($\Delta\alpha_{Ti/Si} = 5.5 \times 10^{-6}\,K^{-1}$) and the difference between Ni and Si ($\Delta\alpha_{Ni/Si} = 10.0 \times 10^{-6}\,K^{-1}$). Moreover, gold has a lower melting point (1064.4 °C) than both nickel and titanium. Therefore it is possible that the dewetting step, as observed on fig. 3.8b, is primarily caused by the mismatch among the thermal expansion coefficients.

Yet this mismatch cannot explain further evolution, nor the aggregation when the initial layer is not continuous, as it is the case when the initial thickness is 2 nm or less. Each of the two mechanisms commonly used to describe the evolution of clusters (Ostwald ripening and kinetic aggregation) leads to a specific size distribution. Comparing the experimental data to these theoretical distributions allows to identify

[36] Carey et al., "Formation of Three Dimensional Ni Nanostructures for Large Area Catalysts", 2004 [Car+04]

[37] Taschner et al., "Synthesis of aligned carbon nanotubes by DC plasma-enhanced hot filament CVD", 2003 [Tas+03]

[38] Merkulov et al., "Patterned growth of individual and multiple vertically aligned carbon nanofibers", 2000 [Mer+00]

[39] Touloukian et al., "Thermal expansion — Non-metallic solids", 1977 [Tou+77]

[40] Rorak et al., "Nanostructured Materials – Clusters, Composites and Thin Films", 1997 [Ror+97]

[41] Vandamme et al., "Scanning probe microscopy investigation of gold clusters deposited on atomically flat substrates", 2003 [Van+03]

[42] LeGore et al., "Aggregation and sticking probability of gold on tungsten trioxide films", 2001 [LeG+01]

the phenomenon and to determine some physical parameters.

Ostwald ripening In this mechanism, aggregates evolve by mass transfer from the smaller ones, whose radius is below a critical value R_c, to the bigger ones. R_c is generally close to the average radius. For "long" evolution times, when a quasi-steady-state is reached, the number of aggregates of size R is given by $f(R,t) = \frac{A}{t} F_i(\frac{R}{R_c})$ where A is a constant and F_i is a function of the reduced variable $u = \frac{R}{R_c}$ which depends on the kinetics-limiting phenomenon.[43] When the kinetics is limited by surface reactions (evaporation or condensation), the distribution function is:

$$F_1(u) = \begin{cases} u \dfrac{\exp\left(-\dfrac{3u}{2-u}\right)}{(2-u)^5} & u < 2 \\ 0 & u \geq 2 \end{cases} \tag{3.1}$$

When the kinetics is controlled by "bulk" diffusion (in our case, by diffusion on the surface of the substrate), it is:

$$F_2(u) = \begin{cases} u^2 \dfrac{exp\left(-\dfrac{2u}{3-2u}\right)}{(3+u)^{7/3}(3-2u)^{11/3}} & u < 1.5 \\ 0 & u \geq 1.5 \end{cases} \tag{3.2}$$

Both functions have been compared to experimental results. As an example, data from annealing at 530 °C for both 2 nm and 3 nm are shown. At temperatures higher than 200 °C, all samples were annealed for 15 min so the time dependence is included in the constant A. The distribution functions should be fitted to the histograms, but then there is a possible bias due to the size of the bins. To avoid this bias, the accumulation function[44] has been computed. It has then been differentiated against the size, and this result has been used to fit the distribution functions.

Two parameters are varied: A and R_c. Best fits are shown on fig. 3.12a and fig. 3.12b. F_1 is plotted in continuous line, F_2 is plotted in dotted line. The fitting results are summarized on table 3.6.

The second function does not fit experimental data at all. The first one, which corresponds to kinetics limited by surface reaction, is in better visual agreements with the data but the numerical fit is still poor. It overestimates the number of small aggregates and underestimates the number of large ones. This mismatch is due to the fact that during Ostwald ripening the size of some particles decreases, which seems not to be the case here.

[43] Jain and Hughes, "Ostwald ripening and its application to precipitates and colloids in ionic crystals and glasses", 1978 [JH78]

[44] The accumulation function G maps the size x to $G(x)$, such as the probability for the size of a given aggregate to be lower or equal to x is $G(x)$.

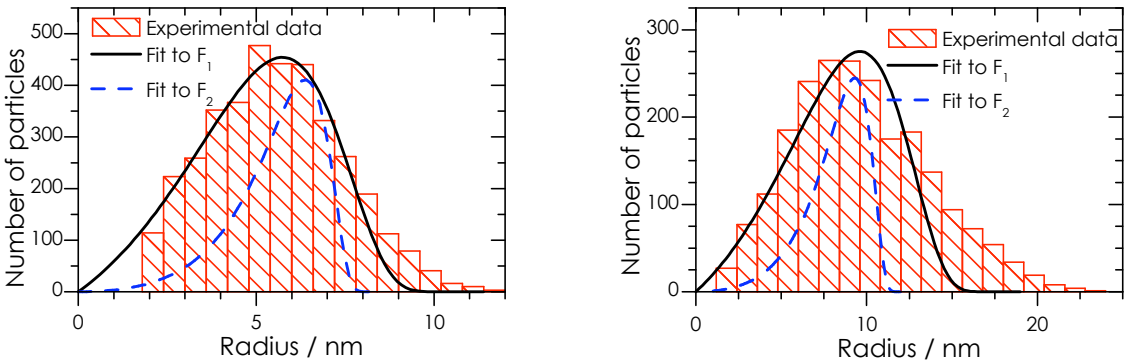

Figure 3.12 – *Radius distribution for a 2*nm *(left) and a 3*nm *(right) layer annealed 15*min *at 530*°C.

Initial thickness	F_1			F_2		
	R_c	A	χ^2	R_c	A	χ^2
2 nm	5.74 ± 0.06	410 ± 10	2.80	5.62 ± 0.08	2700 ± 200	19.5
3 nm	9.6 ± 0.3	210 ± 14	2.37	8.2 ± 0.3	1400 ± 200	9.59

Table 3.6 – *Fitting results for Ostwald ripening distribution functions*

Kinetic aggregation This mechanism, where aggregates diffuse and collide with each other, leads to a continuous increase in the size of the clusters. The evolution of the number n_k of clusters of size k is given by equation 3.3, which was first proposed by Smoluchovski.[45]

$$\frac{dn_k}{dt} = \frac{1}{2}\sum_{j=1}^{k-1} K_{j,k} n_j n_{k-j} - n_k \sum_{j=1}^{\infty} K_{j,k} n_j \tag{3.3}$$

The rate constants (or kernels) $K_{i,j}$ depend on the size of the two colliding clusters. It is generally assumed that they scale homogeneously with i and j as written in eq. 3.4. This scaling can be analytically proved in two limit cases: when the clusters follow a ballistic or a Brownian motion.[46] The scaling coefficient ω is of particular physical significance. When $\omega = 0$, the rate constants are independent of the size of the clusters. When $\omega < 0$, the rate constant decreases when the size of the clusters increases. When $\omega > 0$, the rate constant increases when the size of the cluster decreases. If $|\omega| > 1/2$, the kernels evolve faster than the cluster size, and if $|\omega| < 1/2$, they evolve slower.

$$K_{\lambda i, \lambda j} = \lambda^{2\omega} K_{i,j} \tag{3.4}$$

[45] Smoluchowski, "Three lectures on diffusion, Brown's molecular movements and the coagulation of colloid parts", 1916 [Smo16]

[46] Villarica et al., "Application of fractals and kinetic equations to cluster formation", 1993 [Vil+93]

The asymptotic solution of this problem has been studied by several authors[47] who have shown that, for large values of t and k, n_k follows eq. 3.5, where $a = -2\omega$ and $b \propto t^{1/(2\omega-1)}$.

$$n_k \rightarrow A k^a \exp(-bk)? \tag{3.5}$$

The size of the islands, defined as d^3, where d is the effective diameter, has been fitted to this equation by adjusting parameters A, a and b. The results are shown on fig. 3.13, where on the top part the accumulation functions, both experimental (red squares) and calculated (blue line), are plotted. The experimental size distribution is plotted as red hashed histograms in the bottom part, and the calculated one is shown in continuous black lines.

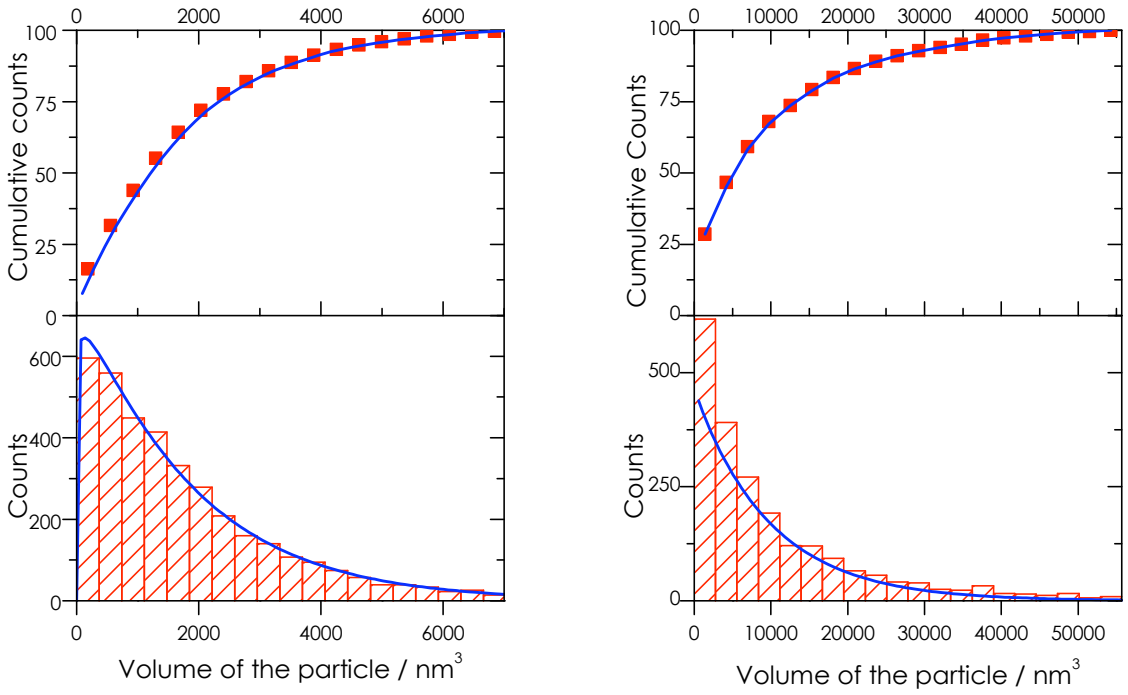

Figure 3.13 – *Size distribution of islands after 15*min *annealing of a 2*nm *(left) and a 3*nm *(right) layer at 530*°C*: experimental data (squares and histograms) and fit to eq. 3.5 (continuous lines)*

The theoretical curves are in very good visual agreement with the experimental data, especially for an initial thickness of 2 nm. The numerical results are summarized on table 3.7 and confirm that the kinetic aggregation describes well the experimental results. For both thicknesses, ω is very close to zero, which means that the rate constants in eq. 3.3 have a very weak dependency on the size of the aggregates. As ω is slightly negative for an initial thickness of 3 nm, the reaction slows down when the

[47] Botet and Jullien, "Size distribution of clusters in irreversible kinetic aggregation", 1984; Villarica et al., "Application of fractals and kinetic equations to cluster formation", 1993 [BJ84; Vil+93]

thickness	$A \times 10^3$	$a \times 10^2$	$b \times 10^4$	$\chi^2 \times 10^8$	$\omega \times 10^2$
2 nm	8 ± 3	0 ± 5	1.00 ± 0.08	3.4	0 ± 2
3 nm	36 ± 2	7 ± 1	5.8 ± 0.1	55	-3.4 ± 0.6

Table 3.7 – *Numerical results of the fit to the equation 3.5 for layers annealed 15*min *at 530*°C

cluster size increases. The evolution may therefore be limited by the diffusion of the aggregates.

3.2.5 Summary

Well separated gold aggregates can be obtained from thin (<4 nm) evaporated layers on ITO upon annealing at temperatures higher or equal to 175 °C. The driving mechanism has been identified as kinetic aggregation limited by diffusion. This result is mainly explained by the low adhesion of gold on ITO and, to a lower extent, the roughness of this substrate.

3.3 CVD growth on transparent conductive oxides

The nature of the substrate is of great importance for the growth of silicon nanowires. Its interaction with the metal controls the formation of the catalyst droplets, hence the size and density of the wires. Moreover, the substrate partially controls the orientation of the wires: when epitaxy is possible (e.g. on crystalline silicon), the orientation of the wires depends on the crystalline orientation of the substrate; when it is not, the orientation is random.

The aim here is to check whether transparent conductive oxides can be good substrates for the growth of silicon nanowires. To do that, growth conditions close to what works for etched or oxidized c-Si will be investigated. Two metals will be used as catalysts: gold, which is the "standard", and copper, which has been reported, in an unpublished work by Billel Kalache,[48] to be an efficient catalyst on ITO (fig. 3.14).

3.3.1 Experimental design

Experiments presented here do not represent a comprehensive study, as the goal here was mainly to investigate the feasibility of the growth.

It has been shown in chapter 1 that an interfacial layer of amorphous silicon could improve the open-circuit voltage of hybrid devices. Hence some samples have been plasma-treated after the CVD growth to deposit a thin layer of a-Si:H.

[48] Unfortunately, the precise growth conditions are not known; the growth temperature was between 550 °C and 650 °C

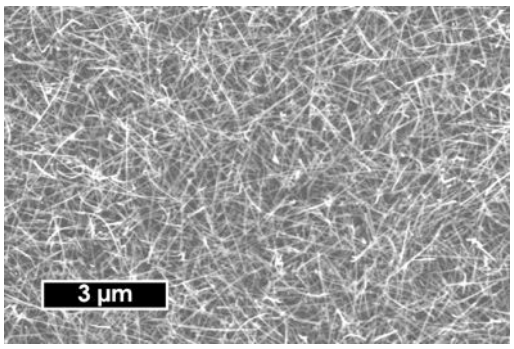

Figure 3.14 – *SEM picture of silicon nanowires grown on ITO at 550°C with Cu as catalyst.*

The CVD growth experiments have been run in a quartz furnace, which was heated with infrared lamps. This reactor was operated at a base vacuum below 1×10^{-5} mbar. The growth temperature was either 530°C or 650°C. The precursor gas was silane (SiH_4) diluted in H_2. When dissociated by a hot tungsten filament at the entrance of the reactor, hydrogen is meant to reduce the radial growth of the nanowires by selectively etching the amorphous silicon and passivating the edges of the wires. As both gases are reductors and the reduction of ITO is thermally activated, this substrate is likely to be reduced at such a high temperature. ZnO is more stable against exposure to reductive gases, so such substrates have been used in addition to ITO.

Figure 3.15 – *CVD reactor used for the growth of silicon nanowires: load-lock (front), quartz tube (center) and heater.*

3.3.2 SEM characterization of the deposited layers

Developments on the growth of silicon nanowires on more classical substrates were done in parallel of this work in the same reactor. This led to an evolution in the detailed experimental conditions. Here only two cases will be presented, which raised major questions.

High temperature growth without tungsten wire

In this first set of experiments, all substrates were ZnO-coated glass on which a 3 nm thick layer of copper had been evaporated.[49]

The flow rates of SiH_4 and H_2 were 10 sccm and 90 sccm, respectively, the pressure was regulated to 5 mbar and the reactor temperature was 650 °C. The duration of the growth was 10 min. After the CVD growth, some samples were transferred in air to the ARCAM PECVD reactor. There, they were exposed to a plasma treatment, first to remove the native oxide layer[50], then to deposit a thin layer of a-Si:H.[51]

When the samples are not exposed to a plasma treatment, no nanowires are formed. The surface is almost uniformly covered with a rough layer, as shown on fig. 3.16a. At some places, however, micrometer-scaled aggregates are visible (fig. 3.16b). These aggregates are covered by smaller structures, which look like beginnings of nanowire. But there are no metallic droplet at the tip of these structures, which would be expected from a Cu-catalyzed growth.

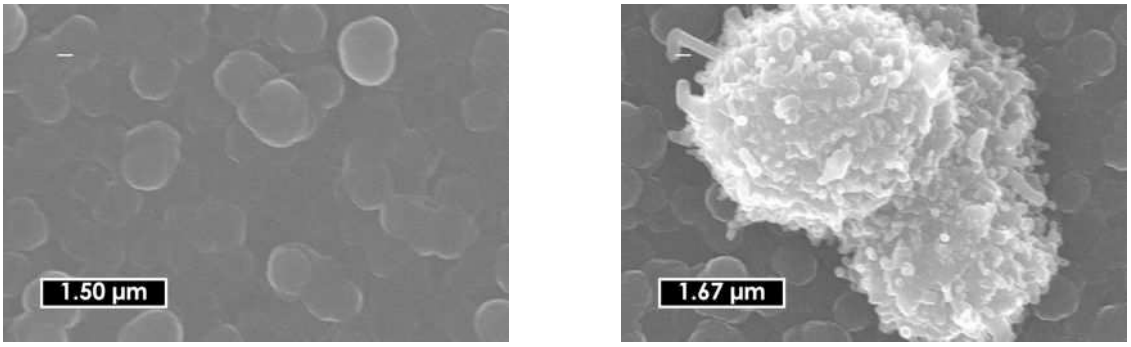

(a) *Typical view of the surface*

(b) *Detailed view of an aggregate with bases of nanowires*

Figure 3.16 – *SEM images of a copper-coated ZnO substrate after 10*min *CVD growth at 650*°C*. Acceleration voltage is 20*kV *and scalebars are 1.5*µm *and 1.67*µm*, respectively*

Samples which have been exposed to plasma treatment, on the other hand, exhibit bunches of nanowires spread over the surface (fig. 3.17a). The background is very

[49] Here the metal has been evaporated by Joule effect heating. The base pressure was 2.7×10^{-6} mbar and the deposition pressure was 3.0×10^{-5} mbar.

[50] 264 mTorr, 200 sccm of H_2, $P_{RF} = 5$ W, $t_{treatment} = 5$ min

[51] 43 mTorr, 50 sccm of SiH_4, $P_{RF} = 0.5$ W, $t_{treatment} = 3$ min

similar to what it is without any plasma treatment. The nanowires grown in bunches are straight but tapered and have a rough surface (fig. 3.17b). Kinked nanowires seem to remain at the center of the bunch.

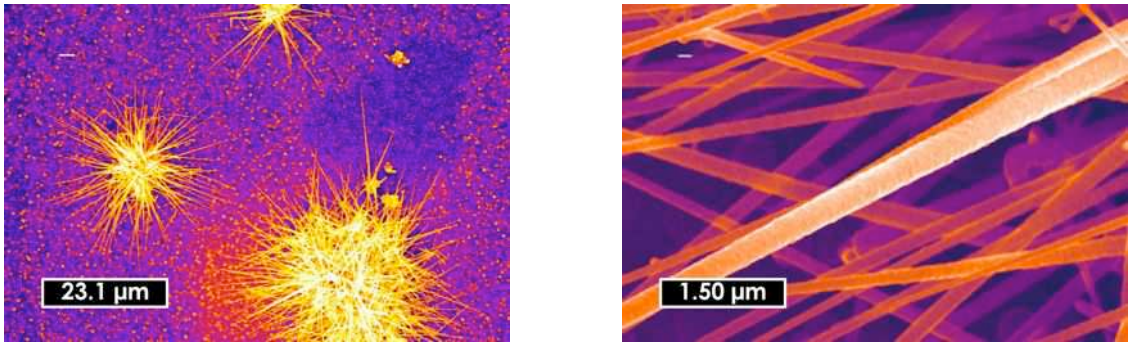

(a) *View of the surface with bunches of nanowires*

(b) *Details of nanowires from a bunch*

Figure 3.17 – *SEM images of a copper-coated ZnO substrate after 10*min *CVD growth at 650*°C *and plasma post-treatment. Acceleration voltage is 20*kV *and scalebars are 23.1*µm *and 1.5*µm*, respectively*

Medium temperature growth with a tungsten wire

In this second set of experiments, the furnace temperature was reduced to 530 °C. A tungsten wire heated through Joule effect (150 W) was placed in front of the gas inlet in order to enhance the dissociation of H_2 to atomic hydrogen. In addition, silane was even more diluted in hydrogen than in the previous set: the gas flow rates were 4 sccm and 96 sccm, respectively. Depositions on crystalline silicon with gold have shown that these conditions dramatically reduced the parasitic deposition of amorphous silicon.

Deposition has been done on Cu-coated ITO and on Au-coated ZnO. Some samples have been treated with plasmas similar to what they were in the previous set,[52] but slightly shorter. A glass control sample indicated that an equivalent 3 nm-thick a-Si:H layer had been deposited during this treatment.

A mixture of curled and straight nanowires grew during the CVD treatment both on Cu-coated ITO (fig. 3.18a) and on Au-coated ZnO (fig. 3.19a). The number density of straight nanowires is the same in both cases ($1.6 \times 10^8\,\mathrm{cm}^{-1}$) but the density of curled nanowires is much higher on ZnO/Au than on ITO/Cu. In both cases, a droplet is visible at the tip of straight nanowires (fig. 3.18b and 3.19b), which is a clue for VLS (with Au) or VSS (with Cu) growth. The average base diameter of the straight nanowires is (26±6) nm on ITO/Cu and (60±8) nm on ZnO/Au. All of them show very little tapering.

The difference between samples with and without plasma treatment is not as large as in the previous set of experiments. But there still is one: on some regions of the

[52] H_2 plasma to remove the native oxide, followed by a SiH_4 plasma to deposit a thin a-Si:H layer

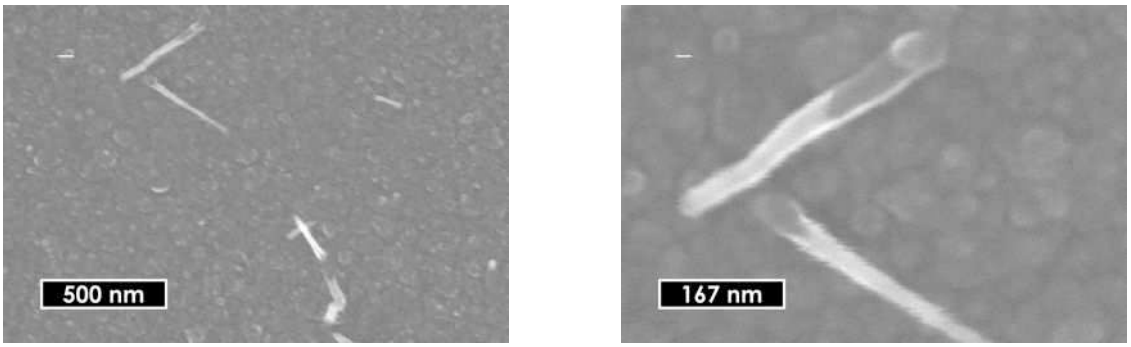

(a) *Extended view (scalebar is 500*nm*)*

(b) *Details (scalebar is 167*nm*); a catalyst droplet is visible at the tip of the straight nanowire*

Figure 3.18 – *SEM images of Cu-coated ITO after CVD at 530*°C *(acceleration voltage: 20*kV*)*

samples exposed to plasmas, the number density of straight nanowires is much larger than it is after thermal CVD only (fig. 3.20).

3.3.3 Analysis

Straight silicon nanowires have been obtained with copper as catalyst at a temperature of 530 °C, which is below the reported temperature window (600 °C-650 °C) for good quality wires.[53] This shift may be due to heating of the substrate by the gases, especially hydrogen, which can carry heat from the tungsten wire. Indeed, whereas the temperature of the furnace was 530 °C, the temperature of the substrate holder was measured during the growth to be 541 °C, and the surface temperature is likely to be even higher.

The most surprising result is that plasma treatment can enhance the density of silicon nanowires (when the CVD is done at 530 °C). It seems even necessary (and efficient) but to grow nanowires, when the CVD is done at 650 °C. In that particular case, the growth mechanism is obviously different, as the wires do not grow *below* a metallic aggregate. It is likely that the isolated aggregates seen after CVD (fig. 3.16) are metallic and behave as catalysts during the plasma treatment. Indeed, growth of several silicon nanowires *on top* of larger metallic aggregates has been reported in some cases. For example, due to the low equilibrium composition of Si in the liquid Ga-Si alloy, multiple silicon nanowires have been obtained on micrometer-sized gallium droplets.[54] Yet in our case this explanation faces two difficulties:

- The aggregates visible after CVD have a typical dimension of about 1 µm, which

[53] Arbiol et al., "Influence of Cu as a catalyst on the properties of silicon nanowires synthesized by the vapour-solid-solid mechanism", 2007 [Arb+07]

[54] Sunkara et al., "Bulk synthesis of silicon nanowires using a low-temperature vapor–liquid–solid method", 2001 [Sun+01]

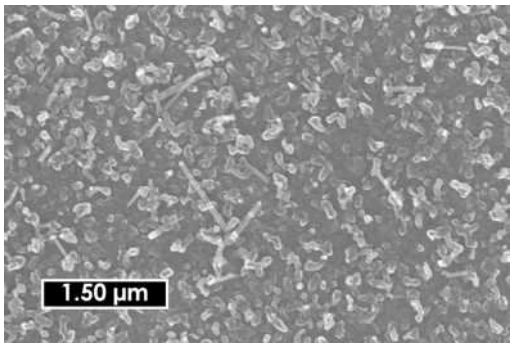

(a) *Extended view (scalebar is 1.50*µm*)*

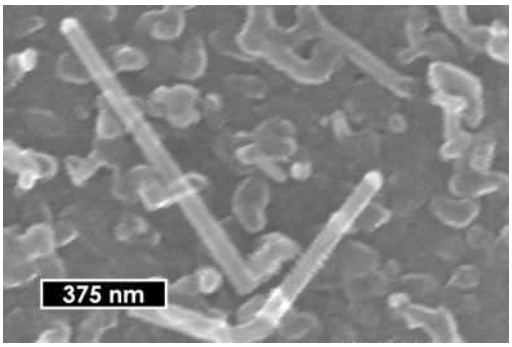

(b) *Details (scalebar is 375*nm*); a catalyst droplet is visible at the tip of the straight nanowires*

Figure 3.19 – *SEM images of Au-coated ZnO after CVD at 530*°C *(acceleration voltage: 20*kV*)*

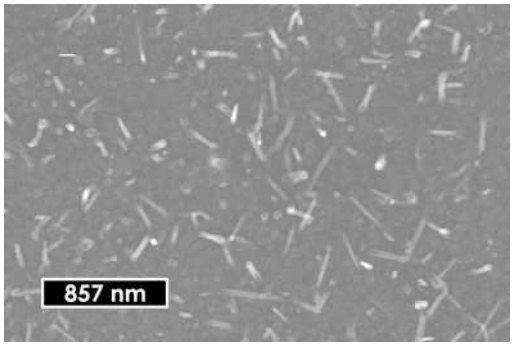

(a) *Extended view (scalebar is 857*nm*)*

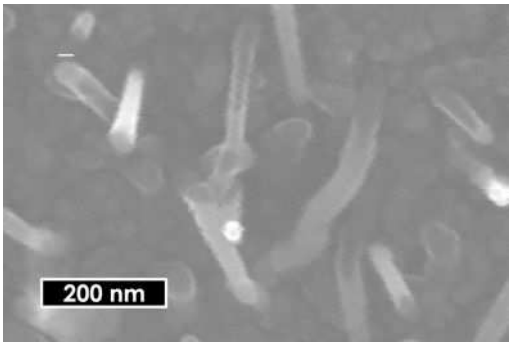

(b) *Details (scalebar is 200*nm*)*

Figure 3.20 – *SEM images of Cu-coated ITO after CVD at 530*°C *and plasma treatment (acceleration voltage: 20*kV*)*

is 40 times as big as it has been measured after annealing at similar temperatures for gold on ITO. Moreover, as copper forms oxides, its adhesion on ZnO or ITO should be stronger and its diffusion more limited.

- Plasma excitation has been recently shown to reduce the required temperature for the growth of silicon nanowires,[55] but the reported reduction (about 100 °C) is much lower than what is observed here (about 400 °C).

So at this stage, no satisfactory explanation can be proposed for this phenomenon. Yet the next chapter will shed new lights on this question. We will see that it is likely that the large aggregates are made of zinc produced by reduction of ZnO upon exposure to the reductive atmosphere (SiH_4 and hydrogen) and by aggregation (the process

[55] Aella et al., "Influence of Plasma Stimulation on Si Nanowire Nucleation and Orientation Dependence", 2007 [Ael+07]

temperature is above the melting point of zinc: 419.5 °C).

Summary of the chapter

The main mechanism to grow silicon nanowires on substrates is the vapor-alloy-solid process which may be split into VLS (vapor-liquid-solid, e.g. with gold) and VSS (vapor-solid-solid, e.g. with copper). In this mechanism, the size and position of the wires are controlled by metallic catalyst aggregates.

The process temperature and the anisotropy of the final structure is determined by the nature of this catalyst. Two characteristics are of major importance: the binary phase diagram, in particular a possible eutectic point, and the dissociation rate of the precursor gas (e.g. silane) at the surface of the metal. The substrate, in turn, has a strong influence on the orientation of the wires, especially if epitaxy is possible.

We learnt from our experiments that SEM, when coupled to an automated image analysis based on ImageJ, is a valuable and robust method to get quantitative information on a large number of small metallic particles on TCOs.

Very thin evaporated gold layers ($e \leq 4$ nm), either continuous or not, evolve toward well separated aggregates upon heating at temperatures higher or equal to 175 °C. Between that value and 600 °C, the annealing temperature has little impact on the size distribution of the final aggregates. The latter is very wide, thus allowing limited control on the size of the silicon nanostructures grown on these catalysts. The final size and number density of the aggregates are essentially controlled by the initial amount of metal.

Finally, a low density of straight nanowires may be obtained on transparent conductive oxides at 530 °C with gold or copper. Surprisingly, plasma post-treatment on samples after CVD leads to the growth of additional silicon nanowires. At high temperatures (650 °C), micro-meter sized aggregates are formed by CVD. They seem to be covered by silicon nanowires upon exposure to plasma treatment.

At this stage, the “classical” CVD growth of silicon nanowires has been adapted to a new class of substrates: TCO-coated glass. Yet the effect of the plasma treatment, in particular the role of hydrogen, remains to be explained. In addition, the growth temperature still needs to be dramatically reduced.

Growth of silicon nanostructures assisted by plasmas

4

The world is full of obvious things which nobody by any chance ever observes.

Sir Arthur Conan Doyle, *The Hound of the Baskervilles*

Contents

In the previous chapter, we have shown that silicon nanowires could be obtained on transparent, conductive oxides by thermal CVD. We also observed that plasma post-treatments could increase the number density of silicon nanowires and that they could even be necessary in some cases. Up to now, this effect has not been explained. Moreover, the growth temperature was above 530 °C, which is still too high. In particular, the substrates are likely to be degraded and the use of flexible substrates like polymers is out of the question.

In this chapter, we intend to explain the effect of the plasma treatment, especially the role H_2 plasmas play: do they "activate" the metal catalysts, which may be oxidized or contaminated? Are they necessary for plasma treatment to enhance the growth of silicon nanowires? Is adding H_2 to the SiH_4 deposition plasma equivalent to pre-treating the samples with H_2 plasma? In addition, we will investigate the possibility of growing silicon nanowires entirely at low temperatures using only PECVD.

An introduction to PECVD and presentation of reactors used in the laboratory can be found in appendix A.

Part of the work presented here is covered by published or submitted papers.[1]

[1] Alet, Palacin, and Cabarrocas, "Low-temperature growth of nano-structured silicon thin films on ITO initiated by metal catalysts", 2009; Alet et al., "In-situ generation of indium catalyst to grow crystalline silicon nanowires at low temperature on ITO", 2008; Yu et al., "Synthesis, morphology and compositional evolution of silicon nanowires directly grown on SnO_2 substrates", 2008 [APC09; Ale+08a; Yu+08]

4.1 Rationale for using plasma-enhanced CVD to grow silicon nanowires

The primary motivation for using plasmas in the growth of silicon nanowires is to reduce the growth temperature. Indeed, in PECVD, the plasma excitation provides energy to dissociate the precursor molecules into more reactive species, whereas in plain CVD this dissociation relies on the interaction with the substrate and, in particular, on the thermal energy the latter provides. As a consequence, plain CVD generally requires a much higher substrate temperature than PECVD. A striking example is given by amorphous silicon nitride. It has been reported to be grown by CVD at temperatures between 800 °C and 1200 °C. Below 1000 °C, the growth rate is limited by the thermally activated chemical reactions.[2] A few years later, similar layers have been grown by RF-PECVD at a substrate temperature of 275 °C.[3] Such a decrease in the growth temperature may reduce the production costs of the deposited films, which is of primary importance in the frame of organic and hybrid solar cells. In addition, it extends the class of substrates which can be used.

4.1.1 Why are plasmas not widely used to grow nanowires?

With the description of the VLS process in mind, one would think that the reduction of the growth temperature is also an advantage for growing nanowires with a very high aspect ratio. Indeed, the decomposition of the precursor gas is thermally activated and the activation energy is higher on the substrate than on the catalysts. So the lower the temperature, the more selectively this dissociation occurs on the catalyst dots as compared to the substrate. Yet, among the large literature available on the growth of silicon nanowires, only seven papers up to now mention the use of plasmas. Why? Some potential issues may explain this situation.

- Long nucleation: the nucleation time in CVD growth was shown to be:[4]

$$\tau = \frac{h^2}{D} \exp \frac{E_a}{kT}$$

  So, for a given size and type of catalyst dots, the nucleation time should increase by about 430 when the temperature goes from 500 °C to 370 °C. But in a recent work, Tom Picraux's group compared thermal growth to plasma enhanced growth on (100) silicon with evaporated gold as the catalyst.[5] Not only did plasma enhancement lead to a significant growth of silicon nanowires, but,

[2] Chu, Lee, and Gruber, "The Preparation and Properties of Amorphous Silicon Nitride Films", 1967 [CLG67]

[3] Sinha et al., "Reactive Plasma Deposited Si-N Films for MOS-LSI Passivation", 1978 [Sin+78]

[4] Kalache, Cabarrocas, and Morral, "Observation of incubation times in the nucleation of silicon nanowires obtained by the vapor-liquid-solid method", 2006 [KCM06]

[5] Aella et al., "Influence of Plasma Stimulation on Si Nanowire Nucleation and Orientation Dependence", 2007 [Ael+07]

in given conditions, four times more ⟨110⟩ nanowires grew with plasma stimulation than without. As explained in chapter 3, ⟨110⟩ nanowires grow preferentially to ⟨111⟩ for smaller wire diameters, hence for smaller catalyst dots. As gold aggregates coalesce upon annealing at high temperature (here, 430 °C), this difference in crystalline orientation means that the growth of nanowires started earlier in the coalescence process in plasma stimulated growth than in thermal growth. In other terms, the nucleation time is shorter, at a given temperature, for plasma stimulated growth than for thermal growth. So this difference should, at least partially, compensate the increased nucleation time upon decreasing the growth temperature.

- Low growth rates: the description of the VLS process, as given in chapter 3, also mentioned that decreasing the temperature leads to lower growth rates. Indeed, the latter may be limited by the dissociation rate at the surface of the catalyst, which is thermally activated. But reactions in plasma lead to the formation of SiH_x species, especially SiH_3 radicals, which are more reactive than SiH_4 molecules.Dehydrogenation of SiH_4 into atomic Si, to be incorporated in the catalyst dot, is not a one-step reaction. It is rather a sequence of reactions of the kind $SiH_x \xrightarrow{E_{ax}} SiH_{x-1} + H$, where the activation energy E_{ax} decreases with x. So the energy barrier is lower for plasma activated growth than for thermal growth. In the study mentioned above, Picraux *et al.* actually measured a 2.5-fold increase in the growth rate at 430 °C upon using plasma stimulation (90 nm min^{-1} vs. 36 nm min^{-1} for thermal growth). The difference is even more striking at lower temperature: at 350 °C, the growth rate for plasma stimulated growth was 61 nm min^{-1}, whereas it was only 5.3 nm min^{-1} for thermal growth. So the growth rate with plasma activation at 350 °C, which is the very lower limit for VLS growth with gold (it is 13 °C below the bulk eutectic temperature), still is twice as much as for thermal growth at 430 °C!

- Poor aspect ratios: as part of the dissociation process occurs in the plasma, and not at the surface of the sample, one could fear that the selectivity of the deposition is lower with plasma excitation than in thermal growth. In that case, the aspect ratio of the nanowires grown by PECVD would be poorer than for wires grown by plain CVD due to parasitic deposition of amorphous silicon on the substrate and on the edges of the wires. This seems indeed to be the case: Picraux *et al.* noticed tapering only on wires grown with plasma excitation and they measured the lateral growth rate to be 1.4 nm min^{-1}. Such tapering of the nanowires has also been observed after growth by PECVD with gold at 390 °C by Griffiths *et al.*[6] Yet diluting the precursor gas (silane) in hydrogen could noticeably reduce this parasitic deposition, as atomic hydrogen is known to selectively etch amorphous silicon.[7]

[6] Griffiths et al., "Plasma assisted growth of nanotubes and nanowires", 2007 [Gri+07]

[7] Nguyen et al., "Preparation of ultrathin microcrystalline silicon layers by atomic hydrogen etching of amorphous silicon and end-point detection by real time spectroellipsometry", 1994; Layadi et al.,

So none of the potential drawbacks of plasmas are real barriers against their use in the growth of silicon nanowires, which makes the little number of reports even more surprising.

4.1.2 Potential advantages of plasmas for the growth of nanowires

Plasmas can help reducing the growth temperature of silicon nanowires without the expected drawbacks. In addition, they could provide specific advantages.

Alignment of the wires

It has been shown that the electric field created by the plasma at the surface of the substrate could lead to the alignment of carbon nanotubes perpendicularly to the substrate.[8] As the metal-catalyzed growth of carbon nanotubes is very similar to the VLS growth of silicon nanowires, such a phenomenon could be expected to occur for the latter, too. In addition, efficient etching of parasitic deposition between wires can be achieved by hydrogen combined with ion bombardment. This effect should lead to a final layer with a higher aspect ratio than obtained by plain CVD. Ion bombardment could also limit the growth of wires which do not grow perpendicular to the substrate, as such wires have a much larger surface exposed to the etching as wires growing perpendicular to the substrate. This way, oriented growth could be achieved even when the substrate is amorphous or when epitaxy is not possible.

Use of alternate catalysts

Gold is the standard catalyst for the growth of nanowires by CVD, but it is one of the worst for electronic applications, as it diffuses in silicon and creates deep centers in the gap. Alternate catalysts such as indium or aluminum, which are p-dopants in silicon, would be more appropriate. Use of indium in CVD growth failed,[9] which may come from the low catalytic activity of this metal in the dissociation of silane, or from its oxidation before deposition starts. This way, using this metal could benefit from plasma-induced dissociation of the precursors. This has indeed been recently reported.[10] Additionally, aluminum could not be used so far as a catalyst in thermal

"Real-time spectroscopic ellipsometry study of the growth of amorphous and microcrystalline silicon thin films prepared by alternating silicon deposition and hydrogen plasma treatment", 1995; Hamers et al., "Contribution of ions to the growth of amorphous, polymorphous, and microcrystalline silicon thin films", 2000; Keudell and Abelson, "The interaction of atomic hydrogen with very thin amorphous hydrogenated silicon films analyzed using in situ real time infrared spectroscopy: Reaction rates and the formation of hydrogen platelets", 1998 [Ngu+94; Lay+95; Ham+00; KA98]

[8] Griffiths et al., "Plasma assisted growth of nanotubes and nanowires", 2007 [Gri+07]

[9] Bootsma and Gassen, "A quantitative study on the growth of silicon whiskers from silane and germanium whiskers from germane", 1971 [BG71]

[10] Iacopi et al., "Plasma-enhanced chemical vapour deposition growth of Si nanowires with low melting point metal catalysts: an effective alternative to Au-mediated growth", 2007 [Iac+07]

CVD growth except if all the process (evaporation, transfer of the samples and deposition) is run under ultra-high vacuum (base pressure: 1×10^{-10} mbar).[11] The reason is that aluminum reacts very fast with oxygen to form a 2 nm- to 5 nm-thick native oxide layer.[12] This native oxide behaves as a diffusion barrier for silicon, so it prevents the formation of the Si-Al alloy, which is required for the growth to happen. Plasma treatments could help getting rid of this limit through etching or reduction of the oxide layer before the deposition. This point will be discussed in detail in section 4.3.

Catalyst-free growth

Silicon nanoparticles can be generated in the bulk of the plasma.[13] In addition, amorphous silicon can be selectively etched by H_2 plasmas. Yassine Djeridane, in an unpublished work, associated these two phenomena to deposit micro-crystalline nanopillars without any catalyst. He obtained such layers by alternating deposition plasmas[14] with etching plasmas[15], each step being 1 min long. As shown on an AFM image of the final layer (fig. 4.1), micro-crystalline layers with a high roughness have been obtained. But the aspect ratio of the pillows still is poor (about 0.2–0.3). One could imagine that further optimization of this process could lead to a catalyst-free deposition of silicon nanowires.

4.2 Low-temperature growth of nano-structured silicon on evaporated metallic catalysts

4.2.1 Choice of experimental conditions

The metal catalysts are the same (copper and gold) as in chapter 3, as one of the goals of this part is to elucidate the observations made on CVD-grown samples treated with plasmas. Moreover, the rationales then given for using them still stand, except that the range of temperatures explored is way below the eutectic temperature of the metal-silicon alloys. Yet it may be expected that local heating of the surface, due to the ion bombardment, will reduce the temperature gap. The metallic layers (equivalent thickness: 1 nm to 3 nm) were evaporated under vacuum by electron beam as described in section 3.2.1. The most comprehensive set of experiments has been done with copper.

[11] Wang et al., "Epitaxial growth of silicon nanowires using an aluminium catalyst", 2006 [Wan+06]

[12] Civale et al., "Aspects of Silicon Nanowire Synthesis by Aluminum-Catalyzed Vapor-Liquid-Solid Mechanism", 2004 [Civ+04]

[13] Cabarrocas, Gay, and Hadjadj, "Experimental evidence for nanoparticle deposition in continuous argon–silane plasmas: Effects of silicon nanoparticles on film properties", 1996; Tanenbaum, Laracuente, and Gallagher, "Nanoparticle deposition in hydrogenated amorphous silicon films during rf plasma deposition", 1996; Cabarrocas et al., "Synthesis of silicon nanocrystals in silane plasmas for nanoelectronics and large area electronic devices", 2007 [CGH96; TLG96; Cab+07]

[14] 1 sccm of SiF_4, 8 sccm of H_2, 36 sccm of Ar; $p = 1.82$ Torr, $P_{RF} = 15$ W.

[15] 10 sccm of H_2, 36 sccm of Ar; $p = 1.82$ Torr, $P_{RF} = 15$ W.

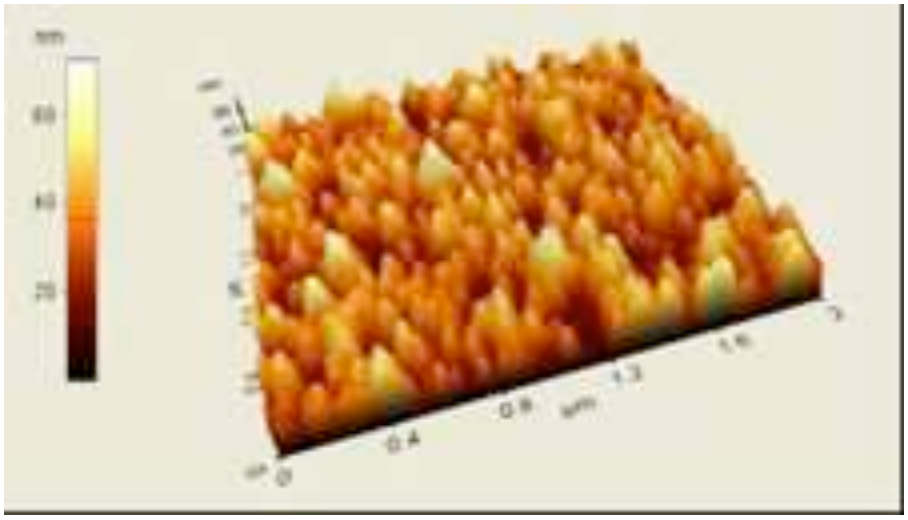

Figure 4.1 – *AFM image of a micro-crystalline nano-pillows deposited by alternate plasmas.*

Two main kinds of plasma conditions have been investigated. The first are pure silane, low pressure and low RF power plasmas. They will be referred to as "a-Si:H plasmas" because they lead to the deposition of hydrogenated amorphous silicon on uniform substrates such as glass or untreated ITO. The typical pressure in such plasmas is around 40 mTorr, the injected RF power is 0.5 W, and the flow rate of silane is 50 sccm. The second class of plasmas will be referred to as "μc-Si plasmas". Indeed, on glass or plain ITO, they lead to the deposition of micro-crystalline silicon layers. They are high pressure (1 Torr to 3 Torr) plasmas where silane (typical flow rate: 3 sccm) is highly diluted in hydrogen (200 sccm). The injected RF power is higher than for a-Si:H plasmas: it is between 10 W and 20 W. All the experiments were done in the ARCAM reactor, which offers a very good control on the process temperature. Only the chamber used for the deposition of intrinsic layers was used.[16]

The first kind of plasmas ("a-Si:H" plasmas) was primarily studied because the bunches of nanowires described in section 3.3.2 were obtained upon treatment under these conditions. The second one ("μc-Si plasmas") was investigated because the high energy ions impacting the surface are likely first to enhance etching of parasitic deposition by hydrogen, second to help crystallization of the layer.

The temperature was mainly kept between 175 °C and 200 °C, which is the standard range for the deposition of a-Si:H and μc-Si. Some tests were made at higher temperature (up to 250 °C) to check if that would increase the anisotropy of the layer.

[16]The ARCAM reactor has three chambers, one for each kind of doping, in order to avoid cross-contamination.

4.2.2 Characterization of the catalytic effect

Two complementary methods can be used to characterize the deposited layers. A first and fast characterization is given by spectroscopic ellipsometry. This measurement can be done in air just after the deposition and requires only a few minutes per sample. Qualitative information can be obtained immediately from the plot of the pseudo-dielectric function of the sample as a function of the photon energy (in particular from its imaginary part $\langle\epsilon_i\rangle$). First, the shape of the curve gives insight into the crystallinity of the layers: a broad and smooth peak centered around 3.5 eV indicates an amorphous layer and shoulders at 3.4 eV and 4.2 eV are characteristic of micro-crystalline layers.[17] Second, calculations based on Bruggeman's effective medium approximation on both amorphous silicon[18] and micro-crystalline silicon[19] have shown that the lower the value of $\langle\epsilon_i\rangle$ at high energies, the more porous or the rougher the layer. Quantitative information, such as the void fraction or the thickness of the layers, can be obtained by fitting the curve to a multi-layer model, where porous layers are described as a mixture of silicon (micro-crystalline or amorphous) and voids. In addition, SEM images provide visual information on the morphology of the layers.

Evidence of a catalytic effect

Using both characterization methods, the catalytic effect of copper has been clearly evidenced. To do that, we partially coated ITO samples with 3 nm of copper and then exposed them to μc-Si plasmas without any pre-treatment. In that case, the pressure was 3 Torr and the inter-electrode distance was 12 mm. The samples have been exposed to the deposition plasma for 20 min. In addition, two different values of the injected RF power have been used: 10 W and 20 W. The imaginary part of the pseudo-dielectric function, as calculated from the ellipsometry measurements, is plotted on fig. 4.2.

The effect of the copper layer is visually striking: for an RF power of 20 W, it leads to a decrease in the value of $\langle\epsilon_i\rangle$ at 4.2 eV from 12.3 to 9.2. The decrease is even stronger for $P_{RF} = 10$ W, at which $\langle\epsilon_i\rangle$ falls from 11.4 to 3.4. From that it can be concluded that (i) copper induces a strong porosity of the layer and (ii) this catalytic effect is more visible at $P_{RF} = 10$ W than at $P_{RF} = 20$ W. This observation is further confirmed by SEM images, as shown on fig. 4.3.

Modeling the ellipsometry spectra gives further insight into the catalytic behavior. It should be noted, though, that due to their high porosity, fitting the layers deposited on Cu-coated ITO was especially difficult. Good convergence could only be obtained for energies in the range 2.5 eV − 4.5 eV and the value of χ^2 was between 5 and 10. For all spectra, we checked on the calculated spectra that the position of the interference

[17] Kumar, Drevillon, and Godet, "In situ spectroscopic ellipsometry study of the growth of microcrystalline silicon", 1986 [KDG86]

[18] Morral, Cabarrocas, and Clerc, "Structure and hydrogen content of polymorphous silicon thin films studied by spectroscopic ellipsometry and nuclear measurements", 2004 [MCC04]

[19] Hamma and Cabarrocas, "Low temperature growth of highly crystallized silicon thin films using hydrogen and argon dilution", 1998 [HC98]

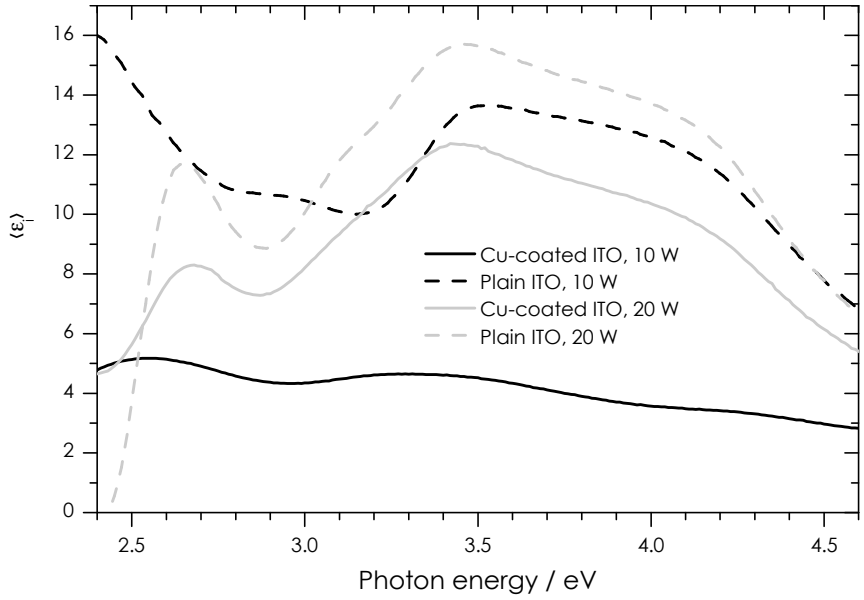

Figure 4.2 – *Imaginary part of the pseudo-dielectric function of the layers deposited by µc-Si plasma on plain and Cu-coated ITO*

peaks (at low energy), which gives information on the thickness of the film, was correct, even if their height was not accurately estimated.

The main results are shown on table 4.1. The amount of deposited silicon is estimated as $d \times (1 - F_v)$, where d is the thickness of the layer and F_v is the void fraction. This value can thus be seen as the thickness of a compact layer containing the same amount of silicon as the deposited layer. It is much larger, in given conditions, on Cu-coated ITO than on plain ITO. This shows that copper has a *real* catalytic effect, *i.e.*, it enhances the deposition rate of silicon. The relative enhancement is larger (factor >2) when $P_{RF} = 10\,\mathrm{W}$ than when $P_{RF} = 20\,\mathrm{W}$ because non-catalyzed deposition is faster in the second case than in the first.

Substrate	P_{RF} (W)	Thickness (nm)	Void fraction (%)	Amount of Si (nm)
Plain ITO	10	40.8 ± 0.3	26.0 ± 0.4	30.2
Cu-coated ITO	10	137 ± 3	47 ± 1	72.6
Plain ITO	20	136.3 ± 0.6	10.9 ± 0.5	121.4
Cu-coated ITO	20	218 ± 8	25 ± 3	163.5

Table 4.1 – *Structure of the layers deposited by µc-Si plasmas, as derived from the ellipsometry spectra*

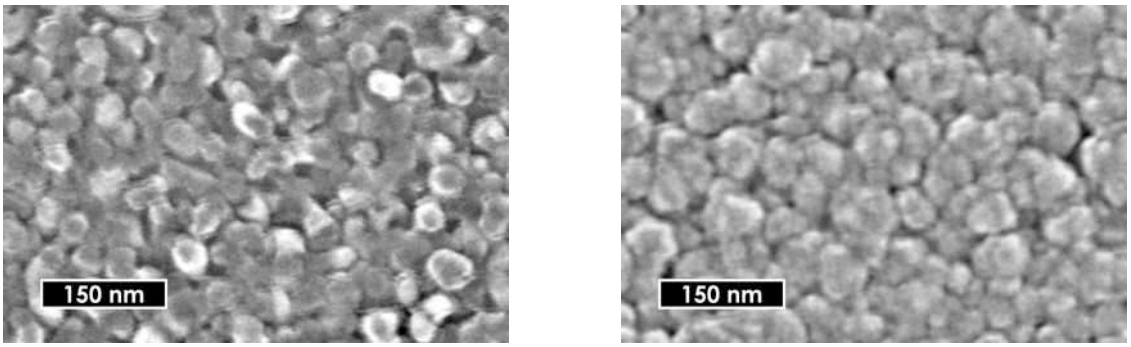

(a) $P_{RF} = 10\,\mathrm{W}$ **(b)** $P_{RF} = 20\,\mathrm{W}$

Figure 4.3 – *SEM images of the silicon layers deposited on Cu-coated ITO by µc-Si plasmas.*

Crystalline structure of the layers

The micro-crystalline structure of the deposited layers is confirmed by Raman measurements, as shown on fig. 4.4. The signal from the layers deposited on Cu-coated ITO is much noisier than for layers deposited on plain ITO.All spectra have a peak around $520\,\mathrm{cm}^{-1}$, which is characteristic of silicon crystals. Yet this peak is slightly shifted (by about $3\,\mathrm{cm}^{-1}$) toward lower wavenumbers on Cu-coated ITO as compared to plain ITO. Such a shift is a clue for smaller crystallites or increased heating,[20] so it further confirms the localized growth of silicon nanostructures. The data have been fitted to Gaussian peaks, given by:

$$y = y_0 + \sum_i \frac{A_i}{w_i \sqrt{\frac{\pi}{2}}} \times \exp\left[-2\left(\frac{x - x_{c,i}}{w_i}\right)^2\right] \tag{4.1}$$

$x_{c,i}$ represents the position of peak i, w_i its width and $\frac{A_i}{w_i\sqrt{\frac{\pi}{2}}}$ its height. In that case, two peaks have been included to model each curve. This gives good quality fits, with determination coefficients larger than 0.99, except for the Cu-coated ITO sample treated at $P_{\mathrm{RF}} = 10\,\mathrm{W}$. The results, as shown on table 4.2, confirm the major contribution of a sharp ($w_i < 10\,\mathrm{cm}^{-1}$) crystalline peak (number 1) to the signal. Its position is between $517\,\mathrm{cm}^{-1}$ and $520\,\mathrm{cm}^{-1}$, which is typical of crystalline silicon. Yet there is a non-negligible contribution of a wider peak (number 2), at lower wavenumbers, to account for the asymetry of the spectra.

Effect of the plasma conditions

Layers have also been deposited on Au- and Cu-coated ITO by a-Si:H plasmas at different temperatures. In that case, the deposition time is only 3 min, as was the case when

[20] Viera, Huet, and Boufendi, "Crystal size and temperature measurements in nanostructured silicon using Raman spectroscopy", 2001 [VHB01]

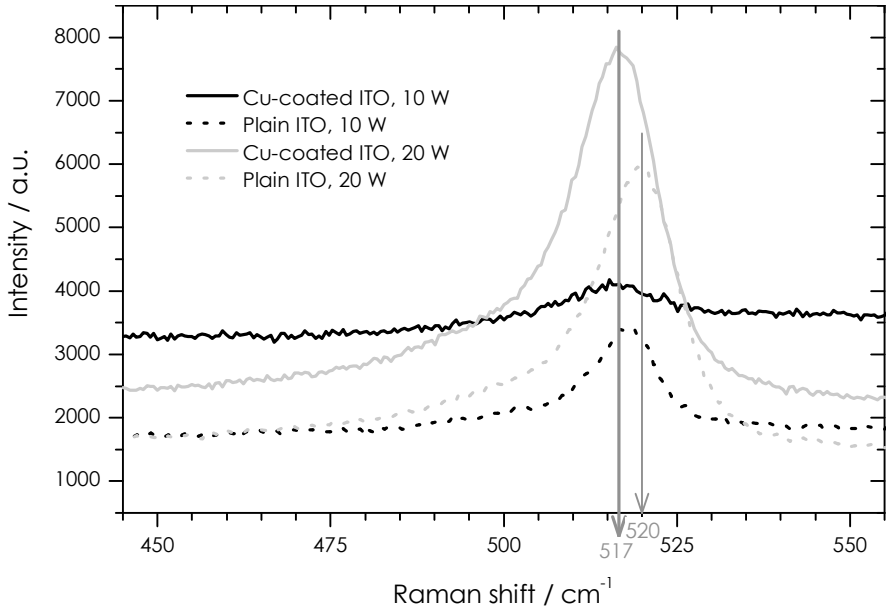

Figure 4.4 – *Raman spectra of the layers deposited on Cu-coated and plain ITO by µc-Si plasmas*

Substrate	P_{RF}/W	$x_{c,1}$/cm^{-1}	w_1/cm^{-1}	$\frac{A_1}{w_1\sqrt{\pi/2}}$	$x_{c,2}$/cm^{-1}	w_2/cm^{-1}	$\frac{A_2}{w_2\sqrt{\pi/2}}$	R^2
Plain ITO	10	517.58 ± 0.04	4.1 ± 0.1	1180 ± 30	512.4 ± 0.3	31.9 ± 0.7	450 ± 20	0.9927
Cu-coated ITO	10	513 ± 6	50 ± 10	800 ± 500	488 ± 1	27 ± 6	-300 ± 300	0.9062
Plain ITO	20	519.71 ± 0.04	10.8 ± 0.1	3500 ± 100	505.4 ± 0.6	28.9 ± 0.8	990 ± 80	0.9955
Cu-coated ITO	20	516.66 ± 0.04	11.2 ± 0.1	4300 ± 100	504.1 ± 0.4	29.9 ± 0.6	1330 ± 80	0.9969

Table 4.2 – *Analysis of the Raman spectra of layers deposited by µc-Si plasmas*

bunches of nanowires were obtained. The imaginary part of their pseudo-dielectric function is plotted on fig. 4.5. No shoulder is visible, and the curves rather show broad peaks. This seems to indicate that the layers are amorphous, but they are very thin so no firm conclusion can be drawn. In addition, Raman measurements failed because only the substrate gave a significant signal. It seems, though, that under similar conditions gold leads to more porous layers. In particular, increasing the temperature from 200 °C to 250 °C leads to an extremely rough layer ($\langle\epsilon_i\rangle < 1$ over most of the spectrum) on Au-coated ITO, while it has little impact on the Cu-coated ITO.

SEM images (fig. 4.6) confirm this impression. At 200 °C, the layer deposited on Cu-coated ITO is made of aggregates and the layer deposited on Au-coated ITO includes few square-shaped columns. But none of them are significantly anisotropic. On the other hand, at 250 °C, the layer deposited on Cu-coated ITO still is made of the same kind of aggregates, but some short nanowires appear in between, which look very similar to what was observed on fig. 3.20. On Au-coated ITO, a dense layer of

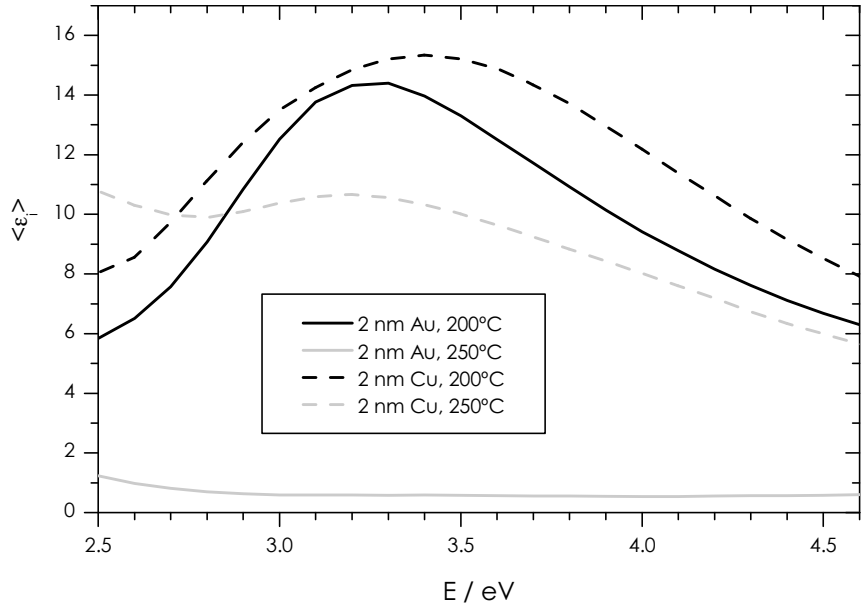

Figure 4.5 – *Imaginary part of the pseudo-dielectric function of layers deposited on gold and copper-coated ITO by a-Si:H plasmas at various temperatures*

columnar structures oriented perpendicular to the substrate has grown. The diameter of these structures is around 100 nm. Their most striking property is that they are very well separated and are in sharp contrast with the background. They are, though, not nanowires, and no trace of the metal is visible.

These results cannot be well explained at this point, but they are likely to be related to the last part of this chapter.

Influence of the substrate

Similar experiments have also been run on metal-coated silicon layers, either single crystalline, amorphous or micro-crystalline. Both gold and copper have been used. The goal here was:

1. investigate whether the bunches observed after CVD experiments could come from sputtering of silicon. Indeed, it was suspected that in these experiments, metal dots were covered by parasitic amorphous silicon. Sputtering this layer off would have made the catalysts facing the gas phase again. As sputtered atoms go to this gas phase, they may then have reacted with the metal.

2. explore the possibility of growing multi-layer structures.

In particular, is it possible to deposit intrinsic nano-structured silicon on top of n-doped silicon thin films? Is the hydrogen plasma treatment enough to obtain nanostructures when the metal is deposited on top of silicon?

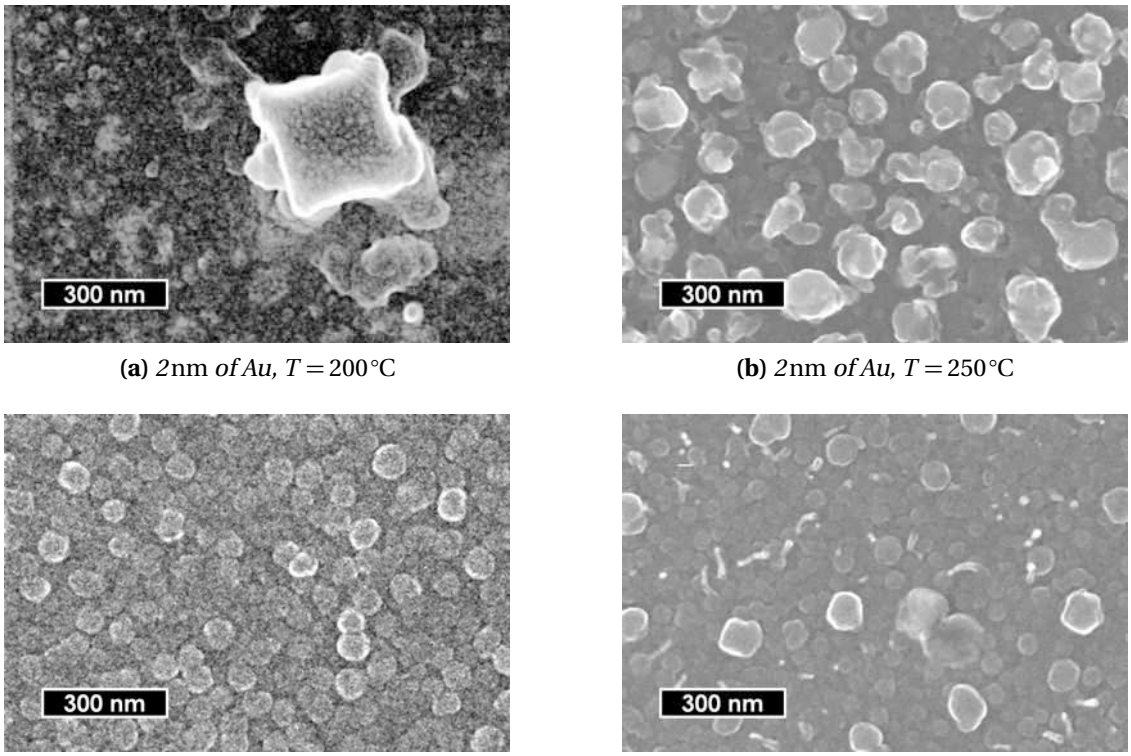

(a) *2*nm *of Au, T* = 200 °C

(b) *2*nm *of Au, T* = 250 °C

(c) *2*nm *of Cu, T* = 200 °C

(d) *2*nm *of Cu, T* = 250 °C

Figure 4.6 – *SEM images of layers deposited on Au- and Cu-coated ITO by a-Si:H plasmas at various temperatures*

When gold is used as the evaporated metal, little or no structuring of the plasma-deposited silicon layer is visible. At best, small aggregates are formed with little topographical contrast with the substrate. This behavior probably comes from the diffusion of gold in silicon during evaporation. Indeed, the substrates were either etched in HF (for crystalline silicon) or kept under vacuum between deposition and evaporation of the metal (for a-Si:H and μc-Si), so no oxide layer could prevent gold from diffusing.

On the other hand, results obtained on copper-coated silicon (especially a-Si:H) are very similar to the layers grown on Cu-coated ITO (fig. 4.7a). So diffusion of copper in the silicon thin films is limited enough to prevent it from disappearing. Yet no structured layer is obtained by exposing the metal-coated silicon substrates, whatever they are, to H_2 plasma. What is visible on fig. 4.7b is only etching, without any growth. So the hypothesis of nanowires obtained by sputtered silicon reacting with catalysts can be excluded.

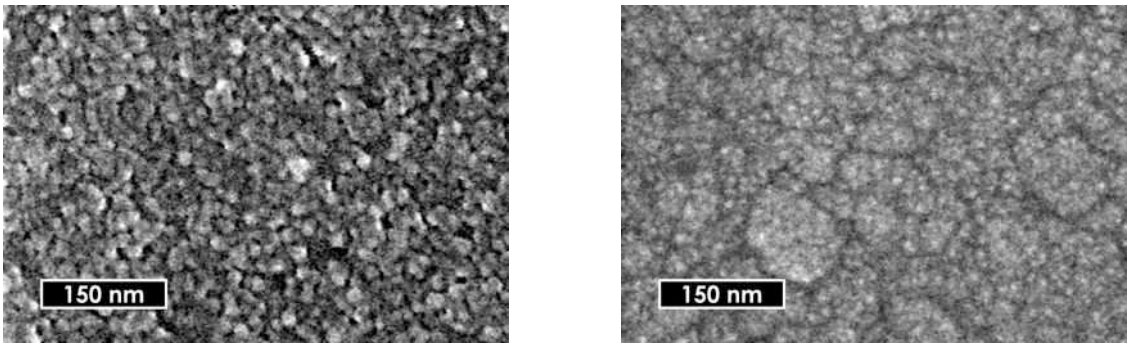

(a) *μc-Si plasma.* **(b)** *Hydrogen plasma*

Figure 4.7 – *Layers obtained by exposing an a-Si:H layer coated with 2*nm *of copper to plasmas (5*min, $T = 175\,°C$, $p = 3\,$Torr, $d = 12\,$mm

4.2.3 Possible growth mechanism

In this section, we will propose a growth mechanism for the anisotropic growth observed when metal-coated ITO is exposed to μc-Si plasmas.

The initial step of this growth is shown on fig. 4.8. With both metals, aggregates are formed after 3 min of exposure to the plasma at 200 °C. These aggregates are larger and better separated from the substrate with copper than with gold. The difference may be explained by the deposition and evolution of the metallic layers on ITO. Indeed, gold does not form oxides, while copper does, so the latter adheres more strongly on ITO than gold. This way, whereas both metals are reported to grow through the Volmer-Weber mode on metal oxides,[21] copper islands are larger and thinner than gold ones, and there is less aggregation upon annealing. This is illustrated on fig. 4.9, which shows metal-coated ITO after 1 h annealing under vacuum at 175 °C. It also seems that the aggregates are better isolated from each other at this initial stage than after 20 min. That means that lateral, isotropic growth dominates after the first few minutes.

The core explanation to account for all these observations is that the metallic layer has a catalytic effect only at the beginning of the deposition. For a continuous catalysis to be possible, it is necessary that the metallic surface remains in contact with the gas phase and, as a consequence, that silicon atoms diffuse away from this surface after their chemisorption.

Now, SiH_4 adsorbs dissociatively on gold surfaces at low temperature and is completely dehydrogenated at 110 °C.[22] Yet the elemental Si hence formed is reported to diffuse in the metallic layer only above 330 °C.[23] Between those two temperatures, a

[21] Diebold, Pan, and Madey, "Growth mode of ultrathin copper overlayers on TiO_2(110)", 1993; Gota et al., "Influence of the substrate oxidation state in the growth of copper clusters on Al_2O_3(0001) surface: a XANES and EXAFS study", 1995 [DPM93; Got+95]

[22] Spencer and Nyberg, "Adsorption of silane and methylsilane on gold surfaces", 2004 [SN04]

[23] Westwater et al., "Nanoscale silicon whiskers formed by silane/gold reaction at 335 °C", 1995;

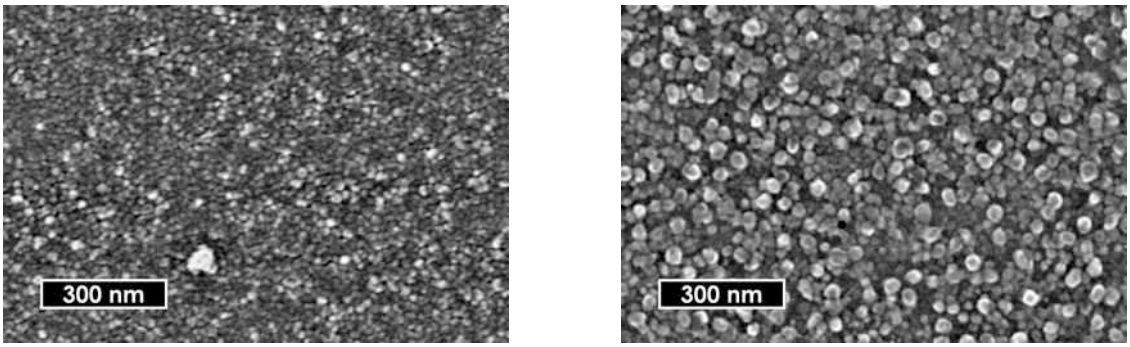

(a) *Metal: gold* **(b)** *Metal: copper*

Figure 4.8 – *SEM images of layers deposited on ITO with a 3*nm *metal coating by 3*min *µc-Si plasmas ($P_{RF} = 12\,W$, $T = 200\,°C$)*

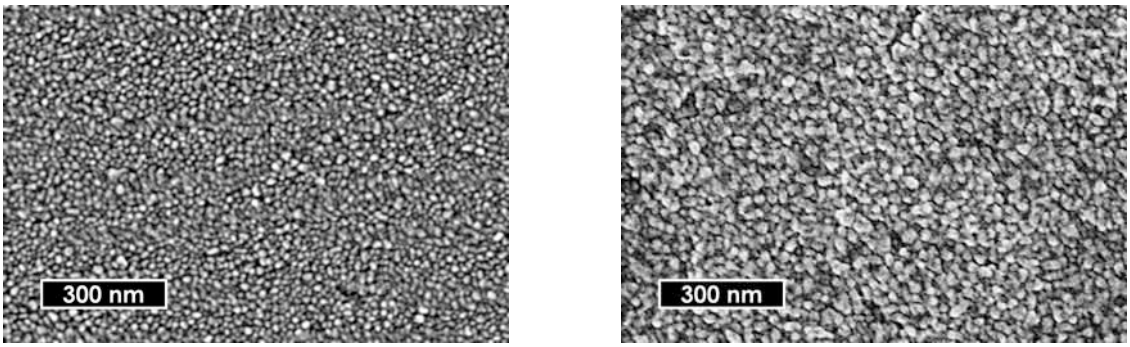

(a) *Gold, nominal thickness: 2*nm **(b)** *Copper, nominal thickness: 3*nm

Figure 4.9 – *SEM images of metal-coated ITO layers after 1 h annealing at 175* °C*, without any deposition of silicon.*

silicide shell should therefore form fast from the vapor phase on the gold layer.

Similar behavior has been reported for copper, with even lower critical temperatures: SiH_4 dissociatively chemisorbs on Cu (111) from −183 °C on,[24] dissociation into elemental Si starts at −43 °C and is total at 127 °C.[25] Moreover, diffusion of the adsorbed Si atoms in the metallic layer starts at 347 °C on Cu (111) and 295 °C on Cu (110).[26] Below that temperature, a stable surface alloy phase is formed. Once again, our experimental conditions lie in the stability domain of this silicide shell.

Spencer and Nyberg, "Adsorption of silane and methylsilane on gold surfaces", 2004 [Wes+95; SN04]

[24]Wiegand, Lohokare, and Nuzzo, "Silicon-hydrogen (Si-H) bond activation on copper: reaction of silane on Cu(111)", 1993 [WLN93]

[25]Curson et al., "Interaction of silane with Cu(111): Surface alloy and molecular chemisorbed phases", 1997 [Cur+97]

[26]Spencer et al., "Adsorption of SiH_4 on copper (110) and (111) surfaces", 2002; Wiegand, Lohokare, and Nuzzo, "Silicon-hydrogen (Si-H) bond activation on copper: reaction of silane on Cu(111)", 1993 [Spe+02; WLN93]

So both metals have a strong catalytic effect on the dissociation of silane, which explains the nucleation of silicon aggregates in the first few minutes of deposition. But, in the range of temperature where our experiments were done, silicon diffusion in the droplets is prevented (or, at least, slowed down) by a stable silicide layer. So the catalyst droplets are fast passivated and do not play any role in the deposition afterwards. In short, metal aggregates have here the same catalytic action than in the growth of nanowires, but they do not act as growth mediators.

This explanation is supported by the fact that adding Ar in a μc-Si plasma during the first 30 s of the deposition inhibits the catalytic effect of copper. In that case, there is no difference in the ellipsometry spectra between the deposition on Cu-coated ITO and plain ITO. This observation may be explained by the high trapping probability of argon on copper.[27] Such trapping will limit the catalytic effect of copper as adsorption of SiH_x cannot occur on sites occupied by argon atoms.

This mechanism is schematically summarized on fig. 4.10.

4.2.4 Outlook

This method to grow silicon nanostructures seems very promising for our application:

- The layers can be made highly porous, so the interface with the polymer would be very large.
- Their thickness (so their light absorption) can be controlled and the surface roughness is not too high, which will help preventing shorts of the polymer layer.
- There are no metallic aggregates on top of the silicon layer, which would behave as recombination centers in devices.

An open question remains the efficiency of the silicide layer to prevent diffusion of the metal in silicon. Our observations show that there is no massive and fast migration of the metal across this layer, because this would allow a long-lasting catalytic effect, but we have no evidence that the amount of metal in silicon is below the critical level for a significant electrical effect (around $1 \times 10^{12}\,cm^{-3}$ in polycrystalline silicon, *cf.* paragraph 3.1.4).

In addition, the proposed growth mechanism works well for the growth at temperatures lower or equal to 200 °C but it does not seem able to account for the observations made at 250 °C. Yet this temperature still lies in the stability domain reported for the silicides. So some additional phenomena must occur in that case.

[27] Jackson, "A semiclassical study of He, Ne, and Ar sticking on metal surfaces", 1991 [Jac91]

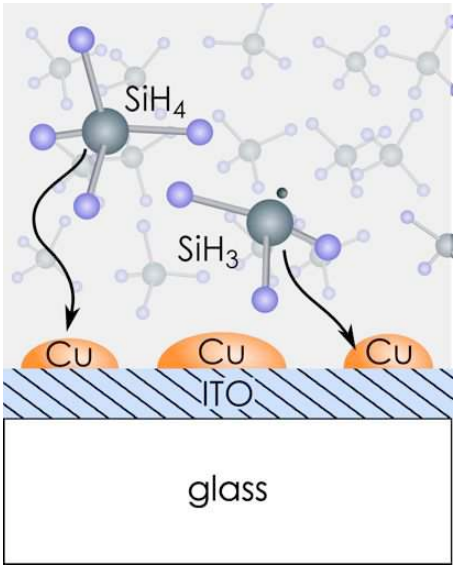

(a) *Adsorption of SiH_4 and SiH_3 on copper aggregates*

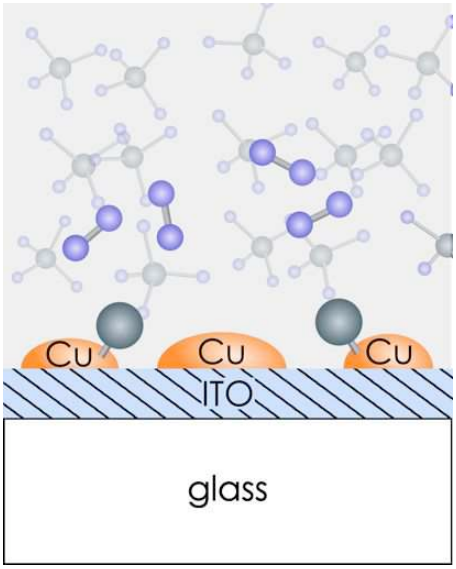

(b) *Dehydrogenation of SiH_x species and release of hydrogen*

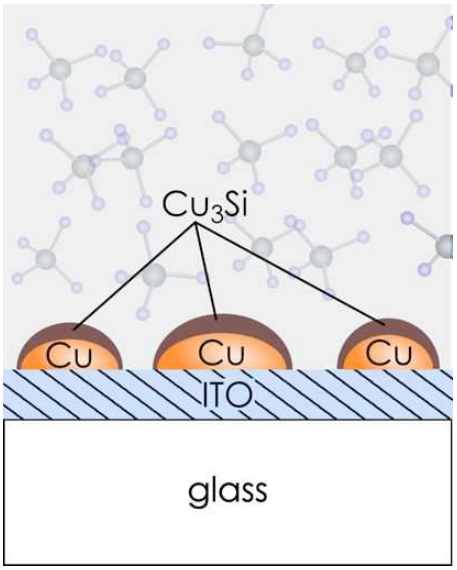

(c) *Formation of a stable Cu_3Si shell*

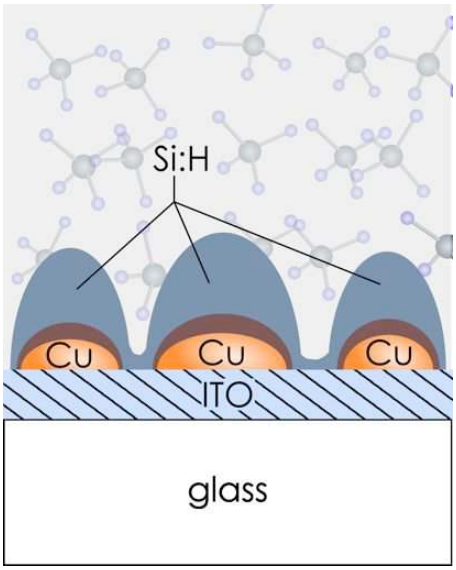

(d) *Deposition of hydrogenated silicon*

Figure 4.10 – *Main steps of the proposed mechanism for the growth on copper aggregates*

4.3 Effect of the hydrogen plasma on the growth with evaporated metallic catalysts

4.3.1 Hydrogen plasma treatments on copper and gold

In all experiments with copper and gold, evaporation was performed in very clean conditions (in the evaporator linked to ODILE glovebox), the samples were transported under argon in airtight containers and were exposed to air only during the time required to load the PECVD reactor. Yet this short exposure could be sufficient to induce significant contamination or oxidation of the metallic layer because the amount of metal deposited on the substrates was very small and its surface was fragmented. In that case, pre-treatment by hydrogen plasma could be useful to reduce the oxide layer and clean the catalysts before deposition.

Surprisingly, such a pre-treatment did not enhance the porosity of layers deposited with copper as the catalyst, and even reduced it. This reduction is evidenced on fig. 4.11: the imaginary part of the pseudo-dielectric function of layers deposited on Cu-coated ITO by a-Si:H plasmas[28] is significantly higher when the samples have been pre-treated with 5 min H_2 plasmas[29] than when they have not.

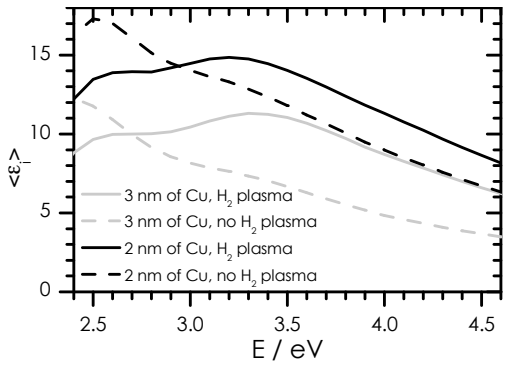

Figure 4.11 – *Imaginary part of the pseudo-dielectric function of samples deposited on Cu-coated ITO by a-Si:H plasmas (3*min*), with or without 5*min *H_2 plasma pre-treatment. Black lines: 2*nm *of Cu; Gray lines: 3*nm *of Cu. Solid lines: with H_2 plasma; dashed lines: without H_2 plasma*

The decrease in porosity is confirmed by SEM images. In addition, the layer is much more uniform when it is deposited without H_2 plasma pre-treatment (fig. 4.12a) than with one (fig. 4.12b).

This behavior can be explained in the same way as the effect of argon in the initial step of the deposition (paragraph 4.2.3): hydrogen is adsorbed at the surface of copper aggregates and it prevents further adsorption of silicon precursors. So it may clean aggregates, but it also passivates their surface, and the latter effect is much stronger. This

[28] $T = 200\,°C$, $d = 22\,mm$, 50 sccm of SiH_4, $p = 43\,mTorr$, $P_{RF} = 0.5\,W$, $V_{DC} = -10\,V$

[29] 200 sccm of H_2, $p = 870\,mTorr$, $P_{RF} = 5\,W$, $V_{DC} = -27\,V$

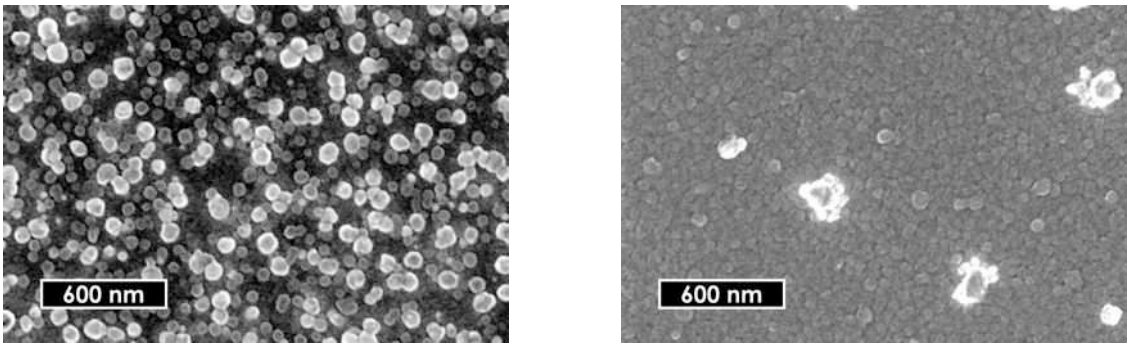

(a) *Without H_2 plasma pre-treatment* **(b)** *With 5*min *H_2 plasma pre-treatment*

Figure 4.12 – *SEM images of silicon layers deposited on Cu-coated ITO by 3*min *a-Si:H plasma at 200*°C

observation also means that our global process, from metal evaporation to growth of silicon layer, is clean and controlled enough not to be improved upon treatment by H_2 plasma.

As gold does not oxidize in air, no or little improvement was expected from H_2 plasma pre-treatment with this catalyst. Still, ellipsometry measurements have shown a little increase in porosity when such pre-treatment was applied before growth by a-Si:H plasma. Yet it seems that this increase rather comes from a modification in the ITO substrate than in the metallic aggregates. Indeed, when the samples are pre-treated with an H_2 plasma, some small structures appear all over the substrate, whether coated by gold or not, whereas larger ones are only present when ITO is coated with gold (fig. 4.13).

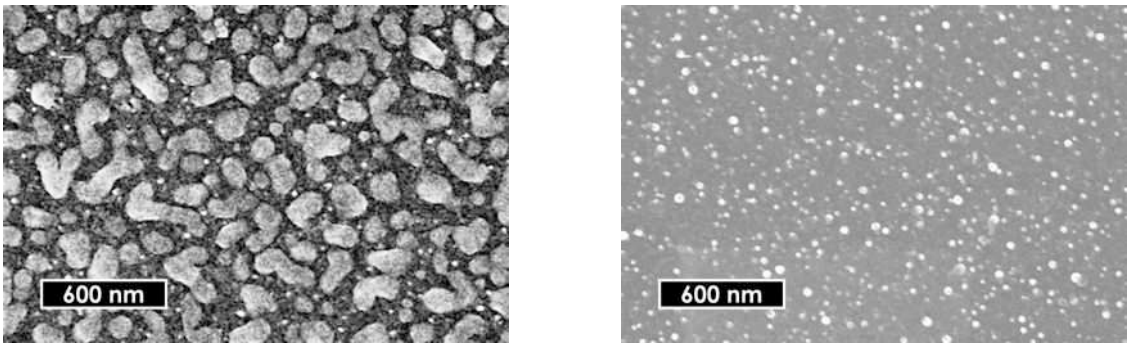

(a) *Gold-coated ITO* **(b)** *Plain ITO*

Figure 4.13 – *SEM images of layers deposited on an ITO substrate partially coated with gold. Samples exposed to 5*min *H_2 plasma pre-treatment followed by 3*min *of a-Si:H plasma ($T = 200$*°C*).*

4.3.2 Hydrogen plasma treatments on indium and aluminum

At the opposite, an "activation effect" of H_2 plasma pre-treatment has been evidenced on indium and aluminum. As mentioned in paragraph 4.1.2, use of both catalysts in the VLS growth of silicon nanowires by standard CVD is impossible, in particular because they are very fast passivated by a surface oxide layer. Martin Frimmer, from Walter Schottky Institute in München (Germany) performed experiments with us in PLASFIL reactor in the frame of his *Diplomarbeit*.[30] He used crystalline silicon substrates on which he evaporated metals. The samples were transported in air from München to Palaiseau so there is no doubt about indium and aluminum layers being oxidized.

Without H_2 plasma pre-treatment, not even separate indium droplets could be obtained upon annealing. On the contrary, dense and long nanowires have been obtained with H_2 plasmas followed by deposition through μc-Si plasmas. An example of successful growth is shown on fig. 4.14a.[31] The length of the nanowires is estimated to be around 1.6 µm and their base diameter 110 nm. There is a metallic droplet at the tip of the nanowires. As it has always been reported for nanowires grown with plasma enhancement, the wires are slightly tapered. Interestingly, not only is H_2 plasma treatment required to obtain active, separate indium catalyst droplets, but plasma activation is also necessary during the growth. Indeed, under conditions similar to what lead to the layer shown on fig. 4.14a, but without plasma during the growth phase, no silicon nanostructure at all could be obtained. Although the sticking coefficient and the dissociation rate of SiH_4 on indium are not documented, this result seems to indicate that indium does not behave as a catalyst in the dissociation of the precursor gases but only as a "growth mediator" *i.e.*, fast diffusion of silicon in the droplets ensures continuous availability of surface sites for adsorption of SiH_x species.

The results obtained with aluminum are less visually striking but are still very important. A low density (3×10^{-3} µm^{-1}) of silicon nanowires could be obtained by deposition with μc-Si plasma on c-Si coated with 1 nm of aluminum treated with 15 min of H_2 plasma (fig. 4.14b). During all the process, the substrate temperature was 600 °C and the RF electrode was kept at 380 °C. The injected RF power was 5 W. This result means that the aluminum oxide layer has been either reduced or etched off by the H_2 plasma pre-treatment. The low density of nanowires finally grown seems to indicate that the metal layer is partially etched off during this pre-treatment.

[30] Frimmer, "Growth of Silicon Nanowires with Alternative Catalysts", 2007 [Fri07]

[31] The substrate temperature was 400 °C during H_2 plasma and 600 °C during deposition; the RF electrode was kept at 380 °C throughout the process. H_2 plasma pre-treatment was 5 min long, exposure to deposition plasma was 60 min long. The flow rate of SiH_4 was 5 sccm, it was 100 sccm for H_2. The injected RF power was about 6 W.

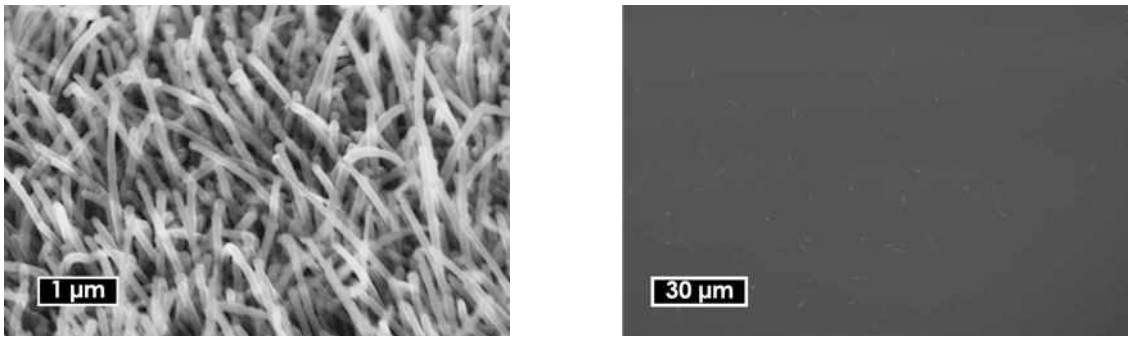

(a) *Catalyst: indium* **(b)** *Catalyst: aluminum*

Figure 4.14 – *SEM images of silicon nanowires grown on metal-coated crystalline silicon pre-treated by H_2 plasma in PLASFIL reactor (after [Fri07])*

4.4 Growth of silicon nanowires with catalysts generated in-situ

4.4.1 Evidence of the growth of silicon nanowires without external catalyst

First observations

Using patterned surfaces is a very convenient way to separate the effects of changes in the substrate, *e.g.*, a metal coating, from modifications in the deposition conditions. Indeed, plasmas depend among others on the surface state of the walls, which may vary from one run to another due to previous depositions. Many results presented in the previous sections come from ITO samples partially covered by masks during gold or copper evaporation.

Deposition on such samples by a-Si:H plasma in PLASFIL lead to a surprising result: not only the gold-coated part, but all the surface of the sample was covered by a strongly diffusive layer. This diffusivity meant that a very porous layer (or even nanowires) was deposited all over the substrate. The deposition conditions were similar to previous ones,[32] except that the substrate temperature was set to 300 °C while the RF electrode was heated to 200 °C. Observation by SEM confirms that the layers deposited on both parts of the substrate are very similar. Both are made of silicon nanorods, about 100 nm in base diameter and a few hundreds of nm in length. All of them are capped with a large metallic droplet, which appears bright on the image. This capping indicates that the nanorods are grown by the VLS process.

[32] 5 min H_2 plasma (100 sccm, $p = 181$ mTorr, $d = 30$ mm, $P_{RF} = 5$ W), followed by 15 min of pure SiH_4 plasma (10 sccm, $p = 55$ mTorr, $P_{RF} = 4$ W)

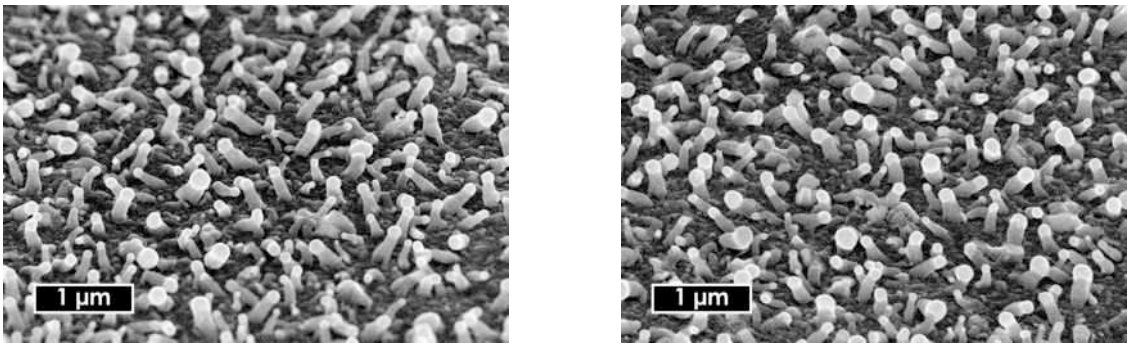

(a) *Au-coated area* **(b)** *Uncoated area*

Figure 4.15 – *SEM images of the layer deposited at 300°C in PLASFIL on an ITO substrate partially coated with gold (Hitachi S-4800, tilt: 45°)*

Evidence of a catalytic effect from ITO

A possible explanation for this observation could be gold being sputtered away by H_2 plasma and re-deposited all over the substrate. To rule this hypothesis out and confirm that the growth is really catalyzed by ITO, growth has been performed on another patterned substrate. This time, no metal was deposited at all, but the ITO was partially etched off with acid.[33] The sample was then cleaned as usual, and loaded in PLASFIL along with a Corning glass sample. All samples were exposed to the same plasma conditions as the sample shown on fig. 4.15.

After deposition, the ITO-coated part of the sample is strongly diffusive, whereas the etched part is translucent, as are thin a-Si:H layers. This is visible on photographs made at ambient light and with flash (fig. 4.16). At ambient light, the layer deposited on ITO looks very dark, while with flash, which provides a strong, directive, white light, it looks very bright.

Raman spectra of the layers deposited this way (fig. 4.17) provide valuable information. First, on the patterned substrate, the layer deposited on the etched part (bare glass) is similar to the layer deposited on the plain Corning glass sample. Both spectra have a broad peak centered around 450 cm^{-1}, which is characteristic of amorphous silicon. On the contrary, the spectrum of the layer deposited on ITO has a sharp peak centered at 500 cm^{-1}. Such a peak is typical of crystalline silicon, but its position is shifted down by 20 cm^{-1} with respect to bulk crystalline silicon. Such a shift can partially come from local heating by the laser beam used in the measurement. It can also be related to a change in crystalline structure as compared to bulk crystalline silicon. In particular, a peak centered at 506 cm^{-1} has been reported to come from a wurtzite (Si-IV) structure.[34]

[33] 5 min immersion in a mixture of nitric acid concentrated at 65% (10 vol.%) and hydrochloric acid concentrated at 37% (90 vol.%)

[34] Prades et al., "Concerning the 506 cm^{-1} band in the Raman spectrum of silicon nanowires", 2007 [Pra+07]

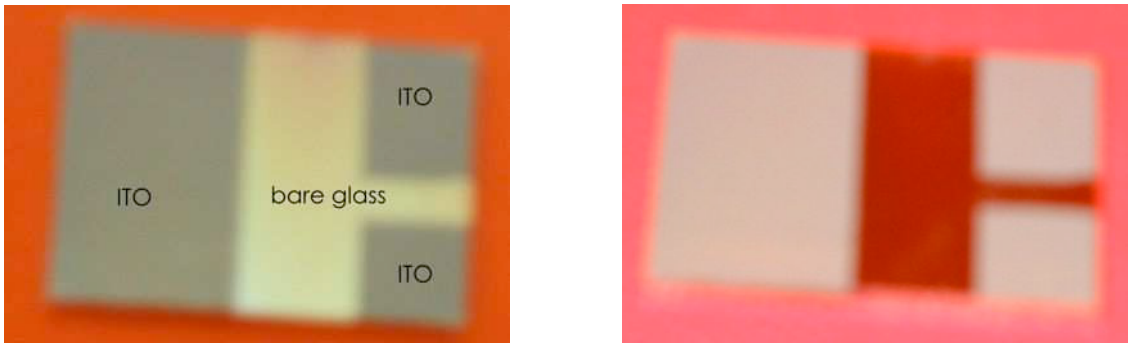

(a) *Without flash* **(b)** *With flash*

Figure 4.16 – *Photos of a sample partially coated with ITO after treatment with H_2 plasma and deposition by an a-Si:H plasma at 300°C.*

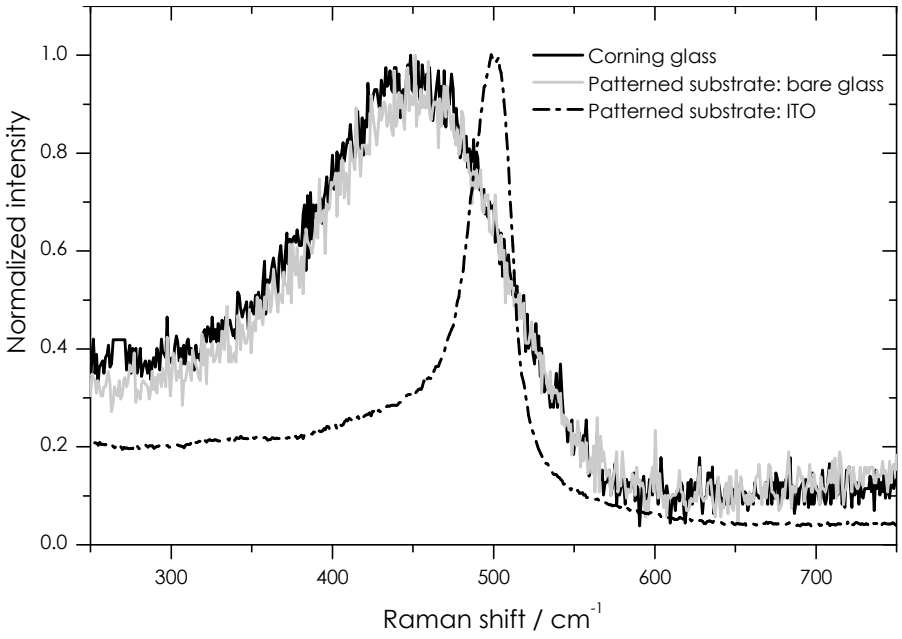

Figure 4.17 – *Raman spectra of the layers deposited on Corning glass and on a patterned ITO sample by H_2 plasma treatment and a-Si:H plasma at 300°C in PLASFIL*

The catalytic effect of ITO is confirmed by SEM images (fig. 4.18a). On the left of the image, the ITO coating had been etched off before deposition. There, the deposited layer is smooth and uniform. On the right of the image, the ITO coating had been protected during the chemical etching. There, a high density of short silicon nanowires has grown. As in fig. 4.15, the nanowires are capped by a metallic droplet, which appears bright on the picture (fig. 4.18b). This indicates that in that case too, nanowires were grown through the VLS mechanism.

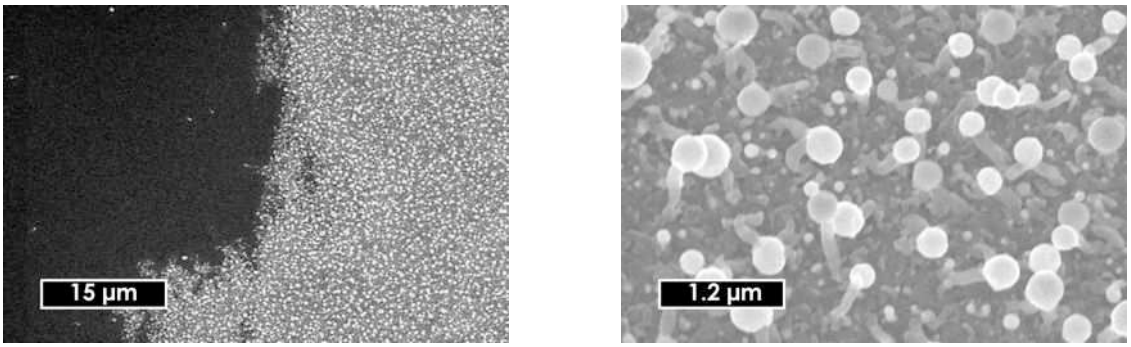

(a) *Interface between the layers deposited on bare glass (left: dark and smooth) and on ITO (right)*

(b) *Detail of the layer deposited on ITO; the metallic capping appears bright*

Figure 4.18 – *SEM images of the layer deposited on a patterned substrate by H_2 plasma treatment followed by a-Si:H plasma at 300°C in PLASFIL.*

Similar results have been obtained on SnO_2-coated glass, which can also be used as transparent conductive substrate. For simplicity, the following discussion will be focused on ITO substrates, except when comparison with SnO_2 is relevant.

4.4.2 Crystalline structure of the wires and influence of the metals

The Raman spectra indicate that the wires are crystalline, but do not provide strong clues on their structure. Moreover, at this point, we still ignore what is the composition of the metallic droplet on top of the wires and if the wires are made of pure silicon. Both questions will be answered by TEM measurements, along with Selective Area Electron Diffraction (SAED) and Energy-Dispersive X-Ray analysis (EDX).[35]

At least two different crystalline structures can be found among these nanowires. As expected, some wires have a cubic structure (Si-I phase), which is the stable structure for bulk crystalline silicon. The wires on which such a structure has been detected have a base diameter larger than 100 nm. They are single crystals, even though the are strongly micro-twinned (fig. 4.19). More surprisingly, an hexagonal phase, known as wurtzite structure (Si-IV), has been clearly identified on other wires (fig. 4.20b). These

[35] All these measurements were carried out by Gilles Patriarche, from *Laboratoire de Photonique et de Nanostructures* (LPN) at CNRS Marcoussis. They were obtained on a Philips CM20-ST microscope operated at 200 kV and equiped with a "Megaview" charge-coupled camera from Soft Imaging System.

wires have smaller diameters than the wires with a cubic structure: about 70 nm. But only a small number has been analyzed, so this difference may not be statistically relevant. Up to now, the existence of Si-IV nanowires remained a controversial question. Indeed, the wurtzite phase is metastable for silicon, but its stability is reported to be increased by decreasing crystal dimensions.[36] In our case the stability of the structure is at least four months. It should be noted that no wurtzite silicon nanowires have been detected to be grown on SnO_2 but only cubic ones (fig. 4.20a).

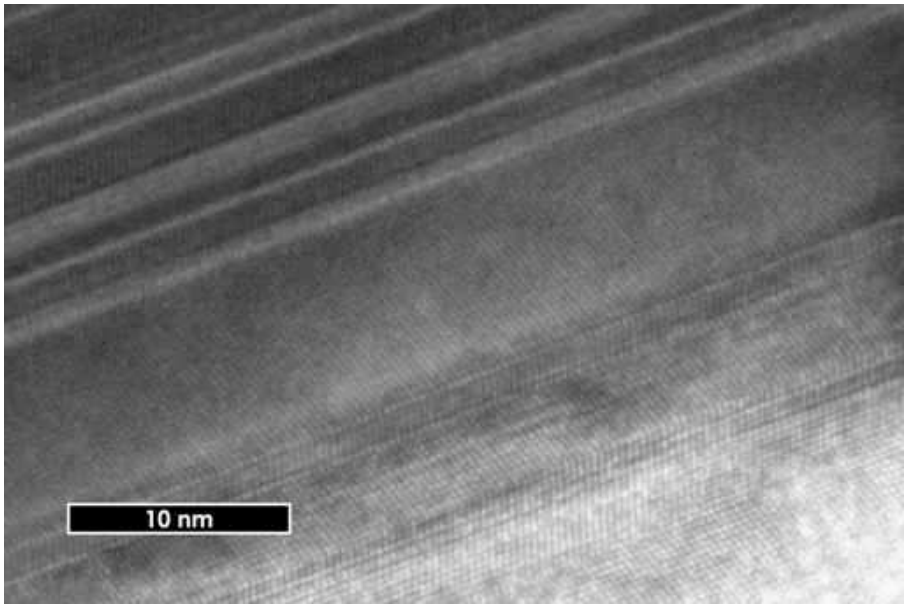

Figure 4.19 – *HRTEM image of a silicon nanowire grown on ITO at 300°C in PLASFIL. This wire is monocrystalline, with micro-twins. It has a cubic structure.*

The amount of metal in the wires has been determined by EDX. Both indium and tin have been detected. Their amount is much higher than their reported solubility in bulk crystalline silicon: 2 at. % and 5 at. % for tin (bulk solubility:[37] 0.1 at. %) and 0.5 at. % for indium (bulk solubility:[38] 36 ppm). In addition, no metallic precipitates were detected. This result is comparable with $Si_{1-x}Sn_x$ alloys grown below 300 °C by Molecular Beam Epitaxy (MBE) with a good structural quality.[39] Such alloys have been reported to be metastable. Annealing them at temperatures higher than 800 °C creates dislocations or induces precipitation of tin.

The catalyst capping, in turn, is made of indium with only 1.5 at. % of tin. For comparison, the ratio between the amounts of indium and tin at the surface of the

[36] FontcubertaiMorral et al., "Synthesis of Silicon Nanowires with Wurtzite Crystalline Structure by Using Standard Chemical Vapor Deposition", 2007 [Fon+07]

[37] Massalski, *Binary Alloy Phase Diagrams*, 1998 [Mas98]

[38] Solmi et al., "Investigation on indium diffusion in silicon", 2002 [Sol+02]

[39] Shiryaev et al., "Pseudomorphic $Si_{1-x}Sn_x$ alloy films grown by molecular beam epitaxy on Si", 1995; Ridder et al., "Precipitation of Sn in metastable, pseudomorphic Si0.95Sn0.05 films grown by molecular beam epitaxy", 2000 [Shi+95; Rid+00]

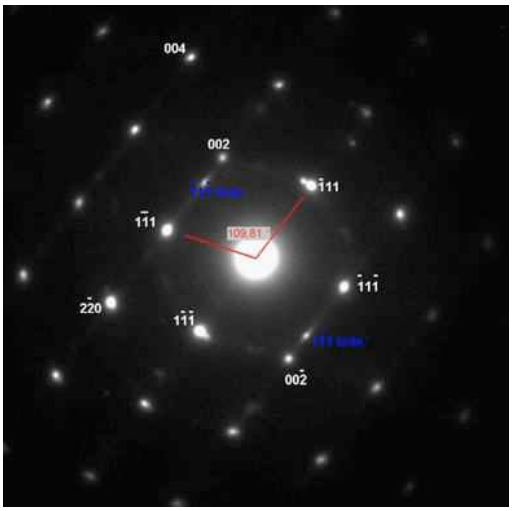

(a) *Diffraction pattern measured along the* ⟨110⟩ *zone axis of a silicon nanowire grown on* SnO_2 *(cubic phase)*

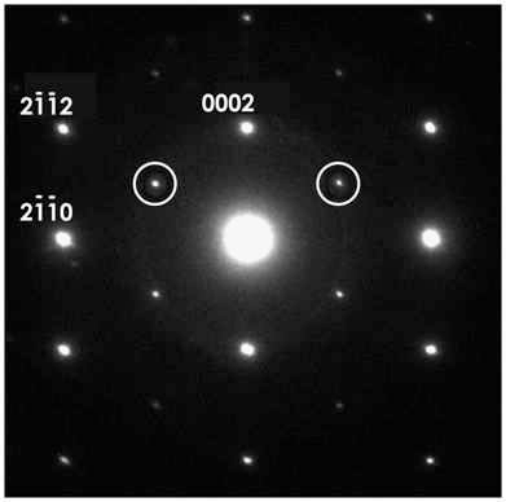

(b) *Diffraction pattern measured along the* ⟨1$\bar{1}$00⟩ *pole axis of a silicon nanowire grown on ITO (wurtzite phase)*

Figure 4.20 – *Selected area electron diffraction patterns measured on silicon nanowires grown at 300°C by* H_2 *plasma and a-Si:H plasma in PLASFIL*

original substrate was measured by X-Ray Photoelectron Spectroscopy (XPS). It was 7.6. It appears, then, that the two metals get separated during the growth process: tin, which is more soluble in silicon than indium, is mainly incorporated into the wires, while indium remains in the catalyst droplet.

It could be noticed on fig. 4.18b that the catalyst cappings are significantly larger than the silicon nanowires. This feature is a major difference with nanowires grown with gold. In that case, the catalyst droplet has the same diameter as the wire and appears like an hemisphere. This difference can be explained by the large difference in the Si/metal interfacial tension between gold and indium. The contact angle of Au-Si droplets on Si (111) is 43° over the temperature range where silicon nanowires are grown,[40] whereas the contact angle of indium on Si (111) at 350 °C is 125°.[41] This difference has two consequences. First, for a given amount of metal, the contact area with silicon will be smaller with indium than with gold. This way, smaller nanowires will grow when catalyzed by droplets of indium than when catalyzed by droplets of gold of the same volume. Second, this difference may explain the existence of the Si-IV phase in silicon nanowires grown with indium catalyst. Indeed, as mentioned in section 3.1, the crystalline structure of the wires is determined by the balance between two components of the free energy: the interfacial tension between the catalyst droplet and the wire and the surface tension at the edges of the growth region of the nanowire. Measurement of the contact angle between Si-IV and indium or calculation of their

[40] Ressel et al., "Wetting of Si surfaces by Au–Si liquid alloys", 2003 [Res+03]
[41] Mattila et al., "Catalyst-free growth of In(As)P nanowires on silicon", 2006 [Mat+06]

interfacial tension would be required to confirm this hypothesis.

4.4.3 Effect of the hydrogen plasma treatment on the substrate

Superficial reduction of transparent conductive oxides has been extensively studied in order to avoid it. Indeed, it was considered a major problem for thin film solar cells because it leads to the incorporation of metal atoms in the silicon layer. These atoms eventually induce shortening of the devices or recombinations[42] Among common TCOs, ITO has been found to be the most sensitive to reduction by hydrogen plasmas, while ZnO remains stable up to 250 °C and SnO_2 has an intermediate reactivity.[43] Significant degradation of ITO when exposed to H_2 plasma occurs from 200 °C on. At 300 °C, it starts after less than 1 min of exposure.[44]

Here this superficial reduction of ITO is an advantage, as it provides metallic indium to catalyze the growth of silicon nanowires. Nevertheless, it is important to check that the electrical and optical properties of the substrates are not significantly damaged during the process. This has been done by exposing ITO samples to H_2 plasma treatment only. As the low pressure plasma (181 mTorr) is not very stable, these experiments have been done at higher pressure (1 Torr). This way, the indicated degradation is an upper limit. Indeed, under given conditions, the flux of atomic hydrogen to the substrate is almost doubled when the pressure is multiplied by 3.[45] That means that samples were exposed here to an hydrogen flux three times as high as in the growth experiments presented above.

The evolution of the absorbance of ITO upon H_2 plasma treatment is shown on fig. 4.21. After short or low-temperature plasma treatments, the increase in absorbance is small. But after 2 min plasma treatment at temperatures higher than 250 °C, the absorbance is twice as much as for pristine ITO.

According to previous studies,[46] composition of the ITO layer after exposure to H_2 treatment is unchanged at 10 nm from the surface. So the increase in absorbance does not come from a change in the "bulk" of ITO, but only in its surface. SEM images show that metallic droplets are formed on the surface after exposure to H_2 plasma. Absorption and diffraction of light by these droplets induce the observed increase in absorbance. The size and density of these droplets depend heavily on how long the treatment was. For a 30 s plasma treatment at 250 °C, the average diameter is 8.3 nm and the number density of droplets is about 4000 μm^{-2} (fig. 4.22a). For a 2 min plasma treatment, the average diameter is 0.2 µm and the number density of droplets

[42] Cabarrocas et al., "Improving tin oxide/hydrogenated amorphous silicon interfaces for solar cell applications", 1990 [Cab+90]

[43] Drevillon et al., "In situ investigation of the optoelectronic properties of transparent conducting oxide/amorphous silicon interfaces", 1989 [Dre+89]

[44] Kuboi, "Degradation of ITO Film in Glow-Discharge Plasma", 1981 [Kub81]

[45] Novikova et al., "Numerical modeling of capacitively coupled hydrogen plasmas: Effects of frequency and pressure", 2003 [Nov+03]

[46] Banerjee et al., "Degradation of tin-doped indium-oxide film in hydrogen and argon plasma", 1987 [Ban+87]

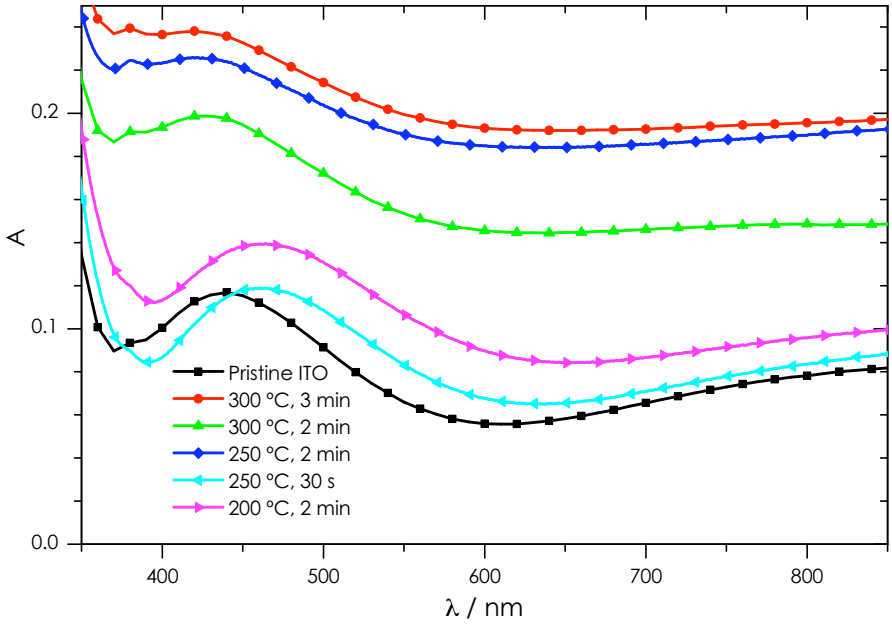

Figure 4.21 – *Absorption spectra of ITO samples after treatment by H_2 plasmas at various substrate temperatures and for various durations*

is $0.3\,\mu m^{-2}$ (fig. 4.22b). So the first treatment condition, which leads to little increase in absorbance, fits also best the requirements for a dense layer of small nanowires. In addition, as the metallic droplets are incorporated in the brush of nanowires during the growth, the effective increase in absorbance by the substrate is expected to be significantly lower than the values reported here.

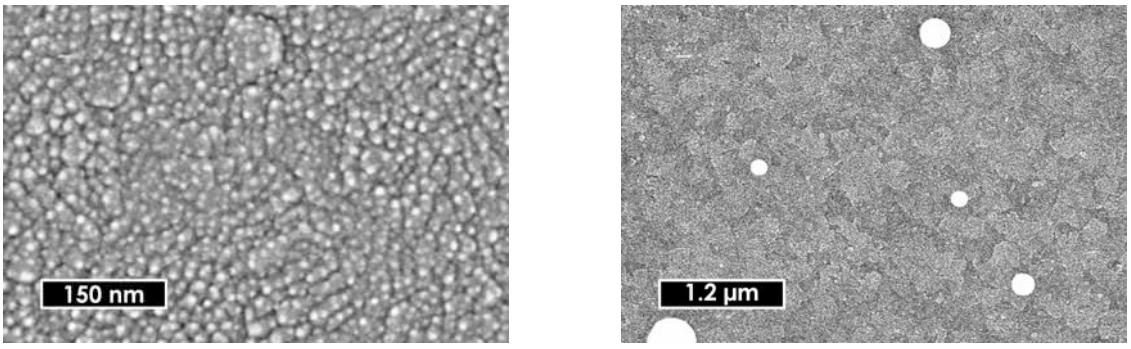

(a) *30*s *plasma treatment* **(b)** *2*min *plasma treatment*

Figure 4.22 – *SEM images of ITO samples treated by H_2 plasma at 250*°C *in PLASFIL*

Finally, the increase in sheet resistance of the ITO layer is also limited. The square resistance of pristine ITO samples is $10\,\Omega/\square$. After 30 s of H_2 treatment at 250 °C, it is increased to $14\,\Omega/\square$. After 2 min, it is $16\,\Omega/\square$. If ITO samples after H_2 plasma treatment are not as performant as originally, they still have good enough electrical and optical

performance to be used in devices.

4.4.4 Effects of the treatment time on the size and density of the wires

The size and density of the nanowires grown by this process follow the same trend as for the metallic droplets. Here the H_2 plasma treatment was done at $p = 181$ mTorr, so the reduction was slower than in the previous paragraph.

When H_2 plasma treatments are long, large aggregates (several µm in diameter) are formed. They still seem to catalyze the growth of some structures with a very poor aspect ratio. Between them, a low density ($0.08\,\mu m^{-2}$) of nanowires has grown (fig. 4.23). For a 2 min H_2 plasma treatment, the number density of nanowires is increased to $1.3\,\mu m^{-2}$, for a 1 min treatment, it is $0.9\,\mu m^{-2}$ and for a 30 s treatment, it raises to $73\,\mu m^{-2}$ (fig. 4.24). The similar number density obtained with treatment times between 1 min and 2 min is surprising. Yet it is consistent with absorption measurements, which show similar absorbance for samples treated for 1 min and 2 min by H_2 plasma.

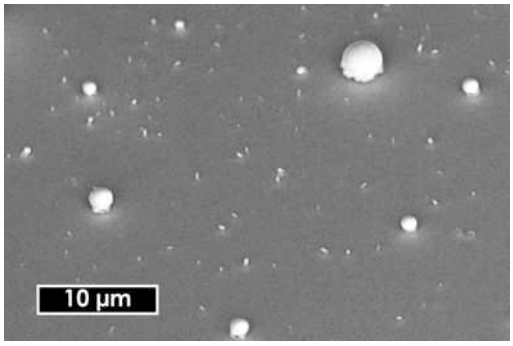

Figure 4.23 – *SEM image of a layer obtained by a 10*min *H_2 plasma treatment followed by 15*min *SiH_4 deposition plasma at 300*°C

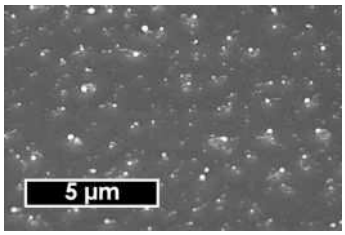

(a) *2*min *H_2 plasma treatment*

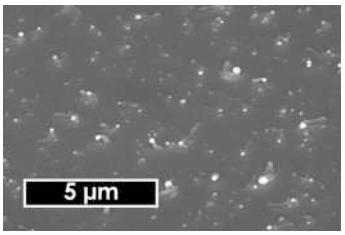

(b) *1*min *H_2 plasma treatment*

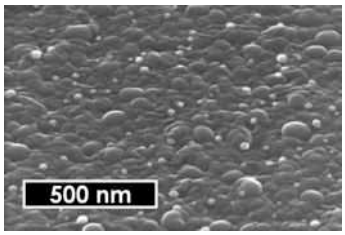

(c) *30*s *H_2 plasma treatment*

Figure 4.24 – *SEM images of layers deposited by H_2 plasma treatment (various durations) followed by 15*min *SiH_4 deposition plasma at 300*°C

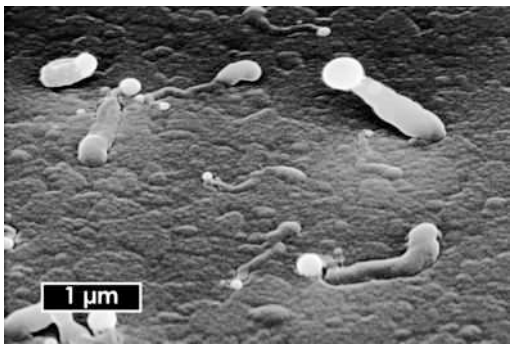

Figure 4.25 – *SEM image of nanowires grown on ITO in PLASFIL (300°C, 5min of H_2 plasma treatment at 1Torr, 15min of SiH_4 deposition plasma). Some of them are creeping on the surface, some of them are standing*

4.4.5 Creeping or standing nanowires?

On the SEM images shown above, some wires did not grow straight and perpendicular to the substrate. They are rather creeping on the surface, although similar growth conditions could give rise to standing nanowires. A typical example of cohabitation between the two kinds of nanowires is shown on fig. 4.25. Obtaining creeping nanowires instead of standing ones has been a major concern in the quest of reproducibility.

Creeping nanowires not only lie on the surface, they are also partly embedded in it (fig. 4.26a). The gap between their edges and the surrounding amorphous surface indicates that this layer is not deposited after the wires, but in the same time or even before. More precisely, the amorphous layer seems to be etched by the catalyst droplet (fig. 4.26b). In a still unpublished work, Linwei Yu has shown that it is indeed the case. He covered In particles (created by superficial reduction of ITO) by a thin a-Si:H layer and then annealed the sample at 500 °C in an SEM. This way, he could follow the evolution of single In droplets. They happen to diffuse at the surface of the layer and to dissolve a-Si:H around them while silicon precipitates as crystalline nanowires behind them. So creeping nanowires grow indeed in-plane, through a "Solid-Liquid-Solid" mechanism where the catalyst moves instead of the precursors!

Another surprising feature on fig. 4.26 is the bending of some silicon nanowires, which started to grow out-of-plane and then turned back to creep on the surface. What is the driving force behind that? Catalyst droplets have been reported to get charged during the VLS growth of silicon nanowires.[47] This charge can eventually lead them to exploding. In our case, the nanowires are grown by PECVD, and there is a strong electric field across the sheath, oriented from the plasma to the electrodes (and the substrate). A possible explanation to the strong bending of these nanowires could be the effect of this strong electric field on charged In catalyst droplets.

One question remains: why do nanowires grown at 300 °C in PLASFIL sometimes

[47] Cao et al., "Instability and Transport of Metal Catalyst in the Growth of Tapered Silicon Nanowires", 2006 [Cao+06]

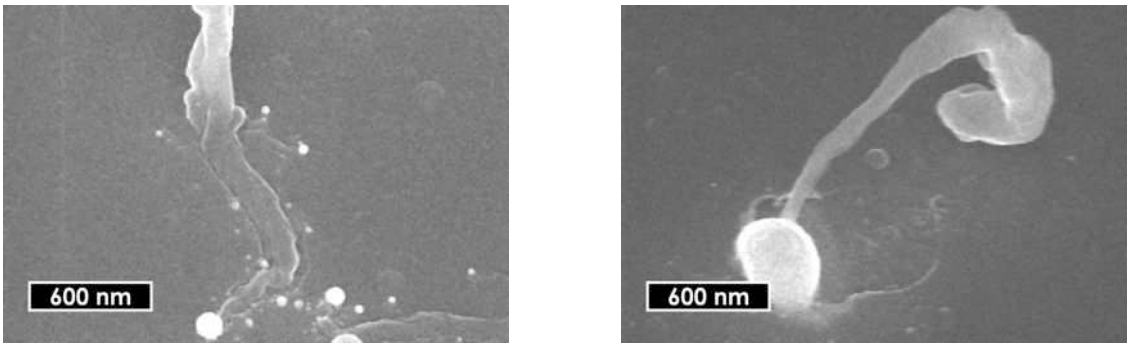

(a) *1*min *of H_2 plasma treatment* **(b)** *1*min *30*s *of H_2 plasma treatment*

Figure 4.26 – *SEM images of creeping nanowires grown in PLASFIL at 300*°C *(H_2 plasma treatment at 1*Torr*, 15*min *SiH_4 deposition plasma*

are standing on the substrate, sometimes are creeping? It seems that this problem comes from variations in the substrate temperature. Indeed, indium aggregates have been reported to be covered by a-Si:H deposited by PECVD at 200 °C.[48] In addition, deposition in ARCAM at a well controled temperature of 250 °C leads to creeping nanowires (fig. 4.27a), which are very similar to what can be obtained in PLASFIL at a setup temperature of 300 °C. This is consistent with the measured sample surface temperature in PLASFIL (between 249 °C and 254 °C under SiH_4 flow). The discrepancy between the setup and the actual surface temperature, mentioned in appendix A, is likely to have increased over time. Indeed, parasitic deposition of a-Si:H on the substrate holder increases the thermal resistance between the heater and the substrate from run to run. When the substrate temperature in PLASFIL is increased to 350 °C (fig. 4.27b) then to 600 °C (fig. 4.27c), standing nanowires become more and more dominant. Hence there is a critical temperature between 250 °C and 300 °C at which the growth rate for indium-catalyzed nanowires becomes larger than for a-Si:H. As indium has negligible catalytic activity for the dissociation of SiH_4, this temperature dependence must come from the diffusion coefficient of silicon in liquid indium.

Summary and outlook

We are now able to grow two different kinds of nanostructured silicon layers. Both of them are original structures. The first one is sponge-like. It is grown at temperatures as low as 175 °C. The most efficient procedure is based on μc-Si plasmas and thin evaporated copper layers as catalysts. Surprisingly, H_2 plasma pre-treatment reduces the efficiency of this process. In such layers, the metal remains confined at the interface between ITO and silicon. This reduces the chance of charge recombination in devices.

[48] Hirao et al., "Coagulation of In Atoms in Hydrogenated Amorphous Silicon Islands Deposited on ITO Films", 1988 [Hir+88]

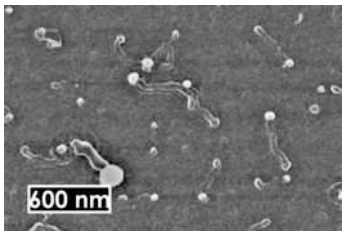

(a) *Growth in ARCAM at 250°C (Cu-coated ITO sample)*

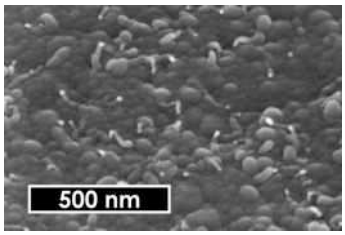

(b) *Growth in PLASFIL at 350°C (5min H_2 plasma treatment at 300°C)*

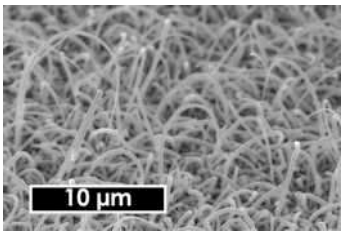

(c) *Growth in PLASFIL at 600°C (5min H_2 plasma treatment at 250°C)*

Figure 4.27 – *SEM images of silicon nanowires grown on ITO at various temperatures.*

The second kind of layers is made of silicon nanowires grown at temperatures above 250 °C without external catalysts. This is the first time such a process is reported. The growth is catalyzed by indium droplets which are created *in-situ* by superficial reduction of ITO by H_2 plasmas. Similar layers can also be obtained on SnO_2. The size and density of the nanowires are controlled by the duration of the H_2 plasma treatment. When the pressure in the reactor is 1 Torr, this duration should be less than 1 min for the indium droplets to be small enough. After such a treatment, the optical and electrical properties of ITO are still reasonably good.

The wires are single crystals, either with cubic or wurtzite (hexagonal) structure. They include a large amount of metal, especially tin, which does not precipitate. This growth of nanowires catalyzed by metallic droplets from the superficially reduced substrate can occur in parallel to the first kind of growth. It is a good explanation for many surprising observations made on layers grown with evaporated catalysts.

The next step is now to try and include such nanostructured silicon layers in hybrid solar cells and to investigate their potential assets as compared to flat layers.

Realization of nano-structured photovoltaic devices

5

Caminante, no hay camino,
se hace camino al andar.

Antonio Machado, *Campos de Castilla*

Contents

BILAYER solar cells based on thin-film silicon and P3HT have been studied in the first two chapters, and their fabrication process has been improved. In the last two chapters, we investigated how to grow nano-structured silicon layers on ITO. We managed to grow silicon nanowires by thermal CVD on this substrate, and we presented a catalyst-free method to grow silicon nano-pillars. In addition, we developed two

new PECVD processes to grow silicon “nano-sponges” (with Cu as catalyst) and silicon nanowires (without external catalyst). These layers have various aspect ratios and characteristic sizes. They should therefore allow to investigate the effect of the nano-structure on the performance of solar cells.

In this chapter, we will then investigate how to adapt the fabrication process to these layers. We will study the electrical response of devices based on three kinds of silicon layers (nano-pillars, CVD-grown nanowires and PECVD-grown nanowires), and compare them with bilayer cells. Finally, we will discuss our results in the light of recently published works by other groups, and we will present some possible ways for further investigation on this topic.

5.1 Deposition of the active layer

5.1.1 Deposition of the polymer layer

Position of the problem

In the bilayer devices presented in chapter 1, the polymer layer was spin-coated on top of the silicon thin films. This method is convenient, especially with small samples like ours, but it works best with homogeneous, smooth substrates. In particular, particles at the surface of the substrate lead to "comets" in the polymer layer, *i.e.*, holes extended perpendicular to the rotation axis during deposition. Nano-pillars layers (*cf.* section 4.1.2) have a RMS roughness of some tens of nm, which is of the same order of magnitude as the thickness of the polymer layer. Hence defects in P3HT are possible. The situation would be even worse on silicon nanowires.

In addition, spin-coating is a dynamic method. The deposited material has little time to organize and fill the porosity. Moreover, rotation of the substrate induces a fluid motion perpendicular to the pores or the nanowires. Therefore, the coverage of the silicon layer is likely not to be conformal. The problem of the deposition of the polymer layer may be schematically summarized on fig. 5.1

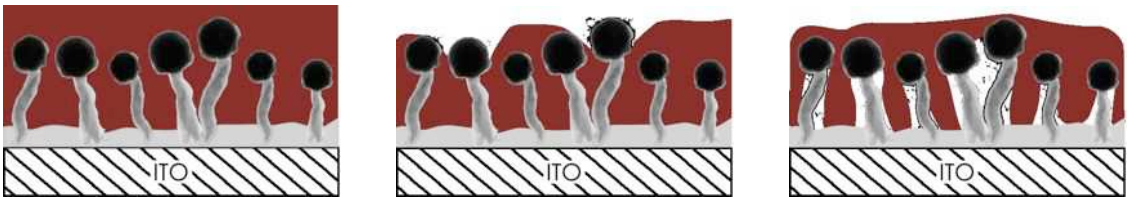

(a) *Goal: complete coverage of the silicon layer and smooth polymer top surface*

(b) *First possible issue: holes at the top of the polymer layer*

(c) *Second possible issue: incomplete infiltration of the silicon layer*

Figure 5.1 – *Schematic pictures of the problem of the infiltration of the nano-structured silicon layer by the polymer*

Two different methods have been investigated to prevent these issues. First, the spin-coated process has been adapted. Second, another deposition method, "doctor blade", has been used. In addition, short post-deposition annealing at 200°C (above the melting point of P3HT) has been tried in order to improve the infiltration of the silicon porous structure.

Spin-coating

Our approach for the deposition on silicon nanowires was to perform several subsequent spin-coating steps, and to increase the concentration of the solution at each step. Our hypothesis was that the less concentrated solutions would efficiently penetrate between the nanowires, while the more concentrated solutions would lead to

a thick layer on top of the nanowires. This approach was inefficient because the deposited polymer layers were partially re-dissolved during the deposition of the next ones. This eventually led to very inhomogeneous layers. In addition, this method did not prevent comets, nor did it ensure that all the nanowires were covered by the polymer. As a consequence, we moved to another deposition method: "doctor blade".

On the opposite, the nano-pillars were successfully covered by spin-coated polymer layers, even with the initial process parameters as described in section 1.1.4.

Doctor blade

"Doctor blade" is a thin film deposition method from a liquid solution. Whereas by spin-coating the solution is spread and dried by the rotation of the substrate, here the substrate is fixed and the solution is spread by a motorized metallic blade. A diagram of this method is shown on fig. 5.2. The samples are maintained by a depression created by a small diaphragm pump through porous spots in the substrate holder. The substrate holder can also be heated to control the evaporation of the solvent.

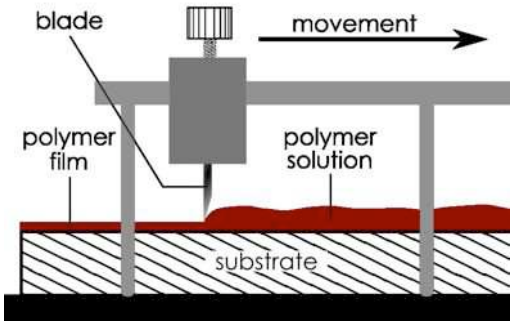

Figure 5.2 – *Diagram of the deposition of a polymer thin film by doctor blade.*

Parameters controlling the thickness and the quality of the polymer layer are: the substrate temperature, the horizontal speed of the blade, the distance between the blade and the substrate, the solvent (viscosity and boiling point), the solution concentration. Before experimenting this method on silicon layer, we investigated the effect of these parameters on glass substrates. It appeared that, as for spin-coating, substrate cleaning was of major importance. We found the best cleaning process for glass to be:

1. Soaking in warm soapy water
2. Rinsing with warm water
3. Rinsing with deionized water at room temperature and drying with N_2
4. 10 min ultrasonic bath in isopropanol
5. 10 min ultrasonic bath in acetone and drying with N_2

The thicknesses of polymer layers deposited on glass with P3HT at $15\,\mathrm{g\,L^{-1}}$ in ortho-dichlorobenzene are shown on tab. 5.1. The best homogeneity of the film (not quantified on the table) has been obtained when the polymer solution dries at the same speed as the blade moves ($T_{\mathrm{sub}} = 80\,^{\circ}\mathrm{C}$, $v_{\mathrm{blade}} = 5\,\mathrm{mm\,s^{-1}}$).

$T_{\mathrm{sub}}/^{\circ}\mathrm{C}$	$h_{\mathrm{blade}}/\mu\mathrm{m}$	$v_{\mathrm{blade}}/\mathrm{mm\,s^{-1}}$	e/nm
70	50	5	30
70	100	2.5	15
70	100	5	18
70	100	20	64
80	100	5	22
80	100	20	35

Table 5.1 – *Influence of doctor blade deposition parameters on the thickness of the polymer layer*

A larger distance (250 µm) between the blade and the substrate has been used for the deposition of P3HT on silicon nanowires to get a thicker layer (70 nm).

5.1.2 Deposition of the silicon layer

Three kinds of nano-structured silicon layers have been investigated in hybrid solar cells: nanowires grown by CVD (*cf.* section 3.3), nanowires grown by PECVD (*cf.* section 4.4),[1] and nano-pillars (*cf.* section 4.1.2). The latter was generally deposited on an intermediate n-doped a-Si:H layer on ITO, and the deposition time was 18 min. A thin layer (about 10 nm) of intrinsic a-Si:H has been deposited on top of these layers to make them more stable against oxidation, and hopefully to increase the open-circuit voltage (V_{oc}). For nano-pillars and CVD-grown nanowires, the samples needed to be transferred from one reactor to another before the a-Si:H layer could be grown, so they have been treated by a 5 min H_2 plasma[2] in ARCAM to remove surface contamination and oxide. This treatment and the deposition of a-Si:H leads to a decrease in the roughness of the nano-pillars layer. The one-dimensional arithmetic roughness R_a, as measured by a profile meter,[3] decreases from 24 Å to 12 Å.

[1] H_2 plasma treatment of the substrate: 100 sccm of H_2, $p = 260$ mTorr, $P_{RF} = 5$ W, $T_{\mathrm{sub}} = 300\,^{\circ}\mathrm{C}$, 8 min; growth plasma: 10 sccm of SiH_4, $p = 56$ mTorr, $P_{RF} = 2$ W, $T_{\mathrm{sub}} = 200\,^{\circ}\mathrm{C}$,15 min

[2] 100 sccm of H_2, $p = 1$ Torr, $P_{RF} = 5$ W

[3] AlphaStep IQ; scanned length: 0.5 mm; scanning speed: $50\,\mu\mathrm{m\,s^{-1}}$; cutting length: 8 µm

5.2 Performance of devices

5.2.1 Devices based on silicon nanowires

Typical J-V characteristics of a device based on CVD-grown silicon nanowires are shown on fig. 5.3. The rectifying ratio is very poor. Surprisingly, this does not seem to come from shorts, as the shunt resistance is 17 MΩ, but rather from an inefficient charge collection under direct bias ($R_s = 6\,\mathrm{M\Omega}$). The most probable explanation is the degradation of the bottom electrode (ZnO) during the growth of the silicon nanowires. Under illumination, a small photo-current is visible: $J_{sc} = 0.1\,\mu\mathrm{A\,cm^{-2}}$, which is three orders of magnitude lower than the typical bilayer devices based on a-Si:H layers (*cf.* section 2.1). The J-V curves in dark and under illumination cross each other at $V = 0.4\,\mathrm{V}$. This indicates some photo-conductivity effect, either in the polymer or the silicon layer.

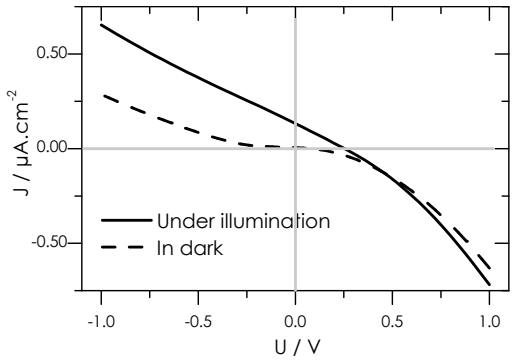

Figure 5.3 – *J-V characteristics of solar cells based on CVD-grown silicon nanowires (substrate: ZnO, catalyst: copper)*

The layer of silicon nanowires is denser and more uniform when it is grown by PECVD than by CVD. Nevertheless, almost all devices based on PECVD-grown silicon nanowires had ohmic J-V characteristics in dark and under illumination, even when the polymer layer was deposited by "doctor blade". As measured current densities at $-1\,\mathrm{V}$ are as high as $1\,\mathrm{A\,cm^{-2}}$, most wires must be in direct contact with the top electrode. As a consequence, the thickness of the P3HT layer should be significantly larger than the current values. But then the performance of the devices may be limited by recombination losses in the polymer. On one device, still, a significant photovoltaic action has been observed ($J_{sc} = 0.25\,\mathrm{mA\,cm^{-2}}$), but with almost no rectification (fig. 5.4).

5.2.2 Devices based on silicon nano-pillars

The performance of devices based on rough micro-crystalline silicon (silicon nano-pillars) with gold as the top electrode[4] was comparable to that of bilayer devices,

[4]These devices were made after the new design as described in section 2.2.1

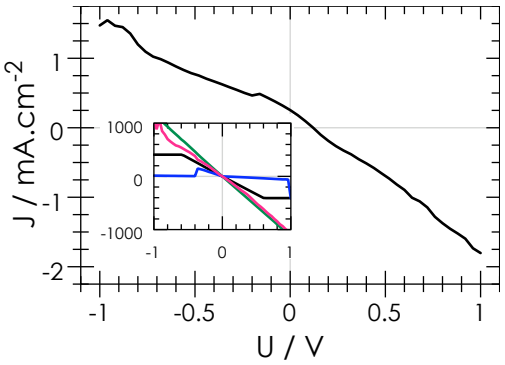

Figure 5.4 – *J-V characteristic under illumination of devices based on PECVD-grown silicon nanowires and spin-coated P3HT (layer thickness: 115*nm*). Main curve: 0.196*cm^2 *cell with photovoltaic action; insets: cells with ohmic characteristics.*

and the homogeneity of the results was good. The average open-circuit voltage was 539 mV (standard deviation: 49 mV) and the average short-circuit current density was 0.243 mA cm^{-2} (standard deviation: 0.035 mA cm^{-2}). In spite of a good fill factor (53.9% on average), the power conversion efficiency is small (0.07% on average). These devices have still two major differences with respect to bilayer devices: the respective contribution by the layers and the effect of annealing.

Contribution of materials

Comparison between the external quantum efficiency and the respective absorption spectra of the silicon and polymer layers (fig. 5.5) shows that only P3HT contributes to the photo-current. From a quantitative point of view, this phenomenon is characterized by an almost perfect correlation between the EQE and the optical density of P3HT (0.95), while the correlation between the EQE and the absorption spectrum of the silicon layer is very low (-0.13). As a comparison, the correlation between the EQE of an optimized bilayer device based on a-Si:H (*cf.* section 1.4) and the absorption spectrum of P3HT is 0.66.

This behavior is easily understood by looking at the band diagram of the device (fig. 5.6). The interface between a-Si:H(i) and P3HT is shown in flat-band condition, as we have no evidence of band bending. On that diagram, it appears that the a-Si:H(i) layer blocks desirable hole transfer, as well as undesirable electron transfer from the micro-crystalline silicon layer to P3HT. On the other side, electrons can still be transferred from P3HT (the electron donor) to silicon (the acceptor). As a consequence, only excitons generated in P3HT can contribute to the photo-current. At first glance, this phenomenon seems to be a major drawback. Indeed, to make efficient devices, it will be necessary to remove the a-Si:H(i) layer. But for more fundamental studies, this blocking layer is very interesting. Indeed, it allows to study the dissociation of excitons generated in P3HT and the collection of associated charge carriers, independently from the generation in silicon. This structure is therefore a valuable tool to

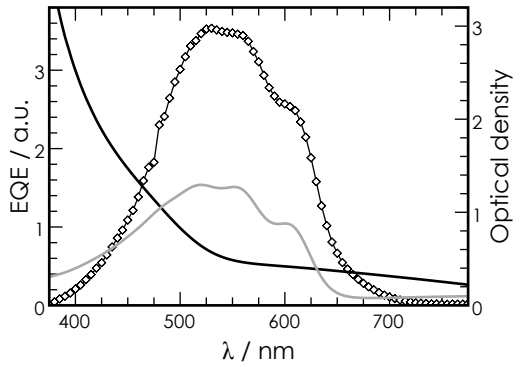

Figure 5.5 – *External quantum efficiency of a device based on silicon nano-pillars and P3HT, with gold as the top electrode; absorption spectra of the layers are given for comparison. Black line: optical density of the silicon layer. Grey line: optical density of P3HT on ITO. Diamonds: external quantum efficiency.*

evaluate the improvement due to changes in the interface morphology (in particular, increase in the interface area).

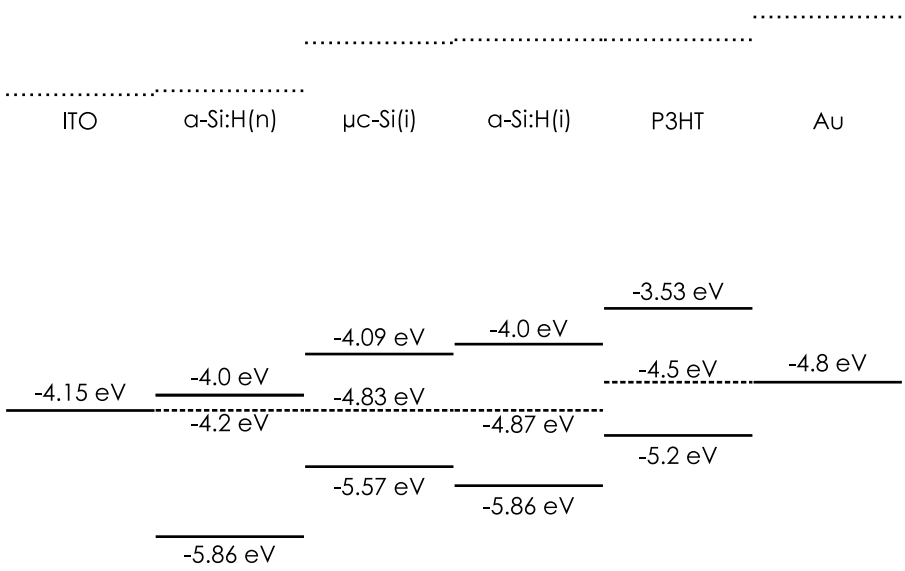

Figure 5.6 – *Tentative band diagram of devices based on silicon nano-pillars*

Effect of annealing

The other major difference between bilayer devices and cells based on silicon nano-pillars is the dramatic effect annealing has on the latter. This is shown on fig. 5.7, where J-V characteristics of devices with Pd/Ag top electrodes are plotted. When the inorganic layer is made of amorphous silicon only (fig. 5.7a), annealing[5] leads to a

[5] 30 s at 200 °C under nitrogen in a glove-box

small increase in fill factor (five points) and short-circuit current density (+5%), but the open-circuit voltage is significantly reduced (-18%). As a result, the power conversion efficiency remains unchanged. At the opposite, when the inorganic layer is based on silicon nano-pillars (fig. 5.7b), all the device output parameters are significantly increased upon annealing: open-circuit voltage (+5%), short-circuit current density (+30%) and fill factor (+88%). As a result, the power conversion efficiency after annealing is three times as much as before.

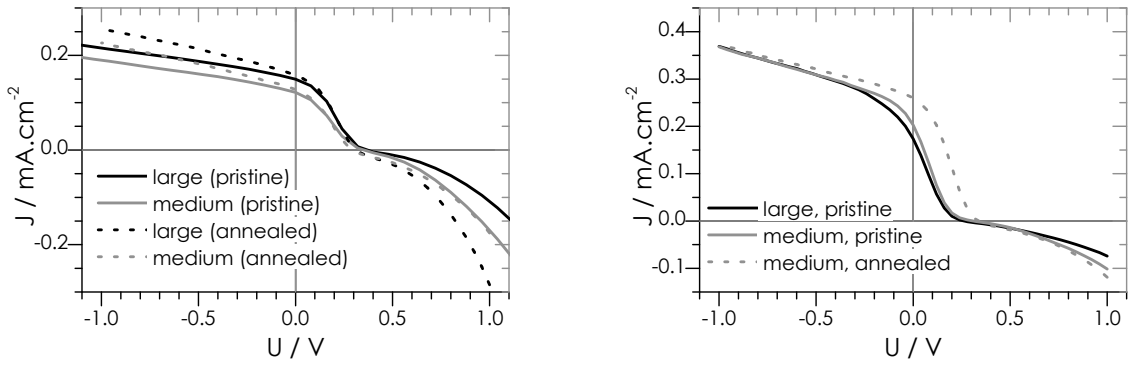

(a) *Silicon layer: a-Si:H(n)/a-Si:H(i)*

(b) *Silicon layer: a-Si:H(n)/Si nano-pillars/a-Si:H(i)*

Figure 5.7 – *J-V characteristics under illumination of hybrid devices with Pd/Ag top electrodes ("large" cells: 0.196*cm^2*; "medium" cells: 0.071*cm^2*)*

The effect of similar annealing is even more striking when the top electrode is gold (fig. 5.8). With devices based on silicon nano-pillars grown on an intermediate a-Si:H(n) layer on ITO, the S-shaped J-V characteristics are transformed into good rectifying diode characteristics (fig. 5.8a). In that case, the fill factor is increased from less than 47% to 58%. The J_{sc} and V_{oc} are also increased, and the power conversion efficiency is consequently enhanced by 50%. In addition, the performance of cells with various active areas is more homogeneous after annealing than before. S-shaped characteristics have been shown in section 2.4 to come from defective contact between P3HT and the evaporated top electrode. The short annealing at high temperature should hence enhance this contact. The mechanism for this improvement is still unclear. Possible explanations include:

- A better morphology at the interface, which could for example reduce voids between P3HT and the metal.
- Chemical reaction between P3HT (in particular, sulphur atoms) and gold.
- Change in the work function of P3HT because of crystallization.

When the substrate is ZnO and no intermediate a-Si:H(n) layer is used, the short-circuit current density is increased by up to 64% upon annealing (fig. 5.8b). As the

open-circuit voltage and the fill factor are also enhanced, the power conversion efficiency is increased by 86%. In that case, the improvement may be explained by the polymer filling the silicon layer in a more conformal way after melting.

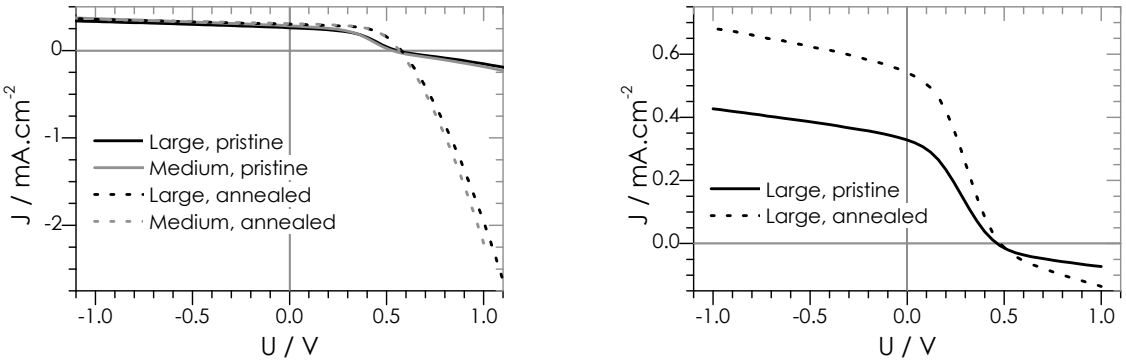

(a) *On ITO, with an a-Si:H(n) intermediate layer*

(b) *On ZnO, without an a-Si:H(n) intermediate layer*

Figure 5.8 – *J-V characteristics under illumination of hybrid devices based on silicon nanopillars with Au as the top electrode*

5.3 Discussion and outlook

The work presented in this thesis is exploratory. We will discuss in this section some possibilities for further investigations and some recent works which may be inspiring. Our focus will be on devices. As mentioned in chapter 1, hetero-junctions between silicon and organic materials are not widely investigated. Personal discussions have shown that several groups have at some point studied such systems, but not necessarily advertised much about this research. Solar cells based on hetero-junctions between crystalline or thin-film silicon and polymers have been recently studied in a sustained way by two groups: Michael McGehee's at Stanford University (especially Vignesh Gowrishankar) and Eric Schiff's at Syracuse University (especially Weining Wang). In addition, some more isolated works have been reported and new projects have been recently initiated on this topic (*e.g.*, by a German consortium led by IPHT Iena).

5.3.1 Performance and analysis of the devices

The closest work to ours is by Gowrishankar *et al.*, who studied solar cells based on two polymer semiconductors (MEH-PPV and P3HT) and flat[6] or nano-structured[7]

[6] Gowrishankar et al., "Exciton splitting and carrier transport across the amorphous-silicon/polymer solar cell interface", 2006 [Gow+06b]

[7] Gowrishankar et al., "Exciton harvesting, charge transfer, and charge-carrier transport in amorphous-silicon nanopillar/polymer hybrid solar cells", 2008 [Gow+08]

layers of hydrogenated amorphous silicon. They also compared them with similar devices based on titania instead of a-Si:H. The structure of their devices was very similar to what has been used in this work: the silicon layer was deposited on ITO-coated glass by Hot-Wire CVD (HWCVD) and its thickness was 20 nm for bilayer devices; the polymer layer was spin-coated and its thickness was 60 nm. Surprisingly, the evaporated top electrode was of silver. The performance of their bilayer devices were very similar to our typical cells: they reported a J_{sc} of 0.64 mA cm^{-2}, a V_{oc} of 555 mV, a fill factor of 57%, and a global power conversion efficiency of 0.20% with P3HT. Much poorer performance were obtained with MEH-PPV.

Their work evidenced two mechanisms to transfer excitons generated in the polymer to a-Si:H: (i) exciton diffusion to the interface and electron transfer to silicon, and (ii) Förster energy transfer to a-Si:H followed by hole transfer to the polymer. In the case of P3HT, the former mechanism accounts for about 70% of the quenched excitons and the latter for about 30%. The contribution by a-Si:H to the photocurrent was low in both cases: at most (with P3HT) 3% of photons absorbed in a-Si:H contributed. This was attributed to poor hole transfer, which can be explained by (i) localization of holes away from the interface due to the low density of occupied valence bandtail states under one-sun illumination, and (ii) a small (<0.1 eV) drop in energy at the interface between the hole quasi-Fermi level in a-Si:H (0.5 eV above E_v) and the HOMO of P3HT.

In section 2.4, we already mentioned that the deep HOMO of P3HT (−4.7 eV to −5.2 eV) was an issue to obtain an ohmic contact with the top electrode. The work by Gowrishankar *et al.* shows that it is also an issue for charge transfer from silicon to P3HT in a p-i-n structure. Therefore, *a major way to improve the performance of hybrid silicon/organic solar cells with this structure would be to replace P3HT by an organic semiconductor with a more shallow HOMO.*

When the a-Si:H layer was nano-structured by block-copolymer lithography and reactive ion etching (RIE),[8] the short-circuit current density was significantly increased to 1.23 mA cm^{-2} and the power conversion efficiency was doubled as compared to flat bilayer devices. In that case, the pores in the silicon layer were about 30 nm to 40 nm wide and their height was about 80 nm. The authors estimated that about 35% of excitons generated in the polymer embedded in the pores could reach the interface with silicon. Hence, there is space for a large increase in the efficiency of the devices by decreasing the size of the pores. In that sense, *Cu-catalyzed "nano-sponge" silicon layer (presented in section 4.2), whose typical pore size is about 15*nm*, is a very promising candidate for hybrid devices. In addition, it is fabricated in a much more straightforward and simple way than the nano-structured a-Si:H layer used by Gowrishankar et al.*

Schiff *et al.* have studied devices based on thin-film silicon and p-type, highly

[8]Gowrishankar et al., "Fabrication of densely packed, well-ordered, high-aspect-ratio silicon nanopillars over large areas using block copolymer lithography", 2006 [Gow+06a]

doped polymers: PEDOT:PSS[9] and polyaniline[10] (PANI). When the silicon thin films[11] were deposited on top of spin-coated PEDOT:PSS by HWCVD, the performance of the devices was stronger than even our best cells. The major difference lied in the V_{oc} they obtained, which was 883 mV, whereas it was at most 730 mV in our cells. This value was slightly larger than for all-silicon cells. An analysis based on device modeling by AMPS software[12] has shown that the PEDOT:PSS layer behaves as an ideal p-type layer.

Wang *et al.* evidenced a logarithmic dependence of the V_{oc} on the conductivity of PANI. This is consistent with common assumptions that (i) the conductivity of the polymer depends exponentially on the position of its Fermi level with respect to its valence band edge[13] and (ii) V_{oc} is the measurement of the difference between the Fermi level in the polymer and the electron quasi-Fermi level in the intrinsic silicon layer under illumination. Nonetheless, when the polymer layer (either PANI or PEDOT:PSS) was spin-coated on top of a-Si:H, the maximum open-circuit voltage was 0.72 V to 0.75 V, which is very similar to our best cells. This polymer-independent maximum could be attributed to interface effects with a-Si:H, in the same way as the saturation of V_{oc} for c-Si/PANI solar cells was attributed to crystalline silicon surface states.[14]

Deposition of silicon on top of the polymer layer seems therefore to be an asset. An additional advantage would be an easier contact to the electrodes (aluminum could be used as the evaporated top electrode on silicon). We investigated some cells based on such structure[15] with a silicon layer deposited by PECVD at very low temperature (80 °C) in order not to degrade P3HT. We did not observe any improvement in the V_{oc}. In addition, the J_{sc} and FF were lower than for our usual cells. A possible explanation could be the lower quality of a-Si:H when deposited at 80 °C instead of 200 °C. Moreover, deposition on top of the polymer is not an option when the silicon layer is to be nano-structured. So it seems that *structures based on polymer layers covered by silicon are of little interest to improve the efficiency of hybrid devices.*

These works by Schiff *et al.* did not mention any contribution by the polymer layer to the photo-current; they only focused on its influence on the V_{oc}. Their conclusion was pessimistic on the industrial relevance of PANI associated to a-Si:H. The conclusions by Gowrishankar *et al.* were also pessimistic on the potential of a-Si:H in hybrid devices, as they could not outperform titania-based cells, even with their best nano-structured a-Si:H layers. Finally, the only results reported so far of cells based on a brush of silicon nanowires (length: 5 µm, diameter: 100 nm) covered by a p-type polymer (poly(9,9-diethylfluorene) or PDEF) were quite disappointing: $V_{oc} = 156$ mV, $J_{sc} =$

[9] Williams et al., "Conducting polymer and hydrogenated amorphous silicon hybrid solar cells", 2005 [Wil+05]

[10] Wang, Schiff, and Wang, "Amorphous silicon/polyaniline heterojunction solar cells: Fermi levels and open-circuit voltages", 2008 [WSW08]

[11] 130 nm of a-Si:H(i), 40 nm of μc-Si(i) and 20 nm of μc-Si(n)

[12] Analysis of Microelectronic and Photonic Structures, http://www.cneu.psu.edu/amps/

[13] $\sigma = \sigma_{00} \exp\left[-\left(E_f^{\text{PANI}} - E_v^{\text{PANI}}\right)/k_B T\right]$

[14] Wang and Schiff, "Polyaniline on crystalline silicon heterojunction solar cells", 2007 [WS07]

[15] ITO/PEDOT:PSS/P3HT/a-Si:H(i)/a-Si:H(n)/Al

$5.9 \times 10^{-2}\,\mathrm{mA\,cm^{-2}}$, $FF = 32\%$.[16] After correction by the low intensity ($25.5\,\mathrm{mW\,cm^{-2}}$) of the light used by the authors to characterize their devices, this is very similar to our cells based on PECVD-grown silicon nanowires (fig. 5.4).

5.3.2 Interface engineering

If little work has been done on silicon/organic junctions, another kind of hybrid cells may be a source of inspiration for improvements: hetero-junctions between metal oxides (ZnO or TiO_2) and polymers. They indeed share several topics with the devices studied in our work: interface modification, characterization of the infiltration of pores by the polymer, improvement of the contact with the top electrode. Significant work on these topics has been done at Imperial College London (departments of physics and chemistry), Stanford University (department of materials science and engineering), and University of California in Santa Barbara.

Modification of the interface between the inorganic electron acceptor and the polymer had two goals in studies using metal oxides: to improve charge transfer and to increase the filling ratio of the pores by the polymer by decreasing the interfacial surface energy. Several groups investigated ruthenium complexes (fig. 5.9) previously used in dye-sensitized solar cells (DSSC). Some of these dyes are amphiphilic. Hence they enhance the wetting of the metal oxides, whose surface is polar, by the hydrophobic polymer solution. Bartholomew and Heeger have shown that sensitizing the surface of nano-structured TiO_2 surface could lead to a tenfold increase in the filling ratio by P3HT.[17] Ravirajan *et al.* have evidenced a relationship between the amphiphilic character of the dye and the increase in the short-circuit current density with ZnO.[18] *This is a clue for the increase in J_{sc}, as observed in section 5.2.2, to be actually due to an improved filling of the porous inorganic layer by the polymer.* This aspect of surface modification would be of little impact in our devices because the surface of the inorganic layer is made of hydrogenated silicon, which is already hydrophobic.

Nonetheless, all treatments to enhance the polymer incorporation in a porous inorganic layer, *e.g.*, annealing and surface modification, require some way to estimate their efficiency. Most groups only give indirect, qualitative characterization through the electrical performance of the devices. Interestingly, Bartholomew and Heeger have shown that Secondary Ions Mass Spectroscopy (SIMS) was a valuable tool to evaluate the polymer incorporation. Another possibility would be to use spectroscopic ellipsometry. Indeed, multi-layer and mixture modelings allow to estimate *e.g.*, the void fraction or the surface roughness of nano-structured silicon layers. For this approach to be successful, an accurate description of the dielectric function of individual materials is required. Campoy-Quiles *et al.* have shown that the standard

[16] Cheng et al., "Fabrication and electrical, photosensitive properties of p-poly(9,9-diethylfluorene)/n-silicon nanowire heterojunction", 2007 [Che+07]

[17] Bartholomew and Heeger, "Infiltration of Regioregular Poly[2,2-(3-hexylthiopene)] into Random Nanocrystalline TiO_2 Networks", 2005 [BH05]

[18] Ravirajan et al., "Hybrid polymer/zinc oxide photovoltaic devices with vertically oriented ZnO nanorods and an amphiphilic molecular interface layer", 2006 [Rav+06]

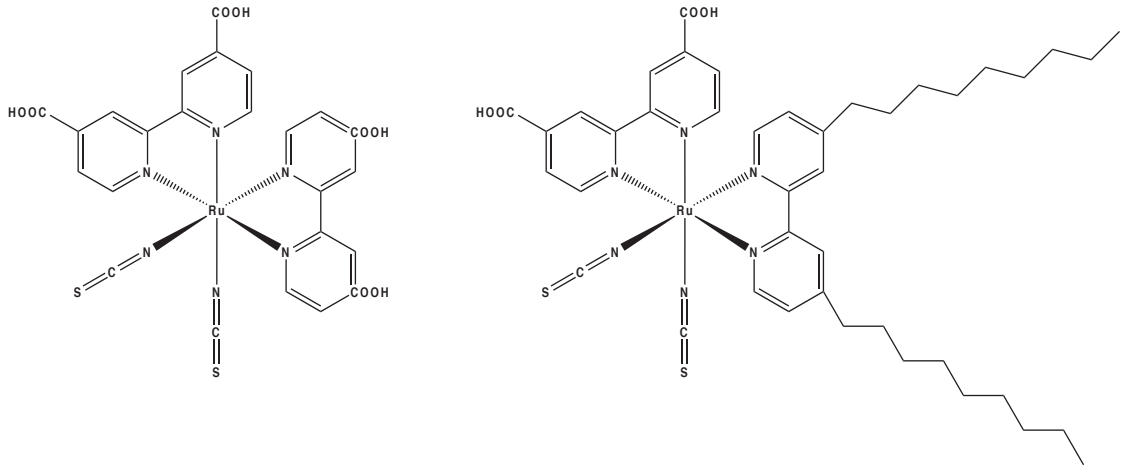

(a) *N3* **(b)** *Z907*

Figure 5.9 – *Dye molecules used as interface modifiers in hybrid solar cells*

critical point model describes best organic semiconductors:[19] it gives the best convergence with a given amount of parameters among the four models investigated, and the extracted parameters are physically meaningful. This model describes the dielectric function as:

$$\epsilon(E) = \epsilon_\infty + \sum_{i=1}^{N} \left[A_i e^{\jmath\phi_i} \left(E - E_{r,i} + \jmath\Gamma_i \right)^n \right]$$

This model is not available in our ellipsometry modeling software, which also limits the number of oscillators to four. Unfortunately, organic semiconductors have fine and asymmetric features in their absorption band. Modeling these features requires a large number of oscillators. That is why we could not obtain a model of the P3HT dielectric function which would allow a good description of ellipsometry measurements for various thicknesses of polymer on oxidized silicon. Hence *the best way to quantify the incorporation of P3HT in nano-structured silicon could be to use SIMS.*

The other aspect of surface modification by dye molecules is to enhance charge separation. This could happen in two ways: (i) Förster energy transfer from P3HT to the dye, followed by electron transfer from the dye to the inorganic semiconductor, and (ii) electron transfer from P3HT to the dye and from the dye to the inorganic semiconductor. The enhancement of charge transfer by the dye has been evidenced on ZnO with Z907 (fig. 5.9b) by Ravirajan *et al.* and on TiO_2 with N3 (fig. 5.9a) by Kudo *et al.*
citeKudo.APL.2007 In addition, ruthenium dyes have deeper HOMO than P3HT, so they prevent hole transfer from P3HT to the metal oxide. This is evidenced by a decrease in the dark current and a consequent increase in fill factor and V_{oc} as compared

[19] Campoy-Quiles et al., "Dimensionality of electronic excitations in organic semiconductors: A dielectric function approach", 2007 [CQ+07]

to devices based on bare metal oxides. These combined actions lead to a dramatic increase in the conversion efficiency when the dyes are introduced (up to fivefold). The LUMO of Z907 (−3.8 eV) lies between the LUMO of P3HT and the conduction band-edge of a-Si:H; its HOMO (−5.4 eV) lies between the HOMO of P3HT and the valence band-edge of a-Si:H. As a consequence, this dye could enhance electron transfer from P3HT to silicon and prevent holes in P3HT to reach the surface of silicon where they could recombine. But its HOMO level is below the reported hole quasi-Fermi level under illumination, so this dye would prevent significant contribution by silicon to the photo-current in devices where the intrinsic layer is a-Si:H.

Another class of surface modifiers has been proposed by Goh *et al.*[20] It is benzoic acid derivatives (fig. 5.10), which in their paper are attached to the surface of the metal oxide (TiO_2) by the acid group, and which bear a functional group R,*e.g.*, NO_2 or NH_2. This functional group allows to tune the molecule dipole over a large range of values and to orient it toward the metal oxide or toward the polymer. The open-circuit voltage scales almost linearly with the dipole moment of the molecule over a range of 0.2 V. The highest V_{oc} (0.65 V) was obtained with NH_2 (largest dipole pointing toward the polymer) and the lowest was obtained with SO_2F (largest dipole pointing toward the metal oxide). The evolution of J_{sc} is more surprising: it is roughly a step function going from 0.45 mA cm^{-2} with NH_2 to 0.8 mA cm^{-2} with SO_2F, and the step does not occur exactly when the dipole moment changes direction. As a consequence of these opposite evolutions, optimal efficiency was obtained for an intermediate value of the dipole moment (with NO_2). In our case, molecules with dipole moments pointing toward the inorganic semiconductor, *i.e.*, molecules with large electron affinities, should enhance electron transfer at the interface between silicon and P3HT. It could also enhance hole transfer from silicon to P3HT, as it reduces the effective gap between the HOMO of P3HT and the conduction band edge of silicon (or the hole quasi-Fermi level, which lies below it at an energy depending on the illumination intensity). This would require verification. But, as similar molecules could be grafted on silicon (*e.g.*, from diazonium salts) *surface modification by phenyl rings bearing an electron-accepting group such as NO_2 is a promising way to improve the performance of devices based on silicon and P3HT.*

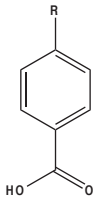

Figure 5.10 – *General formula of benzoic acid derivatives*

The other aspect of interface engineering for hybrid solar cells is the improvement

[20] Goh, Scully, and McGehee, "Effects of molecular interface modification in hybrid organic-inorganic photovoltaic cells", 2007 [GSM07]

of the contact between the active polymer and the top electrode. Some possibilities, including the use of PEDOT:PSS, have been mentioned in section 2.4.2. Ravirajan *et al.* proposed another method to deposit this intermediate PEDOT:PSS layer:[21]

1. The commercial aqueous dispersion of PEDOT:PSS is sonicated for 15 min.

2. It is heated at 90 °C for 15 min.

3. It is filtered with an 0.45 µm filter.

4. It is spin-coated in a water-free atmosphere (this can be obtained by saturating it with acetone vapor).

No direct evidence of the presence of PEDOT:PSS on the active layer after such a deposition was given, but a strong improvement of the performance of devices was observed (the conversion efficiency was almost twice as much with this intermediate layer than without). In the reported experiments, the active polymer was MEH-PPV, which bears a methoxy group and may therefore be less hydrophobic than P3HT. Nonetheless, this confirms that *an intermediate PEDOT:PSS layer is a valuable means to improve the interface between the active polymer and the evaporated electrode. It is therefore worth developing further a process to deposit it on P3HT.*

5.3.3 Optical and electrical modeling

The ultimate potential of hybrid cells based on nano-structured silicon and polymers is still unknown. Modeling such devices would be required to estimate it, and to select the best candidate materials and structures. A minimal realistic model should describe the following features:

1. Behavior of the silicon/organic interface under illumination. Our work and those presented in the previous sections give good insight into this point. To describe it more accurately, a better knowledge of the energetic levels and their possible bending at the interface would be necessary. This could be achieved by *photoemisssion spectroscopy (in particular, Ultra-violet Photoemission Spectroscopy or UPS) and by Kelvin-probe measurements.*

2. Geometry of the organic/inorganic blend and diffusion of excitons in the organic semiconductor. The latter is studied in depth for all-organic solar cells, and a good estimate of the diffusion length can be obtained by photoluminescence quenching experiments. A realistic description of the former is very important, as the probability for an exciton to be quenched depends exponentially on its distance to an interface.

[21] Ravirajan et al., "Efficient charge collection in hybrid polymer/TiO_2 solar cells using poly(ethylenedioxythiophene)/polystyrene sulphonate as hole collector", 2005 [Rav+05]

3. Absorption and diffusion of light in the active layer. Improvement in the efficiency of the devices is expected because of an increased efficiency in the separation of excitons due to the geometry. But that can only happen if light is largely absorbed by the polymer infiltrated in the nano-structured silicon layer. Because of the thickness of the layers (of the order of 100 nm), interference plays a major role in the spatial distribution of light absorption. In addition, the special optical properties of the silicon nano-structured layer, such as light scattering, must be taken into account.

For example, optical modeling of our bilayer devices have shown that the thickness of both the top electrode and the silicon layer has an impact on the generation of charge carriers due to absorption in the polymer layer. In particular, the optimal value of the thickness of the silicon layer has been found to be 57 nm, which lies in the middle of the explored range.[22] Another example is given by Gowrishankar *et al.*[23] who estimated that 28% of photons absorbed in their devices were in fact absorbed in the polymer overlayer (between the silicon nano-structured layer and the top electrode), where the efficiency of exciton separation is very low.

Insights into the optical behavior of the silicon layer have been given by Hu and Chen.[24] They have calculated the absorbance and reflectance of a periodic brush of silicon nanowires (diameter between 50 nm and 80 nm) between 1.1 eV and 4 eV. They have shown that the absorbance of the nanowires is lower than for a dense film at energies between 1.1 eV and 2.5 eV. This phenomenon is explained by the indirect bandgap of crystalline silicon, which requires interaction with phonons for light to be absorbed. This interaction is more difficult in silicon nanowires because of their small size and their high anisotropy. On the other hand, the reflectance is almost zero over all the energy range, which is ideal for photovoltaic devices. These calculations are in good agreement with experimental measurements by Tsakalakos *et al.*[25] In addition, they have shown that very low reflection occurs for incidence angles up to 70° with respect to the normal. Both studies evidenced the importance of collective effects, in particular optical resonances between nanowires. These results are encouraging for solar cell applications, but two questions remain open: *how will these optical properties evolve when the network of silicon nanostructures becomes random, both in size and orientation? Will they be maintained, in particular the low reflectance, when the nano-structured silicon layer is covered by polymer?*

[22] Modeling by Florent Monestier and Jean-Jacques Simon, from Institut Fresnel (Marseille, France) — unpublished results

[23] Gowrishankar et al., "Exciton harvesting, charge transfer, and charge-carrier transport in amorphous-silicon nanopillar/polymer hybrid solar cells", 2008 [Gow+08]

[24] Hu and Chen, "Analysis of Optical Absorption in Silicon Nanowire Arrays for Photovoltaic Applications", 2007 [HC07]

[25] Tsakalakos et al., "Interaction of Light with Si Nanowire Films", 2006 [Tsa+06]

Summary

The performance of our cells compare well with other published results. So far, devices based on silicon nanowires covered by a polymer semi-conductor are disappointing. On the other hand, smoother nano-structured layers, like our nano-pillars or those made by RIE on a-Si:H, are promising. An increase in the exciton harvesting rate due to nano-structure has been evidenced by Gowrishankar *et al.*, and reasonable performance has been obtained with our cells based on silicon nano-pillars. In addition, thermal treatments appeared to be a very efficient way to improve these cells. Yet to make efficient devices, the a-Si:H(i) layer between the nano-pillars and P3HT needs to be removed, as it blocks hole transfer from silicon to P3HT. There is still space for an increase in the collection of excitons generated in P3HT by reducing the characteristic size of the pores in the silicon layer. The "nano-sponge" obtained in section 4.2 has pore diameters of about 15 nm and would therefore by ideal for that. Infiltration of the nano-structured silicon layer by the polymer could be quantified by SIMS. Future work on this topic should address the following points:

- Optical modeling coupled with a realistic description of the geometry, and coupled with models for the diffusion and separation of excitons to estimate the ultimate potential of these cells.
- Surface modification of the silicon surface, not much to increase the wetting by the polymer layer, but mainly to enhance charge transfer between the two materials. This could be done by grafting phenyl rings functionalized with an electron-accepting group, *e.g.*, NO_2.
- Deposition of PEDOT:PSS between P3HT and the evaporated top electrode to enhance hole collection.
- Investigation of other organic semiconductors with a more shallow HOMO than P3HT to hole transfer both from silicon and to the top electrode.

Conclusion

This work aimed at investigating the experimental feasibility of hybrid thin-film solar cells based on nano-structured silicon layers and polymer semiconductors, at studying the behavior of such cells, and at evaluating their potential. As organic semiconductors are meant to reduce the cost of solar cells and to allow their fabrication on flexible substrates, the processes must be simple and work at low temperatures.

Our first step was to investigate the hetero-junction between silicon and P3HT for solar applications. Bilayer devices made of various kinds of silicon thin films (amorphous, micro-crystalline, intrinsic, doped) have been fabricated for that. Significantly higher open-circuit voltages have been obtained when the silicon layer was made of a-Si:H(n) and a-Si:H(i) than with any other structure. This structure has been optimized and power conversion efficiencies as high as 1.6% have been obtained. Noticeably, both materials contributed to the photo-current, and the interface between silicon and P3HT is actually where excitons generated in the polymer are dissociated. Yet the performance of these cells is very sensitive to any processing condition and the best results could hardly be reproduced. In addition, the performance of some cells was hindered by their "S-shaped" J-V characteristics.

The fabrication process has then been simplified in order to make the results more reliable. A new design of samples has been developed to increase the number of cells on each sample, and to have cells with various areas. Thanks to a transport case under vacuum, oxidation of the silicon films before the polymer is deposited can be completely avoided. Yet this did not prevent "S-shaped" characteristics. Indeed, these characteristics have been shown to come from a non-ohmic contact between the evaporated top electrode and the polymer layer. The most promising way to treat this problem is to deposit an intermediate PEDOT:PSS layer with a surfactant additive on top of P3HT. Replacing P3HT by another organic semi-conductor with a more shallow HOMO should also help.

As regards nano-structured silicon thin films, we have demonstrated for the first time the growth of silicon nanowires by thermal CVD on transparent conductive oxides (ITO and ZnO). This growth was obtained at high temperature (530 °C) with two kinds of catalysts deposited *ex-situ*: gold and copper. The number density of nanowires grown this way was too low as compared to our requirements: only a few

per μm^2. Devices based on these nanowires had indeed very bad electrical performance, with a short-circuit current density of less than $1\,\mu A\,cm^{-2}$. The high series resistance seems to indicate that the substrates were degraded during the deposition.

A first step toward the growth of silicon nanowires at a lower temperature has been made when we evidenced that well separated gold aggregates could be obtained by annealing a thin evaporated layer on ITO at a temperature as low as 175 °C. A comprehensive study has shown that the final number density and size of the gold aggregates had no detectable dependence on the annealing temperature, but it varied rapidly with the initial thickness of the evaporated layer. This result was based on measurements obtained by an automated analysis of SEM images. The size distribution of the aggregates is wide, and its shape is characteristic of an evolution driven by kinetic aggregation.

The second step to obtain nano-structured silicon thin films at low temperature was to reduce the growth temperature itself. For that we moved to Radio-Frequency Plasma-Enhanced CVD (RF-PECVD), where chemical reactions are induced by electrons and ions upon external electrical excitation. We obtained "nano-sponge" layers at 175 °C by exposing copper-coated substrates to high pressure (up to 3 Torr) plasmas composed of SiH_4 highly diluted in H_2. These layers are micro-crystalline. With an RF power density of $64\,mW\,cm^{-2}$, the growth rate is approximately $7\,nm\,min^{-1}$ and the void fraction of the layer is 47%. In addition, the typical pore diameter is 15 nm, *i.e.*, about the ideal value of twice the diffusion length of excitons in P3HT. In this growth process, copper, whose catalytic effect has been demonstrated, remains confined at the interface between the substrate and the silicon layer. Hence nanowires cannot be grown this way, but the presence of metal in the active layer is avoided.

At a slightly higher substrate temperature (between 250 °C and 300 °C), crystalline silicon nanowires have been obtained upon exposure to low-pressure (56 mTorr), pure silane plasmas. In that case, the metal catalyst was indium. It was generated *in-situ*, by exposing the ITO substrates to an hydrogen plasma before the growth started. This treatment superficially reduces ITO and leads to the formation of metallic droplets at the surface, without inducing major damages in the optical and electrical properties of the bulk ITO layer. This is a very original result, as neither plasmas nor indium are commonly used to grow silicon nanowires. Most of all, the growth of silicon nanowires from catalysts generated *in-situ* had never been reported before. In addition, the unusual wurtzite crystalline structure has been clearly evidenced on wires grown by this process. A similar method has been used to grow silicon nanowires on SnO_2 substrates. So far, the performance of hybrid solar cells based on these nanowires has been disappointing because direct contact between the wires and the top electrode could not be avoided. But this process could have applications to many other devices, including thin-film silicon solar cells.

Working hybrid devices have finally been made based on silicon nano-pillars. This kind of silicon thin films is an intermediate between flat (amorphous or micro crystalline) layers and silicon nanowires. These devices had limited performance because only P3HT contributed to the photo-current. Indeed, an interfacial a-Si:H(i) layer, intended to increase the open-circuit voltage and to make the silicon layers more stable

against oxidation, blocked hole transfer from silicon to P3HT. There is still space for improvement of these devices: the roughness of the silicon layer can be larger, so excitons generated in P3HT can be better harvested. In addition, thermal treatments, such as annealing above the melting point of P3HT, proved to be a very efficient way to improve the electrical behavior of the devices.

The performance of the devices developed in this work compares very well with published results on resembling devices, and with hybrid cells based on metal oxides and polymer semiconductors. Some authors have drawn pessimistic conclusions on the relevance of hybrid cells based on amorphous silicon and polymers, in particular because of the small contribution by silicon to the photo-current. This is indeed an issue, as contribution by silicon is one of the major potential advantages of these cells as compared to other hybrid devices. It could be improved by surface modification of silicon or by replacing P3HT by an organic semiconductor with a more shallow HOMO. Other experimental work, such as the fabrication and characterization of cells based on silicon “nano-sponge”, and some modeling will be necessary before a definite conclusion can be drawn on the potential of hybrid solar cells based on nano-structured silicon and polymer semiconductors.

PECVD

A

Contents

In this work, plasmas have been used as a deposition tool and not studied for themselves. That is why this short presentation of plasma-enhanced chemical vapor deposition will be given in the frame of materials science rather than plasma physics. For the same reason, it will be focused on capacitively-coupled plasmas operated at radio frequencies (13.56 MHz) and will not cover the broad range of deposition techniques based on low-temperature plasmas. We will rather start with a description of CVD and its derivatives in order to understand why PECVD has been introduced. Then some basics of low-temperature plasmas will be given, and the experimental setups used for this work will be described.

A.1 Chemical vapor deposition

Description

Chemical vapor deposition (CVD) is a method to grow solids from a gaseous source through chemical reactions. A good introduction may be found in *The Materials Science of Semiconductors*.[1]

In this method, precursor gases are introduced in the reactor where substrates lie. Part of the precursor gases is adsorbed on the substrate, may diffuse on its surface and is eventually dissociatively chemisorbed. Reaction by-products desorb and are pumped away, as well as unused precursors. Continuous pumping prevents from reaching an equilibrium between the surface and the gas phase, which could allow products to recombine and desorb. Thanks to the low kinetic energy of the reactants and to their possible diffusion on the surface, CVD is good at producing conformal layers even on rough substrates. In addition to this advantage, as compared to physical vapor deposition methods, the precursors are provided by an external source, which can be changed or refilled without opening the reactor. This possibility reduces the risk of contamination and makes this method more adapted for continuous operation.

Limits

The deposition rate can be limited either by the precursor input or by the surface reaction kinetics. The former is controlled by fluid mechanics in the gas phase: flow rate, density, viscosity, thickness of the boundary layer (where molecules remain for a longer time than in the bulk), *etc.* The latter mainly depends on the temperature, as the forward reaction rate k_f at the surface of the substrate is typically:

$$k_f = k_0 \exp(-\Delta H / k_B T)$$

where ΔH is the energy barrier to overcome for the reactants to be dissociated at the surface. In plain CVD, the only way to increase the deposition rate in the surface reaction limited regime is to increase the temperature of the gases and the substrate.

In addition, a large fraction of the precursor gases are directly pumped out (and mixed with the by-products) without even being adsorbed on the substrate. This loss of valuable, purified gases is of course a problem for industrial applications.

Improvements

Several ways have been investigated to enhance the deposition rate without increasing the process temperature. Indeed, in addition to obvious economical motivations, too high a temperature prevents from using many substrates: polymers, multi-layer substrates where different thermal expansion coefficients could lead to delamination, *etc.*

[1] Rockett, *The Materials Science of Semiconductors*, 2008 [Roc08]

The first improvement was to use light (especially UV or laser beams) to excite molecules in the precursor gas to levels above the energy barrier. This method has several theoretical advantages. First, it reduces the need for heating the substrate. Second, some reactions can be selectively enhanced by adjusting the excitation wavelength to their very activation energy, while the rate of parasitic reactions can be kept unmodified. Unfortunately, its implementation is rather difficult, in particular because it requires (clean) windows in the reactor.

A more successful method is the "catalytic CVD", or "hot-wire CVD". In this method, the dissociation of the precursor gases does not occur at the surface of the substrate, but rather at the surface of a hot metallic filament. This filament (usually tungsten) is heated up to high temperatures (1500 °C to 2000 °C). When the pressure is low enough to prevent gas phase reactions, the radicals formed upon decomposition of the precursor gas are long-lived enough to reach the surface in their excited state. This way, their reaction probability is very high, without any heating of the surface. This method has been successfully used for the deposition of silicon thin films.[2] In that case, it was shown that the precursor gases (SiH_4 and H_2) were dissociated into atomic Si and H, respectively. The decomposition probability of a silane molecule at a filament temperature of 2000 °C is reported to be 40%.

A.2 Presentation of plasma-enhanced CVD

Plasma-enhanced CVD is another method derived from CVD. Here, the precursor gases are partially ionized. The excitation energy is transferred from an electric generator to electrons and ions, which induce reactions.

A.2.1 Physical characteristics of low-temperature plasmas

Plasmas are often referred to as "the fourth state of the matter". It should rather be the first, as most of the (known) matter in the universe is made of plasmas. A plasma may be defined as an ionized gas: it is a gas (there are little interactions among neutral species) where charge neutrality is globally, but not locally, respected.

Plasmas are usually classified as a function of their electron density and their electron temperature (or energy). Both of them vary over several orders of magnitude, which makes physics of plasmas a very rich and diverse field. The plasmas we are interested in for RF-PECVD have typical electron densities in the range $1 \times 10^9\,\mathrm{cm}^{-3}$ to $1 \times 10^{11}\,\mathrm{cm}^{-3}$ and electron temperature about 1 eV to 10 eV. As a comparison, thermal energy at room temperature is 25 meV, the free electron density in a metal is in the range $1 \times 10^{22}\,\mathrm{cm}^{-3}$ to $1 \times 10^{23}\,\mathrm{cm}^{-3}$ and the solar corona has an electron density around $1 \times 10^5\,\mathrm{cm}^{-3}$ and an electron temperature of about 5×10^2 eV.

[2] Matsumura, "Formation of silicon-based thin films prepared by catalytic chemical vapor deposition (Cat-CVD) method", 1998; Veenendaal and Schropp, "Processes in silicon deposition by hot-wire chemical vapor deposition", 2002 [Mat98; VS02]

The local non-neutrality of plasmas is characterized by the Debye length, which is the typical distance over which a space charge region may exist upon perturbation, *e.g.* when an electron or an ion is added. At larger distance, other charges "screen" the perturbation. When only electrons contribute to the screening, the Debye length is:

$$\lambda_D = \sqrt{\frac{\epsilon k_B T}{n e^2}} \tag{A.1}$$

where $n = n_e = n_i$ is the electron density. In a typical RF-PECVD plasma, with $n_e = 1 \times 10^{10}\,\mathrm{cm}^{-3}$ and $T_e = 2\,\mathrm{eV}$, the Debye length is approximately $\lambda_D = 100\,\mu\mathrm{m}$.

Another characteristic value of plasmas is linked to the conservation of charge neutrality: it is the plasma pulsation. It is defined as the frequency of oscillations that occurs after electrons are collectively moved over an elemental distance, thus breaking up charge neutrality and creating a restoring force. As the mass of the charged particles influence these oscillations, the plasma frequency is different for electrons and for ions. A general expression is

$$\omega_{p,j} = \sqrt{\frac{e^2 n_j}{\epsilon_0 m_j}} \tag{A.2}$$

where j is either i (ions) or e (electrons), n_j is the density of species j and m_j is the mass of species j. This pulsation gives information on how the plasma will react to an external electric stimulation. If a periodic stimulation of pulsation ω_{stim} is applied to the plasma, the charged species will be able to "follow" this stimulation (*i.e.* to oscillate at the same frequency) if their plasma pulsation is larger than the stimulation pulsation. On the other hand, if $\omega_{p,j} \ll \omega_{\mathrm{stim}}$ then the species j will remain at fixed positions. In a typical hydrogen RF plasma where $n_e = n_i = 1 \times 10^{10}\,\mathrm{cm}^{-3}$, $f_{p,e} = 901\,\mathrm{MHz}$ and $f_{p,\mathrm{H}^+} = 21\,\mathrm{MHz}$. This means that electrons can react very fast to the RF excitation ($f_{RF} = 13.56\,\mathrm{MHz}$) and follow its oscillations, while H^+ ions cannot. This difference partly explains one of the fundamental properties of "low-temperature" plasmas: *electrons are not in thermal equilibrium with ions and neutrals*. The electron temperature T_e (about 5 eV) is much larger than the ion temperature T_i and the temperature of the neutrals (about 40 meV in the bulk of the plasma). Another part of the explanation is that energy coupling between electrons and ions, which are much heavier, is weak.

A fundamental property of discharge plasmas is *sheaths*. Indeed, plasmas are confined by walls to which fast-moving electrons are faster drained than ions. Hence the electron density falls to zero at the walls, while the ion density decreases but remains positive. So charge neutrality is broken in a region close to the walls, which is called the plasma sheath. The thickness of the sheath is a few Debye length. An electric field, oriented from the bulk of the plasma to the walls, is created by the difference in density between electrons and ions. This electric field, in turn, accelerates ions out of the plasma. So ions heating the walls have more energy than they have in the bulk of the plasma, and they arrive in a direction perpendicular to the wall. This phenomenon is called "ion bombardment". It is, in particular, the basis for anisotropic etching, which is widely used in microelectronics.

A.2.2 Chemistry in the plasma

PECVD stands for Plasma-Enhanced *Chemical* Vapor Deposition, so the chemistry in the plasma is of major importance to us. As for Hot-Wire CVD, the idea is to separate the dissociation of precursor gas from the reactions with the substrate, by making highly reactive species far from the surface of the substrate. A key parameter to the description of the plasma is its ionization ratio α defined as:

$$\alpha = \frac{n}{n_0 + n} \tag{A.3}$$

where n_0 is the density of neutrals species. In such reactors as used for this work, this ionization ratio ranges between 0.1% and 6%.[3] This means that three kinds of species are present in the plasma: electrons, ions and neutrals, which represent most of the volume. The latter can themselves be separated in stable molecules (like SiH_4) and radicals (like SiH_3).

The physics of low-temperature plasmas is generally described for single, monoatomic gases like Ar. In that case, chemical reactions are rather limited. But in deposition plasmas, a huge amount of different chemical reactions can happen. They can be separated in *primary* and *secondary* reactions.

Primary reactions occur between electrons and neutrals. They create ions or radicals. In the case of SiH_4/H_2 plasmas, the products of ionization reactions are $SiH_x^{\pm}$ ($0 \leq x \leq 3$), and $H_y^{\pm}$ ($1 \leq y \leq 2$). The products of dissociation reactions are H and SiH_x ($0 \leq x \leq 3$) radicals.

These species can react either with the substrate, leading to deposition or etching on the surface, or with themselves and electrons. The latter reactions are called *secondary* reactions. They lead to the re-formation of precursor gases or to polysilanes. This kind of reactions can eventually produce silicon nano-clusters and even powders in the bulk of the plasma.

At low pressure and low RF power, secondary reactions are rare. Hydrogenated amorphous silicon is classically deposited under such conditions: the pressure is typically around 50 mTorr and the RF power density is typically $10\,mW\,cm^{-2}$. Its deposition is dominated by SiH_3 radicals produced by primary reactions. On the other hand, when the RF power or the pressure is increased, there are more and more secondary reactions. For example, hydrogenated polymorphous silicon[4] is grown at pressures in the ranger 1 Torr to 2.5 Torr, with power densities of few tens of $mW\,cm^{-2}$. In such a growth, secondary reactions in the plasma are used to form the nano-crystals, and radicals created by primary reactions contribute to the deposition of the amorphous matrix.

[3] Damon-Lacoste, "Vers une ingénierie de bandes des cellules solaires à hétérojonctions a-Si:H/c-Si. Rôle prépondérant de l'hydrogène." 2007 [DL07]

[4] Referred to as pm-Si:H. This material is made of silicon nano-crystals embedded in a matrix of hydrogenated amorphous silicon.

A.2.3 RF-PECVD reactors

General description of a capacitively coupled RF plasma reactor

The reactors used in this work were capacitively coupled, in a diode configuration. A schematic view of such a setup is displayed on fig. A.1. In such a configuration, an alternating potential difference is applied between two electrodes. For deposition, the substrate is placed on the grounded electrode. The precise frequencies (13.56 MHz or its multiples) used in RF reactors have not been chosen on physical bases, but on regulation ones: they are the only ones in the range of radio-frequencies to be allowed by the International Telecommunications Union for industrial, scientific and medical use. The power of generators is also restricted between 200 W and 30 kW.

The energy is transferred to the plasma by capacitive heating. Qualitatively, electrons in the plasma sheath are pushed forth and back when the potential difference between the electrodes changes. This movement leads to a periodic change in the thickness of the sheath and to collisional (ohmic) heating of the electrons. From an electrical point of view, the sheath behaves as a capacitor and a resistor in parallel. In order to transfer energy to the plasma, the resistor behavior must dominate (the average energy dissipated in a capacitor is zero). The ratio between the impedance of the capacitor and the resistor can be estimated as:[5]

$$\frac{|Z_R|}{|Z_C|} = R_s C_s \omega \simeq \left(\frac{\omega}{\omega_{p,i}}\right)\left(\frac{q V_s}{k_B T_e}\right) \tag{A.4}$$

where R_s, C_s and V_s are the resistance, capacitance and potential of (or across) the sheath, respectively. This expression explains why it is very convenient to add argon to the gas mixture to ignite the plasma. Indeed, Ar^+ ions are much heavier than H^+ or SiH_3^+ ions[6], so their plasma pulsation is lower[7] and more energy is transferred to the sheath through ohmic heating.

A matching box is required to ensure that the total impedance of the reactor fits the impedance of the RF source. This matching box for capacitively coupled reactors is made of two variable capacitors and one inductor. One capacitor and the inductor are in series with the generator and the reactor, while the second capacitor is in parallel. The impedance of the capacitors is determined by minimizing the reflected power from the plasma to the generator.

In general, the walls of the reactor are also grounded, which means that the area of the effective grounded electrode is much larger than for the RF electrode. This asymmetry induces a difference in the voltage drop across the sheath at the grounded electrode and the RF electrode, respectively (fig. A.2). The voltage ratio has been shown to

[5] Pointu, Perrin, and Jolly, "Plasmas froids de décharge — Applications et diagnostic", 1997 [PPJ97]

[6] $M_{Ar^+} \simeq 40\,\mathrm{g\,mol^{-1}}$, $M_{H^+} \simeq 1\,\mathrm{g\,mol^{-1}}$ and $M_{SiH_3^+} \simeq 31\,\mathrm{g\,mol^{-1}}$

[7] $\omega_{p,Ar^+} = 21\,\mathrm{MHz}$, $\omega_{p,H^+} = 132\,\mathrm{MHz}$ and $\omega_{p,SiH_3^+} = 24\,\mathrm{MHz}$, while the pulsation of the RF excitation is $\omega_{RF} = 85\,\mathrm{MHz}$

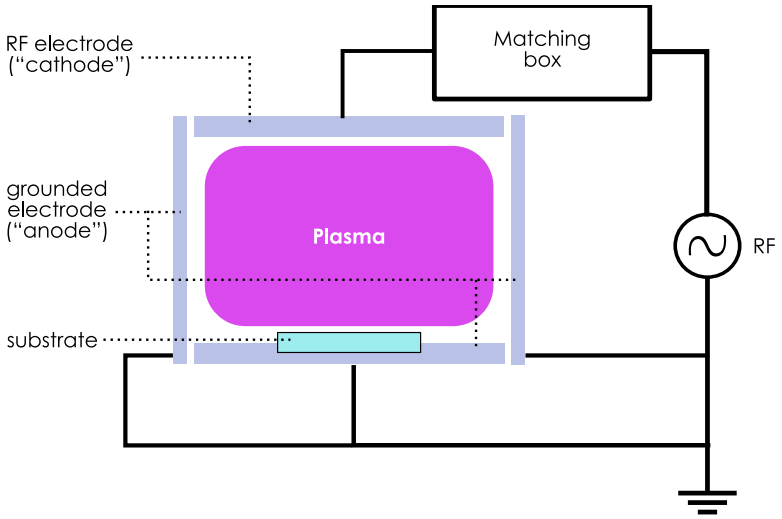

Figure A.1 – *Diagram of a capacitively coupled RF-PECVD reactor in a diode configuration*

be:[8]

$$\frac{V_{s,RF}}{V_{s,\text{ground}}} = \left(\frac{A_{\text{ground}}}{A_{RF}}\right)^{\kappa} \tag{A.5}$$

Theoretically, $1.3 \leq \kappa \leq 4$. Experimentally, κ is typically around 2. Consequently, there is a direct voltage drop between the RF electrode and the grounded electrode when the plasma is on. So the voltage difference between the two electrodes is: $V(t) = V_{RF}\cos\omega t + V_{DC}$. In addition, due to the sheaths, both electrodes are at lower potentials than the bulk of the plasma. The "plasma potential" V_p can be approximated as:

$$V_p(t) = \frac{V_{DC} + V_{RF}(t)}{2} \tag{A.6}$$

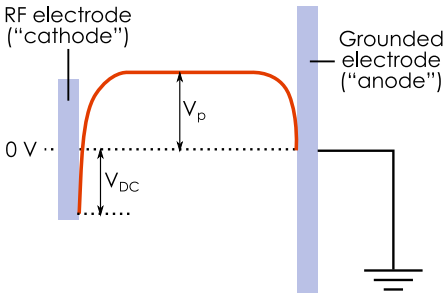

Figure A.2 – *Potential profile across an asymmetric capacitively coupled RF plasma*

As mentionned above, initiating a plasma is a difficult task. It is characterized by the *breakdown voltage*, *i.e.* the minimum voltage to be applied to the electrode for

[8] Koenig and Maissel, "Application of RF Discharges to Sputtering", 1970 [KM70]

the plasma discharge to start. Friedrich Paschen (1865–1947) has shown that, for DC capacitive plasmas, the breakdown voltage was a function of the product $p \times d$, where p is the pressure and d is the distance between the electrodes:[9]

$$V = \frac{apd}{\ln(pd) + b} \tag{A.7}$$

where a and b depend on the gas mixture. A typical curve is plotted on fig. A.3. This relationship is also valid for RF plasmas. More generally, for a given gas mixture, equivalent plasma conditions can be obtained by keeping $p \times d$ constant. This is a convenient scaling relationship.

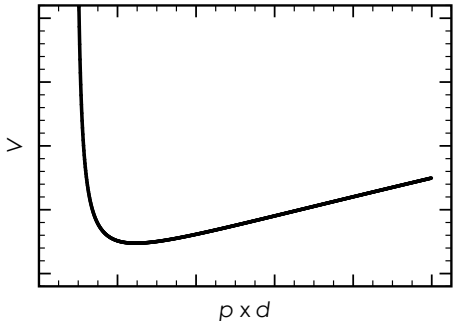

Figure A.3 – *Typical plot of the breakdown voltage in a capacitively-coupled plasma as a function of the product $p \times d$ (Paschen curve).*

Mainly two reactors have been used for this work: ARCAM and PLASFIL. They will be described in more details in the next paragraphs.

ARCAM

ARCAM is central to PICM's activities: it is one of its oldest operating reactors and is almost continuously running. It has been described and characterized in details in a published paper.[10] Its structure is schematized on fig. A.4 and photos are shown on fig. A.5.

As compared to the standard reactor described above, it has some specific properties:

- It is an "oven-like" reactor. It is completely heated by thermocoax cables embedded in its walls, which allows the temperature to be homogeneous. The typical operating temperatures are in the range 150 °C to 250 °C.

[9] Paschen, "Über die zum Funkenübergang in Luft, Wasserstoff und Kohlensäure bei verschiedenen Drucken erforderliche Potentialdifferenz", 1889 [Pas89]

[10] Cabarrocas et al., "A Fully Automated Hot-Wall Multiplasma-Monochamber Reactor For Thin-Film Deposition", 1991 [Cab+91]

- Substrates (up to 10 cm wide) lie face down on a rotating plate which bears six substrate holders. This way, several substrates can be treated in a single run. In addition, the plasma can be started in front of an empty substrate holder and the substrate to be treated can be introduced once the plasma is stable. This features prevents the samples from being exposed to the plasma transitions (a few seconds), which are a major cause of non-reproducibility.

- It has three RF electrodes, each of which is in a separate "plasma box". The plasma boxes allow to isolate the plasma and prevent cross-contamination. Each of them is dedicated to one kind of deposition: intrinsic materials, n-doped materials, and p-doped and carbide materials, respectively. In association with the rotating plate, this feature allows to fabricate multi-layers structures like PIN diodes in a single run and with clean interfaces.

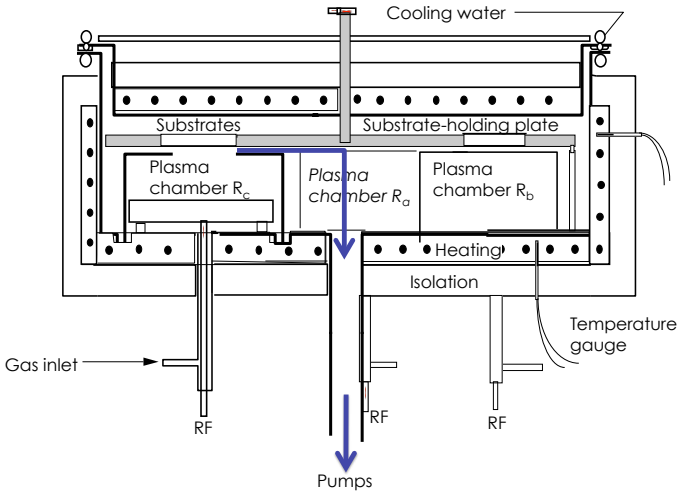

Figure A.4 – *Diagram of ARCAM reactor*

ARCAM has been extensively used in this work, mainly for the deposition of flat silicon thin films for hybrid devices and for the growth of nano-structured silicon thin films from evaporated metal on ITO. It is operated at a base pressure of 1×10^{-6} mbar. Available gases include Ar, SiH_4, H_2, PH_3 (for n doping), B_2H_6 (for p doping), SiF_4, GeH_4. The inter-electrode distance d is between 12 mm and 28 mm.

PLASFIL

At the opposite of ARCAM, PLASFIL is one of the newest reactors in PICM: it has been started during this thesis. The first depositions were done in early October 2007.

PLASFIL was originally intended for growing silicon nanowires with plasma activation. In particular, it has been designed to allow to use gallium, which is one of the

(a) *Side-view*

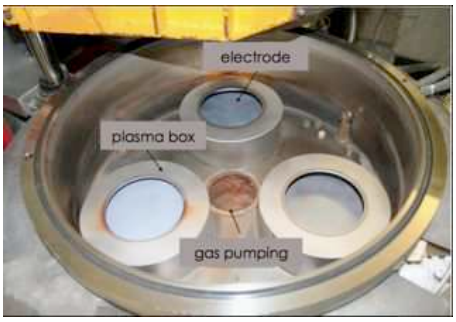

(b) *Top view of the open reactor*

Figure A.5 – *Photos of ARCAM reactor*

most promising alternate catalysts for the VLS growth of silicon nanowires, but is liquid around room temperature (its melting point is just below 30 °C). That is why the substrate holder is horizontal and, unlike most reactors, *below* the RF electrode, so that the substrates lie face up (fig. A.6). In addition, the reactor is opened and closed by moving this substrate holder up and down. This vertical movement is automatically driven by an air jack. This way, substrates remain horizontal throughout the process.

Another specific feature of PLASFIL is the ability to heat the RF electrode and the substrate holder to high temperatures. Heaters are indeed embedded in both of them and are independently regulated. The substrate holder can be heated up to 650 °C and the RF electrode up to 450 °C (the latter is limited by ceramic screws which hold the electrode and break up at higher temperatures). These values are only *nominal* temperatures. Indeed, the regulation is based on measurements made by thermocouples. They are in contact with the heaters, but neither with the surface of the electrodes nor with that of the substrates. Moreover, thermocouples move a bit during the operation (especially when the reactor is opened or closed), which results in variations in the location where the temperature is actually measured. As a consequence, there is a large discrepancy between the nominal temperature and the actual one. For example, for a nominal temperature of 300 °C, the temperature at the surface of 1.1 mm-thick glass samples has been measured with thermal labels to be in the range 254 °C to 260 °C when the reactor is under vacuum (5×10^{-6} mbar) and in the range 241 celsius to 249 °C under hydrogen (260 mTorr). This discrepancy, which is likely to vary, is a possible cause of non-reproducibility of the deposition. For convenience, the temperatures mentioned in this work, unless otherwise reported, are the nominal temperatures.

As can be seen on fig. A.7, the reactor has several windows to monitor the plasma and the deposition. Two of them are now used by an MM-16 ellipsometer by Jobin-Yvon Horiba (not shown here).

The set of available gases is more reduced than in ARCAM. In particular, there is no n-type dopant. But H_2, SiH_4, N_2 and $(CH_2)_3B$ can be used. The reactor is operated at

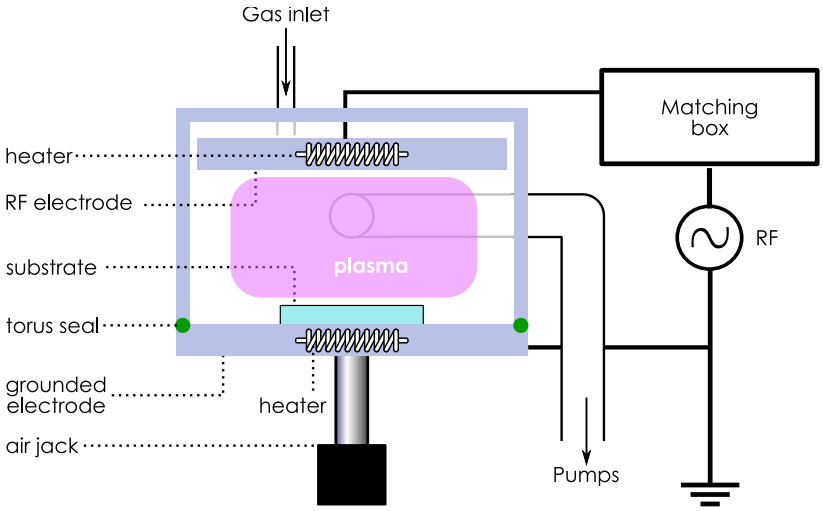

Figure A.6 – *Diagram of PLASFIL reactor*

Figure A.7 – *Front view of PLASFIL reactor*

a base pressure around 5×10^{-6} mbar. The inter-electrode can theoretically be varied between 0 mm and 40 mm but it was kept at 30 mm during this work.

PLASFIL has been used for the growth of silicon nanostructures on ITO and silicon with evaporated metals and, above all, for the growth of silicon nanowires without external catalysts.

Fabrication and characterization methods for thin-film solar cells

B

Contents

THIS APPENDIX is devoted to the presentation of some methods used for the fabrication and characterization of thin-film solar cells. Metal evaporation under vacuum, which has also been used in this work to deposit metal catalysts for the growth of nano-structured silicon layers, will be described. The initial process for the fabrication of multi-layer hybrid solar cells, as derived from the procedure for all-organic devices, will also be presented. Electrical quantities used to describe the behavior of solar cells in dark and under illumination will then be defined. The two main device characterization methods used in this work, J-V characteristics and spectral response measurements, will finally be briefly described.

B.1 Characterization methods

B.1.1 Electrical characteristics

Solar cells are based on an energetic asymmetry, which induces a collective motion of the photo-generated free charge carriers. From an electrical point of view, this asymmetry is characterized in the dark by a *rectifying behavior*, *i.e.*, for a given sign of the potential difference between the electrodes, current flows, whereas for the other, current is blocked. The range of applied potential for which current flows is called *direct polarization*, the other one is called *reverse polarization*. The typical rectifying device is the *diode*. For an ideal one, the relationship between current I and the applied voltage V is given by:

$$I = I_s \left[\exp\left(\frac{qV}{n k_B T} \right) - 1 \right] \tag{B.1}$$

where I_s is the *saturation current* and n is the *ideality factor*. The *I-V characteristics*, *i.e.*, the plot of current vs. applied voltage, of such a device is shown on fig. B.1a.[1]

When the solar cell is illuminated, a photo-current I_{ph} is generated, which is added to the dark current. I_{ph} and I_s have opposite signs, and the current-voltage relationship turns into:

$$I = I_{ph} + I_s \left[\exp\left(\frac{qV}{n k_B T} \right) - 1 \right] \tag{B.2}$$

The photo-current depends on the structure of the device, and on the intensity of the incoming light. In a first approximation, I_{ph} is proportional to the light intensity for a given spectrum. The I-V characteristic of an ideal solar cell for various values of photo-current is plotted on fig. B.1b.

In real devices, though, the electrical performance is hindered by parasitic resistances. The *shunt resistance*, denoted R_{sh}, corresponds to an increase in the absolute value of I_s. It is mainly caused by manufacturing problems such as pinholes[2], which create local shorts between the electrodes. The *series resistance*, denoted R_s, corresponds to difficult extraction of large currents. It is typically caused by poor electrical contacts. The effects of these parasitic resistances on the electrical characteristics of solar cells are shown on fig. B.3. The equivalent circuit is shown on fig. B.2. For the device to perform well, R_s should be as low as possible and R_{sh} as high as possible. In a device with parasitic resistance, the relationship between current and voltage becomes implicit:

$$I = I_{ph} + \frac{V - R_s I}{R_{sh}} + I_s \left[\exp\left(\frac{q(V - R_s I)}{n k_B T} \right) - 1 \right] \tag{B.3}$$

[1] As solar cells are power generators, the current is plotted with the opposite convention as for electronic engineering, where diodes dissipate power. With our convention, I_s is negative.

[2] Micrometer-scaled holes in the active layer of thin-film solar cells

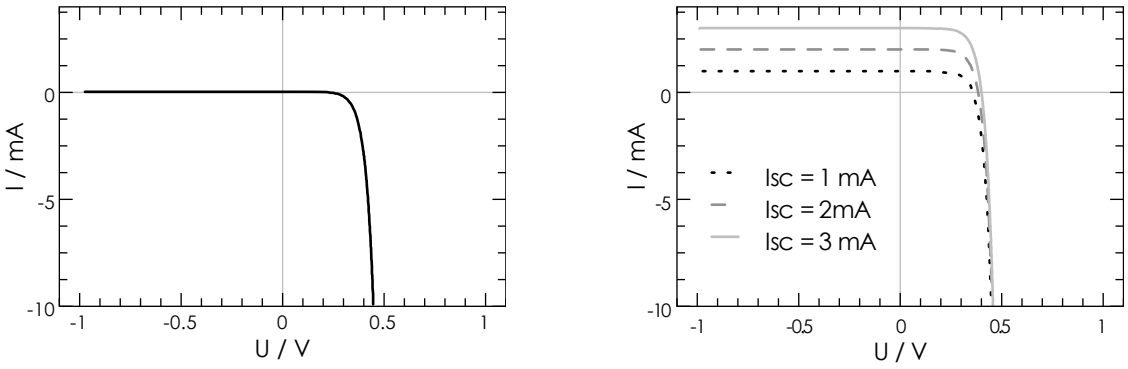

(a) *In dark: ideal diode*

(b) *Under illumination, for various photocurrents*

Figure B.1 – *I-V characteristics of an ideal solar cell in dark and under illumination*

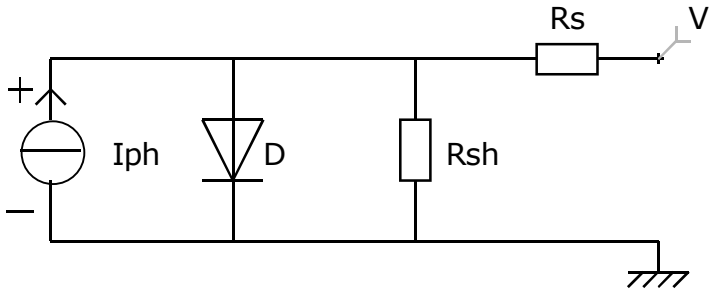

Figure B.2 – *Equivalent circuit for a real solar cell under illumination*

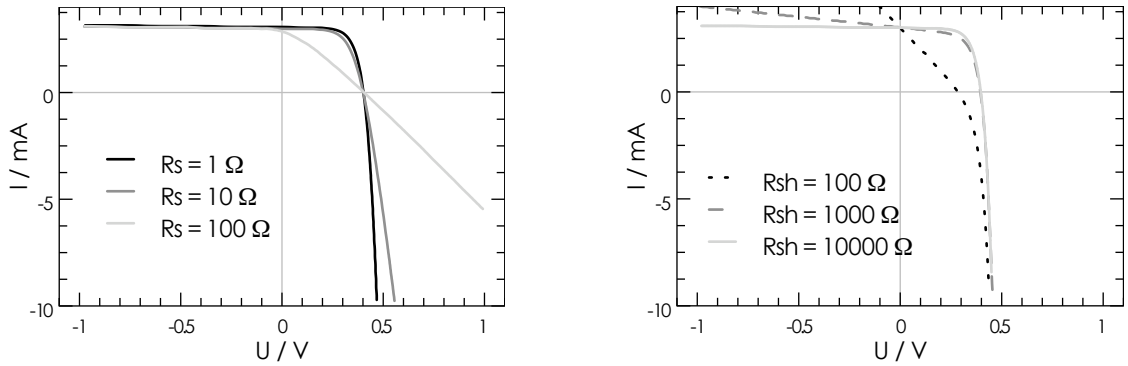

(a) *Various series resistances,* $R_{sh} = 1 \times 10^8\,\Omega$

(b) *Various shunt resistances,* $R_s = 0\,\Omega$

Figure B.3 – *I-V characteristics of non-ideal solar cells with various parasitic resistances*

Characteristic quantities are extracted from the I-V characteristics under standard illumination. They are graphically defined on fig. B.4. The *short-circuit current*, denoted I_{sc}, is the current flowing through the device when the potential difference between the electrodes is zero. For an ideal solar cell (without parastitic resistance), it equals the photo-current I_{ph}. For non-ideal solar cells, $I_{sc} < I_{ph}$. The *open-circuit voltage*, denoted V_{oc}, is the potential difference between the electrodes for which no current flows through the device. The current and voltage at maximum power, denoted I_{max} and V_{max}, respectively, correspond to the maximum output power P_{max}: $P_{max} = I_{max} \cdot V_{max}$. Note that $I_{max} < I_{sc}$ and $V_{max} < V_{oc}$. The fill factor, denoted FF, describes the squareness of the characteristic. It is defined as the ratio between P_{max} and $V_{oc} \cdot I_{max}$, which is the maximum output power of a solar cell with similar V_{oc} and I_{sc}, but with a square-shaped characteristic. Graphically, it is the ratio on fig. B.4 between the dark gray area and the light gray area. Finally, the *power conversion efficiency*, denoted η, is the ratio between the incident light power P_{light} and the maximum output power. These characteristic quantities are related to each other by the following equations:

$$FF = \frac{P_{max}}{V_{oc} I_{sc}} = \frac{V_{max} I_{max}}{V_{oc} I_{sc}} < 1 \tag{B.4}$$

$$\eta = \frac{P_{\text{light}}}{P_{max}} = \frac{P_{\text{light}}}{V_{oc} I_{sc} FF} < 1 \tag{B.5}$$

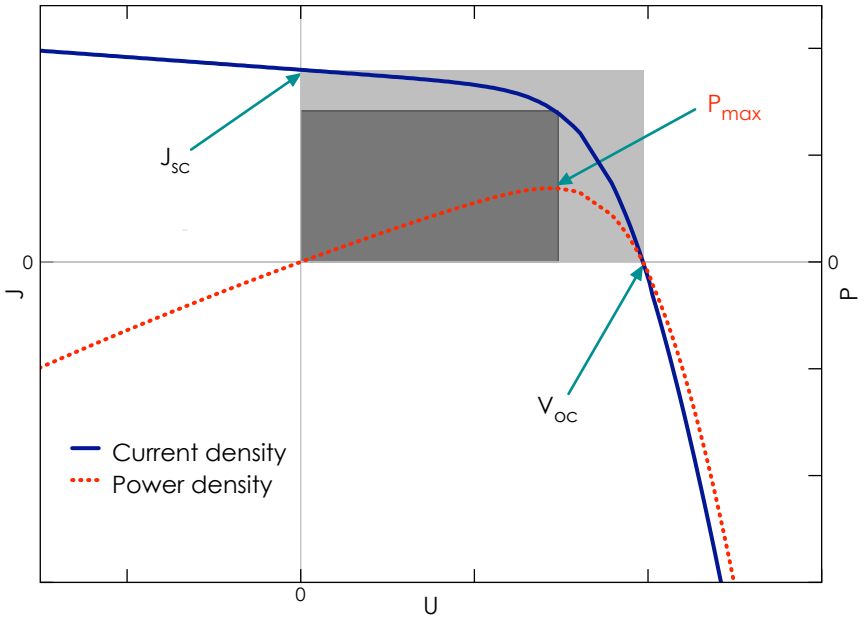

Figure B.4 – *I-V curve and power output of a non-ideal solar cell under illumination demonstrating characteristic quantities ($R_s = 10\,\Omega$, $R_{sh} = 1 \times 10^3\,\Omega$)*

Solar light is not a compact power source (on earth), but rather a flux. It is therefore more natural to measure the power density than the absolute power of the incident

light. In addition, solar cells have a finite surface, which is defined by the intersection between their bottom and top electrodes. The collected current in given conditions is ideally proportional to their surface. That is why it is more convenient and physically more relevant to consider current densities, denoted J and generally given in $\mathrm{mA\,cm^{-2}}$, than intensities.

B.1.2 Measurement methods

J-V characteristics

Most J-V characteristics presented in this study were measured under nitrogen in a glovebox at CEA Saclay and then at INES.[3] A computer driven Keithley 2400 SourceMeter unit was used, as it simultaneously sets the voltage on the electrodes and measures the current flowing through the device. Its source accuracy is $\pm(0.02\% + 600\,\mu\mathrm{V})$. In the 10 mA range (current densities in 0.28 $\mathrm{cm^2}$ cells up to 35.7 $\mathrm{mA\,cm^{-2}}$), its measurement accuracy is $\pm(0.035\% + 600\,\mathrm{nA})$.

AM 1.5 illumination at 100 $\mathrm{mW\,cm^{-2}}$ was provided by a Solar Constant 575 simulator by K.H. Steuernagel, GmhH. This is the standard for solar cell testing, as defined *e.g.*, in the ASTM G173-03 document. It corresponds to the solar spectrum on earth when the sun is at a zenith angle of 48.19°. The complete assumptions on which this standard is based can be found on the website of the U.S. National Renewable Energy Laboratory, as well as the tabulated values.[4] A monocrystalline silicon solar cell calibrated at the Fraunhofer Institut für Solare Energiesysteme was used as a reference before each sequence of measurements.

Spectral response

J-V characteristics inform on how solar cells will eventually behave when operated as power generators, but they are global measurements, and offer only limited possibilities of physical analysis. Spectral response measurements are a valuable tool to get insights into the generation of current under illumination. They are especially useful for tandem or hetero-junction solar cells, where materials with various optical properties are used. Indeed, they give the contribution of each wavelength (or range of wavelengths) to the photo-current. Good practice for spectral response measurements is also standardized (ASTM E1021-84).

Our measurements were done with a white lamp. A mechanical chopper was used to make it a pulsed light source. Incident light was filtered either by a monochromator or by interference filters. The generated photo-current was amplified by a lock-in amplifier synchronized with the chopper. The system was calibrated with a reference photo-diode before each sequence of measurements.

The gross measured value is the *spectral response*, denoted SR, which is the ratio between the generated photo-current and the incident light power as a function of the

[3] Institut national de l'énergie solaire, Le Bourget du Lac, France

[4] http://rredc.nrel.gov/solar/spectra/am1.5/

wavelength. A more convenient value for analysis is the *external quantum efficiency* (EQE), or *incident photon to charge carrier efficiency* (IPCE), defined as the ratio between the number of photo-generated electrons to the number of incident photons as a function of the wavelength. EQE is extracted from the spectral response after the following equation:

$$EQE(\lambda) = \frac{hc}{q\lambda} SR(\lambda) \tag{B.6}$$

B.2 Fabrication techniques

B.2.1 Fabrication of multi-layer hybrid devices

The substrates used for this study were 17 mm × 25 mm ITO-coated glass provided by Präzision Glass und Optik, GmbH. The typical process for fabricating multi-layer hybrid solar cells was as follows.

1. Partial etching of ITO-coated glass substrates: 5 min in a solution of nitric acid at 65% (10 vol.%) and hydrochloric acid at 37% (90 vol.%). The areas not to be etched were protected by galvanoplastic adhesive tape (fig. B.5b).

2. Ultrasonic cleaning of ITO: 2 cycles of 10 min in acetone and 10 min in ethanol followed by twice 10 min plus once 15 min in deionized water. The samples were immediately dried with N_2 plus one-hour storage in an oven.

3. Transfer to an oxygen- and water-free glovebox.

4. Evaporation of four metal contacts: 10 nm of chromium (adhesion layer) covered by 40 nm of gold (fig. B.5c).

5. Transfer in an air-tight container to ARCAM.

6. Deposition of silicon thin films in ARCAM (fig. B.5d).

7. Transfer in an air-tight container to the clean glovebox.

8. Spin-coating of P3HT dissolved in chlorobenzene (fig. B.5e).

9. Evaporation of 50 nm-thick gold top electrodes (fig. B.5f).

This design offers two 28 mm^2 cells per sample.

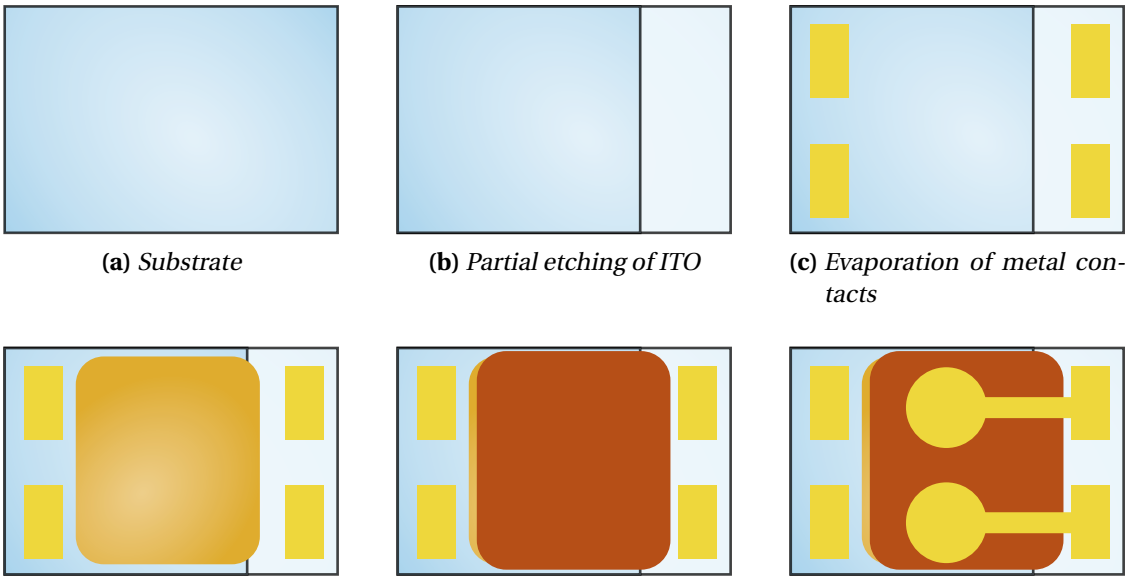

(a) *Substrate*

(b) *Partial etching of ITO*

(c) *Evaporation of metal contacts*

(d) *Deposition of a silicon thin-film*

(e) *Spin-coating of P3HT*

(f) *Evaporation of top electrodes*

Figure B.5 – *Fabrication steps of multi-layer hybrid devices*

B.2.2 Evaporation under vacuum

Presentation of the method

Many materials, especially metals, can be deposited on substrates by evaporation under vacuum. This method allows a good control over the thickness of the deposited layer and a high purity of the material. It is based on heating a solid source to increase the partial pressure of precursor material within the reactor. This vapor then condensates on a solid substrate facing the source, leading to the deposition of a layer. The main difference between evaporators lies in the way the source is heated. We will focus here on the electron beam (e-beam) evaporator, which has been used most extensively during this study. In that kind of equipments, the metallic source is heated by an electron beam from a distant source.

A schematic view of the evaporator is shown on fig. B.6. The metal to be evaporated is directly laid in a copper block of crucibles (our evaporator has four crucibles). Each crucible has a volume of 3.3 cm^3. When the evaporator is operated, cool water is made flowing in this block in order to ensure the temperature of the crucibles remain below its melting point and the eutectic point of its alloys with the metal load. This block is grounded, as is the anode.

The electron beam is provided by a tungsten filament, which is heated up by Joule effect. This filament is connected to the negative pole of a high voltage (20 kV) supply. The maximum dissipated power is 5 kW. The beam is focused by the large hole in the anode, which behaves as an electrostatic lens.

The beam is then deflected by a magnetic field created by the coil and the polar

parts. This field is parallel to the block of crucibles so that the beam is deviated by 180°. Thanks to this deviation, the source of electrons can be protected from the flow of evaporating metal. By modulating the magnetic field, it is possible to scan the metal load with the electron beam, which is very useful when this load is made of a dispersed material (*e.g.*, aluminum powder).

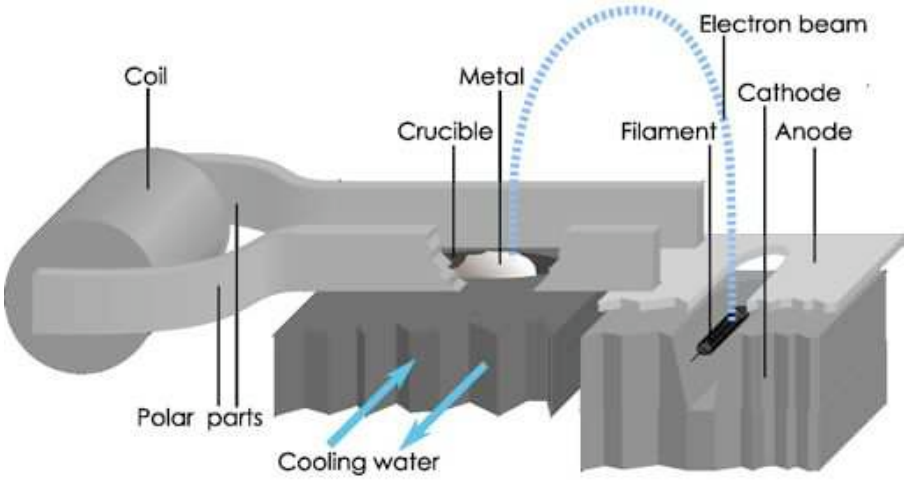

Figure B.6 – *Schematic view of an electron-beam evaporator*

As compared to other kinds of evaporators, the advantages of e-beam evaporators are:

- The evaporated metal is not contaminated thanks to the cooling of the crucibles;
- The crucibles are not consumables: they wear little out because they remain at low temperature throughout the process;
- As the loads do not adhere on the crucibles, different metals can be used subsequently in one crucible;
- When the beam is well focused, almost all the power is dissipated in the metal load;

On the other hand, the disadvantages are:

- A low base pressure is required (less than 5×10^{-6} mbar) to avoid glow discharge;
- The system is complex to operate. In particular, the electron beam must be manually focused and its position on the metal loads must be monitored with a mirror through a small window;
- Dielectric materials and alloys are difficult to evaporate (reactive sputtering is more efficient in that case).

In addition, as for any evaporator, a lot of material is lost upon deposition on the walls and other parts of the setup.

B.2.3 Operating procedure for ODILE

Pump down

Closing the setup Initial state: glovebox at atmospheric pressure, all electrical equipments turned down, all valves closed.

- Ensure the doors of the load-lock are closed.
- Ensure the flap valve between the evaporator and the glovebox is closed.
- Ensure the door of the glovebox is closed. If necessary, close it by tightening the eight handles, first two diametrically opposed by two, then circularly.
- Isolate both gloves with their respective plugs. Leave as little gas in the gloves as possible (press them before tightening the plugs).
- Isolate Photohelic by switching off the buttons labeled “capteur gaz HP” (high pressure gas sensor) and “photohélic”.
- Isolate the gas purification circuit by switching off the buttons labeled “entrée Hubert -> Odile” and “sortie Odile -> Hubert” (Hubert is the name of the refrigerated molecular sieve).
- Close the Ar inlet by switching off the button labeled “EV remplissage” (electropneumatic valve for refilling).
- Close the isolation valve on the pipe between the spin-coater and its pump.

Pumping down

- Ensure the main valve on the Ar pipe (on the wall) is open.
- Ensure the second reducing valve from the left of the Ar control panel is set between 1 bar and 1.2 bar.
- Ensure the main valve on the compressed air pipe (on the wall) is open. Set the output pressure of the reducing valve between 4 bar and 4.5 bar.
- Start water circulation in the cooling circuit of the turbomolecular pump: open the main valve on the wall and the valve labeled “TURBO”. Ensure water flows.
- Open the isolating valve below the Bourdon gauge (left of the glovebox).
- Turn on the three Leybold Vakuum gauges and the controller of the turbomolecular pump.
- Open the flap valve by switching on the button labeled “vanne plateau”.
- Turn on the Alcatel dry backing pump. This is $t = 0$.

- Monitor the pressure on the Bourdon gauge. When it displays -1 bar, isolate it. This happens at $t \simeq 6$ min.
- When all Leybold gauges display a pressure below 5×10^{-1} mbar, turn on the turbomolecular pump. This happens at $t \simeq 11.5$ min. Its acceleration rate, and the value of the pressure when it reaches its full speed indicate the quality of the isolation. For reference, it can reach 27 000 rpm for $t = 15.5$ min and $p = 5 \times 10^{-4}$ mbar.
- Let the pumping go on until the walls reasonably outgas. For reference, the pressure at $t = 1$ h is about 1.3×10^{-4} mbar when the spin-coater is inside the glovebox.

Refilling and regulating the pressure

Preparation Turn on the refrigerating system of the molecular sieve (setup temperature: -50 °C).

Refilling to atmospheric pressure

- Ensure the fourth reducing valve from the left on the Ar control panel is set to 1 bar.
- Close the flap valve above the turbomolecular pump by switching off the button labeled “vanne plateau”.
- Open the Ar inlet by switching on the button labeled “EV remplissage”.
- Turn off the turbomolecular pump.
- Turn off the Alcatel dry backing pump.
- When the pressure in the glovebox reported by the Leybold Ionivac gauge reaches 1 mbar, open the isolating valve below the Bourdon gauge. The pressure must then be monitored on this latter gauge, as the others are not reliable at higher pressure.
- Start the gas circulation in the purification system:
  - open the valve on the glovebox bypass loop by switching on the button labeled “contournement”.
  - open the manual valve on the sieve bypass loop labeled V8.
  - turn on the compressor.
- Turn off the Leybold Vakuum gauges and the controller of the turbomolecular pump.

- When the glovebox is at atmospheric pressure, close the Ar inlet by turning off the button labeled “EV remplissage”. Be careful not to let the pressure in the glovebox go above the atmospheric pressure: there are no poppet valves.

- Close the isolation valve between the Bourdon gauge.

Regulating the pressure

- Ensure the setup pressure of the third reducing valve from the left of the Ar control panel is set to 3 bar.

- Turn on the diaphragm pump.

- Connect the molecular sieve to the purification circuit: open the manual valves labeled V9 and V10 its control panel and close the bypass valve (labeled V8).

- Open the isolating valve above the Photohelic by switching on the button labeled “capteurs gaz HP”.

- Set the lower and upper pressure on the Photohelic, *e.g.*, +0.2 and +0.7, respectively.

- Open the isolating valves at the connection between the gas purification circuit and the glovebox by switching on the buttons labeled “entrée Hubert -> Odile” and “sortie Odile -> Hubert”.

- Turn on the Photohelic and the power supply of its associated electro-pneumatic valves by switching on the button labeled “photohelic”.

- Close the bypass valve by switching off the button labeled “contournement”.

Usage of the glovebox

- Turn on the light (the red button is at the top right side of the door).

- Remove the plugs which isolate the gloves and lay them down on the plate inside the glovebox. For this operation, it may be convenient temporarily to turn down the setup pressures on the Photohelic.

- Put your hands in the gloves and run experiments! Be careful: the pressure regulation system has quite a large response time, so the hands must be entered and taken out of the glovebox slowly.

Spin-coater

- Open the manual isolating valve on the pipe between the spin-coater and its pump (on the left side of the door).
- Turn on the spin-coater vacuum pump by switching on the button labeled “pompe tournette”.
- Turn on the spin-coater by switching on the button labeled “alimentation tournette”. This also turns on the power supply for the magnetic stirrer.
- Put a sample on the substrate holder, drop the solution to be deposited and close the cover.
- Start the program on the blue control panel of the spin-coater.[5]
- When the depositions are done, turn off the spin-coater and the pump, and close the isolating valve between the two.

Standby

- Turn off the Photohelic by switching off the button labeled “photohelic”.
- Close the isolating valve above the Photohelic by switching off the button labeled “capteur gaz HP”.

Stopping the gas purification circuit

- Open the glovebox bypass valve by switching on the button labeled “contournement”.
- Close the valves between the glovebox and the gas purification circuit by switching off the buttons labeled “entrée Hubert -> Odile” and “sortie Odile -> Hubert”.
- Turn off the compressor.
- Close the manual valves labeled V9 and V10, which isolate the molecular sieve.
- Turn off the refrigerating system for the molecular sieve.
- Turn off the diaphragm pump.

[5]For more details, refer to the operation manual of the SCS G3P spin-coater

Safe state

- Close the main valve on the Ar pipe (on the wall).
- Close the main valve on the compressed air pipe (on the wall).
- Close the valves on the water cooling system for the turbomolecular pump.
- Switch off the main power supply below the evaporator.

Notations

c	Speed of light in vacuum	$299\,792\,458\,\mathrm{m\,s^{-1}}$
h	Planck constant	$6.6262 \times 10^{-34}\,\mathrm{J\,s}$
k_B	Boltzmann constant	$1.38 \times 10^{-23}\,\mathrm{J\,K^{-1}}$
q	Charge of the electron	$1.602\,176\,53 \times 10^{-19}\,\mathrm{C}$
χ_m	Electron affinity of the material m	eV
ϕ_m	Work function of the material m	eV
μ_n	Mobility of electrons	$\mathrm{cm^2\,V^{-1}\,s^{-1}}$
μ_p	Mobility of holes	$\mathrm{cm^2\,V^{-1}\,s^{-1}}$
σ	Electrical conductivity	$\Omega^{-1}\,\mathrm{cm^{-1}}$
σ	standard deviation	
E_a	Activation energy	eV
E_g	Bandgap width	eV
E_c	Energy of the lower edge of the conduction band	eV
E_v	Energy of the upper edge of the valence band	eV
J_sc	Short-circuit current density	$\mathrm{A\,cm^{-2}}$
n	Density of free electrons	$\mathrm{cm^{-3}}$
n	Quality factor of a diode	
p	Density of free holes	$\mathrm{cm^{-3}}$
R_s	Series resistance	Ω
R_sh	Shunt resistance	Ω
T	Absolute temperature	K
V_oc	Open-circuit voltage	V
$\bar{x}$	Average value	
CVD	Chemical Vapor Deposition	
DSSC	Dye-Sensitized Solar Cells	
EDX	Energy-Dispersive X-Ray Analysis	
HRTEM	High-Resolution Transmission Electron Microscopy	
ITO	Indium Tin Oxide (more precisely, tin-doped indium oxide: $\mathrm{In_2O_3}$:Sn)	

PCE	Power Conversion Efficiency
P3HT	poly(3-hexylthiophene)
PECVD	Plasma-Enhanced Chemical Vapor Deposition
PEDOT:PSS	poly(3,4-ethylenedioxythiophene):poly(styrenesulfonate)
RF-PECVD	Radio-frequency PECVD
SAED	Selected Area Electron Diffraction
SEM	Scanning Electron Microscopy
TCO	Transparent Conductive Oxide
TEM	Transmission Electron Microscopy
VLS	Vapor-Liquid-Solid
XPS	X-Ray Photoelectron Spectroscopy

Bibliography

[ACB99] A. C. Arango, S. A. Carter, and P. J. Brock. “Charge transfer in photovoltaics consisting of interpenetrating networks of conjugated polymer and TiO2 nanoparticles”. In: *Applied Physics Letters* 74.12 (1999). Pp. 1698–1700. DOI: 10.1063/1.123659.

[Ack02] Jörg Ackermann. “Study of the growth and the electronic properties of thin films based on oligothiophenes : Influence of the molecule structure”. PhD thesis. Université d’Aix-Marseille 2. Faculté des Sciences, 2002.

[Ael+07] P. Aella et al. “Influence of Plasma Stimulation on Si Nanowire Nucleation and Orientation Dependence”. In: *Advanced Materials* 19.18 (2007). Pp. 2603–2607. DOI: 10.1002/adma.200602944.

[Aga+07] P. Agarwal et al. “Breakdown Enhancement in Silicon Nanowire p-n Junctions”. In: *Nano Letters* 7.4 (2007). Pp. 896–899. DOI: 10.1021/nl062681n.

[AI+05] Maher Al-Ibrahim et al. “The influence of the optoelectronic properties of poly(3-alkylthiophenes) on the device parameters in flexible polymer solar cells”. In: *Organic Electronics* 6 (2005). Pp. 65–77. DOI: 10.1016/j.orgel.2005.02.004.

[Alb+06] J. Albuschies et al. “High-density silicon nanowire growth from self-assembled Au nanoparticles”. In: *Microelectronic Engineering* 83.4-9 SPEC. ISS. (2006). Pp. 1530–1533. DOI: 10.1016/j.mee.2006.01.145.

[Ale+06] P.-J. Alet et al. “Hybrid Solar Cells Based on Thin-Film Silicon and P3HT”. In: *European Physical Journal B - Applied Physics* 36.3 (Dec. 2006). Pp. 231–234. DOI: 10.1051/epjap:2006145.

[Ale+08a] Pierre-Jean Alet et al. “In-situ generation of indium catalyst to grow crystalline silicon nanowires at low temperature on ITO”. In: *Journal of Materials Chemistry* 18 (2008). Pp. 5187–5189. DOI: 10.1039/b813046a.

[Ale+08b] Pierre-Jean Alet et al. “Transition from thin gold layers to nano-islands on TCO for catalyzing the growth of one-dimensional nanostructures”. In: *Physica Status Solidi (a)* 205.6 (2008). Pp. 1429–1434. DOI: 10.1002/pssa.200778158.

[AMR04] M.D. Abramoff, P.J. Magelhaes, and S.J. Ram. “Image Processing with ImageJ”. In: *Biophotonics International* 11.7 (2004). Pp. 36–42.

[AMS95] A. Al-Mohamad and M. Soukieh. “Solar cells and high efficiency photodiodes having metal-organic thin film-semiconductor structures”. In: *Thin Solid Films* 271.1-2 (Dec. 1995). Pp. 132–137. DOI: 10.1016/0040-6090(95)06904-6.

[And59] Paul A. Anderson. “Work Function of Gold”. In: *Phys. Rev.* 115.3 (Aug. 1959). P. 553. DOI: 10.1103/PhysRev.115.553.

[And62] R. L. Anderson. “Experiments on Ge-GaAs heterojunctions”. In: *Solid-State Electronics* 5.5 (1962). Pp. 341–344. DOI: 10.1016/0038-1101(62)90115-6.

[APC09] Pierre-Jean Alet, Serge Palacin, and Pere Roca i Cabarrocas. “Low-temperature growth of nano-structured silicon thin films on ITO initiated by metal catalysts”. In: *Thin Solid Films* accepted (2009).

[Arb+07] Jordi Arbiol et al. “Influence of Cu as a catalyst on the properties of silicon nanowires synthesized by the vapour-solid-solid mechanism”. In: *Nanotechnology* 18.30 (2007). 305606 (8pp). DOI: 10.1209/0957-4484/18/305606.

[Att02] André-Jean Attias. “Polymères conjugués et polymères conducteurs électroniques”. In: *Traité Électronique*. E 1862. Techniques de l’Ingénieur, 2002.

[BÖ90] Karl W. Böer. “Survey of Semiconductor Physics”. In: Van Nostrand Reinhold, 1990. Chap. Deep Level Centers, pp. 576–619.

[Ban+87] Ratnabali Banerjee et al. “Degradation of tin-doped indium-oxide film in hydrogen and argon plasma”. In: *Journal of Applied Physics* 62.3 (1987). Pp. 912–916. DOI: 10.1063/1.339699.

[BG71] G. Bootsma and H. J. Gassen. “A quantitative study on the growth of silicon whiskers from silane and germanium whiskers from germane”. In: *Journal of Crystal Growth* 10.3 (Aug. 1971). Pp. 223–234. DOI: 10.1016/0022-0248(71)90188-6.

[BH05] G. P. Bartholomew and A. J. Heeger. “Infiltration of Regioregular Poly[2,2-(3-hexylthiopene)] into Random Nanocrystalline TiO_2 Networks”. In: *Advanced Functional Materials* 15.4 (2005). Pp. 677–682. DOI: 10.1002/adfm.200400277.

[BJ84] R. Botet and R. Jullien. “Size distribution of clusters in irreversible kinetic aggregation”. In: *Journal of Physics A: Mathematical and General* 17.12 (1984). Pp. 2517–2530. DOI: 10.1209/0305-4470/17/2517.

[BL88] F. G. Bell and L. Ley. “Photoemission study of SiO_x ($0 \leq x \leq 2$) alloys”. In: *Phys. Rev. B* 37.14 (May 1988). Pp. 8383–8393. DOI: 10.1103/PhysRevB.37.8383.

[BRN07] Johann Bouclé, Punniamoorthy Ravirajan, and Jenny Nelson. “Hybrid polymer-metal oxide thin films for photovoltaic applications.” In: *Journal of Materials Chemistry* 17.30 (2007). Pp. 3141–3153. DOI: 10.1039/b706547g.

[BW61] P. Benjamin and C. Weaver. “Adhesion of evaporated metal films on glass”. In: *Proceedings of the Royal Society of London series A - Mathematical and physical sciences* 261.130 (1961). Pp. 516–531.

[Cab+07] Pere Roca i Cabarrocas et al. “Synthesis of silicon nanocrystals in silane plasmas for nanoelectronics and large area electronic devices”. In: *Journal of Physics D: Applied Physics* 40.8 (2007). Pp. 2258–2266. DOI: 10.1209/0022-3727/40/2258.

[Cab+90] P. Roca i Cabarrocas et al. “Improving tin oxide/hydrogenated amorphous silicon interfaces for solar cell applications”. In: *Conference Record of the Twenty First IEEE Photovoltaic Specialists Conference* 2 (1990). Pp. 1610–1613. DOI: 10.1109/PVSC.1990.111881.

[Cab+91] P. Roca i Cabarrocas et al. “A Fully Automated Hot-Wall Multiplasma-Monochamber Reactor For Thin-Film Deposition”. In: *Journal of Vacuum Science & Technology A-Vacuum Surfaces and Films* 9.4 (July 1991). Pp. 2331–2341. DOI: 10.1116/1.577318.

[Cao+06] L. Cao et al. “Instability and Transport of Metal Catalyst in the Growth of Tapered Silicon Nanowires”. In: *Nano Letters* 6.9 (2006). Pp. 1852–1857. DOI: 10.1021/nl060533r.

[Car+04] J. D. Carey et al. “Formation of Three Dimensional Ni Nanostructures for Large Area Catalysts”. In: *Material Research Society Symposia*. Vol. 820. Material Research Society. 2004. P. 357.

[CFP54] D. M. Chapin, C. S. Fuller, and G. L. Pearson. “A New Silicon p-n Junction Photocell for Converting Solar Radiation into Electrical Power”. In: *Journal of Applied Physics* 25.5 (1954). Pp. 676–677. DOI: 0.1063/1.1721711.

[CGH96] Pere Roca i Cabarrocas, Patrick Gay, and Aomar Hadjadj. “Experimental evidence for nanoparticle deposition in continuous argon–silane plasmas: Effects of silicon nanoparticles on film properties”. In: *J. Vac. Sci. Technol. A*. Vol. 14. 2. Wickenburg, Arizona (USA): AVS, 1996. Pp. 655–659. DOI: 10.1116/1.580162.

[CGM05] Christophe Cardinaud, Antoine Goullet, and Tiberiu Minea. “Plasmas froids — Réactivité en volume et en surface”. In: ed. by Françoise Massines. Publications de l’Université de Saint-Étienne, 2005. Chap. Introduction aux techniques d’analyse de surface, pp. 181–234.

[Cha+04] J. F. Chang et al. “Enhanced Mobility of poly(3-hexylthiophene) transistors by spin-coating from high-boiling-point solvents”. In: *Chemistry of Materials* 16.23 (2004). Pp. 4772–4776. DOI: 10.1021/cm049617w.

[Cha+06] Ying-Lan Chang et al. “Controlled formation of individually seeded, electrically addressable silicon nanowire arrays for device integration”. In: *Applied Physics Letters* 89.22 (2006). P. 223123. DOI: 10.1063/1.2398900.

[Che+07] Yanzhao Cheng et al. “Fabrication and electrical, photosensitive properties of p-poly(9,9-diethylfluorene)/n-silicon nanowire heterojunction”. In: *Journal of Applied Physics* 102.8 (2007). P. 083516. DOI: 10.1063/1.2798494.

[Chi+03] D. Chirvase et al. “Electrical and optical design and characterisation of regioregular poly(3-hexylthiophene-2,5diyl)/fullerene-based heterojunction polymer solar cells”. In: *Synthetic Metals* 138 (2003). Pp. 299–304. DOI: 10.1016/S0379-6779(03)00027-4.

[Cho+06] Shinuk Cho et al. “Thermal annealing-induced enhancement of the field-effect mobility of regioregular poly(3-hexylthiophene) films”. In: *Journal of Applied Physics* 100.11 (2006). P. 114503. DOI: 10.1063/1.2400796.

[CI03] E. Centurioni and D. Iencinella. “Role of front contact work function on amorphous silicon/crystalline silicon heterojunction solar cell performance”. In: *Electron Device Letters, IEEE* 24.3 (2003). Pp. 177–179. ISSN: 0741-3106. DOI: 10.1109/LED.2003.811405.

[Civ+04] Y. Civale et al. “Aspects of Silicon Nanowire Synthesis by Aluminum-Catalyzed Vapor-Liquid-Solid Mechanism”. In: *Proceedings of 7th Annual Workshop on Semiconductor Advances for Future Electronics (SAFE 2004)*. STW, 2004. Pp. 692–696.

[CLG67] T. L. Chu, C. H. Lee, and G. A. Gruber. “The Preparation and Properties of Amorphous Silicon Nitride Films”. In: *J. Electrochem. Soc.* 114.7 (July 1967). Pp. 717–722. DOI: 10.1149/1.2426715.

[Coa+05] K. M. Coakley et al. “Ordered organic-inorganic bulk heterojunction photovoltaic cells”. In: *MRS Bulletin* 30.1 (2005). Pp. 37–40.

[Cor+07] V. Coropceanu et al. “Charge Transport in Organic Semiconductors”. In: *Chemical Reviews* 107.4 (2007). Pp. 926–952. DOI: 10.1021/cr050140x.

[CQ+07] Mariano Campoy-Quiles et al. “Dimensionality of electronic excitations in organic semiconductors: A dielectric function approach”. In: *Physical Review B (Condensed Matter and Materials Physics)* 76.23 (2007). P. 235206. DOI: 10.1103/PhysRevB.76.235206.

[CR92] Tian An Chen and Reuben D. Rieke. “The first regioregular head-to-tail poly(3-hexylthiophene-2,5-diyl) and a regiorandom isopolymer: nickel versus palladium catalysis of 2(5)-bromo-5(2)-(bromozincio)-3-hexylthiophene polymerization”. In: *Journal of the American Chemical Society* 114.25 (1992). Pp. 10087–10088. ISSN: 0002-7863. DOI: 10.1021/ja00051a066.

[CSS66] D. R. Collins, D. K. Schroder, and C. T. Sah. “Gold Diffusivities in SiO_2 and Si Using the MOS Structure”. In: *Applied Physics Letters* 8.12 (1966). Pp. 323–325. DOI: 10.1063/1.1754459.

[Cur+97] N. J. Curson et al. “Interaction of silane with Cu(111): Surface alloy and molecular chemisorbed phases”. In: *Phys. Rev. B* 55.16 (Apr. 1997). P. 10819. DOI: 10.1103/PhysRevB.55.10819.

[CWR95] T. A. Chen, X. M. Wu, and R. D. Rieke. “Regiocontrolled Synthesis of Poly(3-Alkylthiophenes) Mediated by Rieke Zinc - Their Characterization and Solid-State Properties”. In: *Journal of the American Chemical Society* 117.1 (1995). Pp. 233–244. DOI: 10.1021%2Fja00106a027.

[Day+07] J.-F. Dayen et al. “Electronic transport of silicon nanowires grown in porous Al_2O_3 membrane”. In: *Applied Physics Letters* 90.17 (2007). P. 173110. DOI: 10.1063/1.2731681.

[DB+06] Remi De Bettignies et al. “Accelerated lifetime measurements of P3HT:PCBM solar cells”. In: *Synthetic Metals* 156.7-8 (2006). Pp. 510–513. DOI: 10.1016/j.synthmet.2005.06.016.

[DL07] Jérôme Damon-Lacoste. “Vers une ingénierie de bandes des cellules solaires à hétérojonctions a-Si:H/c-Si. Rôle prépondérant de l’hydrogène.” PhD thesis. École polytechnique (Palaiseau, France), 2007.

[DPM93] U. Diebold, J.-M. Pan, and T. E. Madey. “Growth mode of ultrathin copper overlayers on TiO_2(110)”. In: *Phys. Rev. B* 47.7 (Feb. 1993). Pp. 3868–3876. DOI: 10.1103/PhysRevB.47.3868.

[Dre+89] B. Drevillon et al. “In situ investigation of the optoelectronic properties of transparent conducting oxide/amorphous silicon interfaces”. In: *Applied Physics Letters* 54.21 (1989). Pp. 2088–2090. DOI: 10.1063/1.101511.

[FA06] Vasilis Fthenakis and Erik Alsema. “Photovoltaics Energy Payback Times, Greenhouse Gas Emissions and External Costs: 2004–early 2005 Status”. In: *Progress in Photovoltaics: Research and Applications* 14 (2006). Pp. 275–280. DOI: 10.1002/pip.706.

[Fan+06] Hui Fang et al. “Silver catalysis in the fabrication of silicon nanowire arrays”. In: *Nanotechnology* 17.15 (2006). Pp. 3768–3774. DOI: 10.1209/0957-4484/17/3768.

[Fir+06] Muriel Firon et al. “Photoactive nanocomposite and method for the production thereof”. Pat. WO/2006/018575. Feb. 2006. URL: http://www.freepatentsonline.com/WO2006018575.html.

[FKS84] S. R. Forrest, M. L. Kaplan, and P. H. Schmidt. “Organic-on-inorganic semiconductor contact barrier diodes. I. Theory with applications to organic thin films and prototype devices”. In: *Journal of Applied Physics* 55.6 (1984). Pp. 1492–1507. DOI: 10.1063/1.333407.

[Fon+07] A. FontcubertaiMorral et al. “Synthesis of Silicon Nanowires with Wurtzite Crystalline Structure by Using Standard Chemical Vapor Deposition”. In: *Advanced Materials* 19.10 (2007). Pp. 1347–1351. DOI: 10.1002/adma.200602318.

[Fon81] Stephen J. Fonash. *Solar Cell Device Physics*. Energy science and engineering: resources, technology, management. Academic Press, 1981.

[For+82] S. R. Forrest et al. “Organic-on-inorganic semiconductor contact barrier devices”. In: *Applied Physics Letters* 41.1 (1982). Pp. 90–93. DOI: 10.1063/1.93300.

[Fri07] Martin Frimmer. “Growth of Silicon Nanowires with Alternative Catalysts”. MA thesis. Physik-Department der Technischen Universität München, 2007.

[FSF88] Albert Feldman, Y. N. Sun, and E. N. Farabaugh. “Bonding structure of silicon oxide films”. In: *Journal of Applied Physics* 63.6 (1988). Pp. 2149–2151. DOI: 10.1063/1.341072.

[FW96] Alfonso Franciosi and Chris G. Van de Walle. “Heterojunction band offset engineering”. In: *Surface Science Reports* 25.1-4 (1996). Pp. 1–140. DOI: 10.1016/0167-5729(95)00008-9.

[FWZ06] Hong Jin Fan, Peter Werner, and Margit Zacharias. “Semiconductor Nanowires: From Self-Organization to Patterned Growth”. In: *Small* 2.6 (2006). Pp. 700–717. DOI: 10.1002/smll.200500495.

[GHS03] Adolf Goetzberger, Christopher Hebling, and Hans-Werner Schock. “Photovoltaic materials, history, status and outlook”. In: *Materials Science and Engineering: R: Reports* 40.1 (Jan. 2003). Pp. 1–46. DOI: 10.1016/S0927-796X(02)00092-X.

[Got+95] S. Gota et al. “Influence of the substrate oxidation state in the growth of copper clusters on Al_2O_3(0001) surface: a XANES and EXAFS study”. In: *Surface Science* 323.1-2 (Jan. 1995). Pp. 163–174. DOI: 10.1016/0039-6028(94)00638-5.

[Gow+06a] V. Gowrishankar et al. “Fabrication of densely packed, well-ordered, high-aspect-ratio silicon nanopillars over large areas using block copolymer lithography”. In: *Thin Solid Films* 513.1-2 (2006). Pp. 289–294. DOI: 10.1016/j.tsf.2006.01.064.

[Gow+06b] Vignesh Gowrishankar et al. “Exciton splitting and carrier transport across the amorphous-silicon/polymer solar cell interface”. In: *Applied Physics Letters* 89.25 (2006). P. 252102. DOI: 10.1063/1.2408641.

[Gow+08] Vignesh Gowrishankar et al. “Exciton harvesting, charge transfer, and charge-carrier transport in amorphous-silicon nanopillar/polymer hybrid solar cells”. In: *Journal of Applied Physics* 103.6 (2008). P. 064511. DOI: 10.1063/1.2896583.

[GPA96] N. C. Greenham, X. Peng, and A. P. Alivisatos. “Charge separation and transport in conjugated-polymer/semiconductor-nanocrystal composites studied by photoluminescence quenching and photoconductivity”. In: *Physical Review B* 54.24 (1996). Pp. 17628–17637. DOI: 10.1103/PhysRevB.54.17628.

[Gre+08] Martin A. Green et al. “Short Communication Solar cell efficiency tables (Version 31)”. In: *Progress in Photovoltaics: Research and Applications* 16.1 (2008). Pp. 61–67. DOI: 10.1002/pip.808.

[Gri+07] H. Griffiths et al. “Plasma assisted growth of nanotubes and nanowires”. In: *Surface and Coatings Technology* 201.22-23 (Sept. 2007). Pp. 9215–9220. DOI: 10.1016/j.surfcoat.2007.04.067.

[GSM07] Chiatzun Goh, Shawn R. Scully, and Michael D. McGehee. “Effects of molecular interface modification in hybrid organic-inorganic photovoltaic cells”. In: *Journal of Applied Physics* 101.11 (2007). P. 114503. DOI: 10.1063/1.2737977.

[Ham+00] E. A. G. Hamers et al. “Contribution of ions to the growth of amorphous, polymorphous, and microcrystalline silicon thin films”. In: *Journal of Applied Physics* 88.6 (2000). Pp. 3674–3688. DOI: 10.1063/1.1289523.

[Ham+05] B. H. Hamadani et al. “Doping-dependent charge injection and band alignment in organic field-effect transistors”. In: *Physical Review B* 72.23 (2005). Pp. 1–5. DOI: 10.1103/PhysRevB.72.235302.

[Ham07] Behrang Homayoun Hamadani. “Electronic Charge Injection And Transport In Organic Field-Effect Transistors”. PhD thesis. Rice University, Houston, Texas, 2007.

[Har+80] S. Haridoss et al. “Diffusion of gallium in silicon”. In: *Journal of Applied Physics* 51.11 (1980). Pp. 5833–5837. DOI: 10.1063/1.327541.

[Hau+08] Jens A. Hauch et al. “Flexible organic P3HT:PCBM bulk-heterojunction modules with more than 1 year outdoor lifetime”. In: *Solar Energy Materials and Solar Cells* 92.7 (July 2008). Pp. 727–731. DOI: 10.1016/j.solmat.2008.01.004.

[HC07] L. Hu and G. Chen. “Analysis of Optical Absorption in Silicon Nanowire Arrays for Photovoltaic Applications”. In: *Nano Letters* 7.11 (2007). Pp. 3249–3252. DOI: 10.1021/nl071018b.

[HC98] S. Hamma and P. Roca i Cabarrocas. “Low temperature growth of highly crystallized silicon thin films using hydrogen and argon dilution”. In: *Journal of Non-Crystalline Solids* 227-230.Part 2 (May 1998). Pp. 852–856. DOI: 10.1016/S0022-3093(98)00342-1.

[HDA02] W. U. Huynh, J. J. Dittmer, and A. P. Alivisatos. “Hybrid nanorod-polymer solar cells”. In: *Science* 295.5564 (2002). Pp. 2425–2427. DOI: 10.1126/science.1069156.

[HGM91] J. C. van den Heuvel, M. J. Geerts, and J. W. Metselaar. “The relation between the optical properties and the hydrogen concentration in a-Si:H”. In: *Solar Energy Materials* 22.2-3 (July 1991). Pp. 185–194. DOI: 10.1016/0165-1633(91)90016-E.

[Hir+88] Takashi Hirao et al. “Coagulation of In Atoms in Hydrogenated Amorphous Silicon Islands Deposited on ITO Films”. In: *Japanese Journal of Applied Physics* 27.8 (Aug. 1988). Pp. L1368–L1370. DOI: 10.1143/JJAP.27.L1368.

[HL02] J.A. Haber and N.S. Lewis. “Infrared and X-ray Photoelectron Spectroscopic Studies of the Reactions of Hydrogen-Terminated Crystalline Si(111) and Si(100) Surfaces with Br_2, I_2, and Ferrocenium in Alcohol Solvents”. In: *J. Phys. Chem. B* 106.14 (2002). Pp. 3639–3656. DOI: 10.1021/jp0102872.

[Hoc+05] A.I. Hochbaum et al. “Controlled Growth of Si Nanowire Arrays for Device Integration”. In: *Nano Letters* 5.3 (2005). Pp. 457–460. ISSN: 1530-6984. DOI: 10.1021/nl047990x.

[HOK95] Katsuyoshi Hoshino, Takahiro Ogata, and Hiroshi Kokado. “Improvement in Junction Properties of a n-Si/poly(3-methylthiophene) Heterojunction by Post-Treatment with aq.HF”. In: *Japanese Journal of Applied Physics* 34.9B (Sept. 1995). Pp. L1241–L1243. DOI: 10.1143/JJAP.34.L1241.

[Iac+07] F. Iacopi et al. “Plasma-enhanced chemical vapour deposition growth of Si nanowires with low melting point metal catalysts: an effective alternative to Au-mediated growth”. In: *Nanotechnology* 18.50 (2007). 505307 (7pp). DOI: 10.1209/0957-4484/18/505307.

[Ist+98] Andrei A. Istratov et al. “Intrinsic Diffusion Coefficient of Interstitial Copper in Silicon”. In: *Phys. Rev. Lett.* 81.6 (Aug. 1998). Pp. 1243–. DOI: 10.1103/PhysRevLett.81.1243.

[IW98] A.A. Istratov and E.R. Weber. “Electrical properties and recombination activity of copper, nickel and cobalt in silicon”. In: *Applied Physics A: Materials Science and Processing* 66.2 (Feb. 1998). Pp. 123–136. DOI: 10.1007/s003390050649.

[Jac91] Bret Jackson. “A semiclassical study of He, Ne, and Ar sticking on metal surfaces”. In: *The Journal of Chemical Physics* 94.7 (1991). Pp. 5126–5134. DOI: 10.1063/1.460550.

[JH78] S. C. Jain and A. E. Hughes. “Ostwald ripening and its application to precipitates and colloids in ionic crystals and glasses”. In: *Journal of Materials Science* 13.8 (Aug. 1978). Pp. 1611–1631. DOI: 10.1007/BF00548725.

[KA98] A. von Keudell and J. R. Abelson. “The interaction of atomic hydrogen with very thin amorphous hydrogenated silicon films analyzed using in situ real time infrared spectroscopy: Reaction rates and the formation of hydrogen platelets”. In: *Journal of Applied Physics* 84.1 (1998). Pp. 489–495. DOI: 10.1063/1.368082.

[KCM06] B. Kalache, P. Roca i Cabarrocas, and A. Fontcuberta i Morral. “Observation of incubation times in the nucleation of silicon nanowires obtained by the vapor-liquid-solid method”. In: *Japanese Journal of Applied Physics* 45.4-7 (2006). P. L190. DOI: 10.1143/JJAP.45.L190.

[KDG86] Satyendra Kumar, B. Drevillon, and C. Godet. “In situ spectroscopic ellipsometry study of the growth of microcrystalline silicon”. In: *Journal of Applied Physics* 60.4 (1986). Pp. 1542–1544. DOI: 10.1063/1.337289.

[Ke+05] Lin Ke et al. “Au-ITO anode for efficient polymer light-emitting device operation”. Ed. by R.S. Kumar. In: *Photonics Technology Letters, IEEE* 17.3 (2005). Pp. 543–545. DOI: 10.1109/LPT.2004.841031.

[KHH93] Hiroshi Kokado, Fumio Hosokawa, and Katsuyoshi Hoshino. “Properties of Heterojunction of Si/Poly(3-methylthiophene) as a Function of Polymerization Condition”. In: *Japanese Journal of Applied Physics* 32 (1993). Pp. 189–194. DOI: 10.1143/JJAP.32.189.

[Kim+06] Y. Kim et al. “A strong regioregularity effect in self-organizing conjugated polymer films and high-efficiency polythiophene:fullerene solar cells”. In: *Nature Materials* 5.3 (2006). Pp. 197–203. DOI: 10.1038/nmat1574.

[KM70] H. R. Koenig and L. I. Maissel. “Application of RF Discharges to Sputtering”. In: *IBM Journal of Research and Development* 14.2 (1970). P. 168.

[Kod+06] S. Kodambaka et al. “Diameter-Independent Kinetics in the Vapor-Liquid-Solid Growth of Si Nanowires”. In: *Physical Review Letters* 96.9 (2006). P. 096105. DOI: 10.1103/PhysRevLett.96.096105.

[KRP02] O. Krause, H. Ryssel, and P. Pichler. “Determination of aluminum diffusion parameters in silicon”. In: *Journal of Applied Physics* 91.9 (2002). Pp. 5645–5649. DOI: 10.1063/1.1465501.

[Kub81] Osamu Kuboi. “Degradation of ITO Film in Glow-Discharge Plasma”. In: *Japanese Journal of Applied Physics* 20 (1981). Pp. L783–L786. DOI: 10.1143/JJAP.20.L783.

[Kwo+04] C. Y. Kwong et al. “Poly(3-hexylthiophene):TiO_2 nanocomposites for solar cell applications”. In: *Nanotechnology* 15.9 (2004). Pp. 1156–1161. DOI: 10.1088/0957-4484/15/9/008.

[Lai+07] Darin W. Laird et al. “Advances in Plexcore active layer technology systems for organic photovoltaics: roof-top and accelerated lifetime analysis of high performance organic photovoltaic cells”. In: *Proceedings of SPIE – Organic Photovoltaics VIII*. Ed. by Zakya H. Kafafi and Paul A. Lane. Vol. 6656. 1. San Diego, CA, USA: SPIE, 2007. P. 66560X. DOI: 10.1117/12.734711.

[Lay+95] N. Layadi et al. “Real-time spectroscopic ellipsometry study of the growth of amorphous and microcrystalline silicon thin films prepared by alternating silicon deposition and hydrogen plasma treatment”. In: *Phys. Rev. B* 52.7 (Aug. 1995). Pp. 5136–5143. DOI: 10.1103/PhysRevB.52.5136.

[Lee+04] M.V. Lee et al. “Molecular Modeling of Alkyl Monolayers on the Si(100)-2 x 1 Surface”. In: *Langmuir* 20.21 (2004). Pp. 9108–9113. DOI: 10.1021/la048894e.

[LeG+01] L. J. LeGore et al. “Aggregation and sticking probability of gold on tungsten trioxide films”. In: *Sensors and Actuators B: Chemical* 76.1-3 (June 2001). Pp. 373–379. DOI: 10.1016/S0925-4005(01)00638-4.

[Li+98] A. P. Li et al. “Hexagonal pore arrays with a 50–420 nm interpore distance formed by self-organization in anodic alumina”. In: *Journal of Applied Physics* 84.11 (1998). Pp. 6023–6026. DOI: 10.1063/1.368911.

[LL06] Wei Lu and Charles M Lieber. “Semiconductor nanowires”. In: *Journal of Physics D: Applied Physics* 39.21 (2006). R387–R406. DOI: 10.1209/0022-3727/39/R387.

[Lom+06] I. Lombardi et al. “Synthesis of high density, size-controlled Si nanowire arrays via porous anodic alumina mask”. In: *Chemistry of Materials* 18.4 (2006). Pp. 988–991. DOI: 10.1021/cm052435x.

[Mas+93] Atsushi Masuda et al. “Spectroscopic Study on N_2O-Plasma Oxidation of Hydrogenated Amorphous Silicon and Behavior of Nitrogen”. In: *Japanese Journal of Applied Physics* 32 (1993). Pp. 2794–2802. DOI: 10.1143/JJAP.32.2794.

[Mas98] T.B. Massalski. *Binary Alloy Phase Diagrams*. Ed. by T.B. Massalski. 2nd ed. Vol. 1. ASM International, 1998.

[Mat+06] M. Mattila et al. “Catalyst-free growth of In(As)P nanowires on silicon”. In: *Applied Physics Letters* 89.6 (2006). P. 063119. DOI: 10.1063/1.2336599.

[Mat98] H. Matsumura. “Formation of silicon-based thin films prepared by catalytic chemical vapor deposition (Cat-CVD) method”. In: *Japanese Journal of Applied Physics* 37.6A (June 1998). Pp. 3175–3187. ISSN: 0021-4922. DOI: http://jjap.ipap.jp/link?JJAP/37/3175/.

[MCC04] A. Fontcuberta i Morral, P. Roca i Cabarrocas, and C. Clerc. “Structure and hydrogen content of polymorphous silicon thin films studied by spectroscopic ellipsometry and nuclear measurements”. In: *Phys. Rev. B* 69.12 (Mar. 2004). P. 125307. DOI: 10.1103/PhysRevB.69.125307.

[Mer+00] V. I. Merkulov et al. “Patterned growth of individual and multiple vertically aligned carbon nanofibers”. In: *Applied Physics Letters* 76.24 (2000). Pp. 3555–3557. DOI: 10.1063/1.126705.

[MP84] Robert R. McCaffrey and Paras N. Prasad. “Organic-thin-film-coated solar cells: Energy transfer between surface pyrene molecules and the silicon semiconductor substrate”. In: *Solar Cells* 11.4 (May 1984). Pp. 401–409. DOI: 10.1016/0379-6787(84)90103-0.

[Muk+07] A. K. Mukherjee et al. “Minimization of contact resistance between metal and polymer by surface doping”. In: *Journal of Physics D: Applied Physics* 40.6 (2007). Pp. 1789–1793. DOI: 10.1209/0022-3727/40/1789.

[Nel03] Jenny Nelson. *The Physics of Solar Cells*. 1st ed. London: Imperial College Press, 2003. P. 384.

[Ngu+94] H. V. Nguyen et al. “Preparation of ultrathin microcrystalline silicon layers by atomic hydrogen etching of amorphous silicon and end-point detection by real time spectroellipsometry”. In: *Applied Physics Letters* 65.26 (1994). Pp. 3335–3337. DOI: 10.1063/1.113024.

[Nov+03] T. Novikova et al. “Numerical modeling of capacitively coupled hydrogen plasmas: Effects of frequency and pressure”. In: *Journal of Applied Physics* 93.6 (2003). Pp. 3198–3206. DOI: 10.1063/1.1555678.

[OG91] Brian O’Regan and Michael Grätzel. “A low-cost, high-efficiency solar cell based on dye-sensitized colloidal TiO_2 films”. In: *Nature* 353.6346 (Oct. 1991). Pp. 737–740. DOI: 10.1038/353737a0.

[Ols+07] D.C. Olson et al. “Effect of Polymer Processing on the Performance of Poly(3-hexylthiophene)/ZnO Nanorod Photovoltaic Devices”. In: *Journal of Physical Chemistry C* 111.44 (2007). Pp. 16640–16645. ISSN: 1932-7447. DOI: 10.1021/jp0757816.

[Pas89] Friedrich Paschen. “Über die zum Funkenübergang in Luft, Wasserstoff und Kohlensäure bei verschiedenen Drucken erforderliche Potentialdifferenz”. In: *Annalen der Physik* 273.5 (1889). Pp. 69–96. DOI: 10.1002/andp.18892730505.

[PCC03] Y. Poissant, P. Chatterjee, and P. Roca i Cabarrocas. “No benefit from microcrystalline silicon n layers in single junction amorphous silicon p-i-n solar cells”. In: *Journal of Applied Physics* 93.1 (2003). Pp. 170–174. DOI: 10.1063/1.1524026.

[Pen+02] K.-Q. Peng et al. “Synthesis of Large-Area Silicon Nanowire Arrays via Self-Assembling Nanoelectrochemistry”. In: *Advanced Materials* 14.16 (2002). Pp. 1164–1167. DOI: 10.1002/1521-4095(20020816)14:16<1164::AID-ADMA1164>3.0.CO;2-E.

[Pla07] European Photovoltaic Technology Platform. *The Status of PV Industry*. Photovoltaic Fact Sheets. 2007.

[PPJ97] Anne-Marie Pointu, Jérôme Perrin, and Jacques Jolly. “Plasmas froids de décharge — Applications et diagnostic”. In: *Traité Génie électrique*. D 2 835. Techniques de l’Ingénieur, 1997.

[Pra+07] J. D. Prades et al. “Concerning the 506 cm^{-1} band in the Raman spectrum of silicon nanowires”. In: *Applied Physics Letters* 91.12 (2007). P. 123107. DOI: 10.1063/1.2786606.

[PRS03] F. Padinger, R.S. Rittberger, and N.S. Sariciftci. “Effects of Postproduction Treatment on Plastic Solar Cells”. In: *Advanced Functional Materials* 13.1 (2003). Pp. 85–88. DOI: 10.1002/adfm.200390011.

[Rav+05] P. Ravirajan et al. “Efficient charge collection in hybrid polymer/TiO_2 solar cells using poly(ethylenedioxythiophene)/polystyrene sulphonate as hole collector”. In: *Applied Physics Letters* 86.14 (2005). P. 143101. DOI: 10.1063/1.1890468.

[Rav+06] P. Ravirajan et al. “Hybrid polymer/zinc oxide photovoltaic devices with vertically oriented ZnO nanorods and an amphiphilic molecular interface layer”. In: *Journal of Physical Chemistry B* 110.15 (2006). Pp. 7635–7639. DOI: 10.1021/jp0571372.

[RC78] T. W. Ridler and S. Calvard. “Picture Thresholding Using an Iterative Selection Method”. In: *Systems, Man and Cybernetics, IEEE Transactions on* 8.8 (Aug. 1978). Pp. 630–632. ISSN: 0018-9472. DOI: 10.1109/TSMC.1978.4310039.

[Res+03] B. Ressel et al. “Wetting of Si surfaces by Au–Si liquid alloys”. In: *Journal of Applied Physics* 93.7 (2003). Pp. 3886–3892. DOI: 10.1063/1.1558996.

[Rid+00] C. Ridder et al. “Precipitation of Sn in metastable, pseudomorphic Si0.95Sn0.05 films grown by molecular beam epitaxy”. In: *Materials Science in Semiconductor Processing* 3.4 (Aug. 2000). Pp. 251–255. DOI: 10.1016/S1369-8001(00)00040-8.

[RMK03] D. B. A. Rep, A. F. Morpurgo, and T. M. Klapwijk. “Doping-dependent charge injection into regioregular poly(3-hexylthiophene)”. In: *Organic Electronics* 4.4 (Dec. 2003). Pp. 201–207. DOI: 10.1016/S1566-1199(03)00016-8.

[Roc08] Angus Rockett. *The Materials Science of Semiconductors*. 1st ed. Springer, 2008. P. 622.

[Ror+97] Shane E. Rorak et al. “Nanostructured Materials – Clusters, Composites and Thin Films”. In: ed. by Vladimir M. Shalaev and Martin Moskovits. Vol. 679. ACS Symposium Series. American Chemical Society, 1997. Chap. Changes in Thin-Metal-Film Nanostructures at Near-Ambient Temperatures, pp. 152–168.

[Sar+92] N. S. Sariciftci et al. “Photoinduced Electron Transfer from a Conducting Polymer to Buckminsterfullerene”. In: *Science* 258.5087 (1992). Pp. 1474–1476. DOI: 10.1126/science.258.5087.1474.

[Sch+04] M. Schubert et al. “Carrier redistribution in organic/inorganic (poly(3,4-ethylenedioxy thiophene/poly(styrenesulfonate)polymer)-Si) heterojunction determined from infrared ellipsometry”. In: *Applied Physics Letters* 84.8 (2004). Pp. 1311–1313. DOI: 10.1063/1.1649822.

[SF88] F. F. So and S. R. Forrest. “Dependence of the electrical characteristics of organic-on-inorganic semiconductor contact barrier diodes on organic thin-film composition”. In: *Journal of Applied Physics* 63.2 (1988). Pp. 442–446. DOI: 10.1063/1.340261.

[SG06] B. Sun and N. C. Greenham. “Improved efficiency of photovoltaics based on CdSe nanorods and poly(3-hexylthiophene) nanofibers”. In: *Physical Chemistry Chemical Physics* 8.30 (2006). Pp. 3557–3560. DOI: 10.1039/b604734n.

[Sha+01] Sean E. Shaheen et al. “2.5% efficient organic plastic solar cells”. In: *Applied Physics Letters* 78.6 (2001). Pp. 841–843. DOI: 10.1063/1.1345834.

[Shi+95] S. Yu. Shiryaev et al. “Pseudomorphic $Si_{1-x}Sn_x$ alloy films grown by molecular beam epitaxy on Si”. In: *Applied Physics Letters* 67.16 (1995). Pp. 2287–2289. DOI: 10.1063/1.115128.

[Sin+78] A. K. Sinha et al. “Reactive Plasma Deposited Si-N Films for MOS-LSI Passivation”. In: *J. Electrochem. Soc.* 125.4 (Apr. 1978). Pp. 601–608. DOI: 10.1149/1.2131509.

[Sir+99] H. Sirringhaus et al. “Two-dimensional charge transport in self-organized, high-mobility conjugated polymers”. In: *Nature* 401.6754 (Oct. 1999). Pp. 685–688. DOI: 10.1038/44359.

[SLC75] W. E. Spear and P. G. Le Comber. “Substitutional doping of amorphous silicon”. In: *Solid State Communications* 17.9 (Nov. 1975). Pp. 1193–1196. DOI: 10.1016/0038-1098(75)90284-7.

[SMG03] B. Q. Sun, E. Marx, and N. C. Greenham. “Photovoltaic devices using blends of branched CdSe nanoparticles and conjugated polymers”. In: *Nano Letters* 3.7 (2003). Pp. 961–963. DOI: 10.1021/nl0342895.

[Smo16] M. von Smoluchowski. “Three lectures on diffusion, Brown’s molecular movements and the coagulation of colloid parts”. In: *Physikalische Zeitschrift* 17 (1916). Pp. 585–599.

[SN04] Michelle J.S. Spencer and Graeme L. Nyberg. “Adsorption of silane and methylsilane on gold surfaces”. In: *Surface Science* 573.2 (Dec. 2004). Pp. 151–168. DOI: 10.1016/j.susc.2004.08.043.

[Sol+02] S. Solmi et al. “Investigation on indium diffusion in silicon”. In: *Journal of Applied Physics* 92.3 (2002). Pp. 1361–1366. DOI: 10.1063/1.1492861.

[Spe+02] Michelle J. S. Spencer et al. “Adsorption of SiH_4 on copper (110) and (111) surfaces”. In: *Surface Science* 505 (May 2002). Pp. 308–324. DOI: 10.1016/S0039-6028(02)01378-X.

[SSG05] V. Schmidt, S. Senz, and U. Gosele. “Diameter-Dependent Growth Direction of Epitaxial Silicon Nanowires”. In: *Nano Lett.* 5.5 (2005). Pp. 931–935. DOI: 10.1021/nl050462g.

[STA99] Kunihiro Suzuki, Hiroko Tashiro, and Takayuki Aoyama. “Diffusion coefficient of indium in Si substrates and analytical redistribution profile model”. In: *Solid-State Electronics* 43.1 (Jan. 1999). Pp. 27–31. DOI: 10.1016/S0038-1101(98)00251-2.

[Str82] R. A. Street. “Doping and the Fermi Energy in Amorphous Silicon”. In: *Physical Review Letters* 49.16 (Oct. 1982). Pp. 1187–. DOI: 10.1103/PhysRevLett.49.1187.

[Sug+00] Kiyoshi Sugiyama et al. “Dependence of indium–tin–oxide work function on surface cleaning method as studied by ultraviolet and x-ray photoemission spectroscopies”. In: *Journal of Applied Physics* 87.1 (2000). Pp. 295–298. DOI: 10.1063/1.371859.

[Sun+01] M. K. Sunkara et al. “Bulk synthesis of silicon nanowires using a low-temperature vapor–liquid–solid method”. In: *Applied Physics Letters* 79.10 (2001). Pp. 1546–1548. DOI: 10.1063/1.1401089.

[Sur+06] M. Surin et al. “Relationship between the microscopic morphology and the charge transport properties in poly(3-hexylthiophene) field-effect transistors”. In: *Journal of Applied Physics* 100.3 (2006). P. 033712. DOI: 10.1063/1.2222065.

[SWB02] Pavel Schilinsky, Christoph Waldauf, and Christoph J. Brabec. “Recombination and loss analysis in polythiophene based bulk heterojunction photodetectors”. In: *Applied Physics Letters* 81.20 (2002). Pp. 3885–3887. DOI: 10.1063/1.1521244.

[Tak+05] Kohshin Takahashi et al. “Porphyrin dye-sensitization of polythiophene in a conjugated polymer/TiOp-n hetero-junction solar cells”. In: *Synthetic Metals* 155 (2005). Pp. 51–55. DOI: 10.1016/j.synthmet.2005.05.025.

[Tas+03] Ch. Taschner et al. “Synthesis of aligned carbon nanotubes by DC plasma-enhanced hot filament CVD”. In: *Surface and Coatings Technology* 174-175 (2003). Pp. 81–87. DOI: 10.1016/S0257-8972(03)00712-6.

[Tha+07] A. K. Thakur et al. “Charge injection mechanism across the Au-poly(3-hexylthiophene-2,5-diyl) interface”. In: *Journal of Applied Physics* 101 (2007). P. 104508. DOI: 10.1063/1.2734955.

[TLG96] D. M. Tanenbaum, A. L. Laracuente, and Alan Gallagher. “Nanoparticle deposition in hydrogenated amorphous silicon films during rf plasma deposition”. In: *Applied Physics Letters* 68.12 (1996). Pp. 1705–1707. DOI: 10.1063/1.115912.

[Tou+77] Y. S. Touloukian et al. “Thermal expansion — Non-metallic solids”. In: *Thermophysical properties of matter — The TPRC Data Series*. Vol. 13. IFI/PLENUM, 1977.

[Tsa+06] Loucas Tsakalakos et al. “Interaction of Light with Si Nanowire Films”. In: *Conference Record of the 2006 IEEE 4th World Conference on Photovoltaic Energy Conversion*. Vol. 1. 2006. Pp. 111–113. DOI: 10.1109/WCPEC.2006.279376.

[Van+03] N. Vandamme et al. “Scanning probe microscopy investigation of gold clusters deposited on atomically flat substrates”. In: *Journal of Physics: Condensed Matter* 15.42 (2003). S2983–S2999. DOI: 10.1209/0953-8984/15/S2983.

[Ver+06] Jean-Marie Verilhac et al. “Effect of macromolecular parameters and processing conditions on supramolecular organisation, morphology and electrical transport properties in thin layers of regioregular poly(3-hexylthiophene)”. In: *Synthetic Metals* 156.11-13 (2006). Pp. 815–823. DOI: doi:10.1016/j.synthmet.2006.04.012.

[VHB01] G. Viera, S. Huet, and L. Boufendi. “Crystal size and temperature measurements in nanostructured silicon using Raman spectroscopy”. In: *Journal of Applied Physics* 90.8 (2001). Pp. 4175–4183. DOI: 10.1063/1.1398601.

[Vil+93] M. Villarica et al. “Application of fractals and kinetic equations to cluster formation”. In: *The Journal of Chemical Physics* 98.6 (1993). Pp. 4610–4625. DOI: 10.1063/1.464989.

[Voz+07] C. Voz et al. “Photodiodes based on fullerene semiconductor”. In: *Thin Solid Films* 515.19 (July 2007). Pp. 7675–7678. DOI: 10.1016/j.tsf.2006.11.160.

[VS02] P. A. T. T. van Veenendaal and R. E. I. Schropp. “Processes in silicon deposition by hot-wire chemical vapor deposition”. In: *Current Opinion in Solid State and Materials Science* 6.5 (Oct. 2002). Pp. 465–470. DOI: 10.1016/S1359-0286(02)00104-3.

[Wan+03] Qi Wang et al. “Hybrid organic-inorganic photoconductive diode”. In: *Applied Physics Letters* 83.16 (2003). Pp. 3404–3406. DOI: 10.1063/1.1619559.

[Wan+06] Yewu Wang et al. “Epitaxial growth of silicon nanowires using an aluminium catalyst”. In: *Nature Nanotechnology* 1.3 (Dec. 2006). Pp. 186–189. DOI: 10.1038/nnano.2006.133.

[WE64] R. S. Wagner and W. C. Ellis. “Vapor-Liquid-Solid Mechanism of Single Crystal Growth”. In: *Applied Physics Letters* 4.5 (1964). Pp. 89–90. DOI: 10.1063/1.1753975.

[Wes+95] J. Westwater et al. “Nanoscale silicon whiskers formed by silane/gold reaction at 335 °C”. In: *Materials Letters* 24.1-3 (June 1995). Pp. 109–112. DOI: 10.1016/0167-577X(95)00091-7.

[Wil+05] Evan L. Williams et al. “Conducting polymer and hydrogenated amorphous silicon hybrid solar cells”. In: *Applied Physics Letters* 87.22 (2005). P. 223504. DOI: 10.1063/1.2136409.

[WLN93] Benjamin C. Wiegand, Shrikant P. Lohokare, and Ralph G. Nuzzo. “Silicon-hydrogen (Si-H) bond activation on copper: reaction of silane on Cu(111)”. In: *J. Phys. Chem.* 97.44 (1993). Pp. 11553–11562. DOI: 10.1021/j100146a033.

[WS07] Weining Wang and E. A. Schiff. “Polyaniline on crystalline silicon heterojunction solar cells”. In: *Applied Physics Letters* 91.13 (2007). P. 133504. DOI: 10.1063/1.2789785.

[WSW08] Weining Wang, Eric Schiff, and Qi Wang. “Amorphous silicon/polyaniline heterojunction solar cells: Fermi levels and open-circuit voltages”. In: *Journal of Non-Crystalline Solids* 354.19-25 (May 2008). Pp. 2862–2865. DOI: 10.1016/j.jnoncrysol.2007.10.104.

[Wu+04] Y. Wu et al. “Controlled Growth and Structures of Molecular-Scale Silicon Nanowires”. In: *Nano Letters* 4.3 (2004). Pp. 433–436. DOI: 10.1021/nl035162i.

[Xia+03] Y. Xia et al. “One-Dimensional Nanostructures: Synthesis, Characterization, and Applications”. In: *Advanced Materials* 15.5 (2003). Pp. 353–389. DOI: 10.1002/adma.200390087.

[YF07] Y. Yao and S. Fan. “Si nanowires synthesized with Cu catalyst”. In: *Materials Letters* 61.1 (Jan. 2007). Pp. 177–181. DOI: 10.1016/j.matlet.2006.04.045.

[Yi+06] Y. Yi et al. “Characterization of indium tin oxide surfaces and interfaces using low intensity x-ray photoemission spectroscopy”. In: *Journal of Applied Physics* 100.9 (2006). P. 093719. DOI: 10.1063/1.2361089.

[Yu+08] Linwei Yu et al. “Synthesis, morphology and compositional evolution of silicon nanowires directly grown on SnO_2 substrates”. In: *Nanotechnology* 19 (Dec. 2008). P. 485605.

[Yu+95] G. Yu et al. “Polymer Photovoltaic Cells: Enhanced Efficiencies via a Network of Internal Donor-Acceptor Heterojunctions”. In: *Science* 270.5243 (1995). Pp. 1789–1791. DOI: 10.1126/science.270.5243.1789.

[Zeh+99] R.W. Zehner et al. “Tuning the Work Function of Gold with Self-Assembled Monolayers Derived from $X-[C_6H_4-CC-]nC_6H_4-SH$ ($n = 0, 1, 2$; $X = H$, F, CH_3, CF_3, and OCH_3)”. In: *Langmuir* 15.4 (1999). Pp. 1121–1127. DOI: 10.1021/la981114f.

Titre Cellules photovoltaïques en couches minces à base de silicium nanostructuré et de polymère semiconducteur

Résumé Cette thèse présente un travail exploratoire sur des cellules solaires hybrides, basées sur un matériau inorganique (le silicium) et un polymère (le P3HT). Cette structure a été imaginée pour améliorer les cellules à bas coûts à base de matériaux organiques. Nous démontrons ici sa faisabilité expérimentale et analysons son fonctionnement. L'hétérojonction entre le silicium et le P3HT a été étudiée sur des dispositifs en bicouches planes. Nous montrons qu'elle fournit de l'énergie électrique et que les deux matériaux peuvent contribuer au photocourant. Des rendements de 1,6% ont été obtenus. Un effort constant a été fait pour simplifier et fiabiliser les procédés de fabrication. Deux nouveaux types de silicium nano-structuré ont été développés. Des "nano-éponges", dont la taille typique des pores est de 20 nm, ont été obtenues à l'aide de catalyseurs métalliques par dépôts assistés par plasma à 175 °C. Des nanofils de silicium ont été formés par un procédé inédit : les substrats sont des oxydes transparents conducteurs, les catalyseurs sont générés *in situ* et la température de croissance est inférieure à 300 °C. La phase würtzite a été mise en évidence dans certains fils, et divers modes de croissance ont été observés. Ces deux nouveaux types de couches minces pourront aussi être utilisés dans des cellules solaires inorganiques.

Mots-clés Cellules solaires, hétérojonction, P3HT, nanofils de silicium, PECVD

Title Hybrid thin-film solar cells based on nano-structured silicon and semiconducting polymer

Abstract This thesis presents an exploratory work on a new design of hybrid solar cells, which are based on a junction between an inorganic material (silicon) and a polymer (P3HT). This structure is intended to improve the efficiency of organic based solar cells while maintaining low costs. Here, we investigate its experimental feasibility, and we analyze its performance. The hetero-junction between silicon and P3HT has been studied on bilayer devices. We have shown that this junction generates electrical power under illumination, and that both silicon and P3HT can contribute to the photocurrent. Power conversion efficiencies up to 1.6% have been obtained. A large amount of work has been done to simplify the fabrication process and to improve its reliability. Two new nano-structured silicon layers have been developed. "Nanosponge" layers, where the typical dimension of pores is 20 nm, have been obtained by metal-catalyzed plasma-enhanced CVD at 175 °C. Silicon nanowires have been grown by a completely new process: the substrates are transparent conductive oxides, the catalysts are generated *in situ*, and the growth temperature is below 300 °C. The würtzite (Si-IV) phase has been identified in some wires, and various growth modes are observed. Both kinds of layers may also find applications in inorganic solar cells.

Keywords Solar cells, heterojunction, P3HT, silicon nanowires, PECVD